INSTITUTE *of* TECHNOLOGY SLIGO

# An Investigation into the Keying Behaviour and the Capacity of Plate Anchors in Sand

Bridgeen Barron B.Eng. (Hons.)

This project is submitted in fulfilment of Higher Education and Training Awards Council requirements for the Degree of Master of Engineering

Supervisor: Dr. Conleth O'Loughlin

Submitted to Institute of Technology, Sligo, May 2014

## Declaration

I certify that the material which I submit for assessment leading to the award of M. Eng. is entirely my own work and has not been taken from others, save the extent that such work has been cited and acknowledged within the text of the study.

Signature: …….

## Abstract

This thesis considers the potential of plate anchors as an anchoring option for offshore renewable energy devices such as wave energy converters and floating offshore wind turbines. In this study the performance of a plate anchor vertically installed in sand and subjected to vertical loading has been investigated experimentally. Particular focus was placed on the unrecoverable loss of embedment during the keying process, where the orientation of the plate evolves from vertical to perpendicular to the direction of loading. This is particularly significant for offshore plate anchors as an unrecoverable loss in anchor embedment corresponds with a loss in potential anchor capacity. The loss in embedment during keying was examined for six anchors, all with the same plate geometry, but with anchor padeyes (or load attachment points) that were at differing eccentricities from the plate.

The experiments were conducted at model scale using the geotechnical centrifuge at the Institute of Technology Sligo. To facilitate observation of the anchor orientation and quantification of the loss in embedment during the test, anchor tests were conducted adjacent to a Perspex panel on the centrifuge strongbox. Vertical loading was achieved by pulling a mooring line attached to the anchor padeye at a constant velocity. The location and orientation of the anchor during each anchor test was captured using a high resolution digital camera mounted directly in front of the Perspex panel.

The experimental data show that the loss in embedment of the plate anchor during keying is inversely proportional to the padeye eccentricity, with a padeye eccentricity equal to at least the breadth of the anchor plate giving minimal loss in embedment and hence highest potential anchor capacity. The magnitude of the loss in embedment is very similar to previous findings for clay.

The peak anchor capacity was observed before the end of keying, at a plate orientation between 50 and 80 degrees to the horizontal. Particle image velocimetry was employed to reveal the failure mechanisms during the keying process. These

analyses showed that the peak load corresponds with a sudden transition from a deep localised failure mechanism to a shallow mechanism that extends to the soil surface.

The anchor capacity, expressed in terms of a dimensionless capacity factor, was shown to be in good agreement with previously reported experimental data on pipelines and strip anchors, but only after the peak anchor capacity is exceeded and the anchor behaves like a horizontally oriented anchor subjected to vertical loading. The particle image velocimetry analyses show that the inclination of the slip planes in the shallow failure mechanism are at an angle that is much lower than would be reasonable for a mobilised friction angle. This clearly shows that the normality condition, in which the dilation angle and the friction angle are equal, was not met in these tests and explains why the experimental data are in good agreement with predictions from a limit equilibrium method based on similar principles.

## Acknowledgements

I would like to thank the following people who have kindly contributed in the compilation of this project and without whose help I would have been much disadvantaged.

Firstly, I would like to thank Dr. Conleth O'Loughlin, Associate Professor at the Centre for Offshore Foundation Systems, University of Western Australia whose knowledge and guidance I could not possibly have done without.

I would like to extend my appreciation to Cathal Colreavy for the time he dedicated to the setup of the centrifuge laboratory and Raymond Grennan for his assistance during my period of testing in the centrifuge laboratory. I would also like to thank all my friends.

And finally I would like to express my thanks to my parents, my sisters, brother and my boyfriend for the support and encouragement they have shown me over the years for which I will be eternally grateful.

**Table of Contents**

## List of Figures

## List of Tables

## List of Equations

## Notation

| | |
|---|---|
| A | Area of plate |
| B | Anchor breadth |
| $C_u$ | Coefficient of uniformity |
| $C_z$ | Coefficient of curvature |
| D | Particle diameter size |
| $\delta x$ | Horizontal displacement |
| $\delta z_{plate}$ | Loss of embedment of plate |
| $\delta z_{line}$ | Vertical anchor line displacement |
| e | The perpendicular distance from the centre of the padeye to the centre of the plate |
| g | Earth's gravitational acceleration |
| H | Embedment depth |
| $H_{current}$ | Current embedment depth |
| $H_{initial}$ | Initial embedment depth |
| $H_{sample}$ | Height of sample |
| $h_p$ | Prototype depth |
| $I_D$ | Relative density |
| $K_o$ | At rest coefficient of earth pressure |
| L | Length of anchor plate |
| N | Centrifuge scaling factor (Taylor 1995) |
| $q_c$ | Cone tip resistance |
| R | Distance from the centre of rotation to the surface of the model |
| $R_e$ | Effective radius ($R+2/3H_{sample}$) |
| t | Thickness of anchor plate |
| $\omega$ | Angular velocity of centrifuge (Taylor 1995) |
| $\gamma$ | Unit weight of soil |
| $\Theta$ | Inclination of the plate to the vertical |
| $\gamma'_d$ | Dry density of relevant soil sample |
| $\gamma'_s$ | Particle density of relevant soil sample |
| $\sigma_v$ | Vertical stress |
| $\Psi$ | Angle of dilation |
| $\phi$ | Friction angle |

# CHAPTER 1.0
# INTRODUCTION

## 1.1 Introduction

The requirement for energy in the form of electricity is increasing and is forecasted to continue increasing until 2040 (USIEO 2013) (Figure 1-1). With the depletion of fossil fuel derived electrical energy, energy suppliers are meeting this need by developing devices that extract energy from sustainable resources such as wind and waves. These devices come in the form of wind turbines (Figure 1-2) and wave energy converters (Figure 1-3).

As wind turbines have been in commercial use for many years their design is well established. In more recent years, wind turbines have been deployed offshore as the wind energy resource is higher and more consistent at sea compared with land (EWEA 2009). As offshore development increases, wind farms will be sited in deeper water. In water depths in excess of 50m, it becomes more economical to employ floating rather than fixed bottom wind turbines (Musial *et al.* 2006; Figure 1-4), meaning that the foundation becomes an embedded anchor rather than a monopile, suction caisson or gravity base.

As with floating wind turbines, the majority of wave energy converters (particularly those that oscillate in water) require anchoring. This industry is less mature, with only a few pre-commercial installations worldwide. However as technical maturity grows, commercial deployment of wave energy converters in large integrated arrays (or wave farms) is expected (Ernst & Young Global Ltd., 2013).

The cost of the foundation element for a wave energy device is up to 18% of the installed costs (Figure 1-5, Fitzgerald 2009). An increase in the economic viability of offshore wind turbines and wave energy converters may be realised by reducing either the conservatism in the anchor design, or employing more technically efficient and economical anchor types.

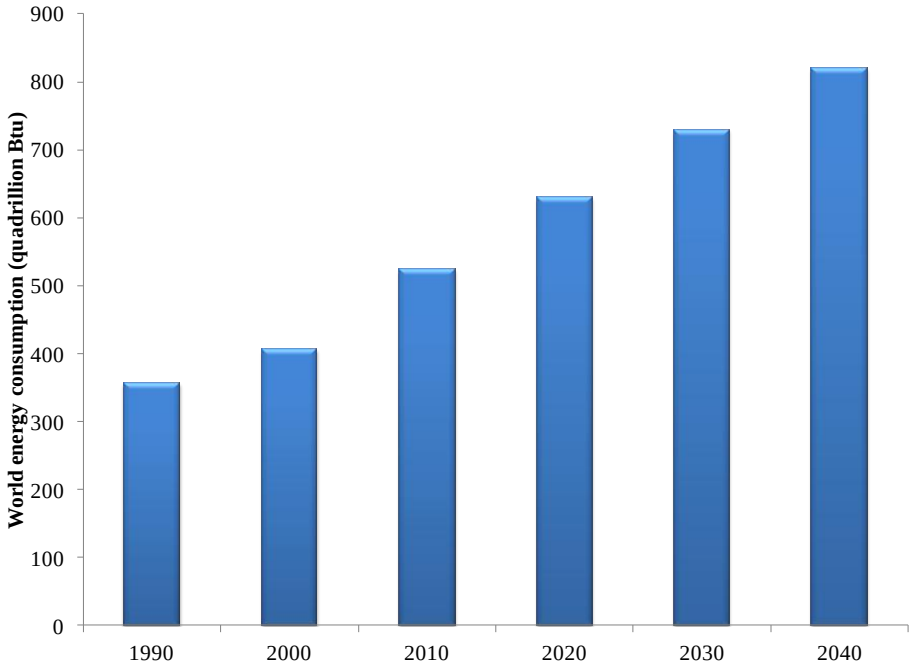


**Figure 1-1 Energy Consumption (after USIEO 2013)**

**Figure 1-2 Wind Turbine Farm (after JoJo Tanks 2013)**


(a)


(b)

(c)

**Figure 1-3 Wave Energy Converters (a) Pelamis (after Pelamis 2013) (b) WaveBob (after Irish Marine Institute 2013) (c) Ocean Energy Buoy (after Ocean Energy 2013)**

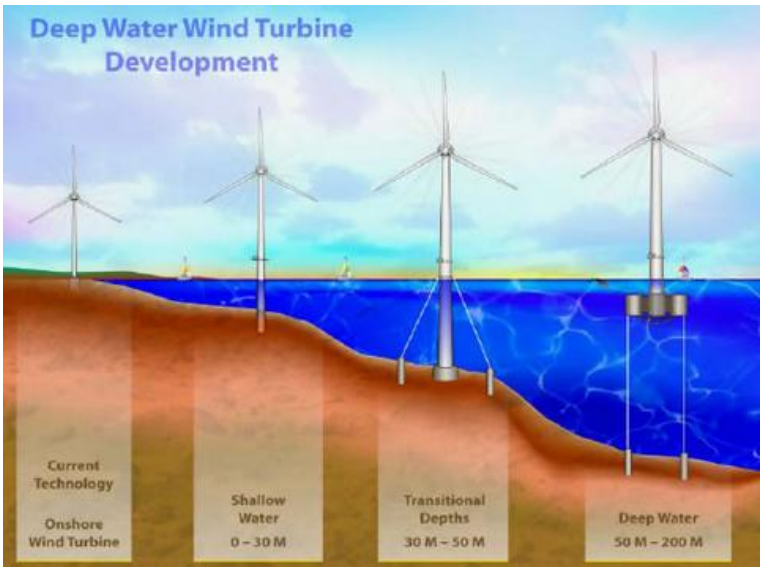


**Figure 1-4 Anchorage into Deeper Waters (after Musial *et al.* 2006)**

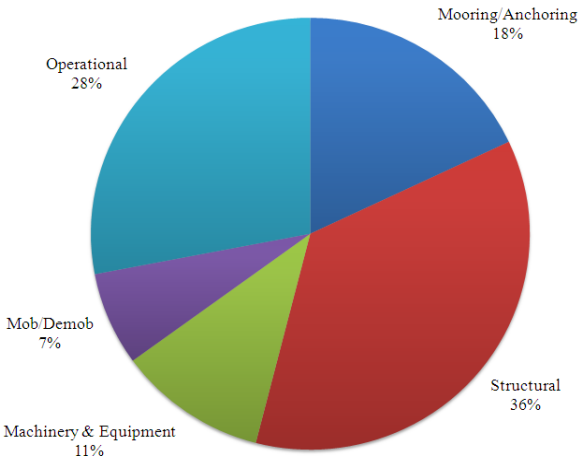


**Figure 1-5 Typical Cost Breakdown for an Offshore Wave Energy (after Fitzgerald 2009)**

## 1.2 Anchoring Options

The oil and gas industry has been mooring large floating facilities for over two decades. These facilities are anchored using either gravity anchors, plate anchors (drag or suction embedment) or piles (driven piles, suction piles or torpedo piles). Of these options the plate anchor is the most technically efficient (O'Loughlin *et al.*, 2006 and Cassidy *et al.*, 2012) as the resistance is derived purely from bearing resistance rather than frictional resistance. Hence a plate anchor would appear to be amongst the most attractive anchoring options for floating ocean energy devices.

Plate anchors are typically installed by dragging along the seabed. The geometry of a drag-in plate anchor is such that dragging causes the anchor to penetrate the seabed. However seabed infrastructure such as existing mooring lines and electrical cables make this model of installation unattractive for wind and wave farms. An alternative approach is to locate a vertical plate at the base of a suction caisson and utilise the caisson to embed the plate anchor. This approach, referred to as a suction embedded plate anchor (SEPLA) has the advantage of known location and embedment depth and avoids the issue of interference with other seabed infrastructure.

The primary stages that the SEPLA undergoes during deployment in clay are illustrated in Figure 1-6 and described below.

*Stage 1 - Suction Installation:* The plate anchor is slotted into the base of the suction caisson and lowered to the seabed. The self-weight of the caisson causes it to penetrate by about half its length. The differential pressure created by pumping water from the interior of the caisson constitutes the driving force to overcome the frictional resistance developed along the caisson wall, until the caisson is fully embedded.

*Stage 2 - Caisson Retrieval:* When the caisson is fully embedded and the plate anchor reaches its design depth, the cassion is retrieved by pumping water back into the caisson, leaving the plate anchor embedded in the seabed in a vertical orientation. When the tip of the cassion reaches the seabed, the caisson is retrieved to the deck of the installation vessel and reused for the next installation.

*Stage 3 - Anchor Keying:* The mooring line connected to the padeye of the plate is tensioned causing the anchor to rotate or 'key'. During this process the plate anchor undergoes unrecoverable embedment loss.

*Stage 4 - Mobilised Anchor:* The anchor has completed keying and is approximately perpendicular to the loading direction at the padeye, maximising the anchor capacity by presenting the maximum projected area to the direction of loading.

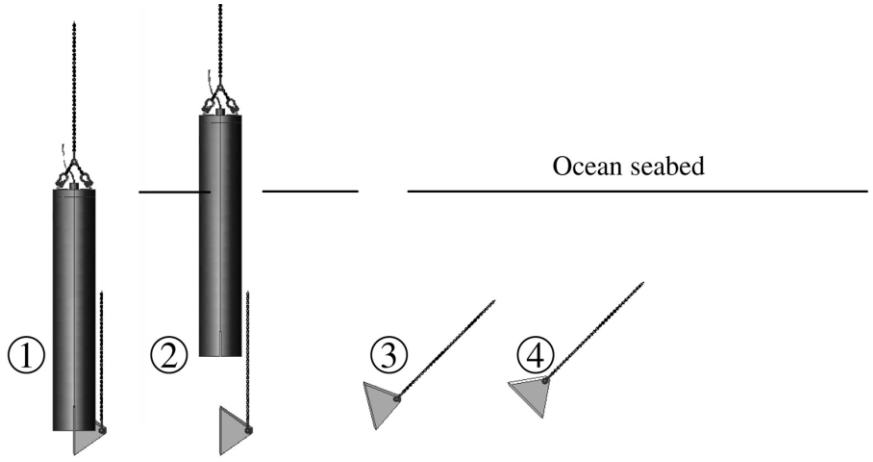


**Figure 1-6 The SEPLA concept (after O'Loughlin *et al.* 2006): (1) Suction Installation (2) Caisson Retrieval (3) Anchor Keying (4) Mobilised Anchor**

The most critical aspect of the SEPLA is the prediction of the loss of embedment the plate anchor undergoes during the keying process (Wilde *et al.* 2001; O'Loughlin *et al.* 2006; Cassidy *et al.* 2012) as a non-recoverable loss in embedment translates to a loss in potential anchor capacity that must be quantified for design.

SEPLAs have been used and studied in clay as this is the dominant soil type in deep water oil and gas developments for which they are suited (O'Loughlin *et al.*, 2006; Gaudin *et al*,, 2009)). Whilst plate anchors have been used and studied in sand, these cases have been limited to either vertically installed plate anchors subjected to horizontal loading or vertically installed plate anchors subjected to horizontal loading. Ovesen (1981), Murray & Geddes (1987) and Dickin (1994) are some of the authors that have addressed the performance of vertically installed plate anchors subjected to horizontal loading in sand (Figure 1-7 (a)). Das *et al.* (1977), Rowe and Davis (1982) and Merifield and Sloan (2006) have reported on vertical installed plate anchors subjected to horizontal loading (Figure 1-7 (b)). To the author's knowledge, there are no studies that have considered the performance of vertically installed plate anchors in sand subjected to vertical loading (Figure 1-7 (c)), a problem which couples keying and capacity mobilisation. This is the focus of the work described in this thesis.

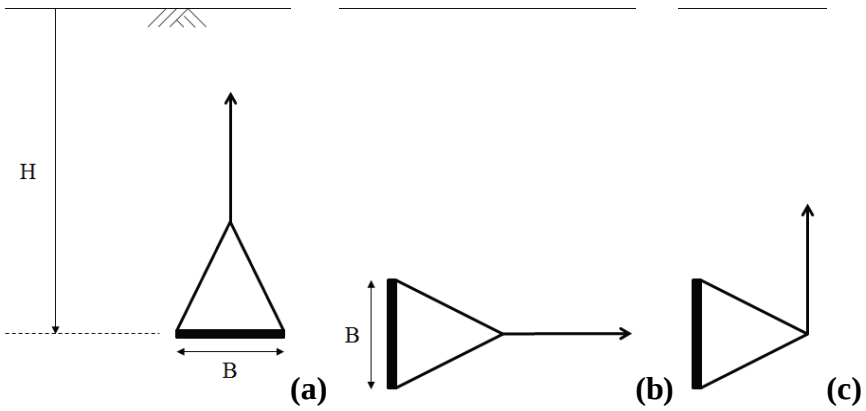


**Figure 1-7 Orientation & Pullout Inclination of Plate Anchors (a) Vertically Loaded Horizontal Anchor (b) Horizontally Loaded Vertical Anchor (c) Vertically Loaded Vertical Anchor**

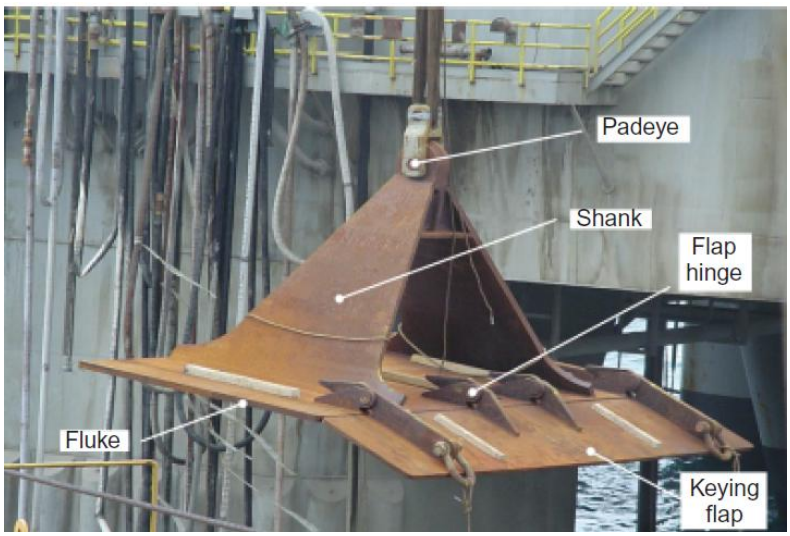


**Figure 1-8 Typical Plate Anchor (after Cassidy *et al.* 2012)**

## 1.3 Objectives

The main objective of this study is to determine if a plate anchor is a viable option for anchoring floating offshore renewable energy devices. This objective will be met by quantifying the influence of the eccentricity ratio on the loss of embedment the plate anchor undergoes during keying and by quantifying the post keying anchor capacity. Installation aspects of the problem are not addressed in this study.

## 1.4 Thesis Structure

The thesis is divided into six chapters. The content of each chapter is described below.

*Chapter 2 - Literature Review:* The chapter initially provides an overview of the existing research on keying of plate anchors in clay (as no data currently exist for sand). The chapter then focuses on the capacity of horizontally embedded plate anchors in sand subjected to vertical loading.

*Chapter 3 – Methodology:* In the initial section of this chapter the principles of geotechnical centrifuge modelling are summarised. A description of the geotechnical centrifuge used in this study is then provided, together with details of the model anchors and the other test apparatus used in the experiments. This chapter

concludes with an account of the procedures followed for sample preparation, test setup, anchor testing and post test analysis.

*Chapter 4 – Results:* In this chapter the results of the sample characterisation and the measured data from the centrifuge tests conducted at 30g are presented.

*Chapter 5 – Discussion:* This chapter provides a detailed interpretation of the test data. The measured loss in embedment during keying is compared with equivalent data for plate anchors in clay. Plate anchor capacity is interpreted as an anchor capacity factor and this factor is compared with previous data and predictions from analytical models.

*Chapter 6 - Conclusion and Recommendations for Further Research:* All major findings are summarised and recommendations for future studies are provided.

# CHAPTER 2.0
# LITERATURE REVIEW

## 2.1 Introduction

In this chapter a review of the published literature focusing on the keying behaviour of plate anchors in clay and the normalised capacity factor for both strip and plate anchors is presented. The studies reviewed include those that have reported on the typical loss of embedment incurred by a plate anchor during keying, the influence of the eccentricity ratio and aspect ratio on the keying process and the influence of the loading angle on the loss of embedment. The latter half of this chapter focuses on the influence of sample density, aspect ratio, embedment depth on the capacity of plates and pipes in sand. These studies include experiments that have been conducted on the laboratory floor, at elevated gravity in a centrifuge and numerical analyses.

## 2.2 Plate Anchors

Before considering previous studies on plate anchors, the notation used here to describe a plate anchor is provided on Figure 2-1.

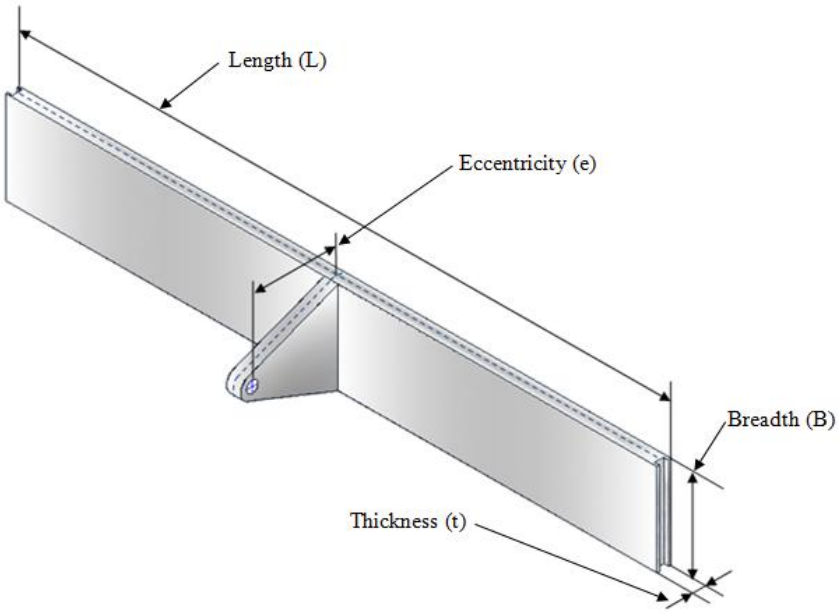


**Figure 2-1 Plate Anchor Geometrical Notation**

Various geometrical ratios are considered in this chapter and throughout the thesis. These include the anchor aspect ratio (L/B) which is the plate length (L) as a ratio of its breadth (B), the anchor thickness ratio (t/B) which is the plate thickness (t) as a ratio of its breadth (B) and the eccentricity ratio, which is the eccentricity of the padeye (e) as a ratio of this breadth (B).

## 2.3 Keying

Keying of a vertically installed plate anchor initiates when sufficient force develops in the mooring line connected to the padeye of the plate anchor. This force causes the plate anchor to rotate or "key" from the initially vertical orientation to an orientation that is near perpendicular to the direction of loading at the padeye. In this way the maximum projected plate area is presented to the direction of loading, maximising the potential plate anchor capacity. However during this process the plate undergoes an irrecoverable loss of embedment. Quantifying this loss in embedment is critical for design, as the plate anchor capacity is determined by the local strength of the soil in the vicinity of the plate and this typically increases with soil depth. Previous studies on keying of plate anchors have focused solely on clay as this is the dominant soil type for oil and gas applications for which SEPLAs have been used (O'Loughlin *et al.*2006; Song *et al.* 2006; Gaudin *et al.* 2009a). To the author's knowledge there have been no previous studies on the keying behaviour of a vertically embedded plate anchor in sand. As such this section reviews previous studies addressing the keying of plate anchors in clay.

### 2.3.1 O'Loughlin *et al.* (2006)

O'Loughlin *et al.* (2006) investigated the performance of a plate anchor with a length L of 80mm and an eccentricity ratio, e/B = 0.17, 0.5 and 1 in centrifuge tests using normally consolidated kaolin clay (Figure 2-2). The anchor tests were conducted at 100g against a Perspex window (Figure 2-3). Digital images were captured during each anchor test and were used to determine the orientation of the plate anchor and the loss of embedment (Figure 2-4, Figure 2-5 and Figure 2-6). As shown by Figure 2-7 and Figure 2-8, the loss of embedment that the plate anchor undergoes during keying is dependent upon the eccentricity ratio. It is evident that plate anchors with an eccentricity ratio, e/B = 0.5 and 1 undergo negligible loss of embedment

compared to a plate anchor with an eccentricity ratio, e/B = 0.17. Figure 2-8 illustrates the influence of the eccentricity ratio on the loss of embedment, $\Delta z_e$ (where $\Delta z_e = \delta z_{plate}$ is the plate displacement). The loss of embedment reduced from 1.5B at e/B = 0.17 to approximately zero for e/B ≥ 1. Consequently O'Loughlin *et al.* (2006) recommended that the eccentricity ratio, e/B should be at least equal to 1.

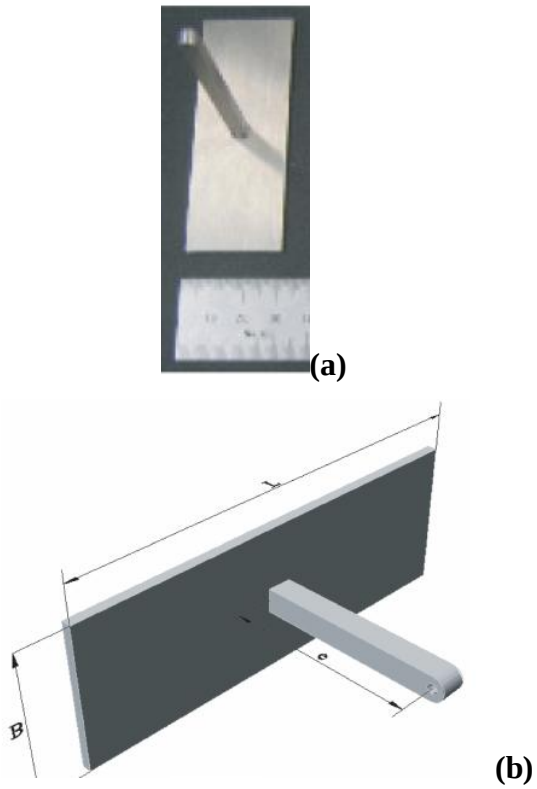


**Figure 2-2 Model Plate Anchors (a) Photograph (b) Schematic of Geometrical Notation (after O'Loughlin *et al.* 2006)**

**Figure 2-3 Testing Chamber with Installed Anchor (after O'Loughlin *et al.* 2006)**

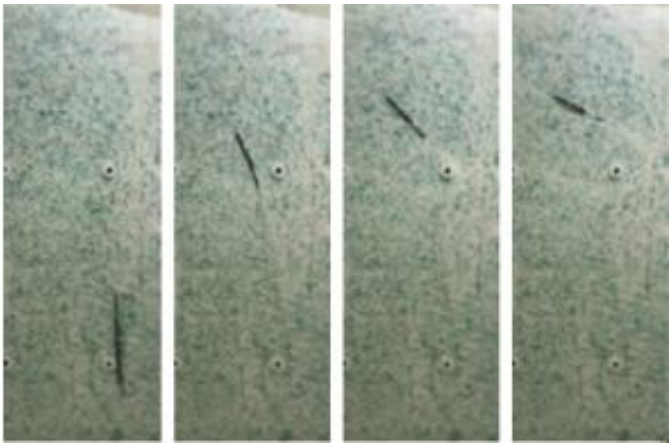

Initial Position Point A | 20° Point B | 40 ° Point C | 60° Point D

**Figure 2-4 Plate Rotation during Keying (e/B = 0.17) (after O'Loughlin *et al.* 2006)**

Initial Position Point A | 20° Point B | 40° Point C | 60° Point D

**Figure 2-5 Plate Rotation during Keying (e/B = 0.5) (after O'Loughlin *et al.* 2006)**

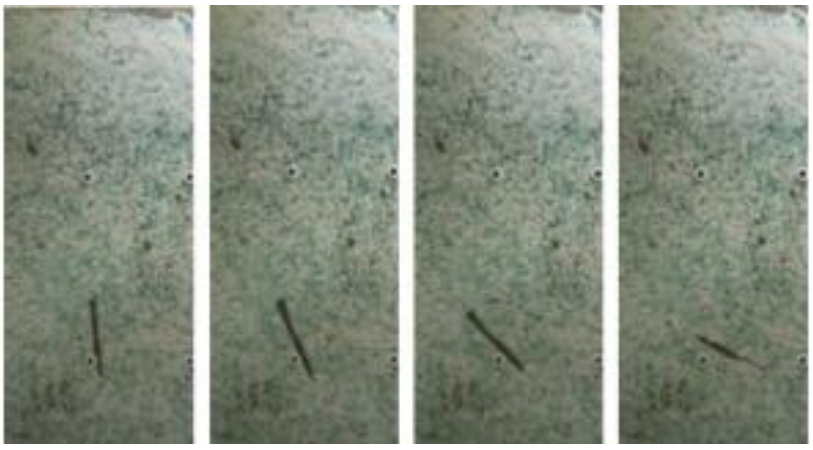

Initial Position Point A | 20° Point B | 40 ° Point C | 60° Point D

**Figure 2-6 Plate Rotation during keying (e/B = 1) (after O'Loughlin *et al.* 2006)**

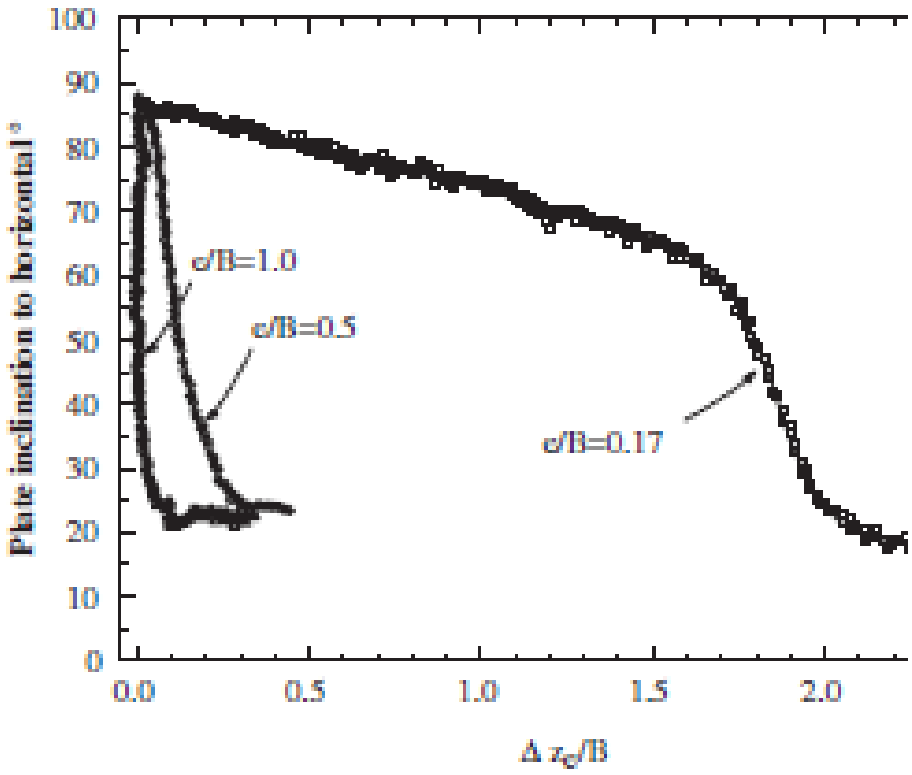


**Figure 2-7 Plate Rotation (90° - Θ vs. $\delta z_{plate}/B$) (after O'Loughlin *et al.* 2006)**

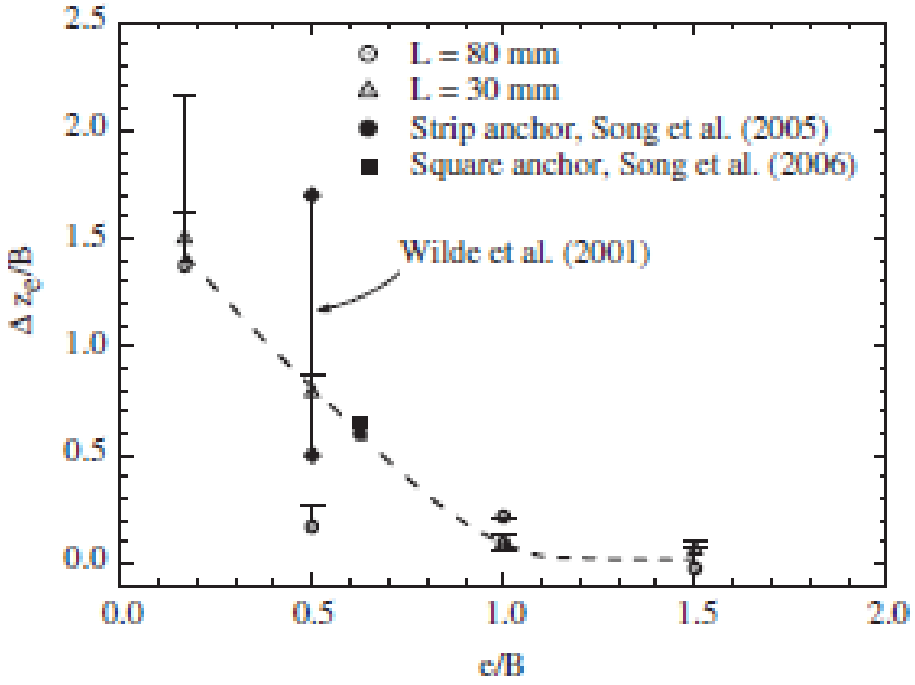


**Figure 2-8 $\delta z_{plate}/B$ vs. e/B at Peak Load (after O'Loughlin *et al.* 2006)**

### 2.3.2 Song *et al.* (2006)

Song *et al.* (2006) performed anchor tests on vertically installed plate anchors to investigate the influence of various loading inclinations on the keying behaviour. The tests were conducted in a drum centrifuge at 100g using a transparent soil sample with an undrained shear strength of 18kPa (Figure 2-9). The plate anchor used in this study was square, 40 × 40mm with a thickness of 2.50mm and an eccentricity ratio, e/B = 0.625 (Figure 2-10).

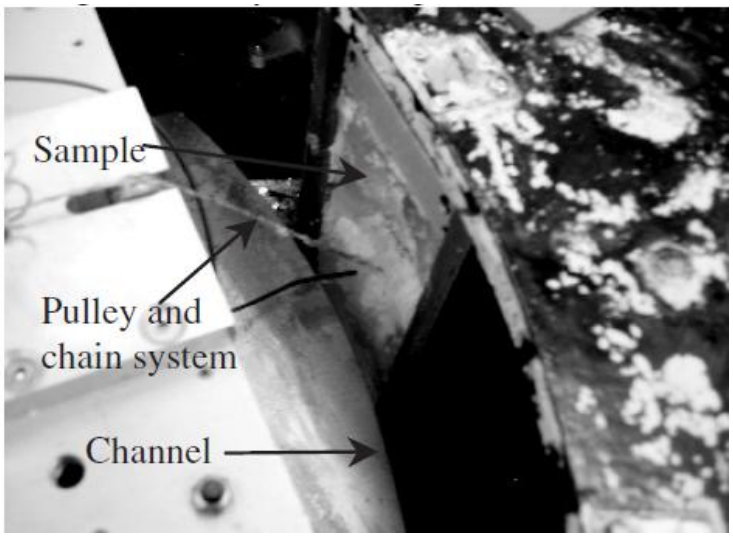


**Figure 2-9 Drum Centrifuge Test Setup in Transparent Soil Sample (after Song *et al.* 2006)**

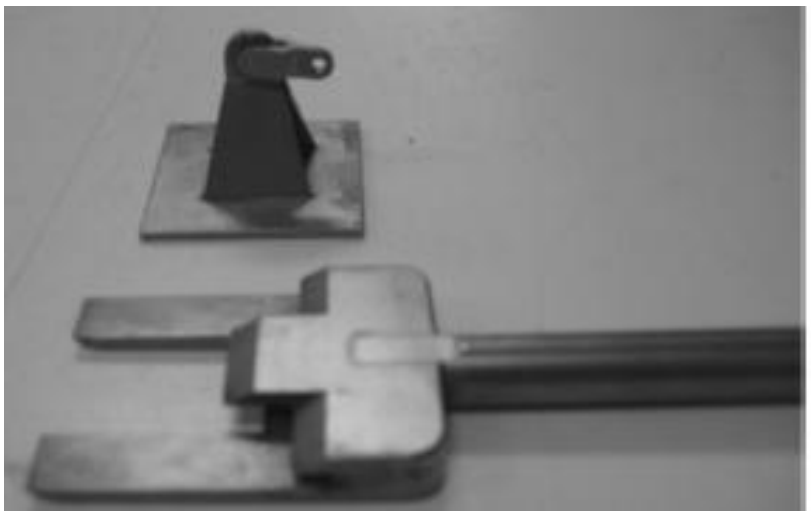

**Figure 2-10 Plate Anchor (after Song *et al.* 2006)**

Pre-embedded beads in the sample were used to observe and quantify the displacement of the soil around the plate anchor during each anchor test. A digital camera, placed in front of the Perspex window on the side of the sample allowed images to be captured during the keying process, from which the orientation of the anchor and the soil movement was measured.

Song *et al.* (2006) identified five main phases of the keying and pullout process for a square anchor with an eccentricity ratio, e/B = 0.625. The five phases are shown on the load – displacement response (Figure 2-11) and the corresponding anchor orientation is shown in Figure 2-12 for a vertical pullout. A summary is provided below:

*Point 1'- 2':* In this phase the anchor chain tightens but the anchor does not move.

*Point 2'- 3':* In this phase the padeye of the anchor moves vertically causing the plate to initiate rotation. Note that the influence of the anchor movement on the surrounding soil is clearly illustrated by the movement of the beads in the vicinity of the plate anchor.

*Point 3'- 4':* In this phase the plate anchor continues to rotate and experiences a loss of embedment. The capacity of the anchor increases rapidly as the plate anchor becomes normal to the loading inclination.

*Point 4'- 5':* In this phase the anchor has fully rotated and continues to displace at a constant orientation.

Song *et al.* (2006) reported that for the plate anchor to fully rotate in the transparent sample the plate anchor undergoes a vertical displacement $\delta z_{plate}$ = 0.65B for vertical loading and 0.33B for a loading inclination of 60 degrees. The capacity was shown to be independent of the load inclination.

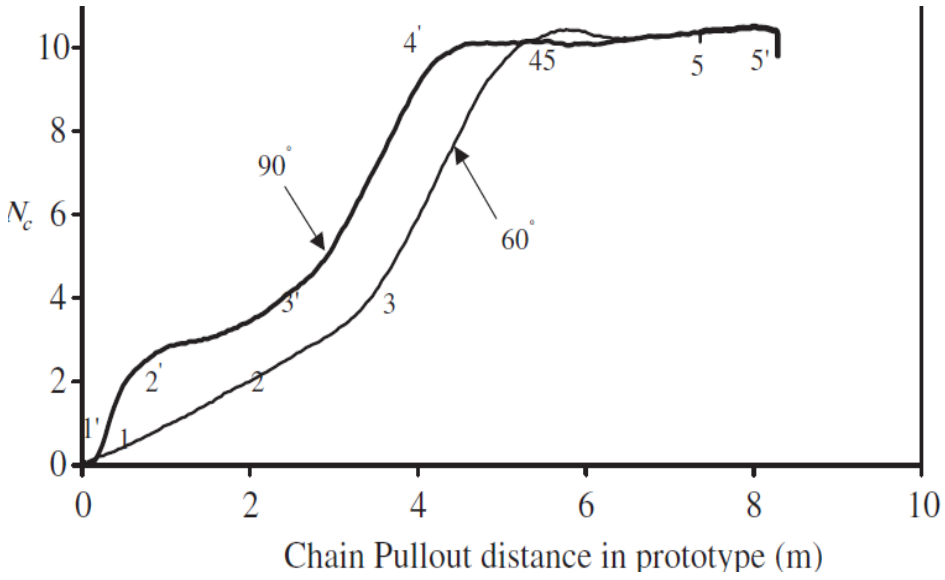


**Figure 2-11 Load – displacement Response during Pullout and Keying (Line Displacement) (after Song *et al.* 2006)**

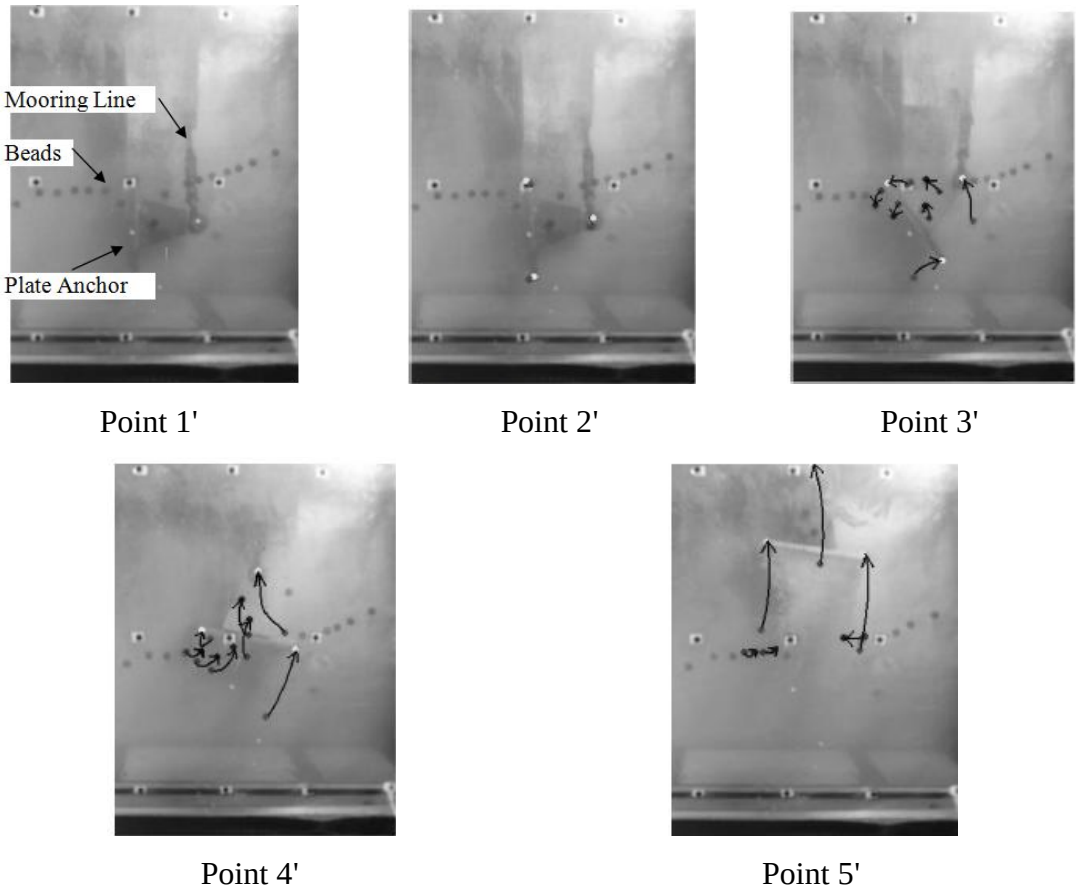


**Figure 2-12 Anchor Orientation during Anchor Test (after Song *et al.* 2006)**

### 2.3.3 Gaudin *et al.* (2009a)

Gaudin *et al.* (2009a) reported on the influence of varying the loading inclination of plate anchors. This experimental study considered two plate anchors with an eccentricity ratio, e/B = 0.25 and 1, but both with an aspect ratio, L/B = 4 (Figure 2-13). In total ten anchor tests in normally consolidated kaolin clay were conducted at 100g in a drum centrifuge (Figure 2-14). As in the O'Loughlin *et al.* (2006) study, the anchor tests were conducted against a Perspex window, which allowed digital images of the anchor-Perspex interface to be captured during keying (Figure 2-15). Gaudin *et al.* (2009a) reported on the failure mechanisms, loss of embedment, influence of the loading inclination and the impact of the eccentricity ratio on anchor keying.

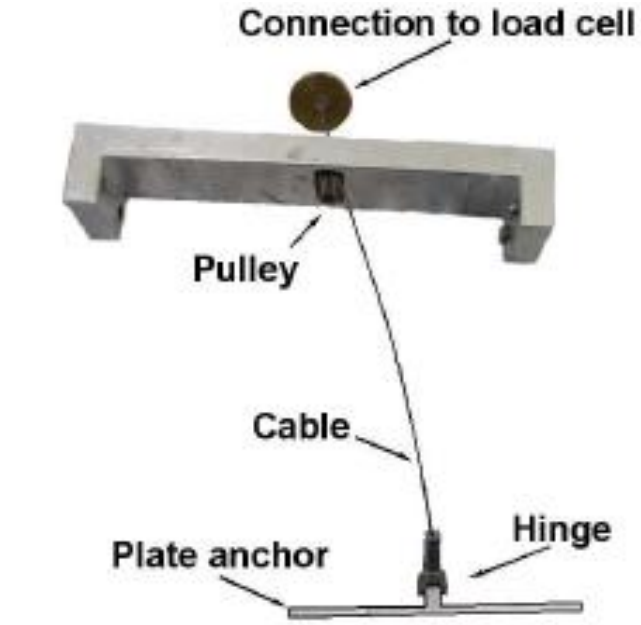


**Figure 2-13 Setup (a) Anchor Model (b) Sample Box (after Gaudin *et al.* 2009a)**

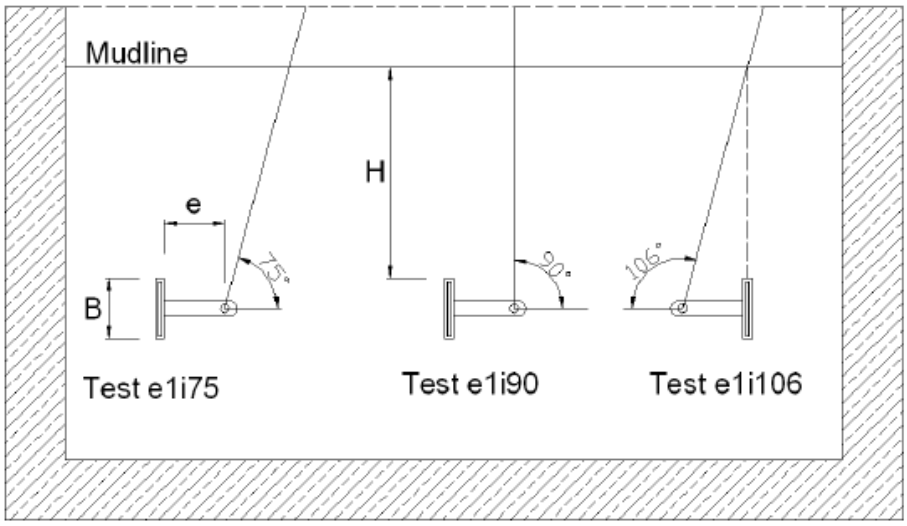


**Figure 2-14 Test setup (after Gaudin *et al.* 2009a)**

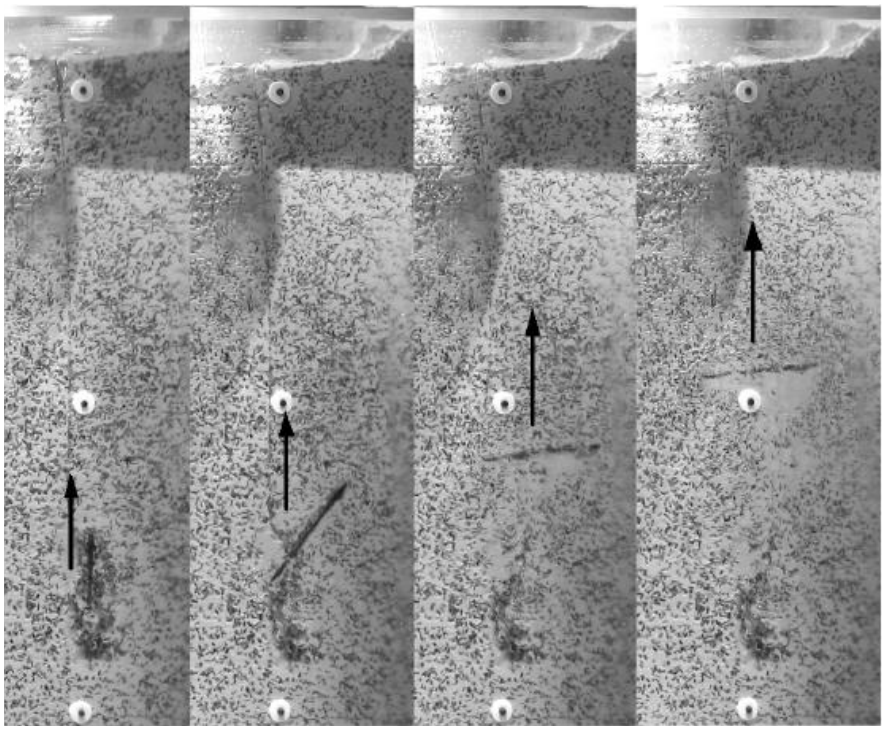

**Figure 2-15 Anchor Orientation at Four Different Successive Stages during a Vertical Pullout (e/B=0.25) (after Gaudin *et al.* 2009a)**

Particle Image Velocimetry (PIV) analyses were used to identify the failure mechanism of the soil in the vicinity of the plate anchor during keying and pullout. The PIV analyses demonstrated a deep failure mechanism for an initial embedment depth of 3B and an eccentricity ratio, e/B = 1, which developed with a fast rotation of the plate anchor without substantial loss of embedment. Gaudin *et al.* (2009a)

also showed that as the eccentricity ratio increases the loss of embedment decreases as a higher eccentricity ratio mobilises a larger failure mechanism during the keying process (see Figure 2-16 and Figure 2-17).

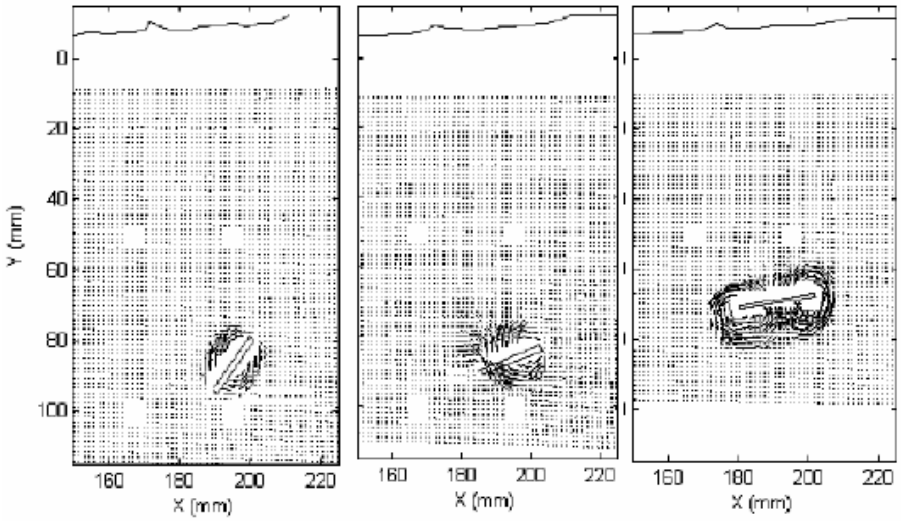


**Figure 2-16 Failure Mechanism (e/B = 1) (after Gaudin *et al.* 2009a)**

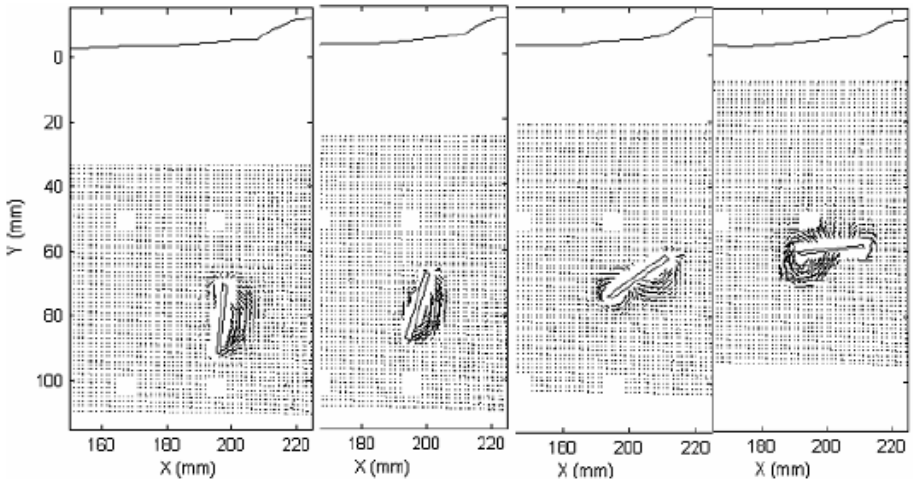


**Figure 2-17 Failure Mechanism (e/B = 0.25) (after Gaudin *et al.* 2009a)**

Gaudin *et al.* (2009a) quantified the loss of embedment with respect to the loading inclination for each eccentricity ratio group. Figure 2-18 shows that for e/B < 1, vertical loading causes higher loss of embedment than a plate anchor pulled a lower inclination.

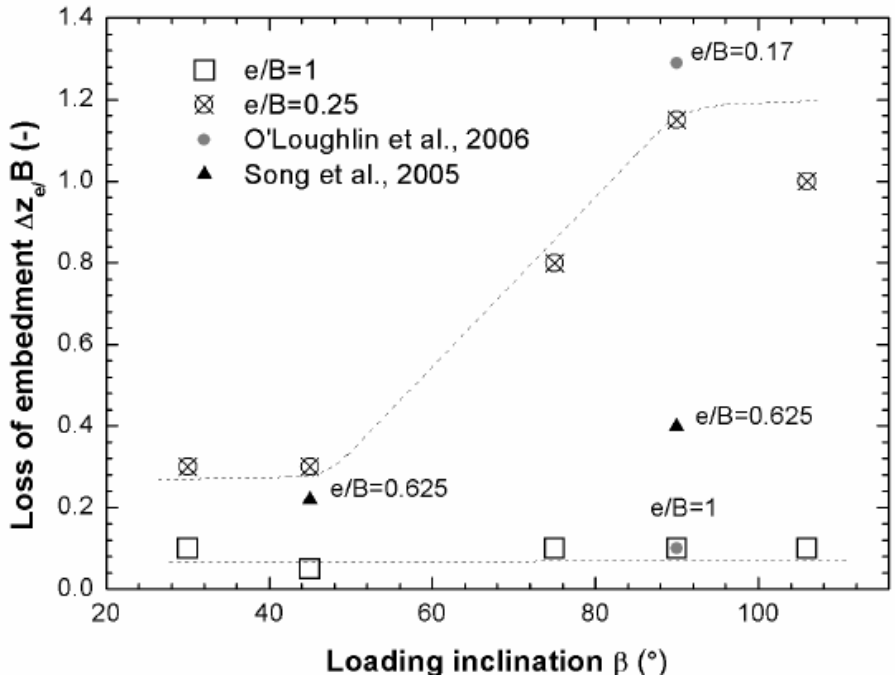


**Figure 2-18 Loading Inclination vs. Loss of Embedment ($\delta z_{plate}/B$) (after Gaudin *et al.* 2009a)**

### 2.3.4 Song *et al.* (2009)

Song *et al.* (2009) reported results from centrifuge tests on transparent soil and large deformation finite element (LDFE) analyses that investigated the influence of anchor geometry, anchor submerged unit weight and loading angle on the loss of embedment a plate anchor undergoes during the keying process.

Song *et al.* (2009) quantified the influence of the thickness ratio t/B on the loss of embedment, $\delta z_{plate}$ and found that as the thickness ratio increases, the loss of embedment decreases (Figure 2-20). Regardless of the plate thickness, an eccentricity ratio, e/B = 1 was found to be optimum eccentricity ratio.

Song *et al.* (2009) used the results from the centrifuge tests and the finite element analyses to develop an expression to determine the loss of embedment of a plate anchor. In their analyses they found that the loss of embedment could be expressed as Equation 2-1.

$$\frac{\delta z_{plate}}{B} = \frac{n}{\left(\frac{e}{B}\right)\left(\frac{t}{B}\right)^{0.3}\left(\frac{M_0}{ABs_u}\right)^{0.1}}$$ **Equation 2-1**

where the anchor geometry coefficient $\left(\frac{e}{B}\right)\left(\frac{t}{B}\right)^{0.3}\left(\frac{M_0}{ABs_u}\right)^{0.1}$ combines the geometrical effects that have an effect on embedment loss during keying, ($\frac{t}{B}$is the thickness ratio (where t is the thickness and B is the anchor breadth), $A$ is the area of the anchor plate, $s_u$ is the undrained shear strength and $M_0$ is the initial moment about the anchor centre(Figure 2-19)). The exponent n = 0.15 for a best fit to the data, and n = 0.2 could be used as a conservative design estimate.

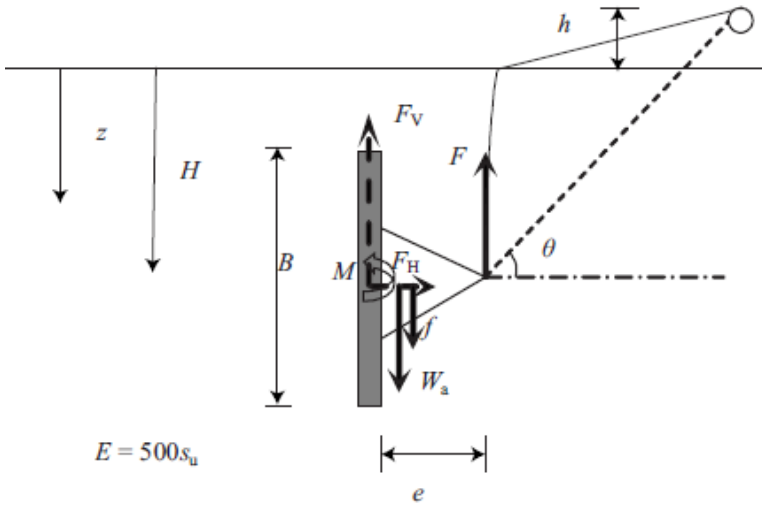


**Figure 2-19 Schematic of Anchor Notation (after Song *et al.* 2009)**

Song *et al.* (2009) recommended that the anchor geometry co-efficient $\left(\frac{e}{B}\right)\left(\frac{t}{B}\right)^{0.3}\left(\frac{M_0}{ABs_u}\right)^{0.1}$ should be at least 0.3, such that the loss in embedment during keying does not exceed two thirds of the plate height.

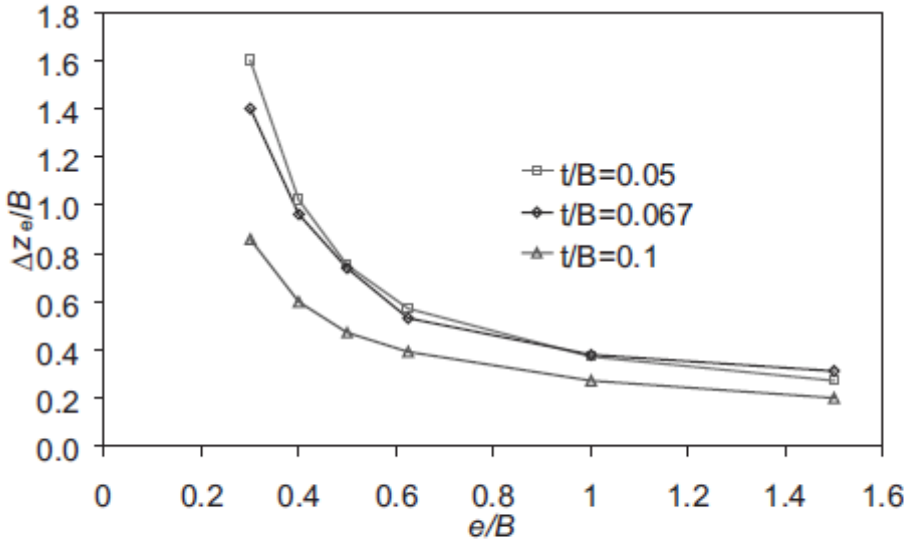


**Figure 2-20 Influence of Anchor Thickness on the Loss of Embedment (after Song *et al.* 2009)**

Song *et al*. (2009) reported that the loss of embedment the plate anchor undergoes to reach the final angle of rotation increases when the loading angle increases (Figure 2-21). It was found that when the plate anchor was subjected to a vertical loading the plate anchor experienced a loss of embedment of 0.5B to reach its final rotation. However, when the plate anchor was subjected to a loading inclination of 30° to the horizontal, the plate anchor experienced a loss of embedment of approximately 0.27B to reach its final rotation.

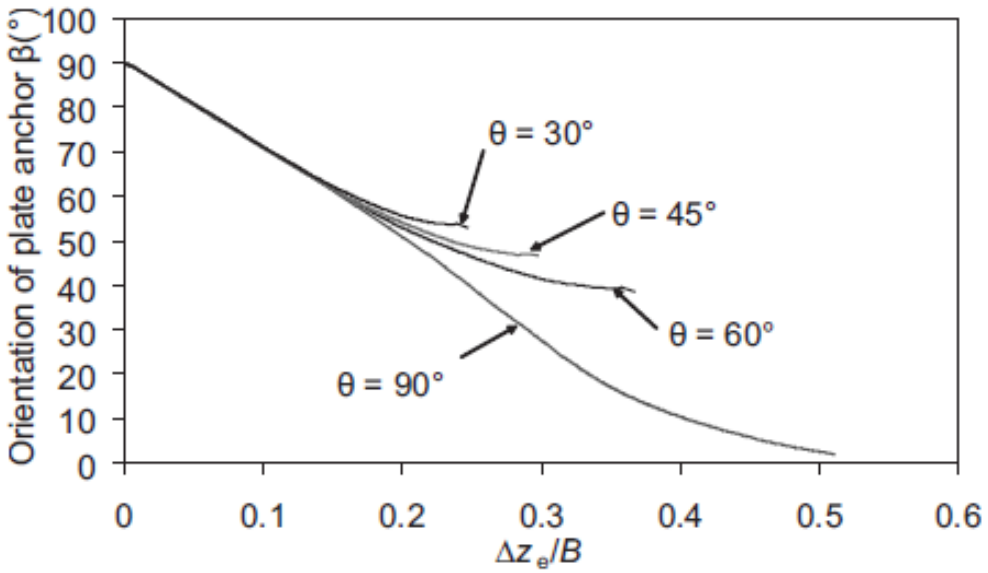


**Figure 2-21 The Effect of Loading Angle on the Loss of Embedment (e/B = 0.625, t/B = 0.05 and $\gamma_a'$ = 60kN/m$^3$) (after Song *et al.* 2009)**

### 2.3.5 Wang *et al.* (2011)

Wang *et al.* (2011) used 2D and 3D LDFE analyses to understand the keying process and to predict the loss of embedment of plate anchors in clay. The results of this study used centrifuge data reported by O'Loughlin *et al.* (2006) and Gaudin *et al.* (2009a). This study identified several factors that influence the loss of embedment of a plate anchor as summarised in Equation 2-2 below:

$$\frac{\delta z_{plate}}{B} = f\left\{\left(\frac{e}{B}\right),\left(\frac{B}{L}\right),\left(\frac{t}{B}\right),\left(\frac{s_{u0}}{\gamma' B}\right),\left(\frac{E}{s_u}\right),\left(\frac{kB}{s_{u0}}\right),\left(\frac{\gamma'_a t}{B s_{u0}}\right)\right\} \qquad \textbf{Equation 2-2}$$

where $\left(\frac{e}{B}\right)$ is the eccentricity ratio, $\left(\frac{B}{L}\right)$ is the aspect ratio (L is the anchor length), $\left(\frac{t}{B}\right)$ is the thickness ratio, $\left(\frac{s_{u0}}{\gamma' B}\right)$ is the local strength ratio (where $s_{u0}$ is the local soil strength at the initial embedment depth of the anchor), $\left(\frac{E}{s_u}\right)$is the soil rigidity index (soil stiffness ratio) (where $E$ is Young's Modulus and $s_u$is the undrained shear strength) and $\left(\frac{kB}{s_{u0}}\right)$ is the soil non-homogeneity index (where $k$ is the soil strength gradient).

Of these groups, Wang *et al*. (2011) concluded that the most influential on the loss of embedment of a plate anchor during keying are the anchor geometry, the soil strength and the loading eccentricity ratio.

Wang *et al.* (2011) showed that their LDFE model gave good agreement with the results. A numerical parametric study led to the following expression for the loss of embedment of a square plate anchor subjected to a vertical loading:

$$\frac{\delta z_{plate,max}}{B} \approx a\left\{\left(\frac{e}{B}\right)\left(\frac{t}{B}\right)^{p}\right\}^{q} \qquad \textbf{Equation 2-3}$$

where $\delta z_{plate,max}$ is the ultimate loss in anchor embedment and the coefficients a = 0.144, p = 0.2 and q = -1.15. They recommend that Equation 2-3 can be used as an upper bound expression for embedment loss for rectangular anchors with aspect ratios greater than 2.54.

The most significant factor that controls the loss of embedment has been found to be the eccentricity ratio (Figure 2-22). Wang *et al.* (2011) recommended that the eccentricity ratio of a plate anchor should never be less than 0.5B.

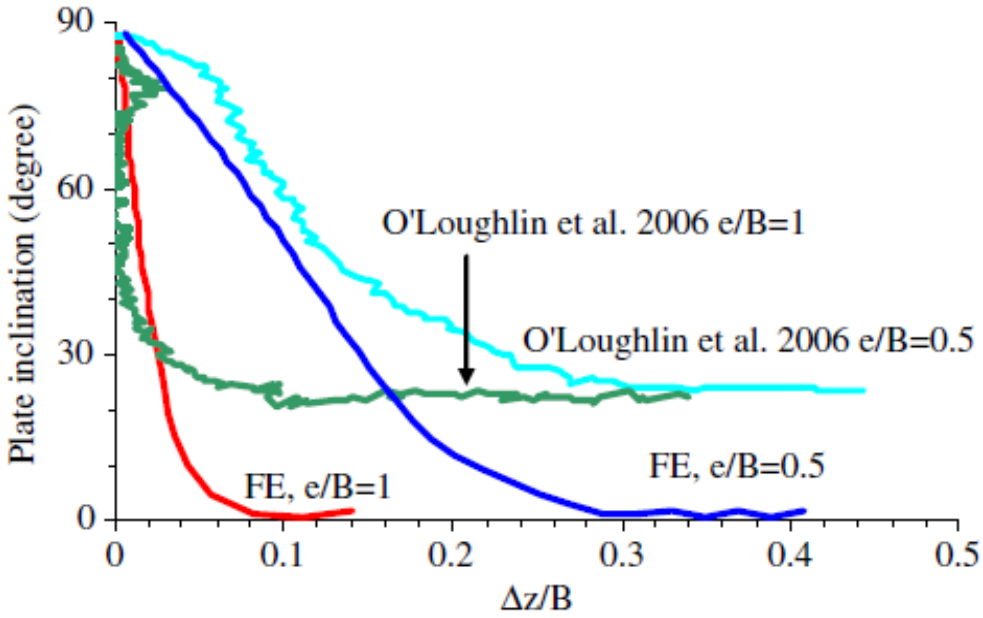


**Figure 2-22 Keying Responses of Strip Anchors in Kaolin Clay (Vertical Loading) (after Wang *et al.* 2011)**

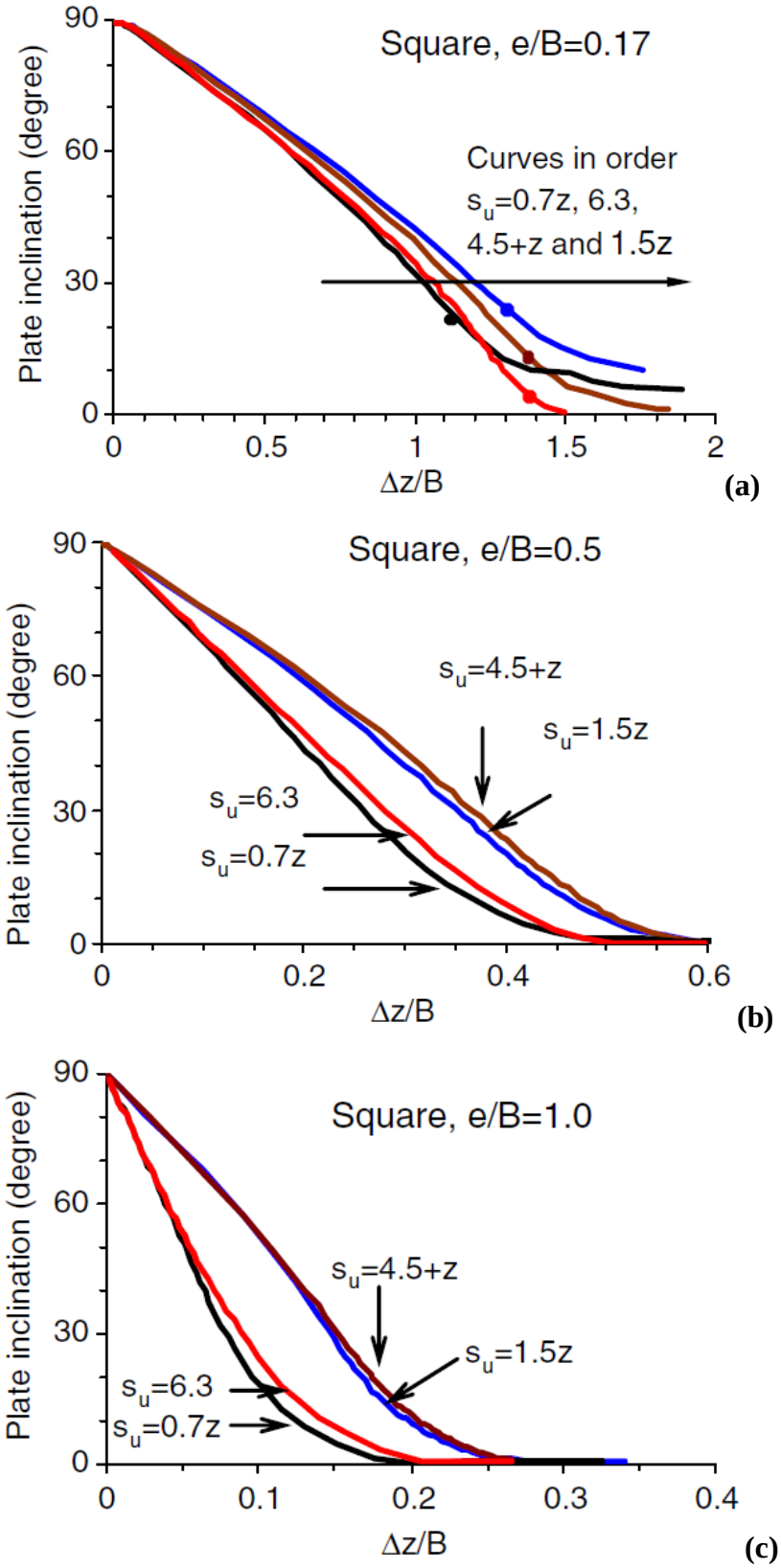


**Figure 2-23 Effect of soil strength profile on the keying response of square anchors (a) e/B = 0.17, (b) e/B = 0.5 and (c) e/B = 1**

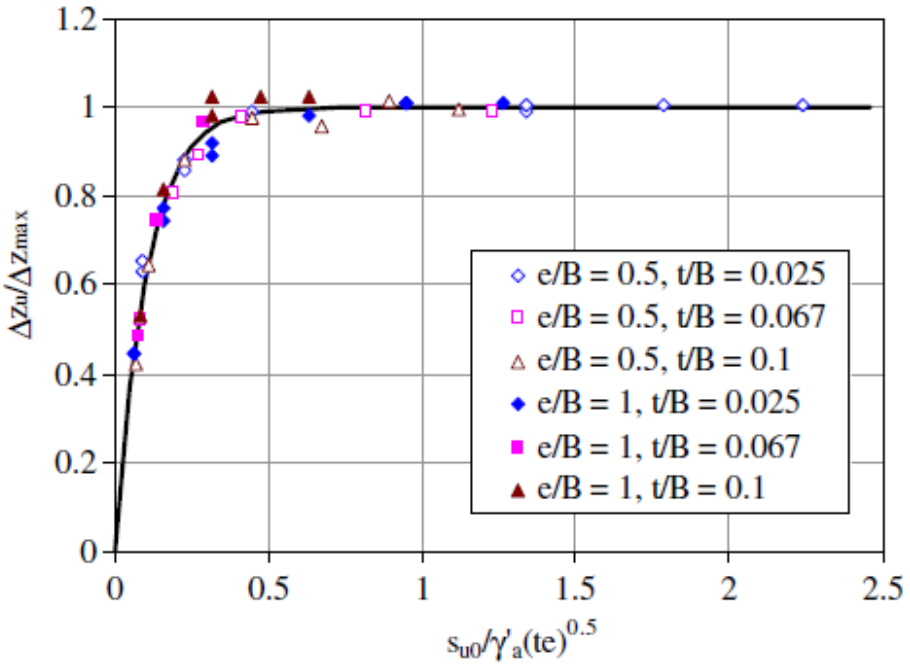


**Figure 2-24 Effect of the Anchor thickness on the Ultimate Loss of square Anchors (Vertical Loading) (after Wang *et al.* 2011)**

### 2.3.6 Cassidy *et al.* (2012)

Cassidy *et al.* (2012) describe a plasticity model developed to assess the keying of a plate anchor in clay. The motion of the plate (Figure 2-25) during keying was determined using a yield envelope for combined (vertical, horizontal and moment) loading and an associated flow rule. Results computed using the plasticity model were verified using centrifuge data and results from LDFE analyses.

**Figure 2-25 Model Anchor with Keying Flap (after Cassidy *et al.* 2012)**

This plasticity model allows for a thorough assessment of the influence of altering the location of the padeye (eccentrically from the plate and vertically from the top of

the plate) and changing the soil conditions and the loading inclination. In this study it was reported that increasing the distance of the padeye from the top of the plate anchor decreases the loss of embedment and the capacity of the anchor due to the sliding trajectory of the anchor (Figure 2-26). The disadvantage of increasing the distance of the padeye from the top of the anchor was found to be offset as the anchor has the opportunity to increase its embedment depth and thus the potential bearing capacity. The loss of embedment ranged from 0.2B to 1.5B for loading inclinations of 40° to 90° from the horizontal.

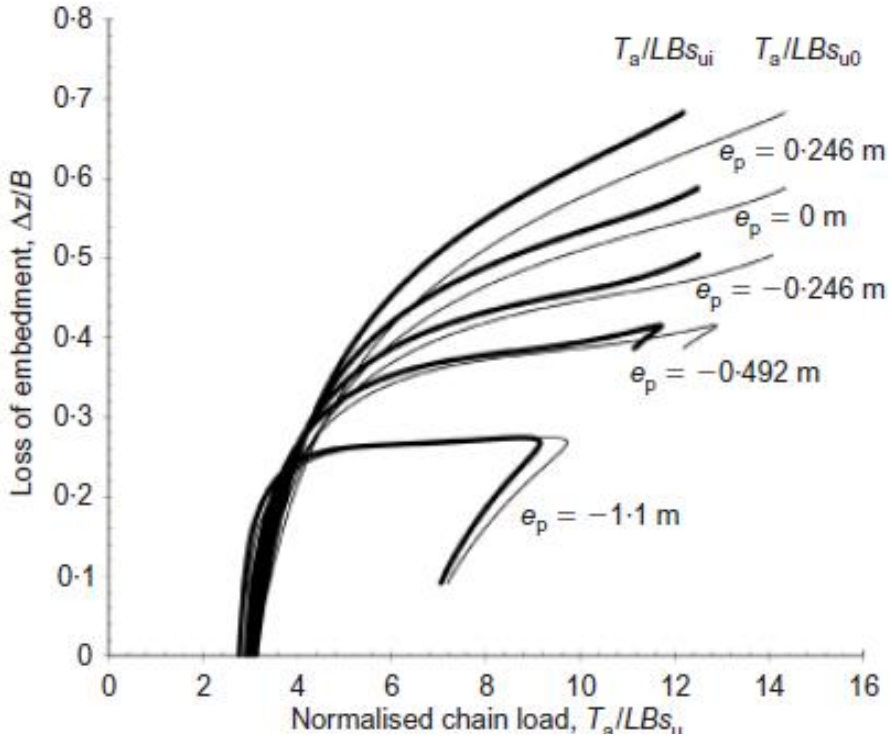


**Figure 2-26 Loss of Embedment ($\delta z_{plate}/B$) vs Normalised chain Load (after Cassidy *et al.* 2012)**

Cassidy *et al.* (2012) suggest that the optimum padeye offset is dependent on the strength gradient of the soil. Figure 2-27 illustrates that as the strength gradient increases, the effectiveness of $e_p$ becomes more prevalent such that the optimum offset for a strength gradient k = 0.313kPa/m is $e_p/B$ = 0.053 and for a strength gradient k = 2.5kPa/m is $e_p/B$ = -0.237 ($e_p/B < 0$, the padeye location is lower than the central point of B, where $B = B_{flap} + B_{plate}$).

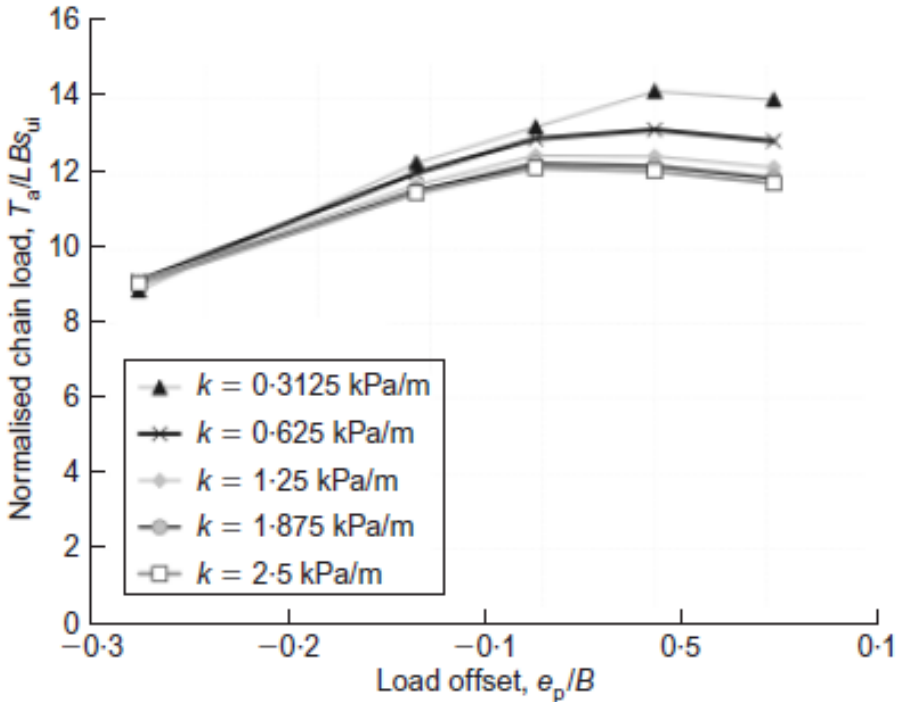


**Figure 2-27 Optimum Padeye Offset (after Cassidy *et al.* 2012)**

## 2.4 Capacity

After keying the plate anchor is assumed to be orientated perpendicular to the direction of loading at the padeye. Although this assumption may not be valid for inclined loading (due to the frictional and bearing resistance on the embedded chain; Neubecker and Randolph, 1995), it is a reasonable assumption for horizontally orientated plates subjected to vertical loading. The capacity per unit length, $Q_u$, for a horizontally orientated plate anchor subjected to vertical loading is formulated in terms of the effective unit weight of the soil, $\boldsymbol{\gamma'}$, the plate embedment depth, H, the breadth of the plate, B and a dimensionless capacity factor, $N_\gamma$:

$$N_\gamma = \frac{Q_u}{\gamma' BH} \qquad \textbf{Equation 2-4}$$

The dimensionless capacity factor, $N_\gamma$, is dependent on the relative density of the sample (and hence the friction angle), the embedment ratio of the plate (H/B) and the plate aspect embedment ratio (L/B). This section provides a review of the literature on determination of $N_\gamma$. These studies include experimental work at single and

elevated gravities in addition to analytical and numerical analyses. Both plate anchors and pipelines are considered as the latter behaves in a similar manner to a strip anchor (White *et al.*, 2008).

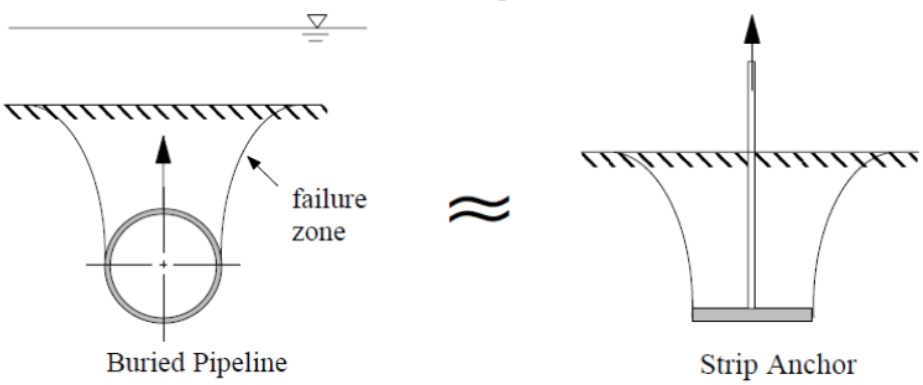


**Figure 2-28 Failure Mechanism of Strip Anchor (after Merifield 2002)**

### 2.4.1 Murray & Geddes (1987)

Murray & Geddes (1987) presented experimental data from anchor tests conducted at 1g using a horizontal plate anchor embedded in sand and subjected to vertical loading. The tests investigated the influence of the aspect ratio ($1 \leq L/B \geq 10$), embedment depth, sample density (medium and very dense) and plate surface roughness on the capacity factor.

The results from the anchor tests are provided in Figure 2-29 and Figure 2-30. Evidently the capacity factor is strongly dependent on the embedment ratio, but also on the sample density (and hence the friction angle) and the anchor aspect ratio. For an anchor with an aspect ratio, L/B = 10, at an embedment ratio, H/B = 5, the capacity factor, $N_\gamma$ ~ 6, for medium dense sand, increasing to $N_\gamma$ ~ 7.8 for dense sand. When the embedment ratio is reduced to H/B = 4, $N_\gamma$ ~ 5.5 for medium dense sand, increasing to $N_\gamma$ ~ 6.75 for dense sand.

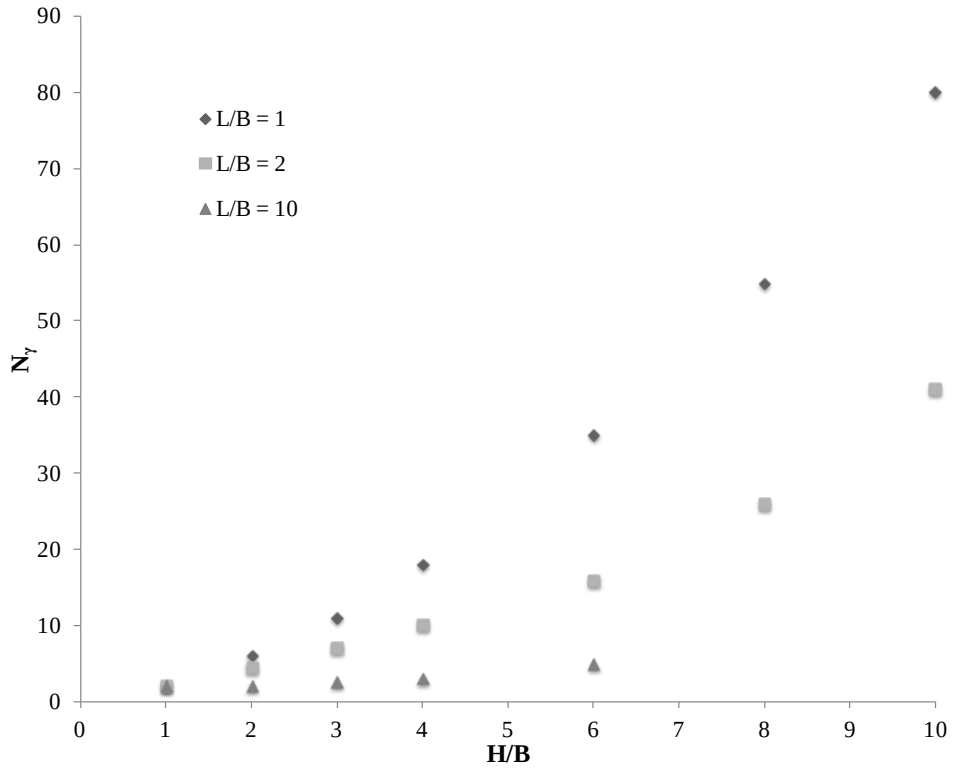


**Figure 2-29 Capacity Factor vs. Embedment Ratio for a Dense Sample (after Murray and Geddes 1987)**

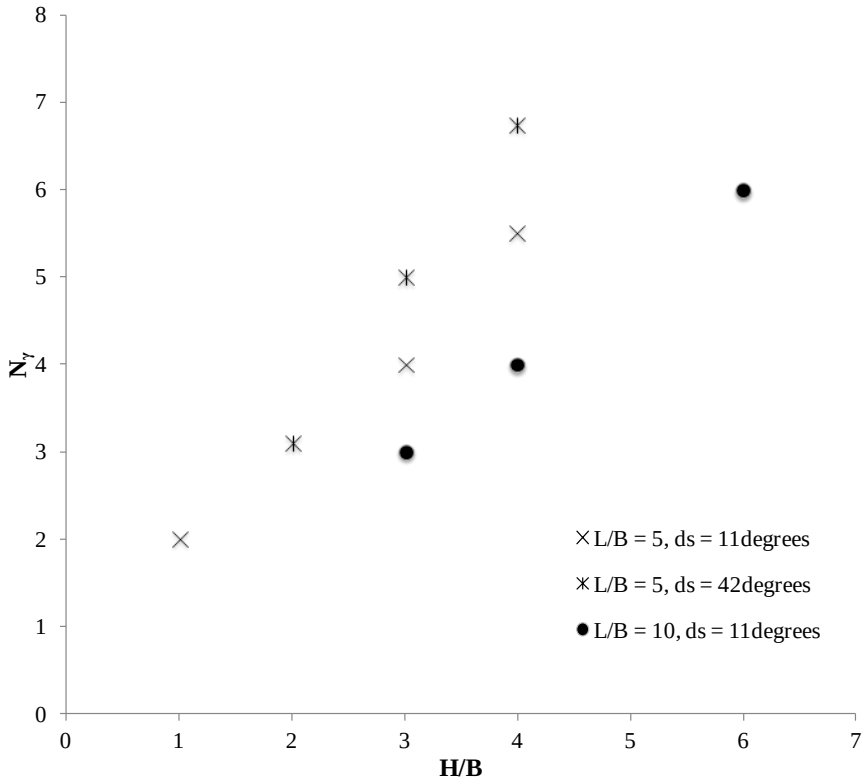


**Figure 2-30 Capacity Factor vs. Embedment Ratio for a Medium Dense Sample (ds = surface friction angle) (after Murray and Geddes 1987)**

### 2.4.2 Dickin (1988)

Dickin (1988) conducted 41 anchor tests in a geotechnical centrifuge on horizontal embedded plate anchors at 40g in dry uniform Erith sand. The average density of the samples was reported to be 16kN/m$^3$ (dense) and 14.42kN/m$^3$ (loose). Four aspect ratios were considered: L/B = 1, 2, 5 and 8 up to an embedment ratio, H/B = 8.

The results showed that as the aspect ratio of a plate anchor increases the capacity factor decreases regardless of the embedment ratio (Figure 2-31). Dickin (1988) found that varying the aspect ratio from 1 to 8 caused the capacity factor, $N_\gamma$, to decrease by approximately 75%. For instance a plate anchor embedded at a depth H = 5B with an aspect ratio, L/B = 1 has a $N_\gamma$ ~20, whereas an anchor with L/B = 8 has a $N_\gamma$ ~ 6.

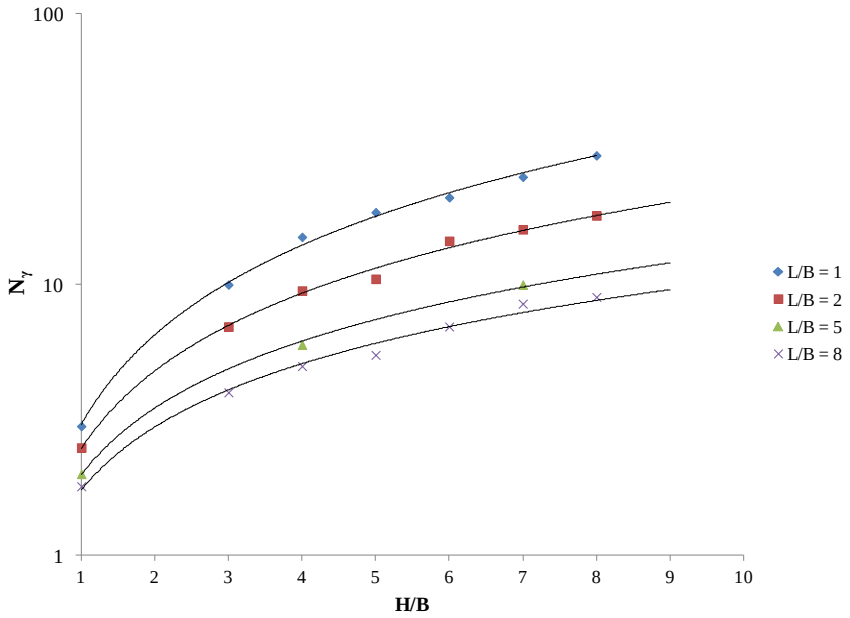


**Figure 2-31 Variation of Capacity Factor with Embedment Ratio for 1m Horizontal Anchors in Dense Sand (after Dickin 1988)**

### 2.4.3 Dickin (1994)

Dickin (1994) conducted a series of centrifuge tests at 40g on pipes and strip anchors, each with aspect ratio, L/B = 8.52, embedded such that 1.5B ≥ H ≤ 7.5B. The results showed that the maximum uplift force on a pipe and a strip anchor in sand was strongly influenced by the embedment ratio, particularly as the density

increases. Dickin (1994) found from these model tests that the uplift resistance for a pipe and a strip anchor is approximately the same, regardless of the embedment depth (Figure 2-32). The results from these model tests are presented in Figure 2-33, where the capacity factor is seen to almost linearly dependent on the embedment ratio (particularly for dense sand), and is higher for dense sand than for loose sand.

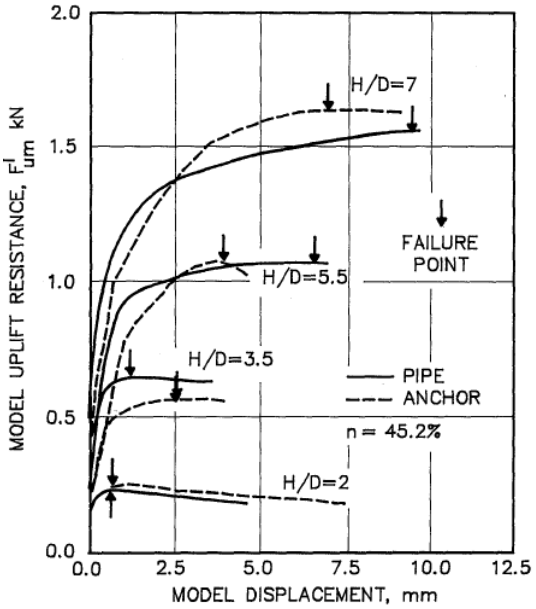


**Figure 2-32 Comparison between the Uplift Resistance for a Plate Anchor and Strip Anchor (L/B of 8.53) (after Dickin 1994)**

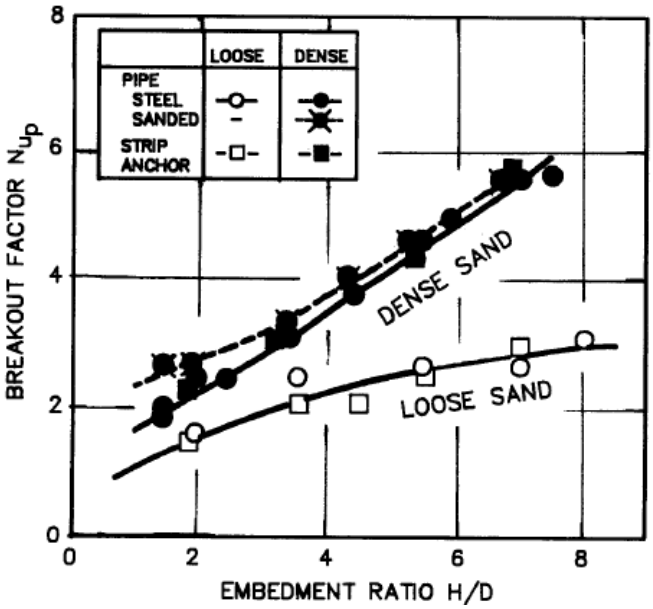


**Figure 2-33 Comparison between Capacity Factor for 1m Diameter Pipes and Strip Anchors in Centrifuge Model Tests (after Dickin 1994)**

### 2.4.4 Ng & Springman (1994)

Ng & Springman (1994) developed an upper bound plasticity solution to determine the uplift resistance of pipelines in medium to dense sand, based on data from a series of centrifuge tests at 40g. The vertical slip model developed by Schaminee *et al.* (1990) was modified to take account of the angle of dilation for medium to dense sand and considered all the forces acting on an incremental width of the pipeline during uplift (Figure 2-34). The Ng & Springman (1994) plasticity solution requires the soil to obey normality, where the angle of dilation is equal to the friction angle. Their model can be expressed rather simply as:

$$Q_u = \gamma'(DH^* + H^{*2}\tan\phi) \qquad \textbf{Equation 2-5}$$

where H* is the model pipe burial depth from soil surface to the centre of the pipe, D is the pipe diameter, $Q_u$ is the uplift resistance per unit length on the model pipe during the tests, $\gamma'$ is the submerged unit weight of soil and $\phi$ is the friction angle.

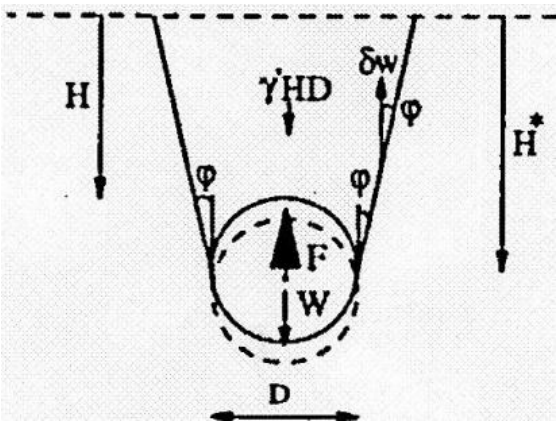


**Figure 2-34 Plastic Slip Mechanism (after Ng & Springman, 1994)**

The capacity factor for pipelines in medium to dense sand is

$$N_\gamma = \left(\frac{H^*}{H}\right)\left(1 + \frac{H^*}{D}\tan\phi\right) \qquad \textbf{Equation 2-6}$$

Ng and Springman (1994) verified Equation 2-6 by comparing it to published full scale results. For plate anchors H* = H and D = B, such that Equation 2-6 becomes:

$$N_\gamma = \left(1 + \frac{H}{B}\tan\phi\right) \qquad \textbf{Equation 2-7}$$

### 2.4.5 Merifield and Sloan (2006)

Merifield and Sloan (2006) used three different numerical methods to estimate the capacity factors for horizontally and vertically installed anchors installed at various depths. Their findings for horizontal anchors subjected to vertical loading are considered here. Merifield and Sloan (2006) employed the upper and lower bound theorems of limit analysis and displacement finite element method to determine the capacity factors for various soil strength profiles (friction angles), embedment depths and anchor geometries.

In their analyses, Merifield and Sloan (2006) found that as the friction angle increased beyond 34° the range between the lower and upper bound solution increased. Merifield and Sloan (2006) presented failure mechanisms from the numerical analyses that illustrate how increasing the friction angle, $\phi' \geq 30°$, results in larger failure mechanism and consequently a higher $N_\gamma$. Similar trends were evident when the embedment depth was increased. For $\phi' = 20°$, $N_\gamma$ increases from ~ 1.8 at H/B = 2 to ~4.5 at H/B = 10, compared with a much higher corresponding increase for $\phi' = 40°$; $N_\gamma$ increases from ~ 2.8 at H/B = 2 to ~9.5 at H/B = 10.

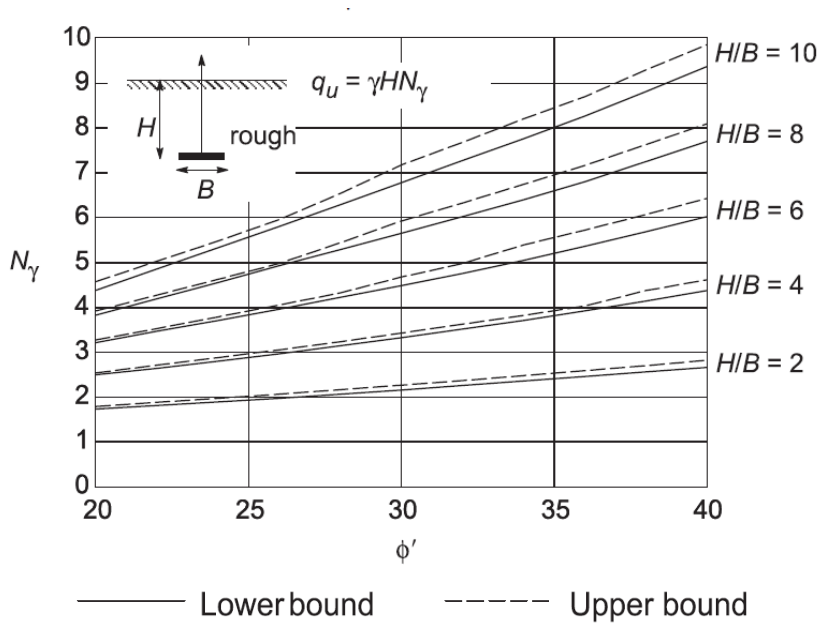


**Figure 2-35 Capacity Factor for Horizontal Anchors in Sand (after Merifield and Sloan 2006)**

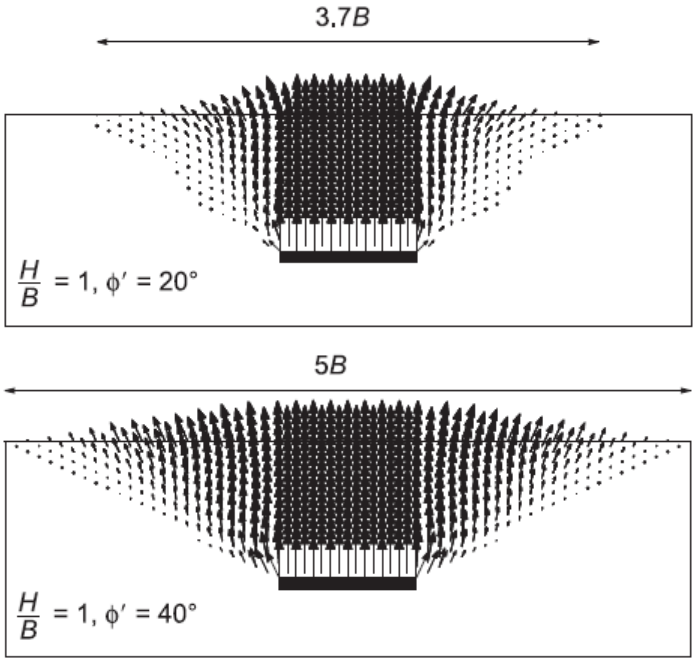


**Figure 2-36 Observed Velocity Plots from Upper Bound Analyses (a) φ' = 20° (b) φ' = 40° (after Merifield and Sloan 2006)**

### 2.4.6 White *et al.* (2001)

White *et al.* (2001) conducted 11 model tests at 10g in a mini drum centrifuge using a pipe with length 120mm and diameter 22mm (aspect ratio, L/B = 5.45). The pipe was embedded at an embedment ratio of 3.14D in fine silica sand, prepared at relative densities in the range $I_D$ = 15% to 67%. Coloured sand layers were used in the sample to facilitate measurement of the sand displacement. Images captured at various points during loading are linked to the load – displacement response (Figure 2-37).

At a displacement $\delta z_{pipe}$ =0.26D the sand displaced as a block with shear planes at 16 to 18 degrees to the vertical. As the pipe displacement increases to 1D, the failure mechanism transitions to a circular mechanism around the pipe periphery. White *et al.* (2001) found that the peak uplift resistance corresponds to the sliding block mechanism.

White *et al.* (2001) have taken account of the influence of the embedment depth, dilatancy, at-rest lateral stresses and density of the sand and have derived an alternative distribution of normal stress along the sliding planes (Figure 2-38).

$$\frac{P}{\gamma' HDL} = f(\frac{H}{D}, I_D, K, \phi)$$ **Equation 2-8**

where $P$ = F is the load, $D$ is the diameter of the pipe and $I_D$ is the relative density

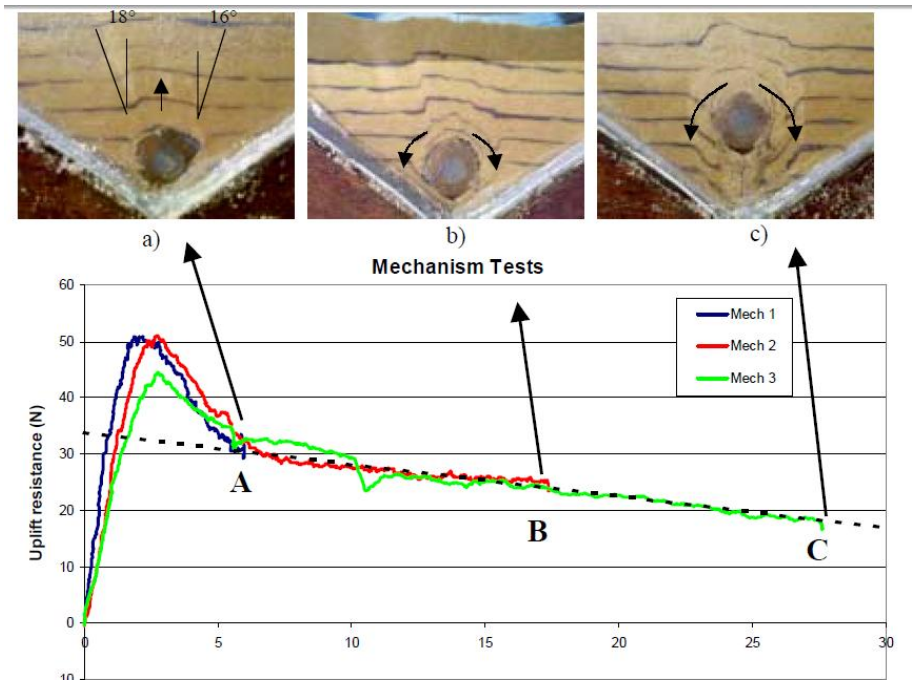


**Figure 2-37 Pipe Displacement at 0.26D, 0.60D and 1D (after White *et al.* 2001)**

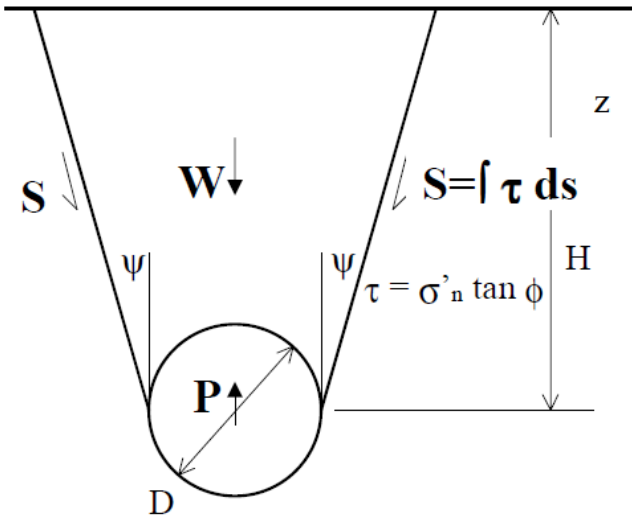


**Figure 2-38 Sliding Block Mechanism with Shear Planes at ψ to the Vertical (after White *et al.* 2001)**

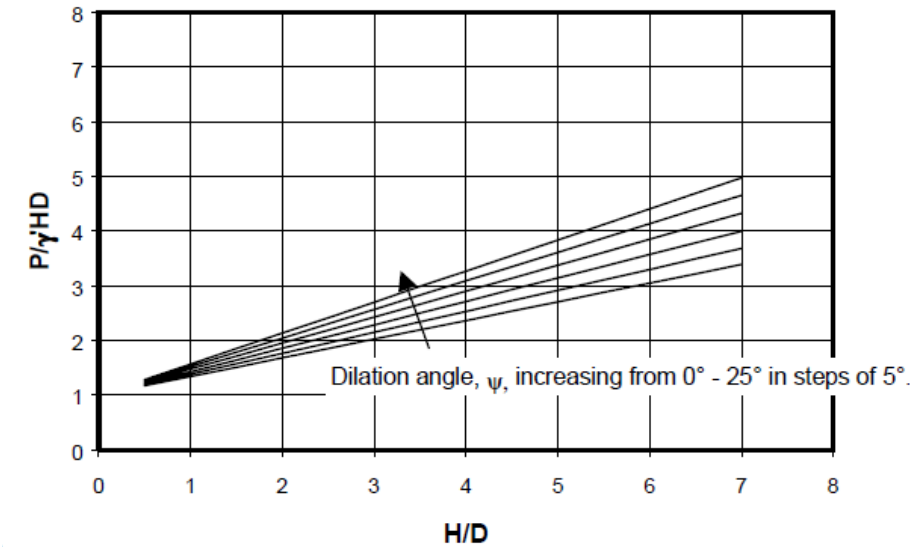


**Figure 2-39 Normalised Uplift Resistance against Embedment Ratio, $\varphi'_{crit}$ = 32° (after White *et al.* 2001)**

They have found that the peak uplift resistance is associated with a shearing mechanism along planes angled at ψ to the vertical, and that peak resistance is strongly dependent on density. Based on this observation White *et al.* (2001) developed Equation 2-9.

$$F'_{up} = \tan\psi + \left(\tan\phi_{peak} - \tan\psi\right)\left[\frac{(1+K_o)}{2} - \frac{(1-K_o)(\cos 2\psi)}{2}\right]$$

**Equation 2-9**

where the angle of dilation, ψ, is determined from Bolton's (1986) stress dilatancy theory, $\phi'_{peak}$ is the peak friction angle , $F'_p$ is the peak uplift resistance, $K_o$ is the at rest coefficient of earth pressure.

Using Equation 2-9 White *et al.* (2001) developed three design charts, Figure 2-39, Figure 2-40 and Figure 2-41, specifically for a peak friction angle $\phi'_{peak}$ of 32°, 40° and 48°. White *et al.* (2001) reported that increasing the relative density by 20% increases the uplift resistance by 30%, whereas to achieve the same increase in uplift resistance using depth would require an increase of 50%.

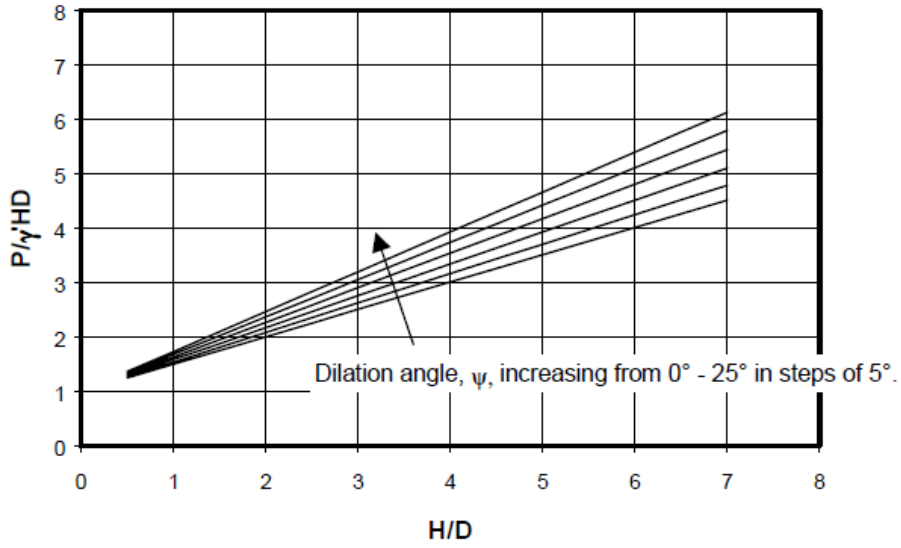


**Figure 2-40 Normalised Uplift Resistance against Embedment Ratio, $\varphi'_{peak}$ = 40° (after White *et al.* 2001)**

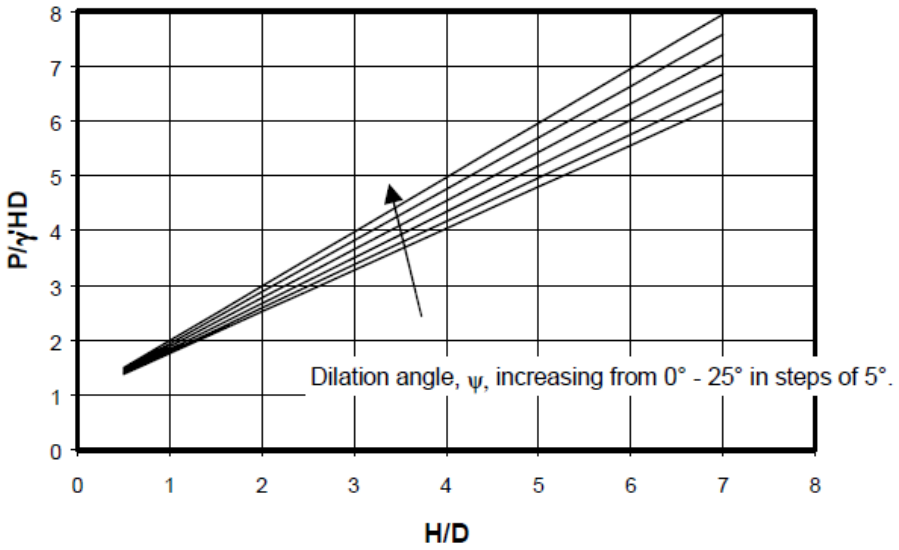


**Figure 2-41 Normalised Uplift Resistance against Embedment Ratio, $\varphi'_{peak}$ = 48° (after White *et al.* 2001)**

### 2.4.7 Chin *et al.* (2006)

Chin *et al.* (2006) conducted centrifuge tests to assess the behaviour of pipelines in loose and dense sands. The model pipe was installed at various depths in uniform loose, $\gamma$ = 14kN/m$^3$, and dense, $\gamma$ = 17kN/m$^3$, dry Congleton sand. The centrifuge tests were conducted at 10g using an 19mm diameter pipe with an aspect ratio, L/B = 16.05.

Chin *et al.* (2006) found from this investigation that the peak resistance of pipelines was reached within small pipe displacements. As shown by Figure 2-42, the peak resistance increased with increasing embedment depth and at a higher rate in the dense sand.

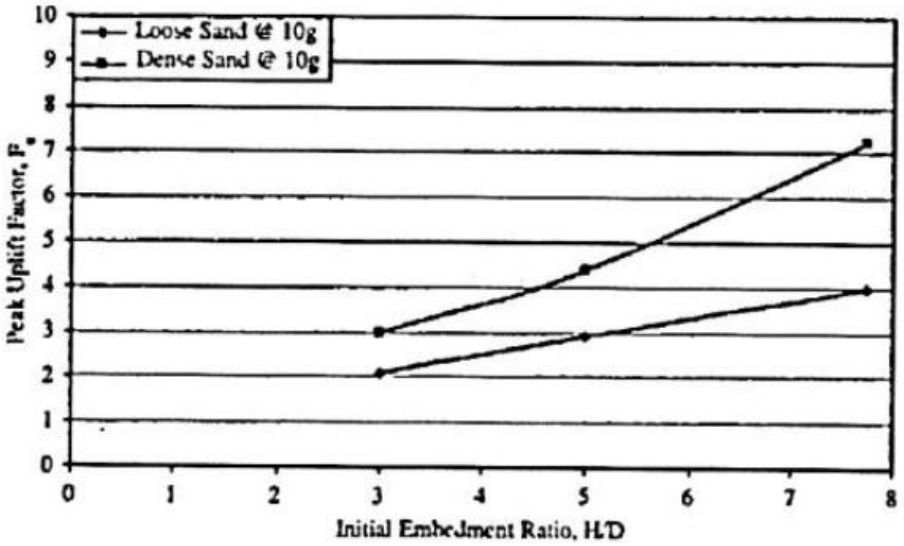


**Figure 2-42 Capacity Factor against Embedment Depth (after Chin *et al.* 2006)**

### 2.4.8 White *et al.* (2008)

White *et al.* (2008) developed a conservative limit equilibrium solution to determine the capacity factor of pipelines and strip anchors in sand. The limit equilibrium solution developed has been verified by 115 model tests and is applicable to pipeline and strip anchors that are embedded in silica sand with relative densities ranging from 10% to 92% and embedment ratio, H/B, ranging from 1 to 8. The 115 model tests used to verify this limit equilibrium model included 61 tests carried out using model pipes and 54 tests using model anchors with L/B > 8.

White *et al.* (2008) defined the dimensionless capacity factor as:

$$N_\gamma = 1 + F_{up}\frac{H}{B} \qquad \textbf{Equation 2-10}$$

where $F_{up}$ is as previously defined in Equation 2-9 using Bolton's (1986) stress dilatancy theory.

Figure 2-43 compares the results of the White *et al.* (2008) limit equilibrium solution with the results from the model test database. Evidently, the limit equilibrium method is capable of predicting peak resistance over a wide range of relative density and relative dilatancy ($0 < I_R > 4$). The agreement decreases as the embedment depth increases, which is due to the transition from a shallow failure mechanism (upon which the limit equilibrium method is based) to a deep failure mechanism. The scatter of results shown in Figure 2-43 (b) illustrates that Bolton's (1986) stress dilatancy theories take account of the capacity factor and sample density for each test.

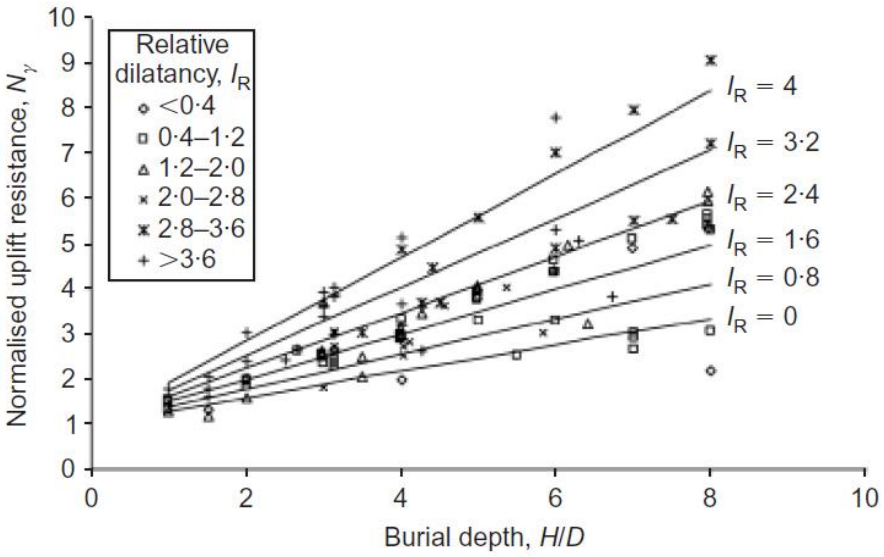


**(a)**

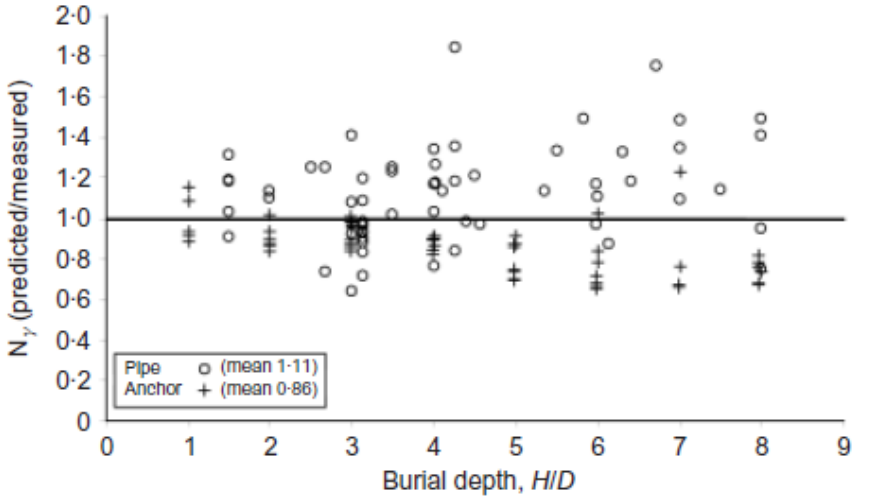


**(b)**

**Figure 2-43 Comparison of Model Test Database and Limit Equilibrium Solution (after White *et al.* 2008)**

White *et al*. (2008) used Equation 2-9 and Equation 2-10 to develop design charts for predicting the breakout resistance of plate anchors and pipes buried in silica sand (Figure 2-44). In Figure 2-44 (a) and (b) White *et al*. (2008) have presented the capacity factor ($N_\gamma$) as a function of the embedment ratio (H/B), the relative density ($I_D$), the effective unit weight ($\gamma$'), the soil strength, the capacity ($F$) and the pipe diameter (D) for three different pipe diameters and four different relative densities ($I_D$ = 0.1, 0.3, 0.5 and 0.7). Figure 2-44 (a) and (b) show that as H/B increases, the influence of $\phi'_{peak}$ on $N_\gamma$ reduces i.e. this occurrence increases as the $\gamma$' increases.

When the $I_D$ is equal to 4 (the upper limit of $\phi'_{peak}$ has been reached), $N_\gamma$ is the same at low embedment depths, (H/D < 3) regardless of the pipe diameter. When $I_D$ = 1, the response is the same for each pipe diameter regardless of H/D as the lower limit of $\phi'_{peak}$ is reached.

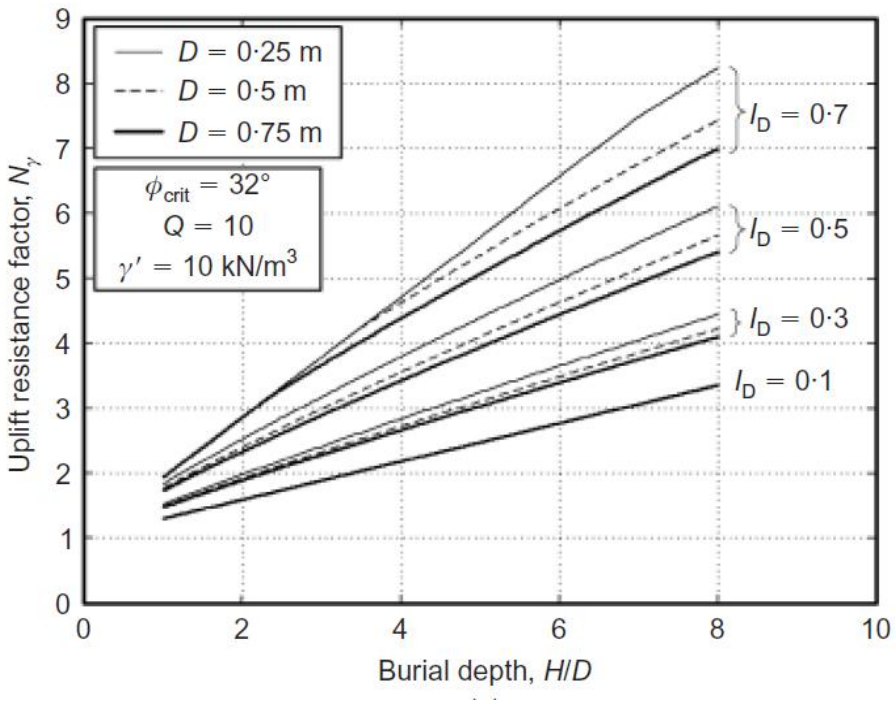


**(a)**

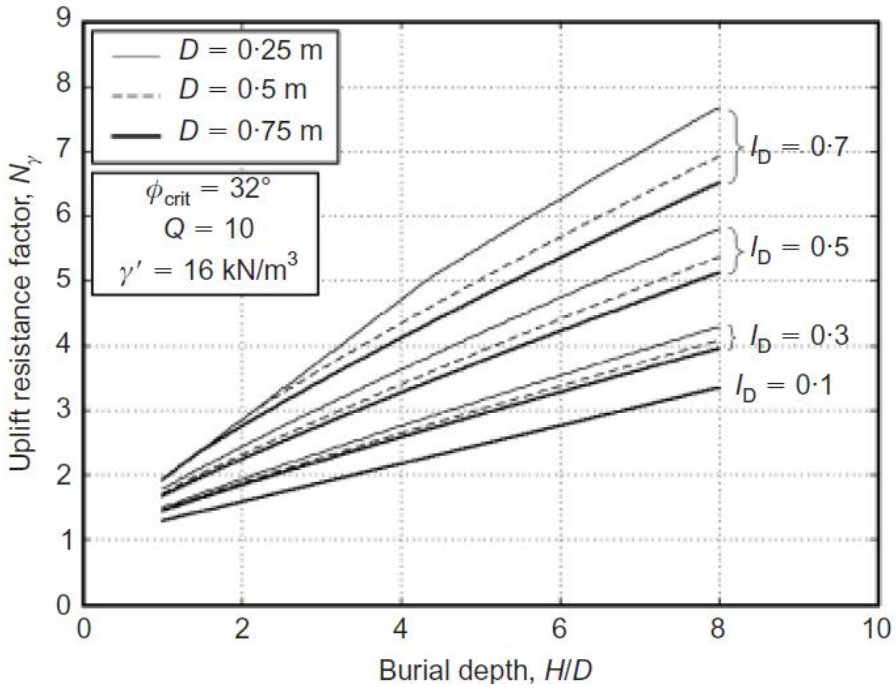


**(b)**

**Figure 2-44 Design Charts for Peak Uplift Resistance (a) submerged example ($\gamma$' = 10kN/m$^3$) (b) dry example ($\gamma$' = 16kN/m$^3$) (after White *et al.* 2008)**

## 2.5 Summary

The previous sections summarise the main literature on the keying of plate anchors in clay and the capacity factor for anchors in sand. Although this study is concerned with plate anchors in sand, no such studies have been undertaken for a plate anchor installed in a vertical orientation and then keyed. The literature for clay highlights the strong dependence of loss on embedment on the eccentricity of the padeye (Figure 2-45), with a lesser dependency on loading inclination, plate aspect ratio and strength profile. To keep embedment loss within acceptable limits, the eccentricity of the padeye eccentricity should be no less than half the plate breadth, with minimal loss in embedment obtainable for padeye eccentricities of one plate breadth or higher.

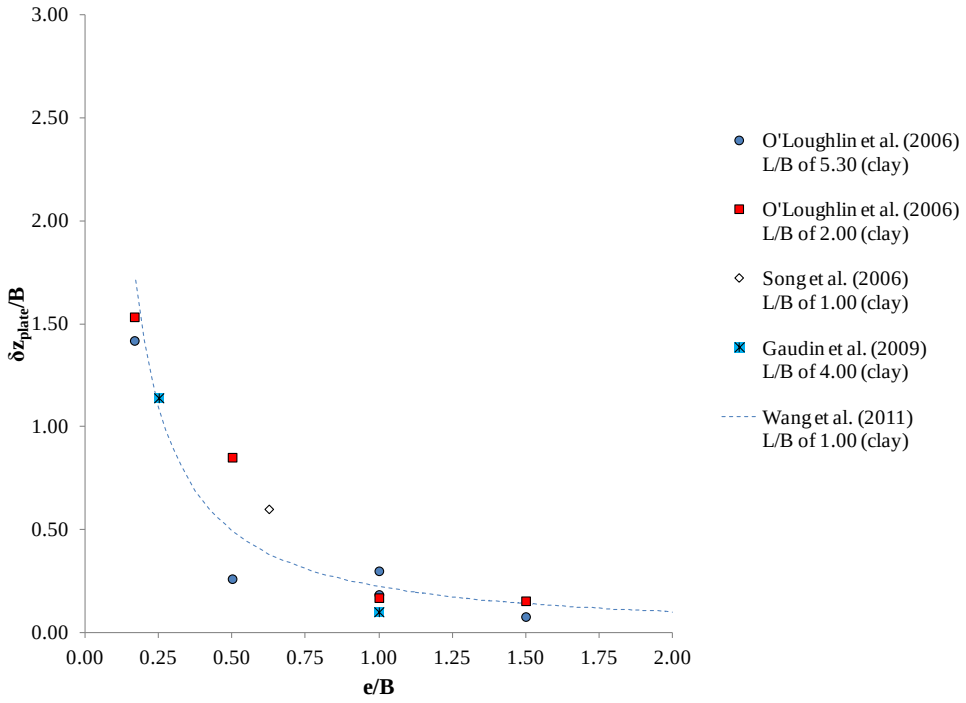


**Figure 2-45 Loss of Embedment Loss during Keying: Dependence on Padeye Eccentricity**

The most influential parameters that affect the anchor capacity factor are the density of the sample (and hence the friction angle), the anchor aspect ratio and the embedment depth. This finding holds true for both plate anchors and pipes and has been reported for studies that have been conducted at 1g, in the centrifuge and results that have been determined numerically. Once the aspect ratio of an anchor or pipe exceeds 5, the influence of the embedment depth and the aspect ratio become less influential on the dimensionless capacity factor.

The studies indicate that for a loose sand, the capacity factor, $N_\gamma$, increases from ~1.8 at H/B = 2 to ~4.5 at H/B = 10, whereas for a dense sand $N_\gamma$ increases from ~2.8 at H/B = 2 to ~9.5 at H/B = 10.

# CHAPTER 3.0
# METHODOLOGY

## 3.1 Introduction

As there have been no studies conducted to date on the keying induced loss of embedment a plate anchor undergoes in sand, the main focus of this study was to quantity the unrecoverable embedment loss and to determine the dimensionless capacity factor for each anchor test.

The anchor tests in this study were conducted in the geotechnical centrifuge in the Institute of Technology Sligo. The anchor tests were carried out in dense sand in a strongbox with Perspex panels. The orientation of the anchor during the anchor tests conducted against the Perspex window was captured by a series of images. These images were synchronised to the loading. The camera was setup perpendicular to the Perspex window. A LED light illuminated the test area. The images captured were used to illustrate the failure mechanisms the movement of the anchor caused. PIV analysis was used to show the failure mechanisms the anchor underwent during the anchor test. The orientation of the anchor was extracted from each image and related to the load on the anchor at that time.

This chapter gives an outline of the principles behind centrifuge testing and a description of the test equipment used to conduct the anchor tests. This is followed by a breakdown of the procedures followed for the test setups and the steps involved in the post test analysis to assess the anchor behaviour during the keying process.

## 3.2 Beam Centrifuge

The centrifuge tests were conducted in a small geotechnical centrifuge located at the Institute of Technology, Sligo (Figure 3-1). The centrifuge is a 9g-tonne machine and has a maximum effective radius of 0.75m giving a maximum acceleration level of 300g. The centrifuge accommodates two strongboxes (Figure 3-2 and Figure

3-3a). In flight each strongbox acts as a counter weight to the other (Figure 3-3b). A detailed description of the centrifuge is given by O'Loughlin *et al.* (2010).

**Figure 3-1 External View of Centrifuge (after O'Loughlin *et al.* 2010)**

**Figure 3-2 Internal View of Centrifuge in Beam Mode – Loading**

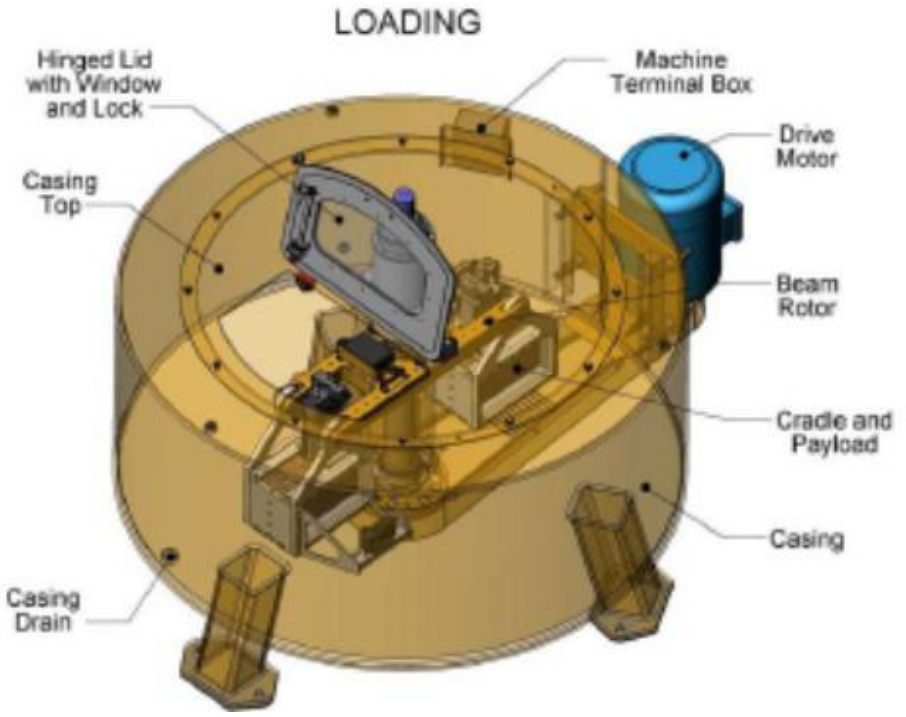


**(a)**

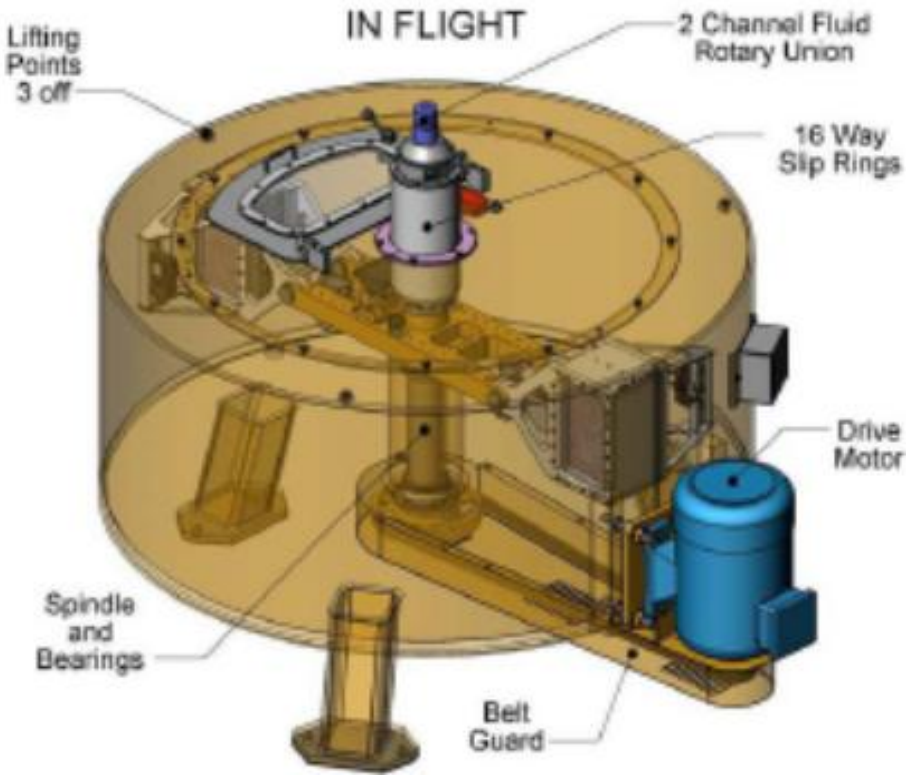


**(b)**

**Figure 3-3 Schematic of Centrifuge (a) Loading (b) In-flight (after O'Loughlin *et al.* 2010)**

The rotary stack located in the centre of the centrifuge accommodates sixteen slip rings. These slip rings allow power to be supplied to the centrifuge and allow for communication with the actuator.

The data generated from the tests conducted within the centrifuge is transmitted wirelessly to a desktop computer located adjacent to the centrifuge. The channels transmit at a sampling rate of up to 1 MHz at 16-bit resolution (O'Loughlin *et al.*, 2010). A software programme called Digi-DAQ allows for the data from several testing apparatus to be viewed and stored simultaneously. This software programme converts the raw data (voltage) from the tests into meaningful units using calibration factors that have been inputted by the user. The data acquisition system used in the centrifuge is described by Gaudin *et al.* (2009b).

### 3.2.1 Principles of Centrifuge Testing

Conducting geotechnical tests requires accurate organisation, time management and a substantial budget. Therefore, many geotechnical tests are conducted on reduced scale models in a laboratory. The issue with model laboratory tests conducted at Earth's gravity is the very low self-weight stresses within the sample, which can be one or two orders of magnitude lower than what would be experienced by the equivalent prototype in the field. Model tests conducted in a geotechnical centrifuge have the advantage that the stress level in the sample can be made similar to that in the equivalent prototype. This is a result of the artificial gravitational force Ng (where N is the centrifuge's acceleration and g is Earth's gravitational acceleration = 9.81m$^2$/s) that is created by spinning the centrifuge.

The vertical stress $\sigma_{vp}$ in the prototype of height $h_p$ with a density $\gamma'$ (where $\gamma' = \rho g$ ($\rho$ is the unit weight)) is given by:

$$\sigma_{vp} = \rho g h_p \qquad \textbf{Equation 3-1}$$

The vertical stress $\sigma_{vm}$ in a soil model of height $h_m$ with a density $\gamma'$ is given by:

$$\sigma_{vm} = \rho N g h_m \qquad \textbf{Equation 3-2}$$

In order to have stress similitude between the prototype and the model:

$$\rho g h_p = \rho N g h_m \qquad \textbf{Equation 3-3}$$

which may be achieved when

$$h_m = \frac{h_m}{N} \qquad \textbf{Equation 3-4}$$

Equation 3-4 is the reference scaling law for centrifuge modelling, which states that dimensions in the model are scaled by N. Other scaling laws can be established using similar principles; the most common laws are summarised in Table 3-1

**Table 3-1 Scaling Laws (after Taylor 1995)**

| **Parameter** | **Dimensions** | **Scale Factor (Model: Prototype)** |
|---|---|---|
| Acceleration | $LT^{-2}$ | $1:N^{-1}$ |
| Length | L | 1:N |
| Area | $L^2$ | $1:N^2$ |
| Stress | $L_1T^{-2}$ | 1:1 |
| Force | $LT^{-2}$ | $1:N^2$ |
| Time | $LT^{-2}$ | 1:1 |
| Velocity | T | 1:N |

The artificial gravitational force Ng, induced by the centrifuge is equal to the inertial acceleration $\omega^2 R_e$, (where $\omega$ is the angular velocity and $R_e$ is the effective radius) experienced by a model. Although the artificial gravity force created in the centrifuge does not increase linearly with depth (Taylor, 1995), the error between the stress profile in the centrifuge model and in the prototype may be minimised by setting the g level at an effective radius $R_e = R + 2/3H$ (where R is the distance from

the centre of the centrifuge to the surface of the model and H is the depth of the model) (Figure 3-4).

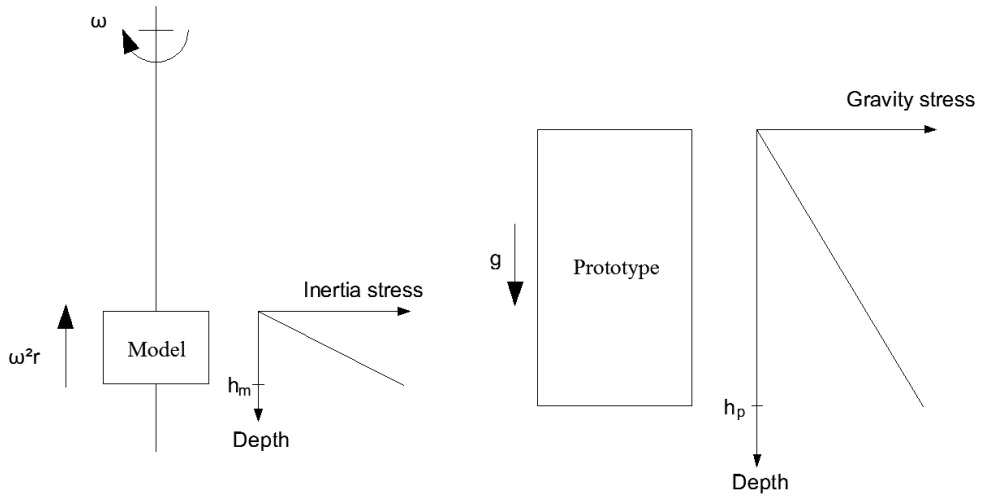


**Figure 3-4 Inertial Stress in Centrifuge Model & Corresponding Prototype Gravitational Stress (after Taylor 1995)**

### 3.2.2 Strongboxes

All model tests were conducted in a 'strongbox'. The original internal dimensions of the strongbox were 100 mm × 300 mm × 180 mm (width × length × maximum sample height) (Figure 3-5). The strongbox was modified by replacing the original 35mm thick Perspex with 15mm thick Perspex. This alternation increased the overall width of the strong box to 140mm. The original height and length of the strongbox were not altered. To ensure the new Perspex window stayed in place, four spacers were fabricated. Two spacers were place at each end of the strongbox, one at the top and the other at the bottom of the strongbox. The modified width of the strongbox is shown in Figure 3-6.

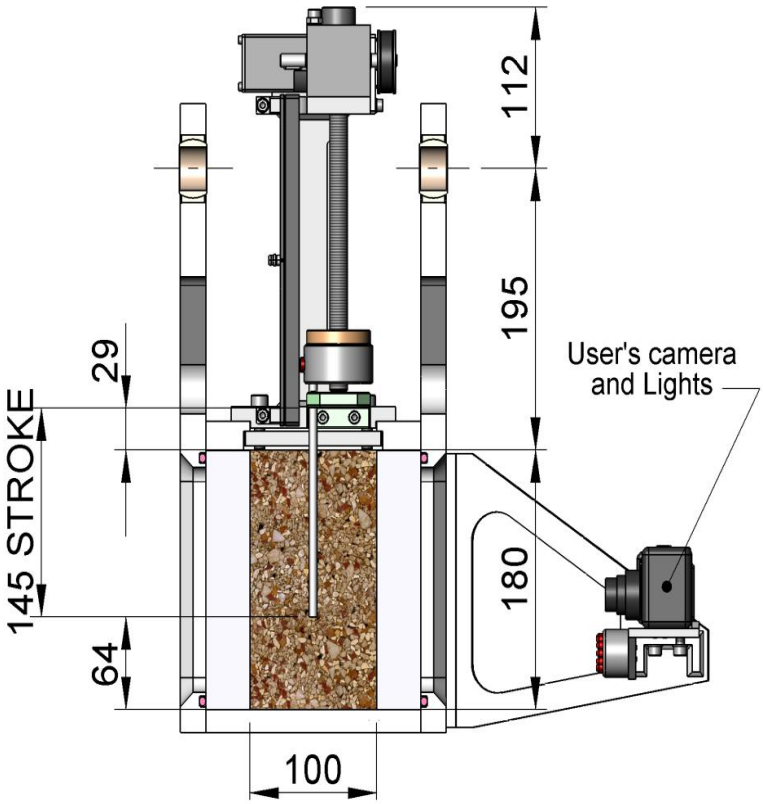


**Figure 3-5 Side View of Actuator and Original Strongbox (after Thomas Broadbent and Sons Limited. 2010)**

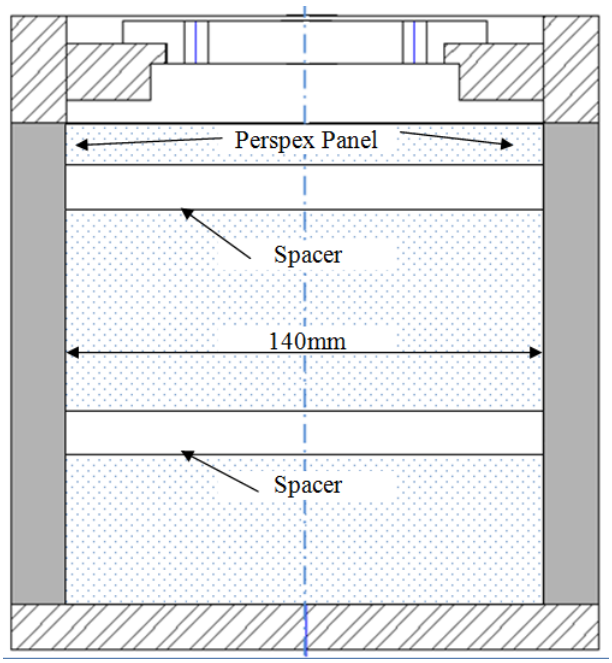


**Figure 3-6 Side View of Modified Strongbox**

### 3.2.3 Linear Actuator

The linear actuator (Figure 3-7) used for the entire series programme of tests has been described in detail by O'Loughlin *et al*. (2010). The actuator has a capacity of ± 2kN, a linear stroke of ± 145mm and linear velocities in the range ± 10 mm/s. . The balluff is a linear variable differential transformer (LVDT) that measures the displacement of the brass nut. EASI-V controls the direction and the velocity of 80 V DC brushless servo motor. EASI-V is a generic software programme designed for controlling the direction, and the velocity of servo motors. The velocity of the actuator was set to 1mm/s for the entire series of tests.

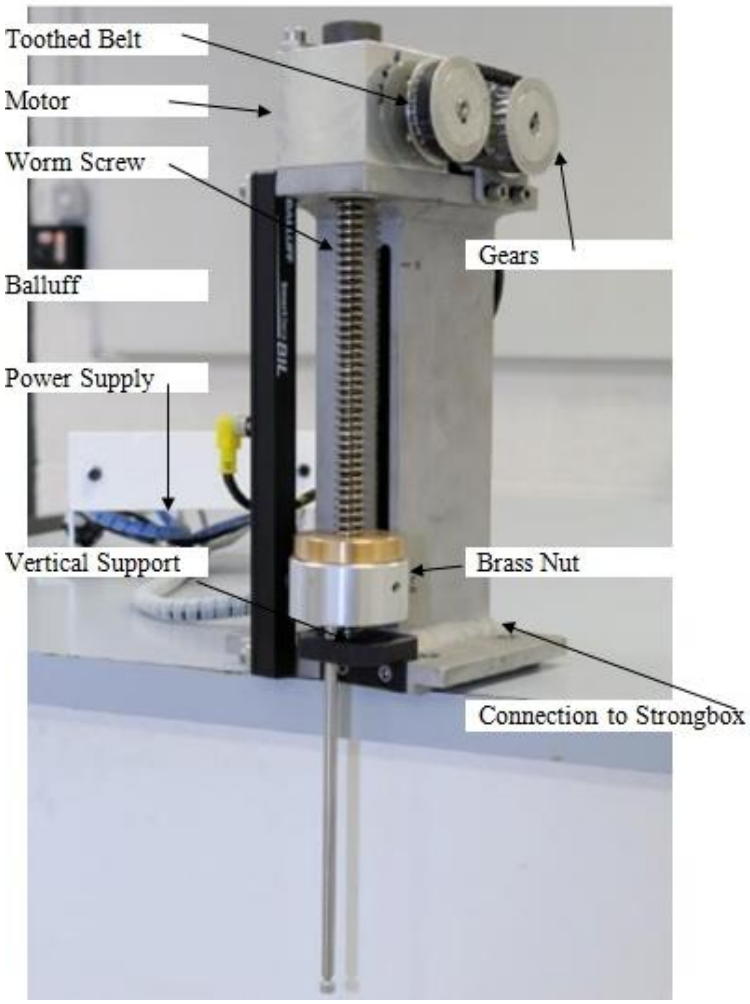


**Figure 3-7 Linear Actuator (after O'Loughlin *et al.* 2010)**

### 3.2.4 Digital Camera

A Canon s70 Powershot (with a resolution of 3264 × 2448 pixels) captured the orientation of the plate anchor during each anchor test conducted against the Perspex window (Figure 3-8). These images were used to quantify the displacement and rotation of the plate during keying and also in the PIV analyses (described further in Section 3.5.1) to illustrate the failure mechanisms at various stage during the tests. The method used to extract this information from the images is described in Section 3.4.


**Figure 3-8 Canon Camera**

A custom made camera mount was fabricated from aluminium and Perspex. The mount held the camera in a fixed position with the camera's optical axis perpendicular to the window of the strongbox, and supported the camera lens during elevated acceleration levels when the centrifuge was spinning (Figure 3-9). The cradle was designed so that the camera could be located at different positions, so that the best field of view for each anchor test conducted against the Perspex window could be obtained (Figure 3-10).

**Figure 3-9 Side View of Camera on Camera Mount**

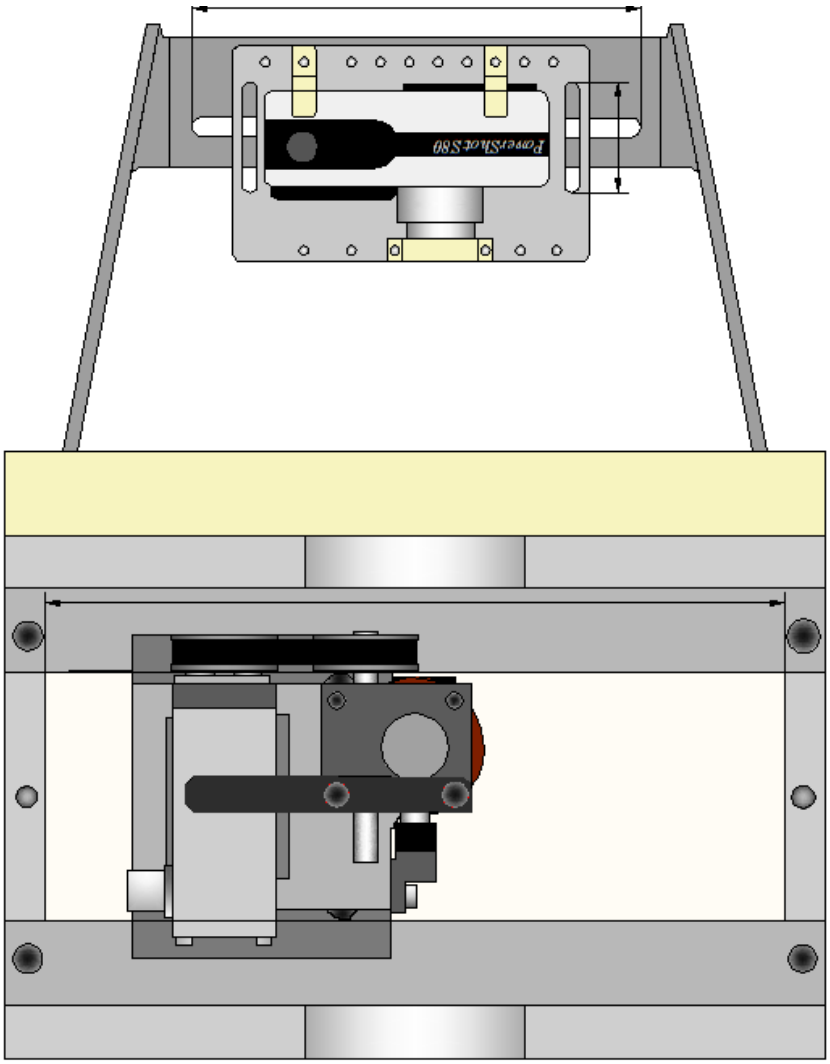

**Figure 3-10 Plan of Test Setup (Schematic)**

In each test the camera was set to 'continuous shooting mode' which allowed consecutive images to be captured at an average of 1.5 frames per second. The test area was illuminated with a bar of LED lights. These lights, which spanned the length of the strongbox, were located at the top of the strongbox and provided uniform lighting to the test area. The LED bar was connected to the strongbox using a custom mount fabricated from aluminium and Perspex (Figure 3-11).

Triggering of the camera shutter was achieved by connecting two wires from either terminal of the electrical switch (underneath the shutter button, see Figure 3-8) to two slip ring channels, which allowed the camera to be controlled externally by an on/off switch.

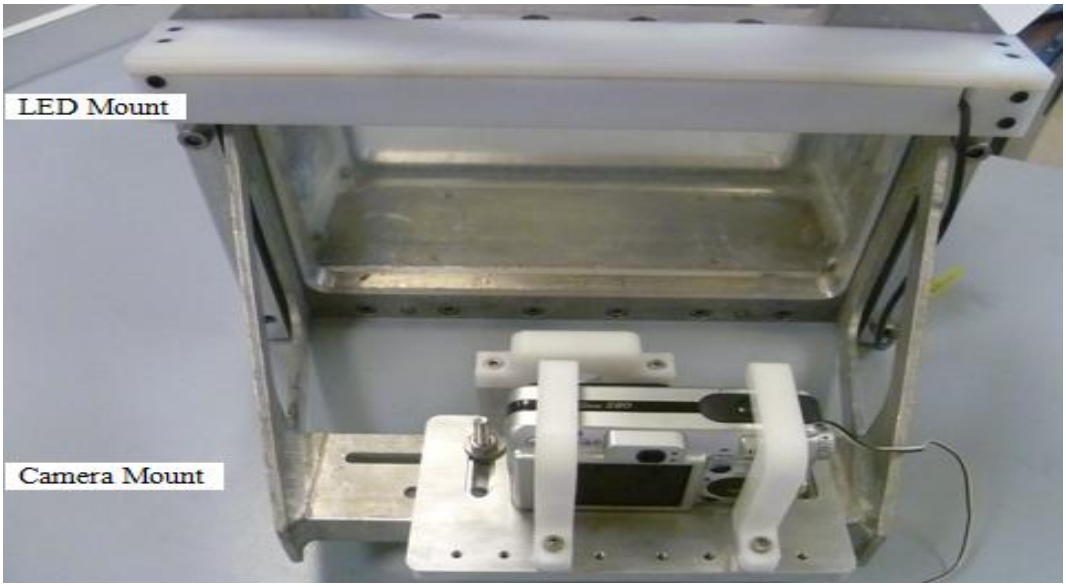


**Figure 3-11 Camera and Lighting Setup**

Synchronising the displacement of the anchor plate from the camera images to the measured data was achieved by measuring the signal in the modified camera switch circuit using the same data acquisition as used for the load and displacement measurements. An example of the synchronisation is provided in Figure 3-12.

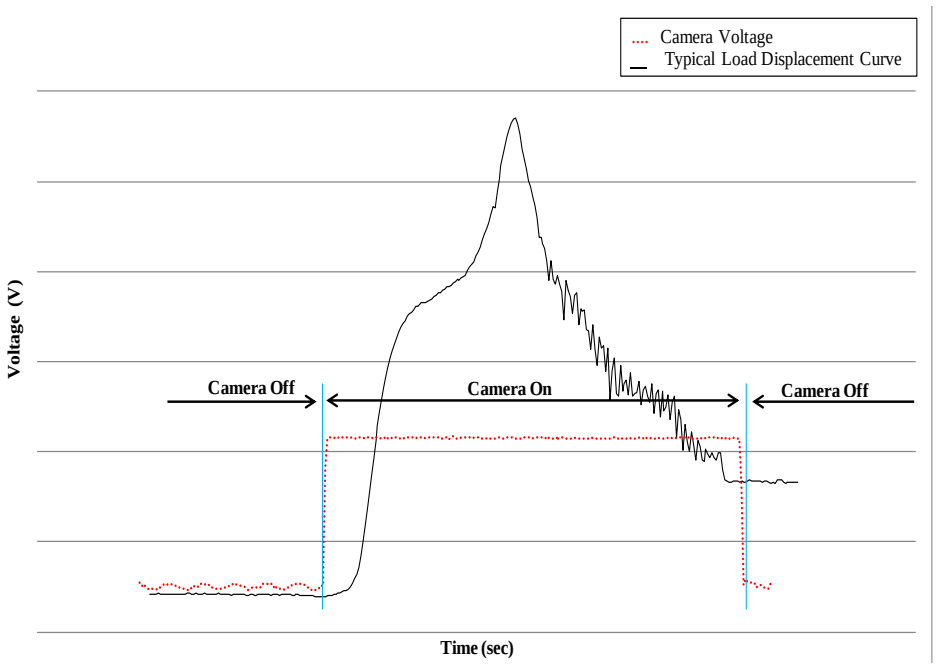


**Figure 3-12 Voltage Plot**

### 3.2.5 Load Cells and Mooring Line

The load exerted on the plate anchor and the mooring line during each anchor test was measured by an 'in-line' 2kN miniature load cell (Figure 3-13). The resolution of the load cell was 0.0189N. This load cell was located to the travelling nut on the lead screw, in series with the mooring line.


**Figure 3-13 Load Cell**

The mooring line used throughout this study was fabricated from galvanised steel which had a diameter of 2mm and a capacity of 2.55kN. The mooring line was connected to the load cell using a custom made rotary union (as illustrated in Figure 3-14) which allowed twisting of the mooring line without developing torsion on the load cell. Crimps were used to connect the mooring line to the load cell and to the anchor (Figure 3-15).

The calibration factor of the load cell used for the anchor pullout was checked in the centrifuge laboratory before conducting each test series. The load cell was connected to the DAQ and a hanger. Once communication was achieved with the digi DAQ 1 kg weights were added to the hanger. As the weights were applied to the hanger the output voltage was recorded. The calibration factor did not change throughout the anchor tests.

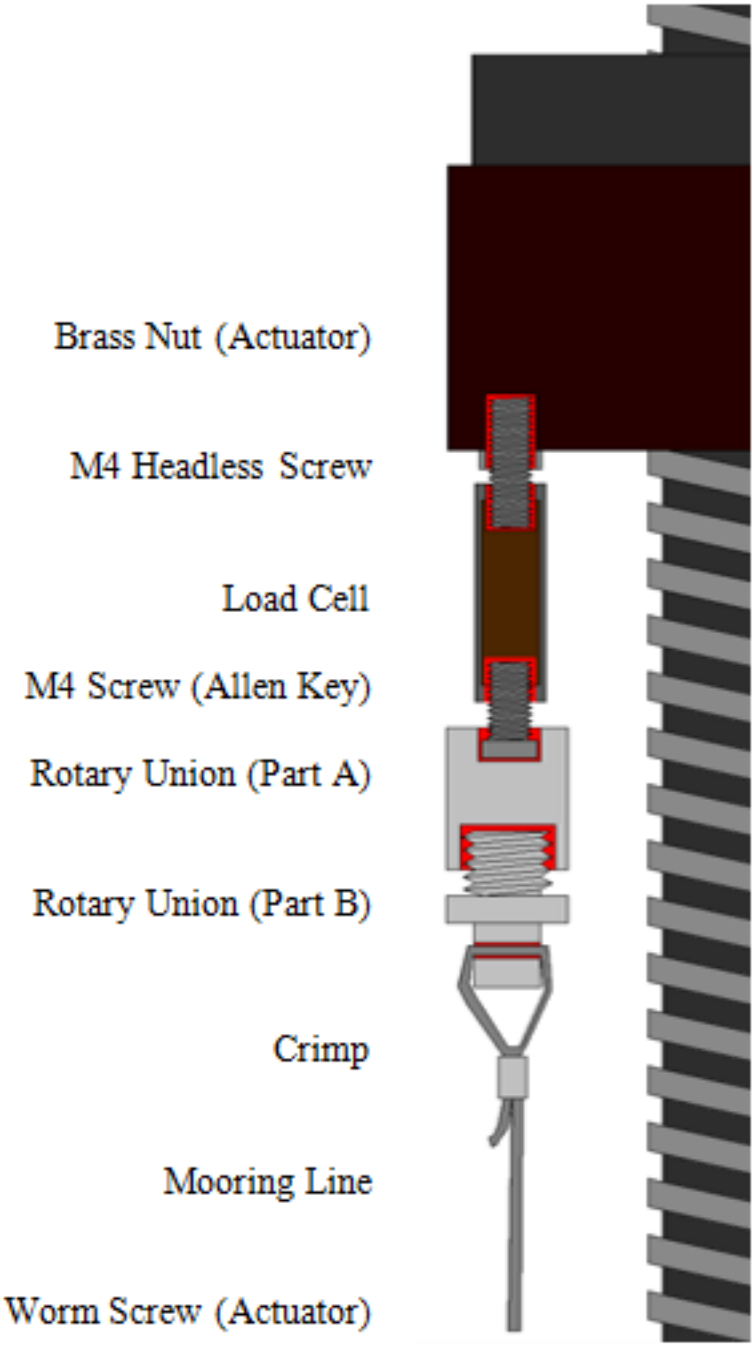


**Figure 3-14 Connection Details (Above Surface)**

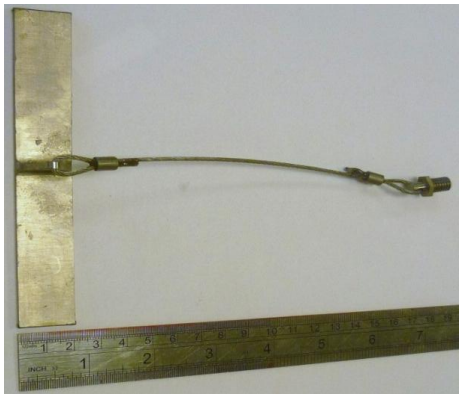

**Figure 3-15 Connection Details (Below Surface)**

### 3.2.6 Cone Penetrometer

A model cone penetrometer (CPT) was used to characterise each sample and to provide for a means of assessing sample uniformity and repeatability (Figure 3-16). The CPT had a total length of 175mm, diameter of 10mm, a 60° cone apex and a maximum tip resistance capacity of 60MPa. The resolution of the cone penetrometer was 0.993kPa. The cone penetrometer was connected to the travelling nut on the lead screw of the linear actuator using a headless screw, as used for connecting the load cell (Figure 3-14).


**Figure 3-16 Cone Penetrometer**

### 3.2.7 Model Anchors

Six plate anchors were employed in this study, each with a different padeye eccentricity. The geometric notation adopted and the features of the anchor used in this study are described in Section 2.2. Each anchor was fabricated from stainless steel with length L = 140mm, breadth B = 20mm and thickness t = 3mm. The padeye eccentricity, e, differed for each anchor, with e in the range 5 to 40 mm, representing eccentricity ratios in the range e/B = 0.25 to 2. As each anchor test was conducted at 30 g, the equivalent prototype anchor measures 4.2 × 0.6m.

A schematic and a photo for each anchor are provided as follows:

- e/B = 0.25: Figure 3-17 and Figure 3-18
- e/B = 0.5: Figure 3-19 and Figure 3-20
- e/B = 0.75: Figure 3-21 and Figure 3-22
- e/B = 1: Figure 3-23 and Figure 3-24
- e/B = 1.5: Figure 3-25 and Figure 3-26
- e/B = 2: Figure 3-27 and Figure 3-28

The length of the each plate anchor was equal to the width of the strongbox. A groove was machined to accommodate an O-ring at the plate-Perspex interface. Each plate anchor had an aspect ratio, L/B = 7. As the ends are constrained the behaviour is equivalent that of a strip rather than a rectangular anchor and a thickness ratio, t/B = 0.15. The surface of the anchor was not polished, although it may be considered to be relatively smooth.

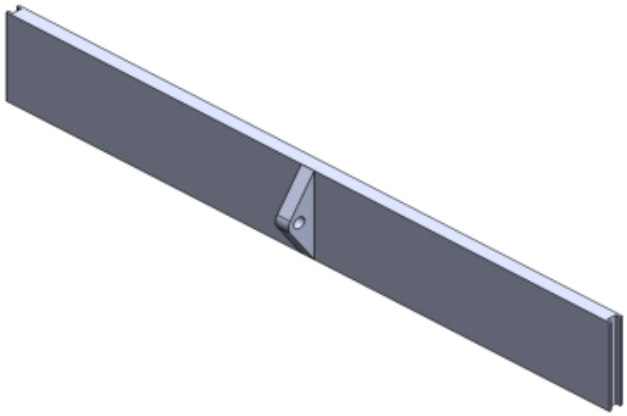

**Figure 3-17 Plate Anchor e/B = 0.25 (3D Schematic)**

**Figure 3-18 Plate Anchor e/B = 0.25 (Photo)**

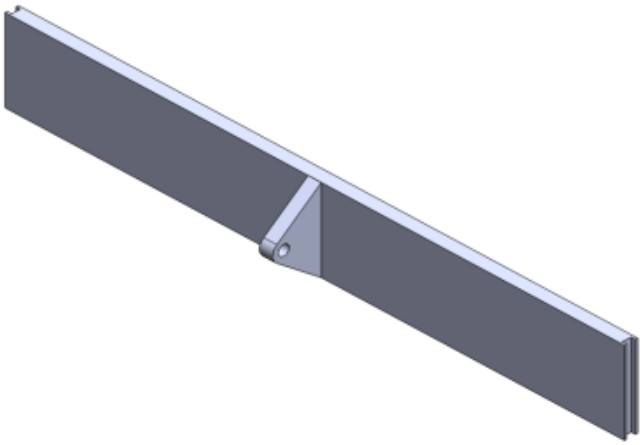

**Figure 3-19 Plate Anchor e/B = 0.5 (3D Schematic)**

**Figure 3-20 Plate Anchor e/B = 0.5 (Photo)**

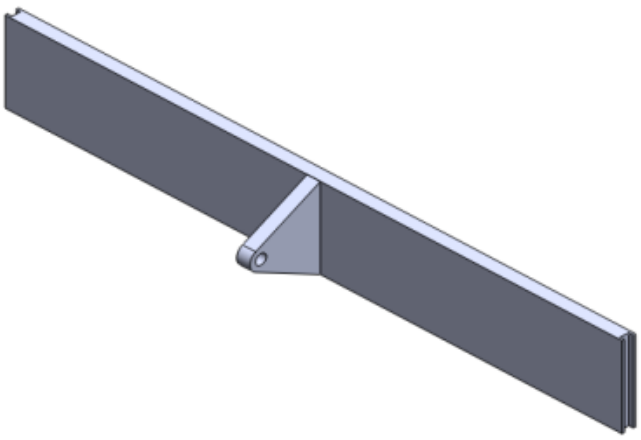

**Figure 3-21 Plate Anchor e/B = 0.75 (3D Schematic)**

**Figure 3-22 Plate Anchor e/B = 0.75 (Photo)**

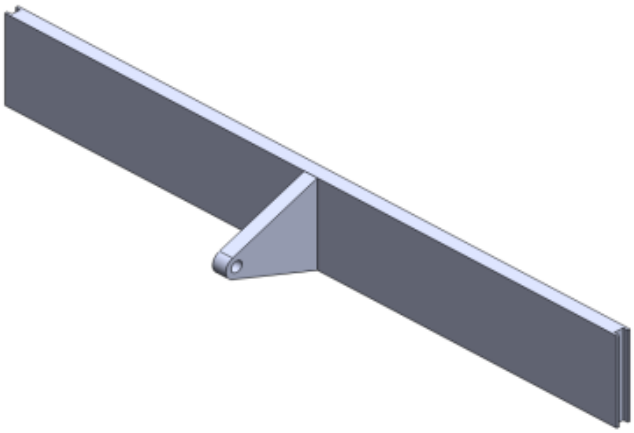

**Figure 3-23 Plate Anchor e/B = 1 (3D Schematic)**

**Figure 3-24 Plate Anchor e/B = 1 (Photo)**

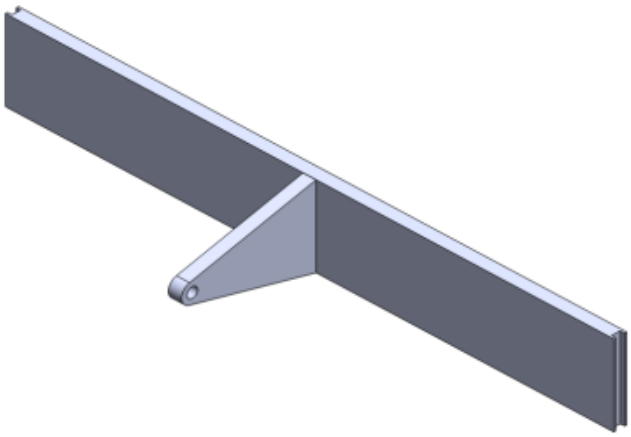

**Figure 3-25 3D Plate Anchor e/B = 1.5 (3D Schematic)**

**Figure 3-26 Plate Anchor e/B = 1.5 (Photo)**

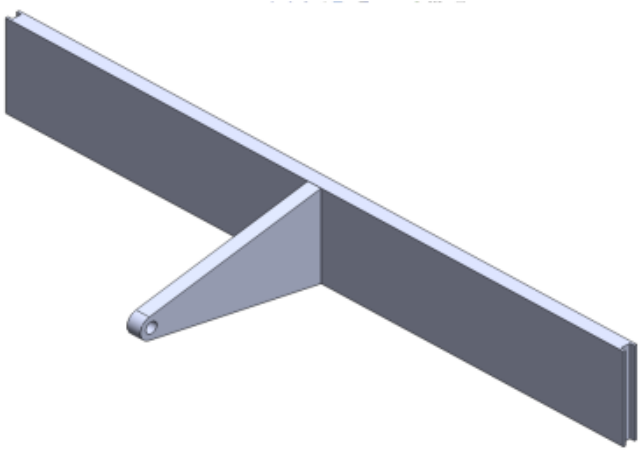

**Figure 3-27 3D Plate Anchor e/B = 2 (3D Schematic)**

**Figure 3-28 Plate Anchor e/B = 2 (Photo)**

## 3.3 Experimental Setup

### 3.3.1 Sand Properties

Congleton silica sand was used throughout this study and was supplied by Mineral Marketing Ltd. in the UK. The sand properties presented in Table 3-2 have been measured by Lauder (2010) and reported by Bransby *et al.* (2010).

**Table 3-2 Properties of Silica Sand (after Lauder 2010)**

| **Property** | $D_{10}$ | $D_{30}$ | $D_{60}$ | $C_u$ | $C_z$ | $\gamma'_{d,min}$ | $\gamma'_{d,max}$ | $\phi'_{crit}$ | $\phi'_{peak}$ |
|---|---|---|---|---|---|---|---|---|---|
| **Unit** | (mm) | (mm) | (mm) | (-) | (-) | ($kN/m^3$) | ($kN/m^3$) | ($^o$) | ($^o$) |
| **Value** | 0.10 | 0.12 | 0.14 | 1.4 | 1 | 14.59 | 17.58 | 32 | 44 |

Additional sieve analyses were conducted in accordance with the procedure outlined in British Standards BS 1377-2 (1990). The particle size distribution is shown in Figure 3-29, together with that reported by Lauder (2010). $D_{10}$, $D_{30}$, $D_{50}$ and $D_{60}$ were found to be 0.1mm, 0.14mm, 0.15mm and 0.17mm respectively, which are in reasonable agreement with those reported by Lauder (2010). Using these values and the values reported by Lauder (2010) the Congleton silica sand classifies as uniform sand.

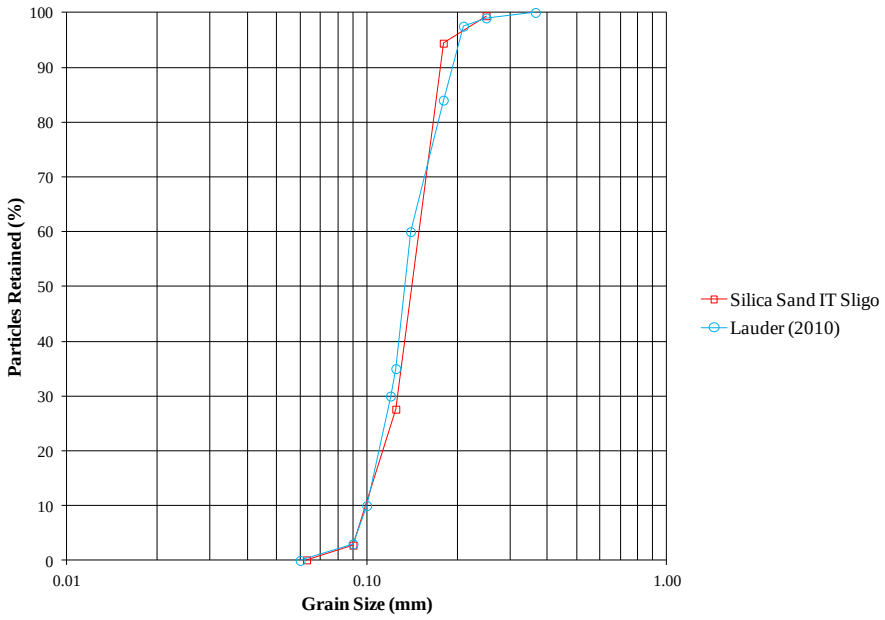


**Figure 3-29 Sieve Analysis**

### 3.3.2 Sample Preparation

The following procedure was followed to achieve a consistent dense sample for each test series (Figure 3-30). The silica sand was oven dried for 24 hours at 180°C. Sand was first placed in the drainage holes on the bottom of the strongbox. Then 1.5kg of silica sand was evenly placed and subsequently tamped to achieve a layer thickness of 13-14mm. Tamping of each sand layer was achieved using a Perspex sheet of length 280mm and width 139mm that was placed over the levelled sand and struck in a clockwise rotation 30 times for 10 revolutions for each layer[1]. To monitor the sand level and hence the density, six height measurements were taken from the top of the strongbox (one at each of the corners and two in the middle). This process was repeated until the required sample height was reached.

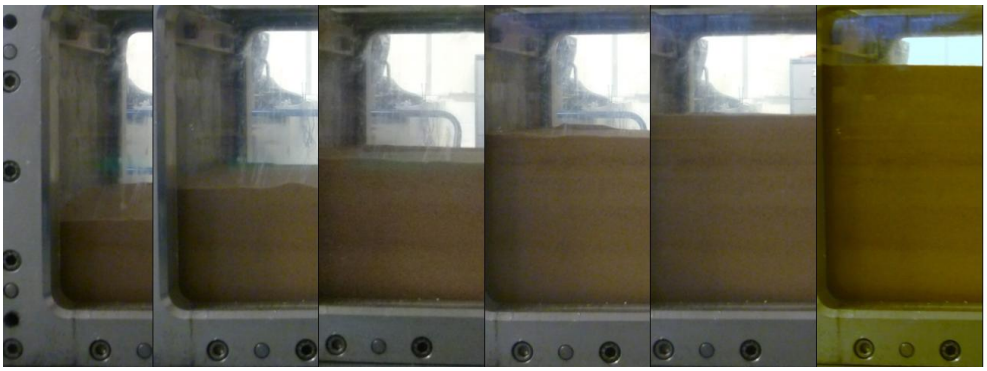

**Figure 3-30 Preparation of Sample**

### 3.3.3 Sample Characterisation

Sample characterisation was carried out prior to conducting any anchor tests. Two CPTs were conducted to check the consistency and uniformity of each sample. Gui *et al.* (1998) reported that the rate of installation of the CPT penetrometer has a minimal effect on a dense sand sample. The cone penetrometer was inserted at a rate of 1mm/s along the centre line of the strongbox. A typical setup is shown in Figure 3-31 and the location of the CPT tests is shown in Figure 3-32.

[1] Note that as the sheet was not the length of the strongbox, the sheet had to be moved to cover the entire plan area of the sample.


**(a)**

**(b)**

**(c)**

**Figure 3-31 Installation of Cone Penetrometer (a) Side view of cone penetrometer (b) Side view of CPT setup (c) Plan view positioning actuator**

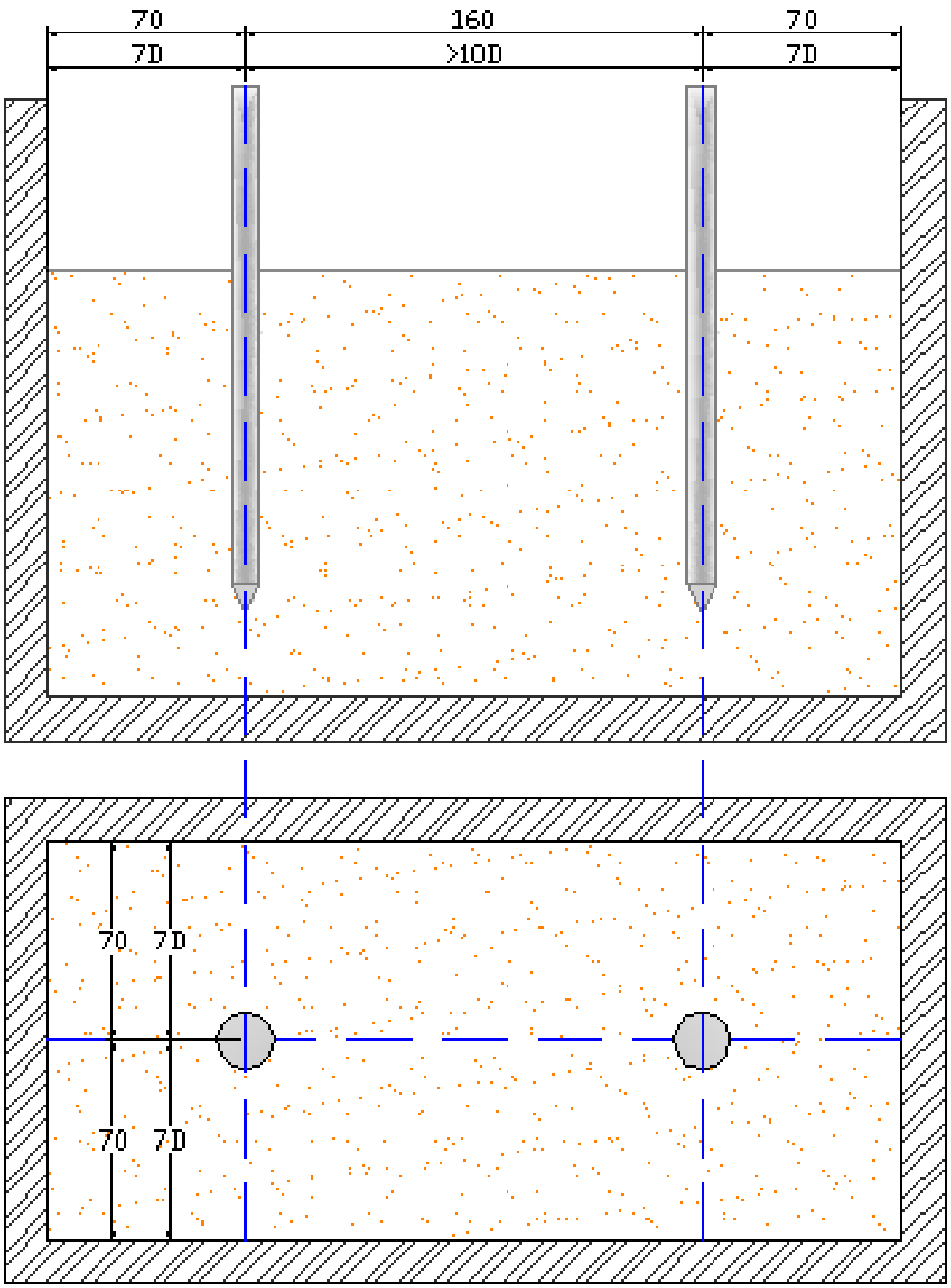


**Figure 3-32 Location of Cone Penetrometer for Cone Penetration Tests**

### 3.3.4 Testing Assembly

These tests were conducted with the anchor orientated in two ways. The majority of the anchor tests were conducted with the edge of the anchor against the Perspex face (i.e. the anchor plate was perpendicular to the Perspex window), whilst others were

conducted with the centre line of the anchor plate along the centre line of the strongbox (i.e. the anchor plate was parallel to the Perspex window).

The installation method for both setups was conducted in the centrifuge at 1g (the centrifuge was stationary). The plate anchor was installed vertically using a custom fabricated mandrel (Figure 3-33). The steps involved in the installation process are illustrated in Figure 3-34 and are described in the caption of Figure 3-34. The anchors were installed to an embedment ratio, H/B = 5, measured to the centre of the plate. It is worth noting that installation at 1g rather than at the testing acceleration level of 30g was not considered to affect the subsequent anchor performance as the tests were conducted in dry sand, which would create a drained response either at 1g or at 30g.

**Figure 3-33 Mandel used to Install the Plate Anchor**

The installation process caused a wedge of sand to translate vertically downwards with an adjacent surface heave either side of the installation site (Figure 3-34). This surface disturbance was not "repaired" as similar surface disturbance is also likely to occur *in situ*.

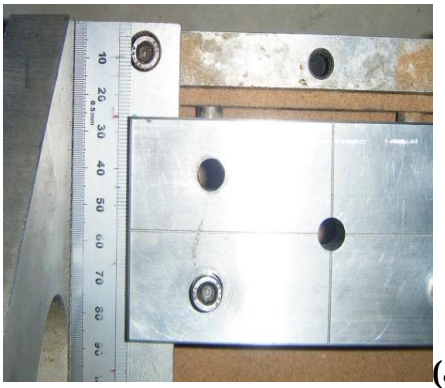
(a)

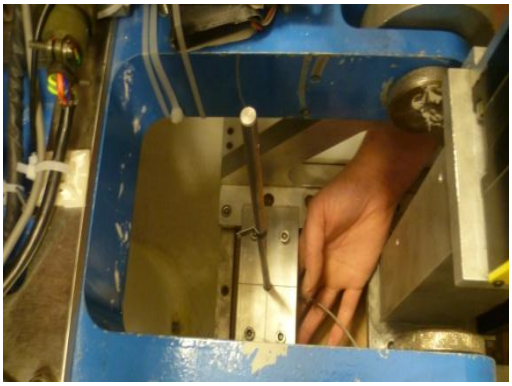
(b)

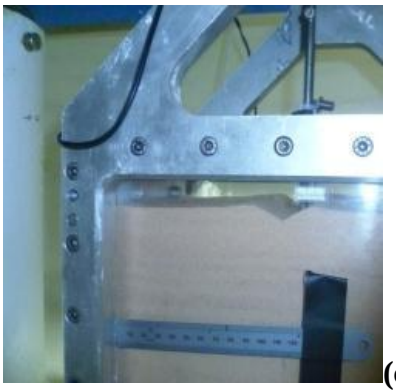
(c)


(d)


(e)

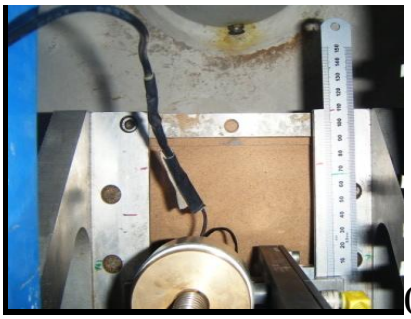
(f)

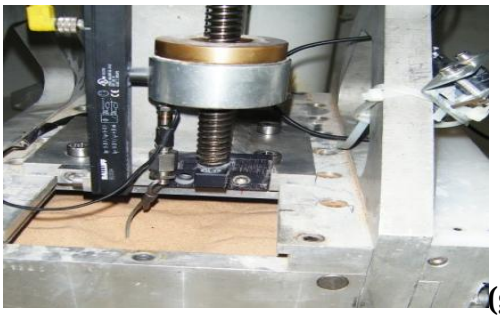
(g)

**Figure 3-34 Anchor Installation (a) Installation guide (b) Installation of plate anchor (c) Anchor installation at 1g showing disturbance of the sample surface (d) Monitoring the distance from the start of the field of view to the centre of plate anchor (e) Measuring distance from the start of the field of view to the centre of plate anchor (f) Measuring distance from the external wall of the strongbox to the edge of the actuator (g) Connection between the anchor wire and the actuator**

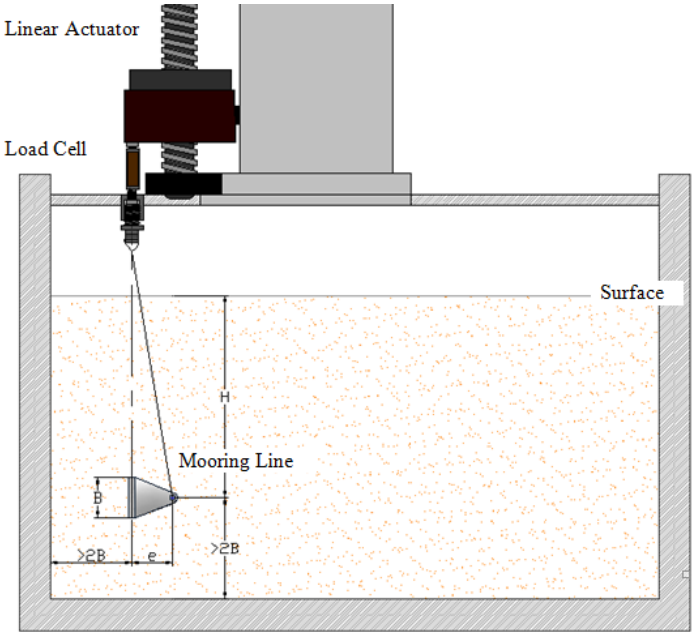


**Figure 3-35 Test Setup before Anchor Test (Schematic)**

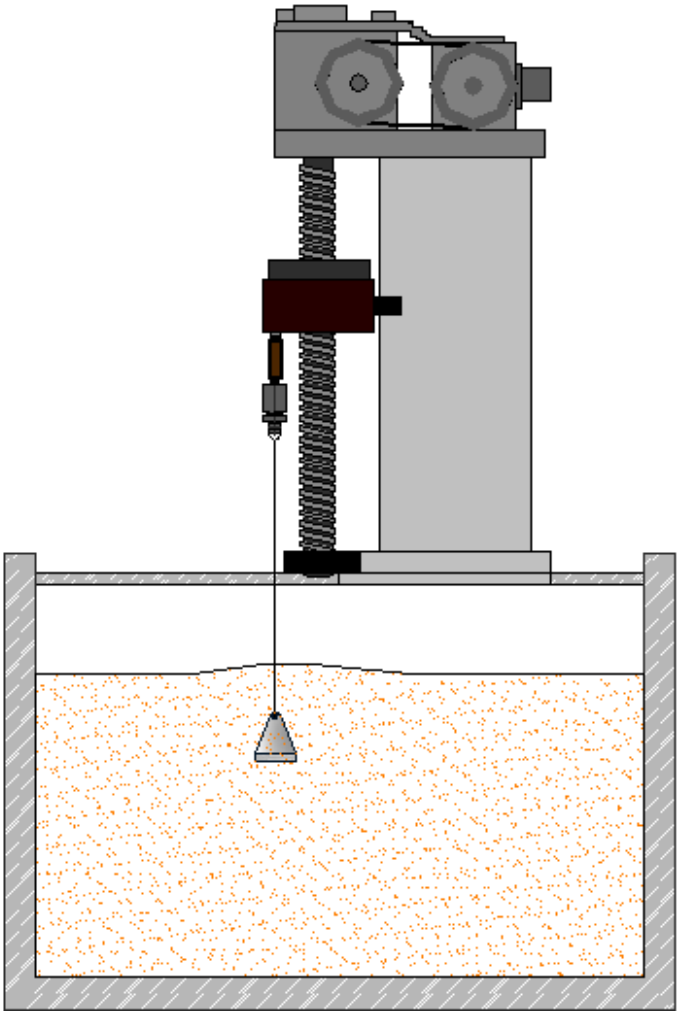

**Figure 3-36 Test Setup after Anchor Test (Schematic)**

Once the actuator was positioned and secured, the load cell was connected to the mooring line as illustrated in Figure 3-14 and described in Section 3.2.5. The LED lighting was switched on and the camera mount was positioned to capture the test area. The camera was switch on and securely mounted to resist the high acceleration levels. A photo showing the side view of the setup of the testing equipment is given in Figure 3-37 and a plan is given in Figure 3-38.

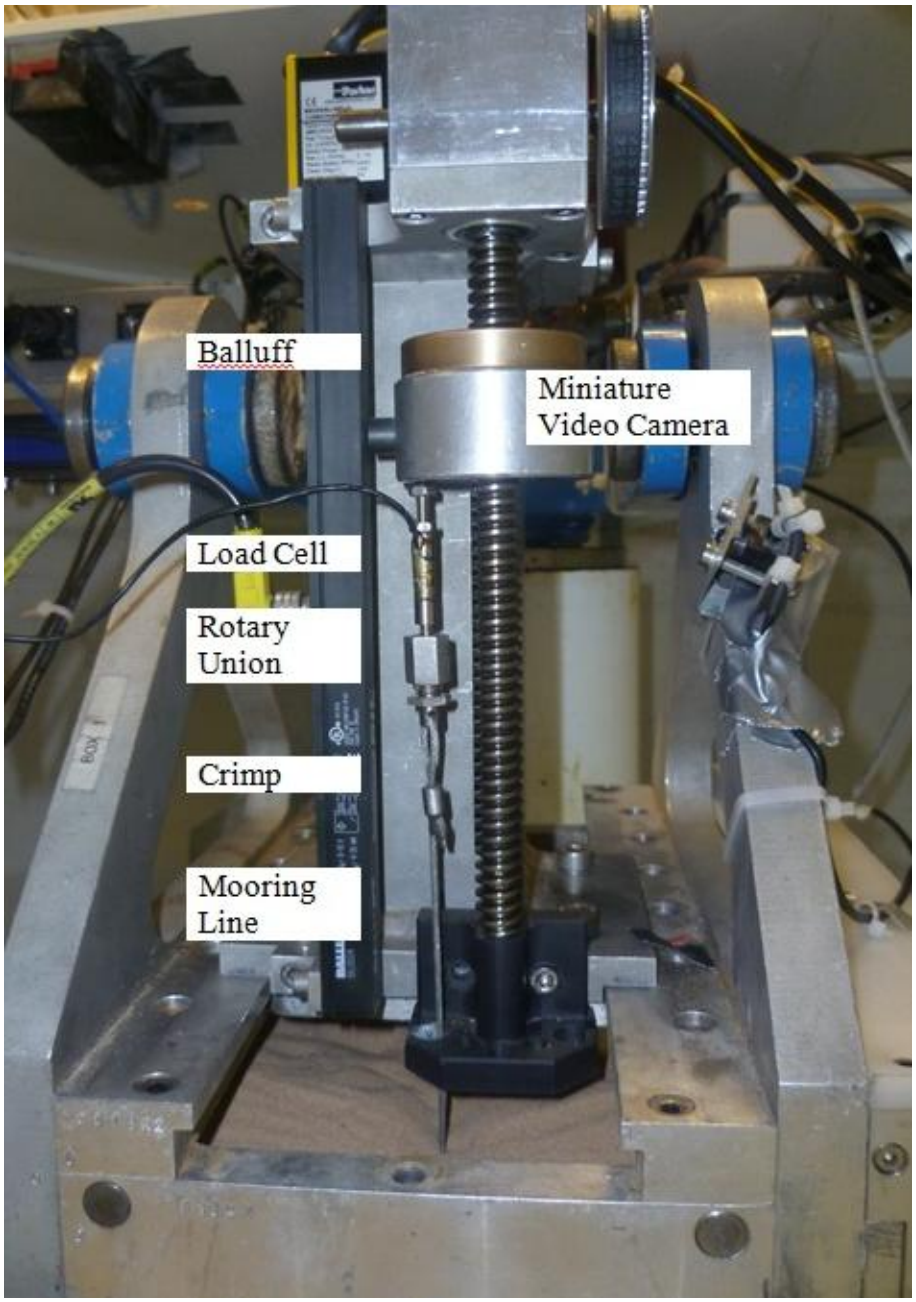


**Figure 3-37 Side View of Test Setup**

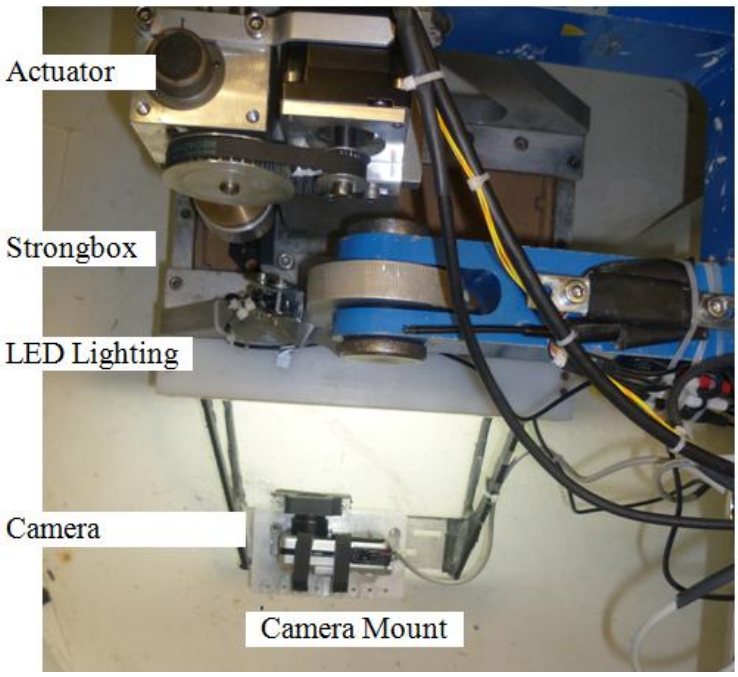


**Figure 3-38 Test Setup**

The typical test arrangement for the anchor tests conducted against the Perspex interface and in the centre of the strongbox is given in Figure 3-39 and Figure 3-40, respectively.

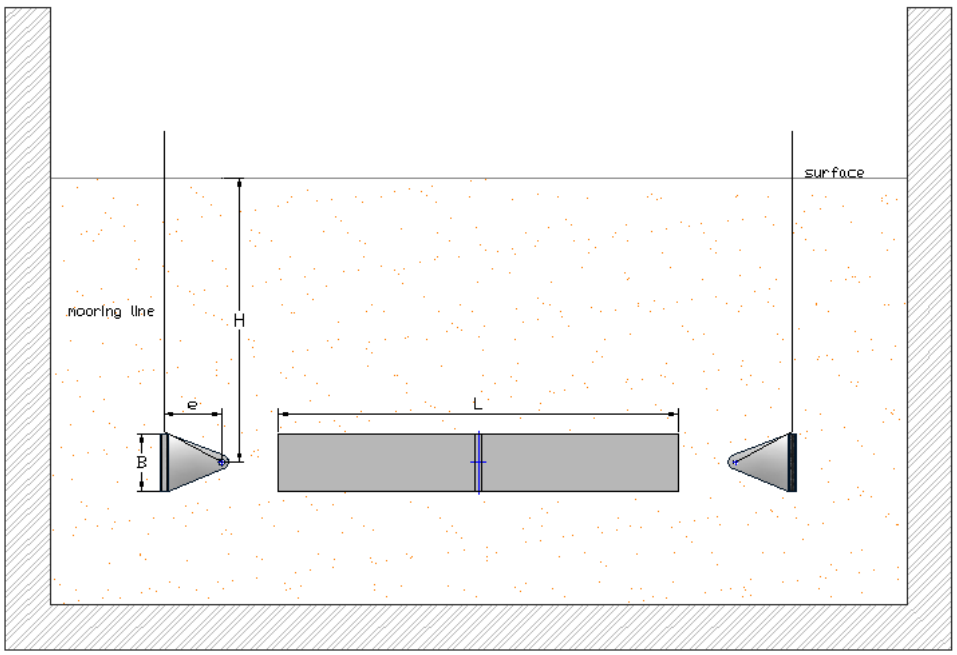


**Figure 3-39 Typical Test Setup No. 1 (Schematic)**

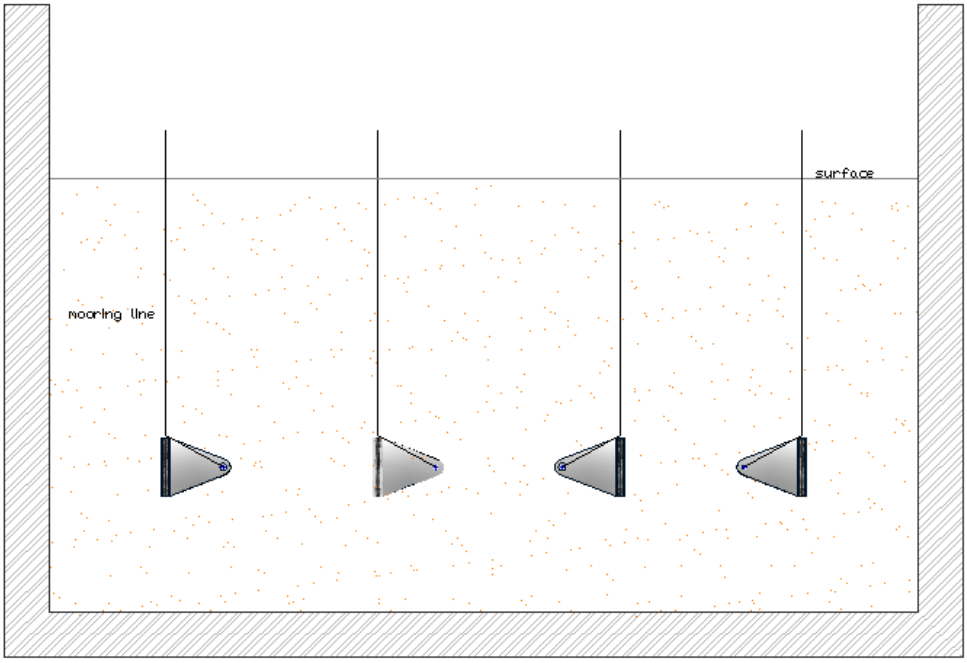


**Figure 3-40 Typical Test Setup No. 2 (Schematic)**

### 3.3.5 Test Procedure

When the sample was set up as described in the previous sections the centrifuge was spun up to 30g. Once the centrifuge reached 30g the continuous shoot mode[2] was enabled on the camera and the actuator was turned on. Images were captured at a rate of 1.5 frames per second. The load development was monitored and shortly after the peak load was reached the actuator was stopped and the camera turned off and the centrifuge spun down.

## 3.4 Post Test Analysis

The post test analysis for this study has been categorised in four stages. A description of each stage is given below and a summary of each is provided in Figure 3-41.

*Stage 1:* Synchronisation of the data with the camera images was made by comparing the load cell data with the camera switch voltage level.

[2] Digital images are captured continuously at even intervals.

*Stage 2:* The camera images were imported into Auto CAD to quantify the evolution of plate displacement and rotation. The number of images captured during each pullout ranged from 90 for lower eccentricity ratios to 150 for higher eccentricity ratios. A suite of tests eliminated the need to consider parallax for this project.

*Stage 3:* Windows Movie Maker was used to convert the images that captured the orientation of the anchor during each anchor test into a short video. The video of each anchor test was used to determine the key behavioural aspects in each test and to identify the image pairs where the PIV analyses would be conducted.

*Stage 4*: Conduct PIV analyses on the image pairs selected in Stage 3 and presenting the output from these analyses as instantaneous velocity fields (described in detail below).

## 3.5 Summary

In this chapter, the principles behind the geotechnical centrifuge at IT Sligo have been explained. The functionality and the geometry of the test equipment used, the characteristics of the silica sand and the preparation, testing and post test analysis procedures followed in this study have been outlined.

The centrifuge testing was conducted over five test series, before conducting the anchor tests two CPT tests were conducted to verify the preparation methodology followed. Anchor tests were conducted with the same anchor eccentricity ratio to verify the responses obtained. PIV analysis was used to illustrate failure mechanisms.

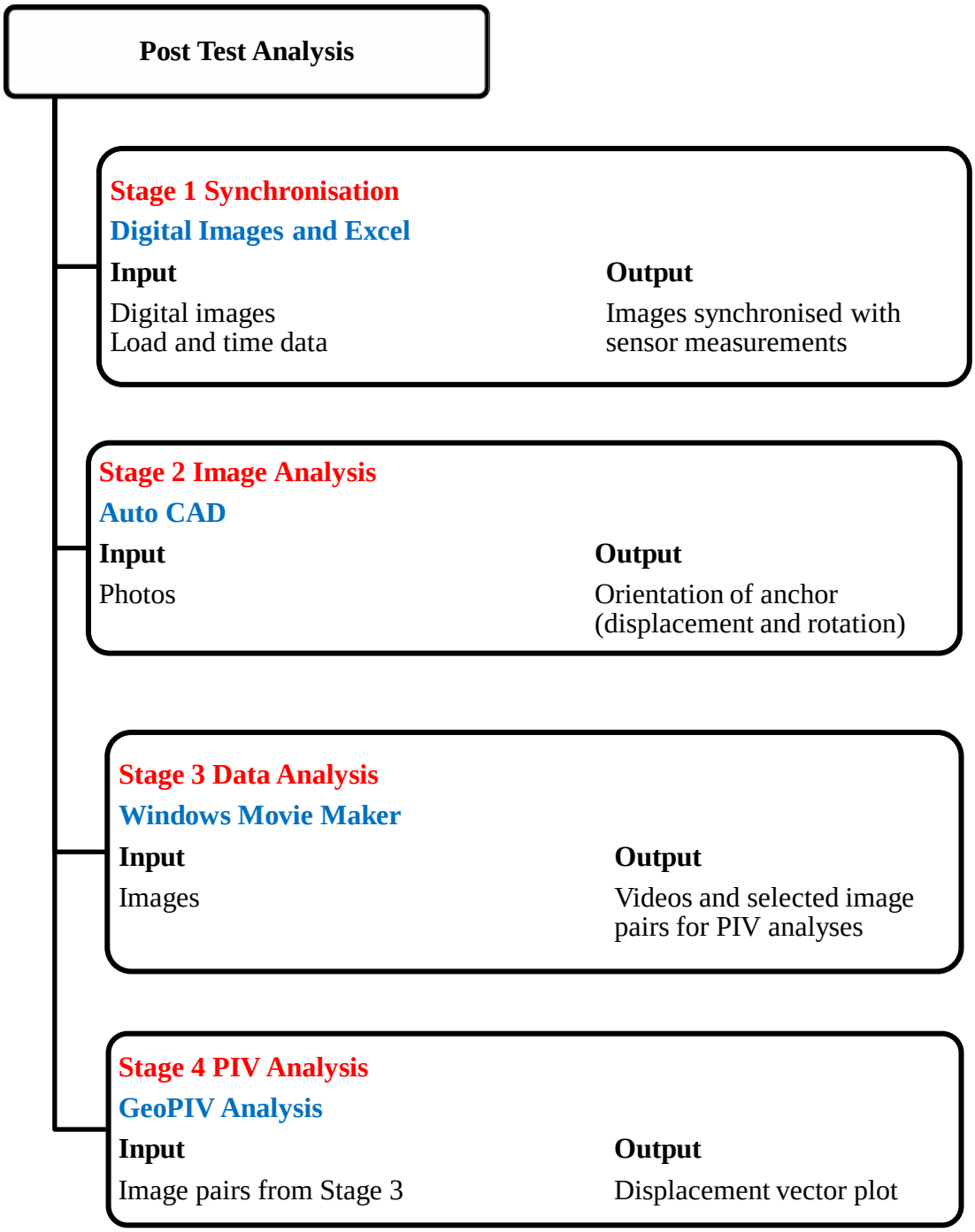


**Figure 3-41 Post Test Analysis**

### 3.5.1 Particle Image Velocimetry Analysis

The soil failure mechanisms around the anchor at the sand Perspex interface during a selected number of anchor tests have been determined using GeoPIV8 developed by White *et al.* (2003). GeoPIV is a non-invasive image analysis technique used to track planar soil displacements.

GeoPIV tracks the inherent texture (i.e. spatial variation of brightness) of soil grains through a series of images. Each image is divided into a mesh of interrogation PIV patches. The size of each patch is determined previously by visually assessing the extent of movement the area of interest undergoes. Patch spacing is selected on the basis of measurement point density. The displaced location of each patch in a subsequent image is obtained by determining the location of highest correlation between each patch and a larger search region from a following image. The principles behind GeoPIV are outlined in Figure 3-42.

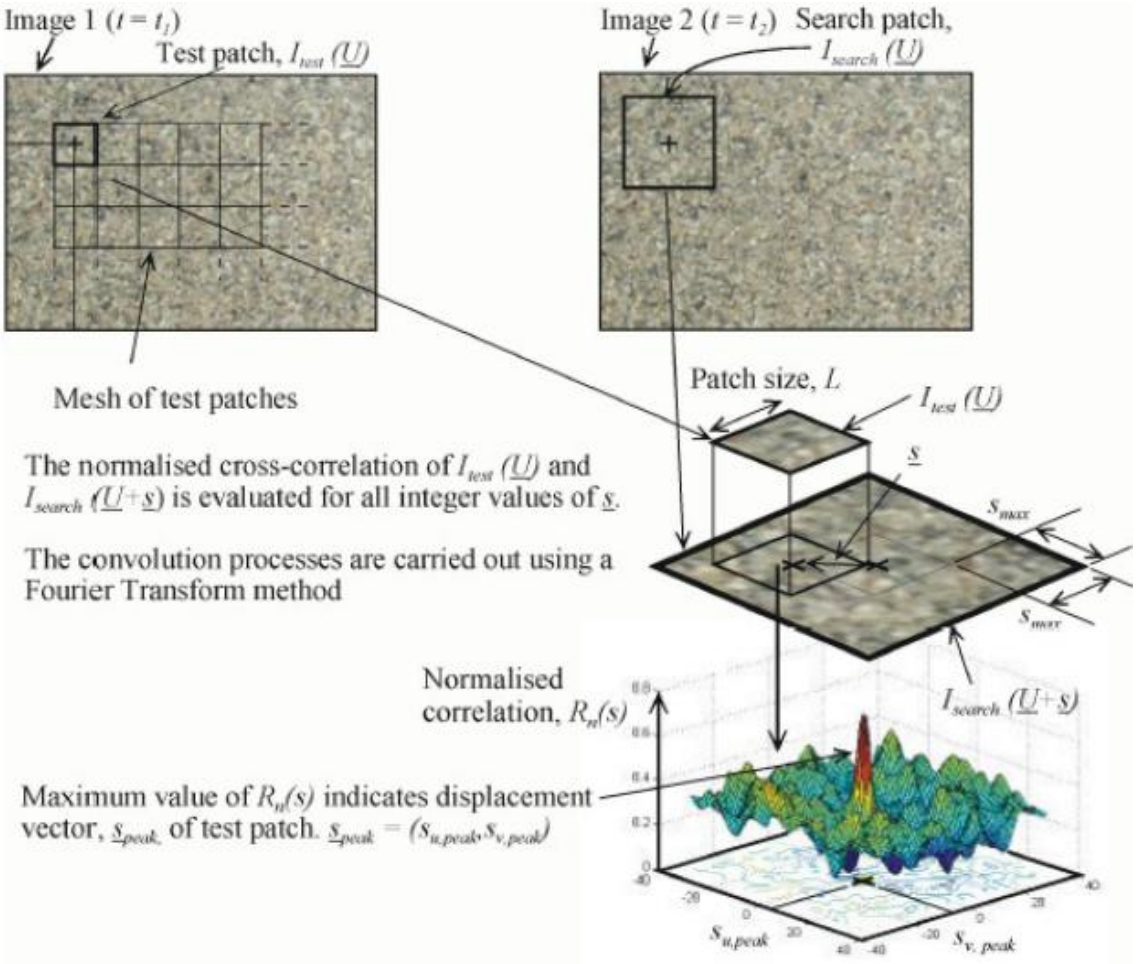


**Figure 3-42 Principle of PIV Analysis (after White *et al.* 2003)**

In this study the following procedure was followed to quantify and illustrate the failure mechanism at each point of interest

- Choose a pair of consecutive images.
- Select an area of interest, and then an appropriate mesh size to best represent the failure mechanism.

- Remove any ‘wild vectors’ (measurement points where the displaced vector could not be determined) from the resulting instantaneous velocity field.
- Apply the scaling factor to the measurements (from pixels to mm) and then move the origin to coincide with the centre of the anchor plate. Note: the scaling factor was dependent of the location of the camera. In each image ten lines 5mm long at a distance of 5mm apart were captured, when the images were imported into AutoCAD a scaling factor was derived.
- Overlay the original and current soil surface profile, orientation of the anchor and the mooring line position onto the vector field.

# CHAPTER 4.0
# RESULTS

## 4.1 Introduction

To fulfil the objectives of this research project model tests have been conducted in the geotechnical centrifuge at the Institute of Technology, Sligo. The results of these tests together with the sample characterisation tests are presented in this chapter. The notation employed to identify each test includes the test series number, test type and strongbox number. For example TS3 01 eb 0.25 B1 refers to the first anchor test (01) conducted in the third series of tests (TS3) with a plate anchor with an eccentricity ratio, e/B = 0.25 (eb 0.25) in strongbox number 1 (B1), whereas TS5 CPT 04 B2 refers to the fourth cone penetration test (CPT 04) conducted in the fifth series of tests (TS5) in strongbox number 2 (B2).

## 4.2 Sample Characterisation

### 4.2.1 Effect of Sand Particle Size

Before considering the sample state when spun to 30 g, it is worth reflecting on the potential scale effects that may exist due to particle size effects. The ratio of the mean particle size ($D_{50}$) to the smallest dimension of the strip anchor (t = 3mm) is 4.67% which is within the range of 3-5% recommended by Taylor (1995).

### 4.2.2 Sample Characteristics and Uniformity

The evolution of sample density with increasing sample height (during sample preparation, Section 3.3.2) is shown in Figure 4-1 and Figure 4-2. The average sample density was found to be $\gamma' = 17.19 kN/m^3$ with an average relative density, $I_D$ = 89%. Table 4-1 provides a summary of the average sample density and relative density for each test series. The maximum and minimum dry densities were both extracted from Lauder (2010). For each sample the average relative density was derived from Equation 4-1.

$$I_D = \left(\frac{\gamma'_d - \gamma'_{d,min}}{\gamma'_{d,max} - \gamma'_{d,min}}\right)\left(\frac{\gamma'_{d,max}}{\gamma'_d}\right)$$ **Equation 4-1**

where $I_D$ is the relative density, $\gamma'_d$ is the dry density, $\gamma'_{d,max}$ is the max dry density and $\gamma'_{d,min}$ is the min dry density.

**Table 4-1 Sample Density for Each Test Series**

| | $\gamma'$ | $I_D$ |
|---|---|---|
| | **(kN/m$^3$)** | **(%)** |
| TS3 B1 | 17.12 | 86.73 |
| TS3 B2 | 17.26 | 90.94 |
| TS4 B1 | 17.12 | 86.96 |
| TS4 B2 | 17.2 | 89.33 |
| TS5 B1 | 17.2 | 89.31 |
| TS5 B2 | 17.15 | 87.65 |
| TS6 B1 | 17.1 | 86.14 |
| TS6 B2 | 17.28 | 91.49 |
| TS7 B1 | 17.32 | 92.66 |
| TS7 B2 | 17.12 | 86.8 |
| Variation | ±0.14 | ±3.84 |
| Average | 17.19 | 88.8 |
| Maximum | 17.32 | 92.66 |
| Minimum | 17.1 | 86.14 |

Two Cone Penetration Tests (CPTs) were carried out at 30g before the anchor tests. The location of each CPT was consistent between samples (Figure 3-32) and was along the centreline of the strongbox. Gui *et al.* (1998) and Bolton *et al.* (1999) both recommend that CPTs should be carried out 10 CPT diameters from rigid boundaries. The CPTs were located along the centreline of the box (70 mm from the

closest rigid boundary = 7 CPT diameters), which is less that the recommended minimum spacing (Gui *et al.*, 1998; Bolton *et al.*, 1999). However as the CPT locations are the same in each sample the profiles serve as a useful indication of the repeatability of each sample. Bolton *et al.* (1999) reported that as the relative density increases the affect of the boundary condition increases particularly when the distance is less than 10 CPT diameters from the closest rigid boundary. The recommended distance could not be achieved in this setup however. In each CPT test the boundary distance in three directions was 7 CPT diameters from the closest rigid boundary which allowed for each CPT test to be compared.

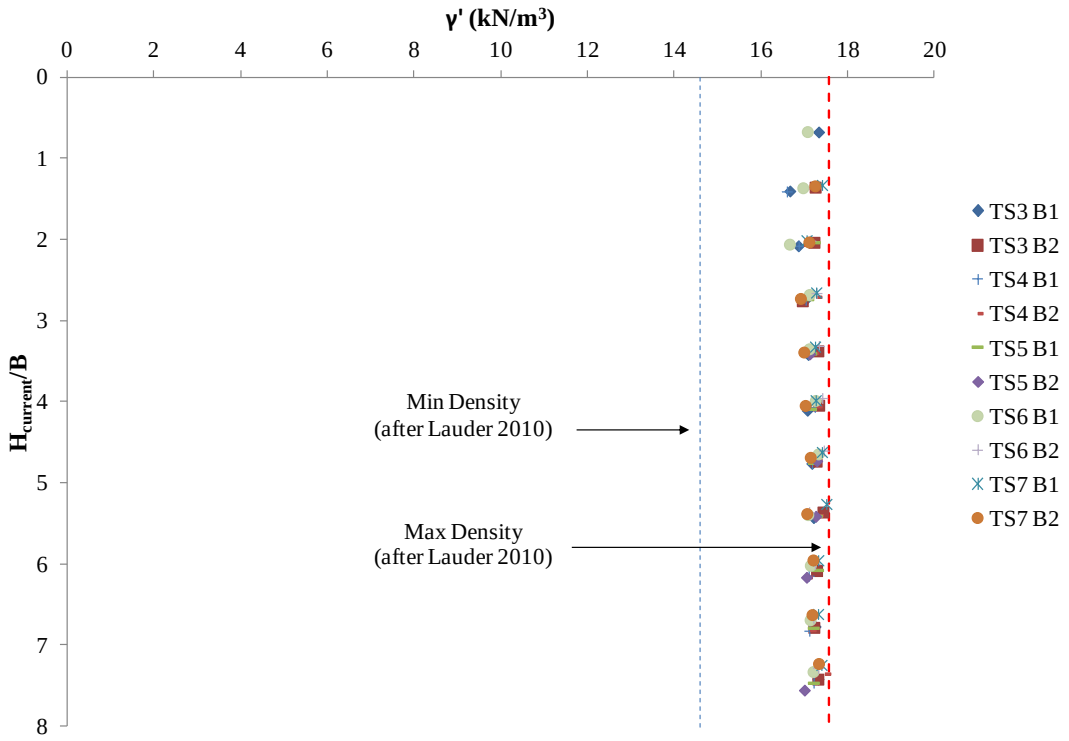


**Figure 4-1 Density Profile**

A representative CPT test from each sample is presented in Figure 4-3. As expected for a sample with constant $I_D$ with depth, the tip resistance increases linearly with increasing stress level after 3 to 4 cone diameters ($\sigma_v$ = 15 to 20 kPa). The good agreement between profiles (≤10% from the mean tip resistance) both within and between strongboxes indicates that the preparation technique produced repeatable samples.

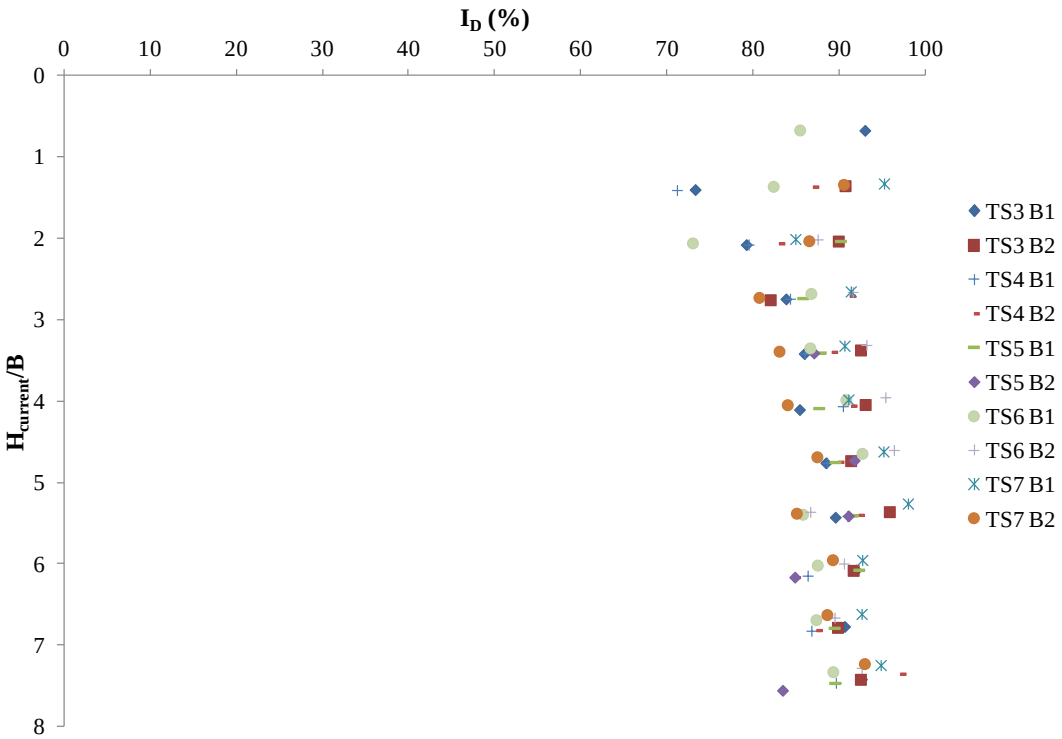


**Figure 4-2 Relative Density Profile**

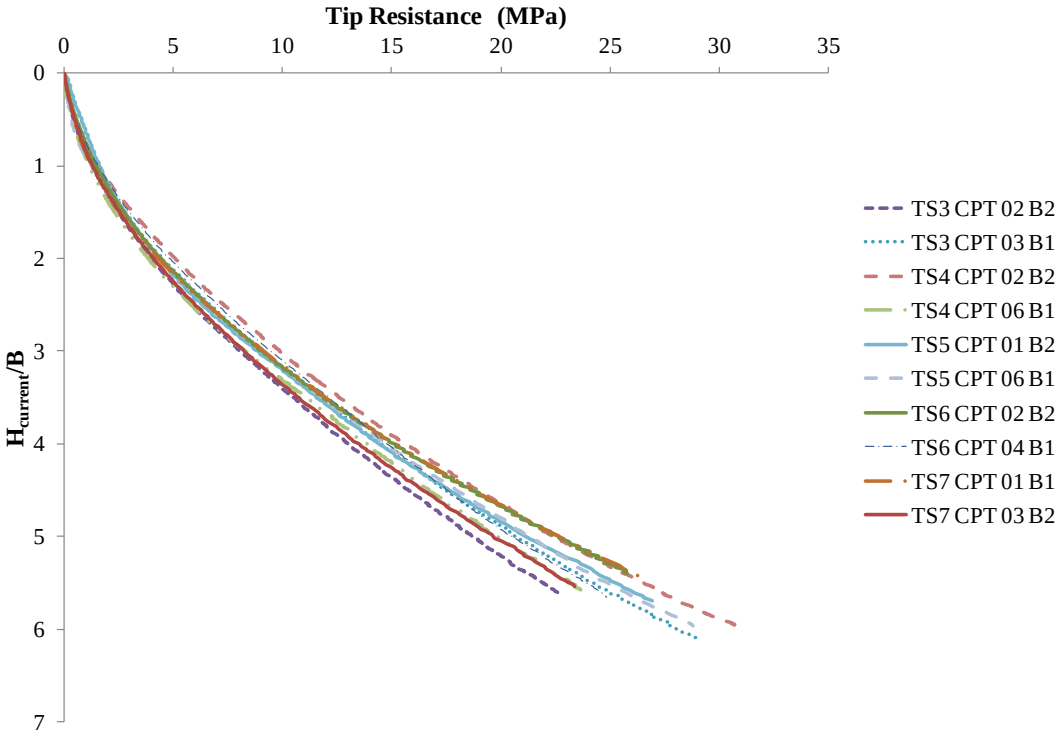


**Figure 4-3 CPT Profile (Representative Samples)**

## 4.3 Anchor Tests

Table 4-2provides a summary of the thirty seven anchor tests that were conducted for this study. The test programme includes six different padeye eccentricity ratios and anchor tests both at the Perspex interface and within the centre of the strongbox.

Table 4-2 summarises the peak load measured during the anchor pullout and the displacement of the anchor mooring line to this peak load. It is worth noting that due to excessive electrical noise on the line displacement sensor in TS3, TS4 and TS5, the mooring line displacement was determined using the extraction rate of the actuator (1mm/s). The reliability of this approach was confirmed through a number of control experiments (at 1g and 30g (Figure 4-4, Figure 4-5, Figure 4-6 and Figure 4-7)) which compared displacement measurements derived using the line displacement rate (1mm/s) with independent measurements from the LVDT.

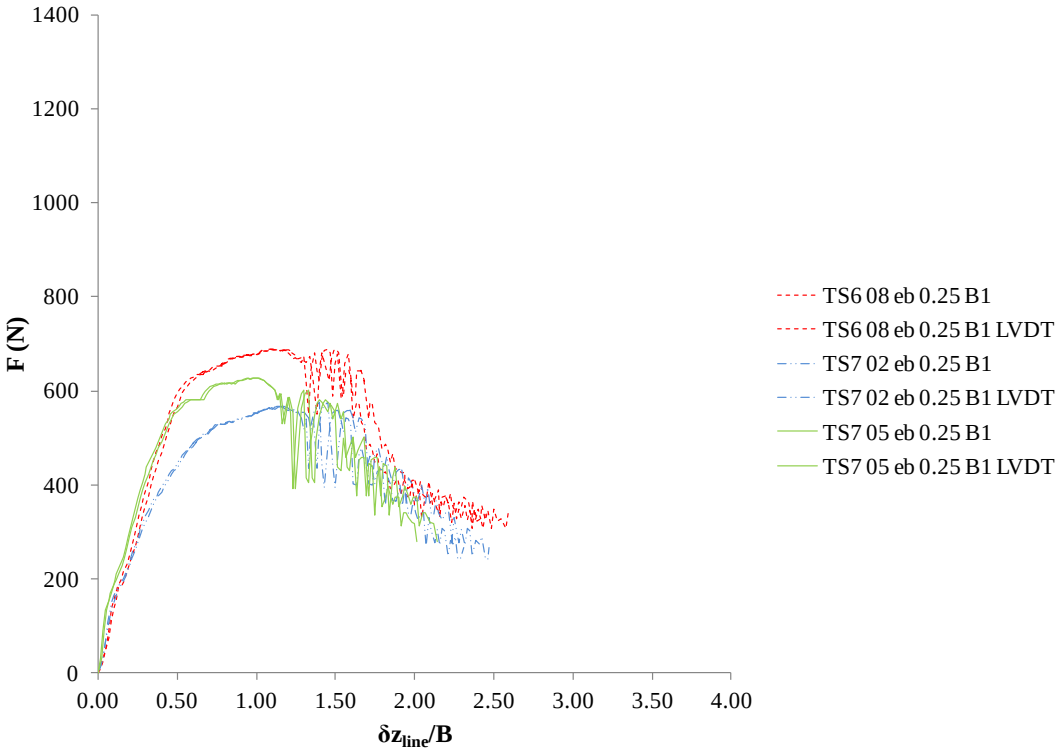


**Figure 4-4 Comparison of Extraction Rate vs. LDVT Recordings (e/B = 0.25)**

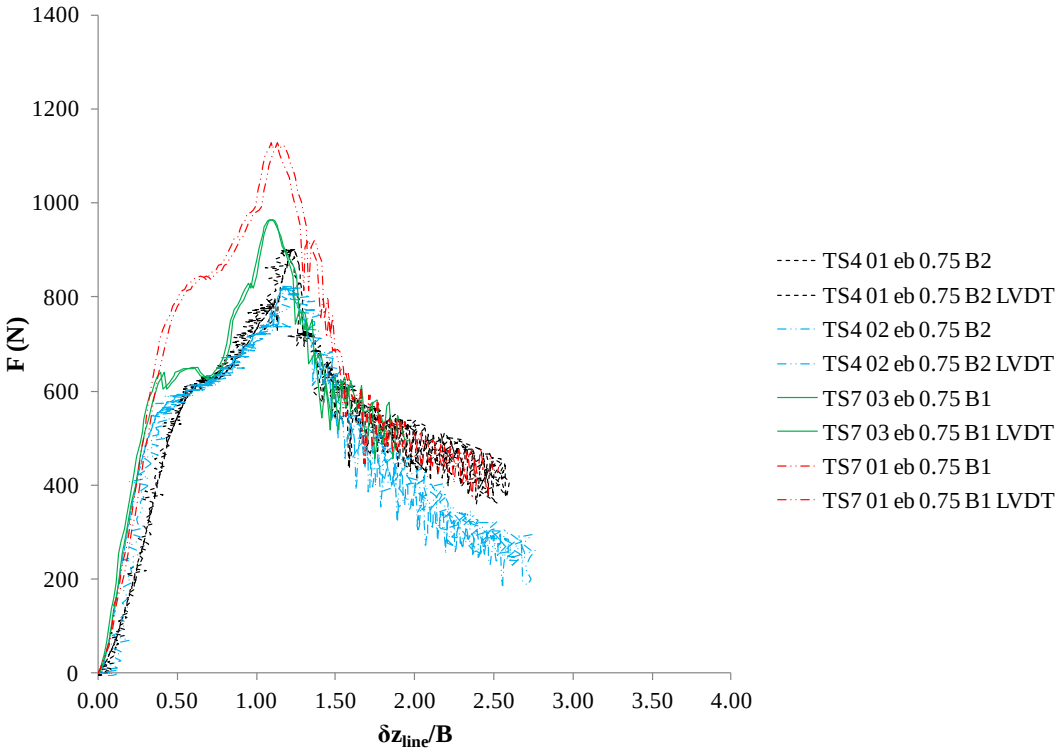


**Figure 4-5 Comparison of Extraction Rate vs. LDVT Recordings (e/B = 0.75)**

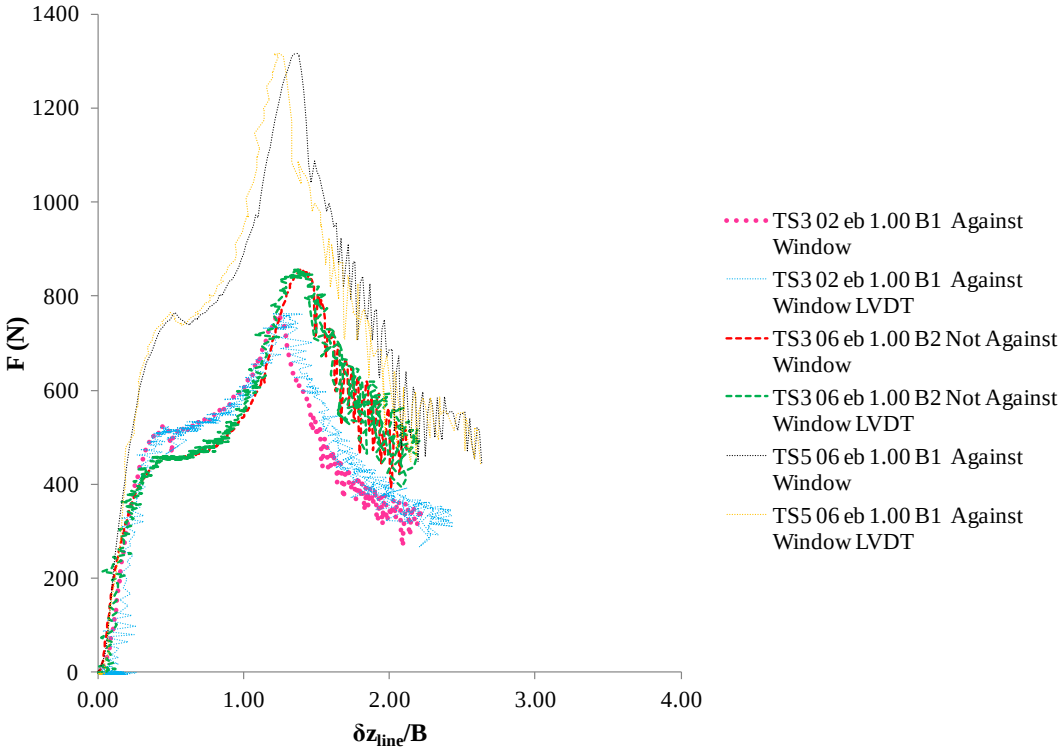


**Figure 4-6 Comparison of Extraction Rate vs. LDVT Recordings (e/B = 1.00)**

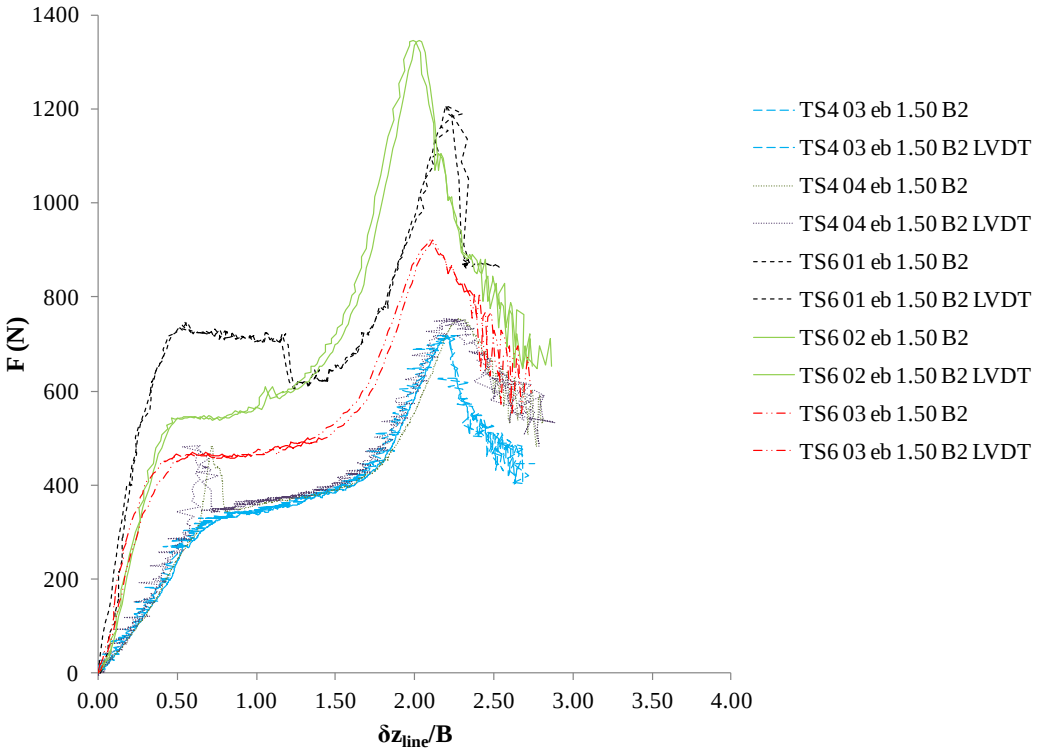


**Figure 4-7 Comparison of Extraction Rate vs. LDVT Recordings (e/B = 1.50)**

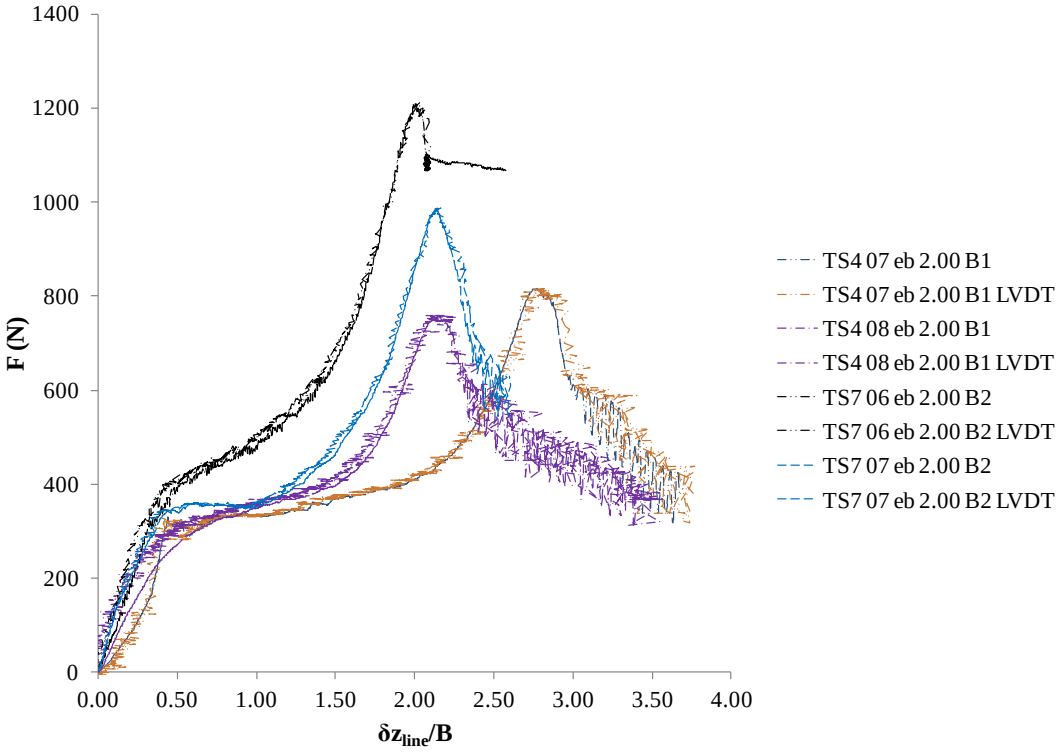


**Figure 4-8 Comparison of Extraction Rate vs. LDVT Recordings (e/B = 2.00)**

A typical load – displacement response during anchor keying and pullout is shown on Figure 4-9 for a test conducted at the Perspex interface with e/B = 1. The response is typical of that for clay (e.g. Gaudin *et al.* 2006) with an initial stiff response as the anchor begins to rotate, followed by a softer response as the rotation angle increases, and a final stiff response as the effective eccentricity of the padeye reduces and anchor capacity is fully mobilised (at a plate inclination to the vertical of 65°). The inclination of the anchor to the vertical, as assessed from the digital images captured during the test, is also shown at selected points on Figure 4-9.

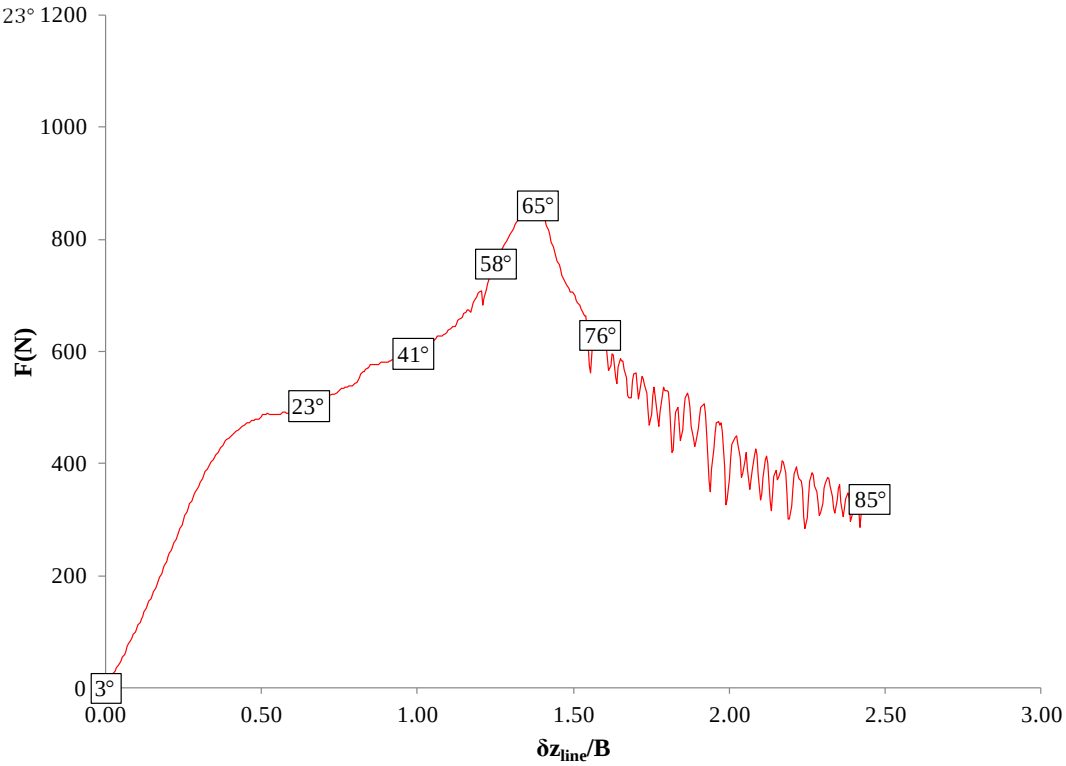


**Figure 4-9 Typical Load - Displacement Response with Plate Inclination to the Vertical**

**Table 4-2 Summary of Anchor Tests**

| | **Window** | **e/B** | **$H_{initial}$/B** | **$F_{peak}$** | **$\delta z_{line}$/B** |
|---|---|---|---|---|---|
| | **Y/N** | **(-)** | **(-)** | **(kN)** | **(-)** |
| TS3 01 eb **1.00** B1 | Y | 1 | - | 887 | 1.33 |
| TS3 02 eb **1.00** B1 | Y | 1 | 4.39 | 762 | 1.24 |
| TS3 03 eb **1.00** B1 | N | 1 | - | 817 | 2.75 |
| TS3 04 eb **1.00** B2 | Y | 1 | 4.6 | 862 | 1.37 |
| TS3 05 eb **1.00** B2 | Y | 1 | 4.72 | 942 | 1.39 |
| TS3 06 eb **1.00** B2 | N | 1 | - | 857 | 1.41 |
| TS4 01 eb **0.75** B2 | Y | 0.75 | 5.3 | 904 | 1.25 |
| TS4 02 eb **0.75** B2 | Y | 0.75 | 4.51 | 836 | 1.25 |
| TS4 03 eb **1.5** B2 | Y | 1.5 | - | 722 | 2.27 |
| TS4 04 eb **1.5** B2 | Y | 1.5 | - | 760 | 2.32 |
| TS4 05 eb **0.50** B1 | Y | 0.5 | 4.97 | 861 | 1.17 |
| TS4 06 eb **0.50** B1 | Y | 0.5 | 4.91 | 907 | 1.2 |
| TS4 07 eb **2.00** B1 | Y | 2 | 4.24 | 820 | 2.8 |
| TS4 08 eb **2.00** B1 | Y | 2 | 4.99 | 770 | 2.21 |
| TS5 01 eb **0.25** B2 | Y | 0.25 | 5.43 | 817 | 1.37 |
| TS5 02 eb **0.25** B2 | Y | 0.25 | 5.88 | 827 | 1.33 |
| TS5 05 eb **1.00** B1 | Y | 1 | 5.38 | 1041 | 1.32 |
| TS5 06 eb **1.00** B1 | Y | 1 | 5.43 | 1316 | 1.37 |
| TS5 07 eb **1.00** B1 | N | 1 | - | 890 | 1.43 |
| TS5 03 eb **2.00** B2 | Y | 2 | 5.54 | 1066 | 2.03 |
| TS5 04 eb **2.00** B2 | Y | 2 | - | 907 | 1.7 |
| TS6 01 eb **1.5** B2 | Y | 1.5 | 4.76 | 1207 | 2.2 |
| TS6 02 eb **1.5** B2 | Y | 1.5 | - | 1345 | 2.03 |
| TS6 03 eb **1.5** B2 | Y | 1.5 | - | 920 | 2.11 |
| TS6 04 eb **0.50** B1 | Y | 0.5 | 5.31 | 1069 | 0.89 |
| TS6 05eb **0.25** B1 | Y | 0.25 | - | 859 | 1.17 |
| TS6 06 eb **0.50** B1 | Y | 0.5 | 4.72 | 1025 | 0.96 |
| TS6 07 eb **0.25** B1 | Y | 0.25 | - | 791 | 1.07 |
| TS6 08 eb **0.25** B1 | Y | 0.25 | 5.04 | 690 | 1.45 |
| TS7 01 eb **0.75** B1 | Y | 0.75 | - | 1129 | 1.13 |
| TS7 02 eb **0.25** B1 | Y | 0.25 | 4.98 | 576 | 1.4 |
| TS7 03 eb **0.75** B1 | Y | 0.75 | 6.83 | 964 | 1.1 |
| TS7 04 eb **0.25** B1 | Y | 0.25 | 4.83 | 668 | 1.31 |
| TS7 05 eb **0.25** B1 | Y | 0.25 | 5.17 | 627 | 1 |
| TS7 06 eb **2.00** B2 | Y | 2 | - | 1214 | - |
| TS7 07 eb **2.00** B2 | Y | 2 | 5.2 | 987 | - |
| TS7 08 eb **2.00** B2 | Y | 2 | - | - | - |

### 4.3.1 Load Displacement Response

Figure 4-10 through to Figure 4-15 show the load – displacement response for each anchor test categorised according to the eccentricity ratio. The data are presented as load, F, vs. line displacement normalised by the anchor breadth, $\delta z_{line}/B$. Figure 4-16 compares the response for each padeye eccentricity, using a selected representative test for each padeye eccentricity and the peak loads and corresponding mobilised line displacements are summarised in Table 4-3.

**Table 4-3 Summary of Representative Samples**

| | $F_{peak}$ | $\delta z_{line}/B$ |
|---|---|---|
| TS6 08 eb **0.25** B1 | 690 | 1.45 |
| TS4 06 eb **0.50** B1 | 907 | 1.20 |
| TS4 02 eb **0.75** B2 | 836 | 1.25 |
| TS3 04 eb **1.00** B2 | 862 | 1.37 |
| TS5 03 eb **2.00** B2 | 1066 | 2.03 |

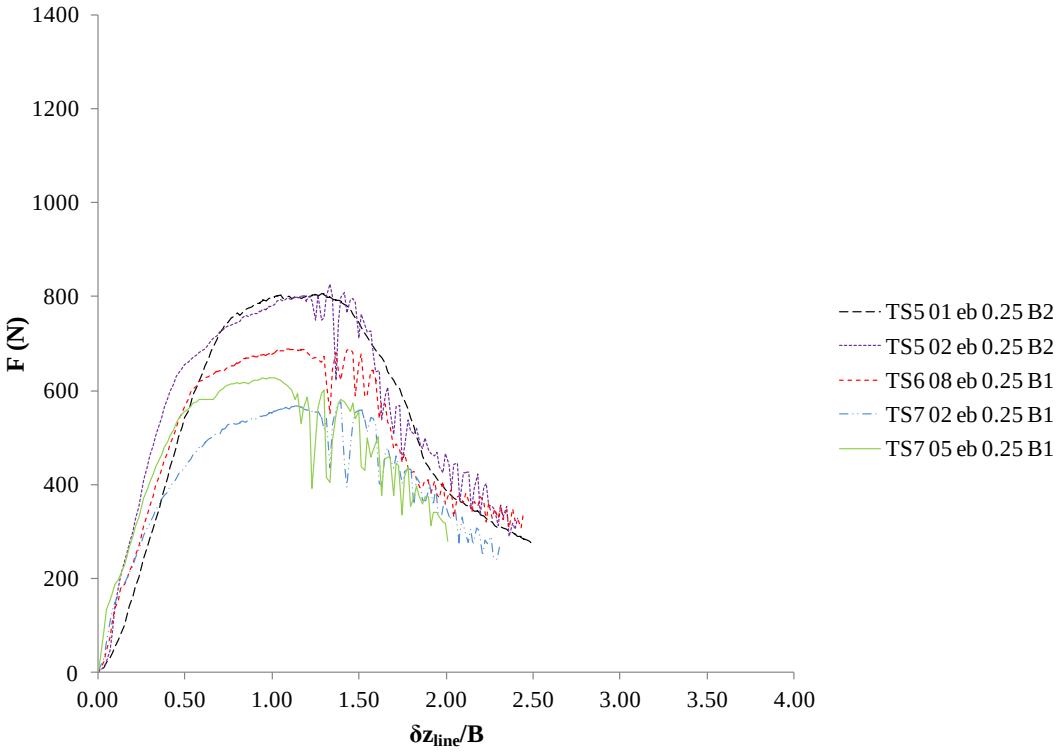


**Figure 4-10 Load - Displacement Response during Keying and Pullout (vertical anchor line displacement) (e/B = 0.25)**

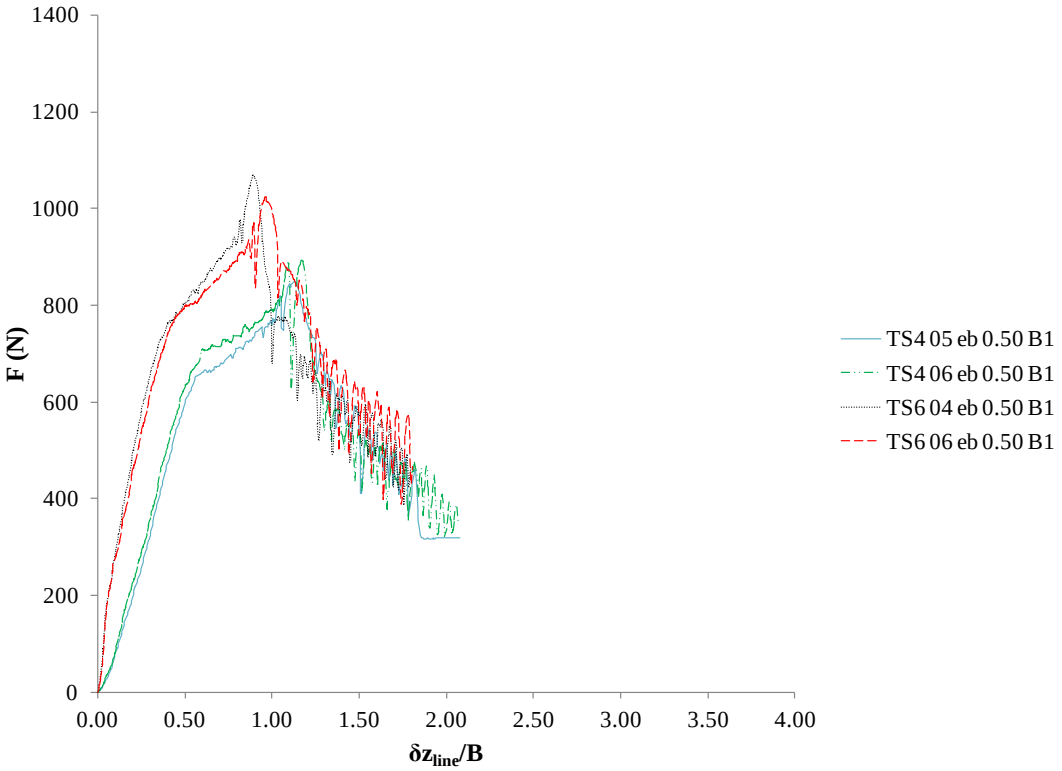


**Figure 4-11 Load - Displacement Response during Keying and Pullout (vertical anchor line displacement) (e/B = 0.50)**

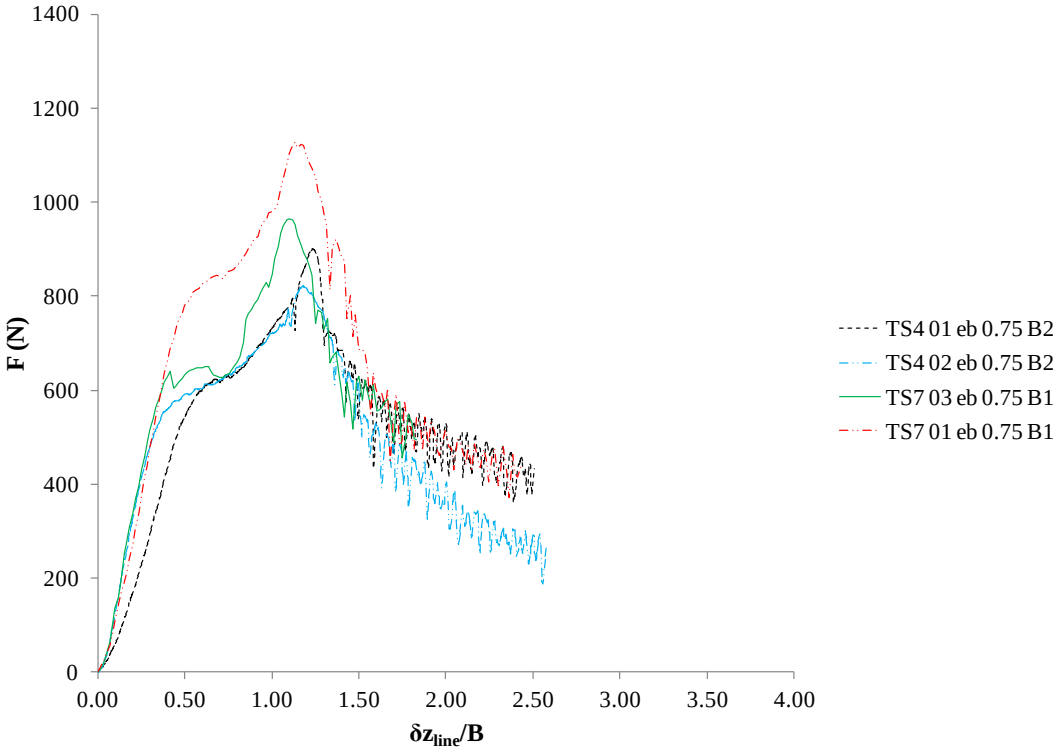


**Figure 4-12 Load - Displacement Response during Keying and Pullout (vertical anchor line displacement) (e/B = 0.75)**

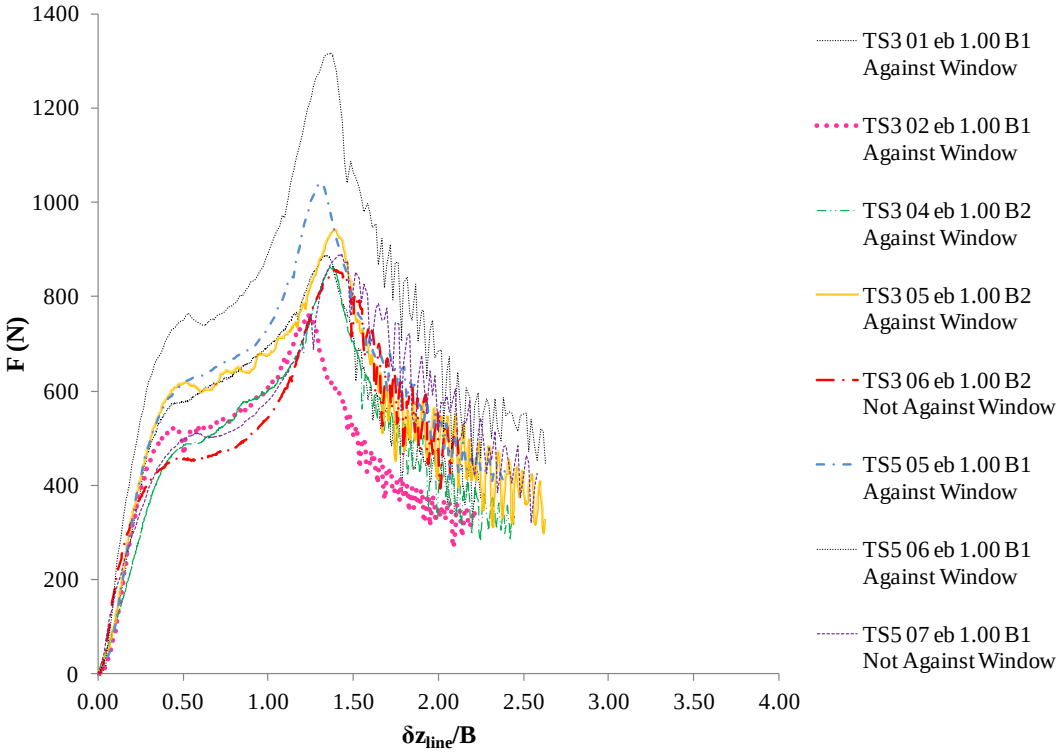


**Figure 4-13 Load - Displacement Response during Keying and Pullout (vertical anchor line displacement) (e/B = 1)**

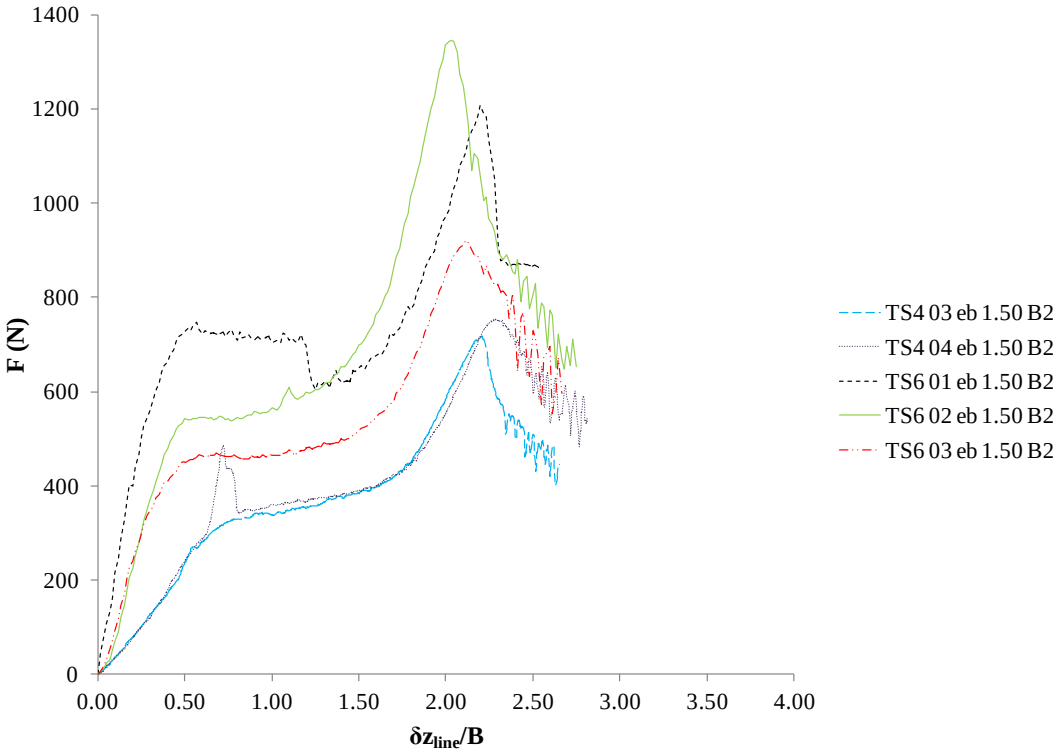


**Figure 4-14 Load - Displacement Response during Keying and Pullout (vertical anchor line displacement) (e/B = 1.5)**

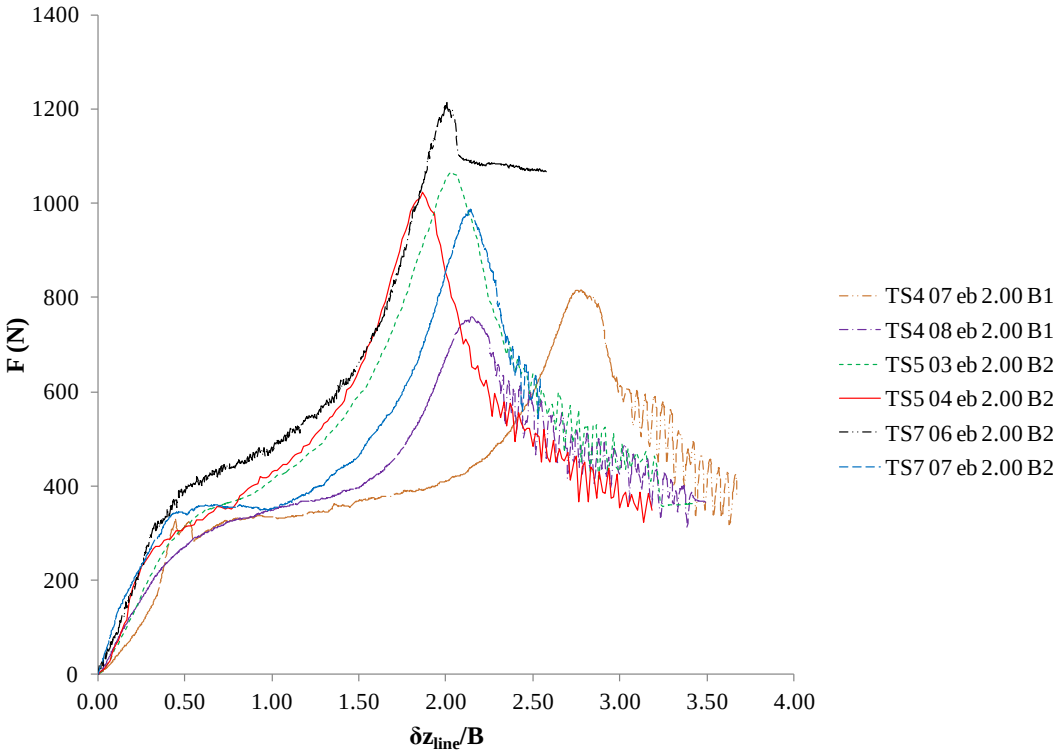


**Figure 4-15 Load - Displacement Response during Keying and Pullout (vertical anchor line displacement) (e/B = 2)**

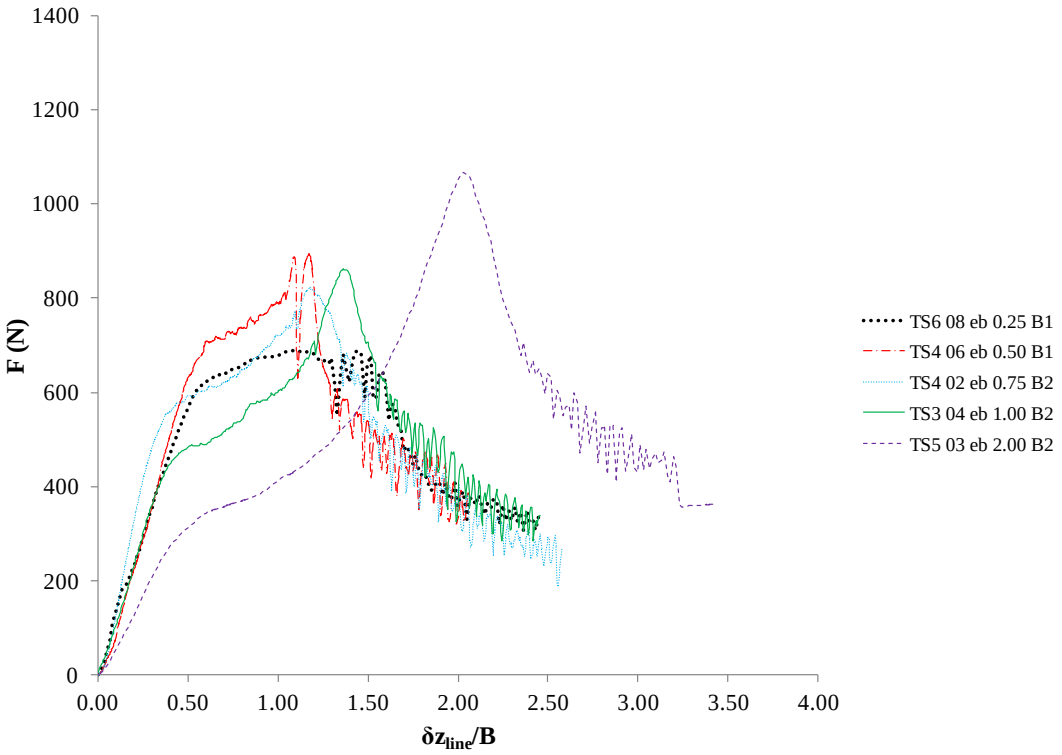


**Figure 4-16 Load - Displacement Response during Keying and Pullout (vertical anchor line displacement) (Representative Tests)**

Two features are evident from Figure 4-16. First, as the eccentricity ratio, $e/B \geq 0.5$ the mooring line displacement required to reach the peak load, $F_{peak,}$ increases. However it is worth noting that the mooring line displacement represents the movement of the anchor padeye but not the movement of the plate. Second, the relative load, $F/F_{peak}$, at which the load starts to plateau decreases with increasing eccentricity ratio. Both features are considered in more detail in Chapter 5.

### 4.3.2 Quantification of Frictional Resistance

The frictional resistance created between the Perspex face and the O-ring's edge on the anchors ends was quantified by conducting two anchor tests, TS3 06 eb 1.00 B2 and TS5 07 eb 1.00 B1, in the centre of the strong box.

The load – displacement response (and notably the peak load, $F_{peak}$) recorded for the anchor tests conducted in the centre of the strongbox lies within the range of peak loads recorded for the plate anchor against the Perspex. This indicates that the friction induced by conducting the anchor tests against the Perspex is small relative to the bearing resistance of the plate (Figure 4-13) and has no affect on the peak load.

Similar findings were reported by Gourvenec and O'Loughlin (2006), who showed similar bearing resistance profiles for half model footing tests conducted adjacent to a Perspex panel and full footing model footing tests conducted in the interior of the strongbox. Hence it is reasonable to use the load data from the tests conducted adjacent to the Perspex panel.

## 4.4 Load and Anchor Orientation

The mooring line displacement is not considered to be representative of the plate anchor displacement as it reflects the trajectory of the padeye and includes some mechanical reorientation and straightening of the mooring line. The anchor displacement can more reliably be determined from the digital images captured of the plate during keying. The anchor displacement was extracted from the digital images imported in to AutoCAD, this data was synchronised with the load data of

the corresponding anchor test. The digital images also permit the plate orientation to be determined during keying.

A summary of the vertical anchor displacement, $\delta z$, (measured at the centre of the plate) and orientation, $\Theta$, (measured to the vertical) before keying and at the peak load are provided on Table 4-4. These measurements were possible for eighteen of the thirty seven anchor tests conducted adjacent to the Perspex (see Appendix A). In the remaining tests the anchor end did not remain visible throughout the test, due to sand ingress between the O-ring and the Perspex.

This level of analysis was completed on eighteen of the thirty seven anchor tests conducted against the Perspex interface. The results have been presented as load, F, vs. normalised plate displacement, $\delta z_{plate}/B$, (Figure 4-17 to Figure 4-21) and $\delta z_{plate}/B$ vs. inclination of the plate to the vertical, $\Theta$, (Figure 4-23 to Figure 4-28).

Good agreement within each eccentricity ratio group is evident. The loss of embedment, $\delta z_{plate}$, is seen to decrease with increasing eccentricity ratio, e/B (Figure 4-22). There is also an increase in $\Theta$ at $F_{peak}$ with increasing e/B, and the rate of rotation with respect to loss of embedment increases with increasing $\delta z_{plate}$ (Figure 4-28). Although Figure 4-28 shows that the plate anchors evolve to a tolerably steady final angle, this angle is not reached at the peak load.

**Table 4-4 Summary of Data from Load - Displacement Plots**

| | $H_{initial}/B$ | $\Theta_{initial}$ | $F_{peak}$ | $\delta z_{line}/B$ | $\delta z_{plate}/B$ | H/B | $\Theta$ |
|---|---|---|---|---|---|---|---|
| | (-) | (°) | (kN) | (-) | (-) | (-) | (°) |
| TS6 08 eb **0.25** B1 | 5.04 | 8 | 690 | 1.45 | 1.08 | 3.96 | 61 |
| TS7 02 eb **0.25** B1 | 4.98 | 0 | 576 | 1.40 | 1.17 | 3.81 | 56 |
| TS7 04 eb **0.25** B1 | 4.83 | 10 | 668 | 1.31 | 0.94 | 3.89 | 58 |
| TS7 05 eb **0.25** B1 | 5.17 | 13 | 627 | 1 | 0.89 | 4.28 | 49 |
| TS4 06 eb **0.50** B1 | 4.91 | 8 | 907 | 1.20 | 0.43 | 4.48 | 59 |
| TS6 04 eb **0.50** B1 | 5.31 | 13 | 1069 | 0.89 | 0.37 | 4.94 | 57 |
| TS6 06 eb **0.50** B1 | 4.72 | 8 | 1025 | 0.97 | 0.39 | 4.33 | 59 |
| TS4 01 eb **0.75** B2 | 5.3 | 22 | 904 | 1.25 | 0.11 | 5.19 | 60 |
| TS4 02 eb **0.75** B2 | 4.51 | 4 | 836 | 1.26 | 0.22 | 4.29 | 63 |
| TS7 01 eb **0.75** B1 | - | 8 | 1129 | 1.13 | 0.22 | - | 57 |
| TS7 03 eb **0.75** B1 | 6.83 | 2 | 964 | 1.10 | 0.18 | 6.65 | 57 |
| TS3 04 eb **1.00** B2 | 4.6 | 3 | 862 | 1.37 | 0.22 | 4.38 | 64 |
| TS5 05 eb **1.00** B1 | 5.38 | 8 | 1041 | 1.32 | 0.18 | 5.2 | 61 |
| TS5 06 eb **1.00** B1 | 5.43 | 3 | 1316 | 1.37 | 0.18 | 5.25 | 71 |
| TS4 07 eb 2.00 B1 | 4.24 | 4 | 820 | 2.80 | 0.12 | 4.12 | 75 |
| TS4 08 eb **2.00** B1 | 4.99 | 7 | 770 | 2.22 | 0.15 | 4.84 | 74 |
| TS5 03 eb **2.00** B2 | 5.54 | 17 | 1066 | 2.03 | 0.08 | 5.46 | 70 |
| TS7 07 eb **2.00** B2 | 5.2 | 18 | 987 | - | 0.13 | 5.07 | 83 |

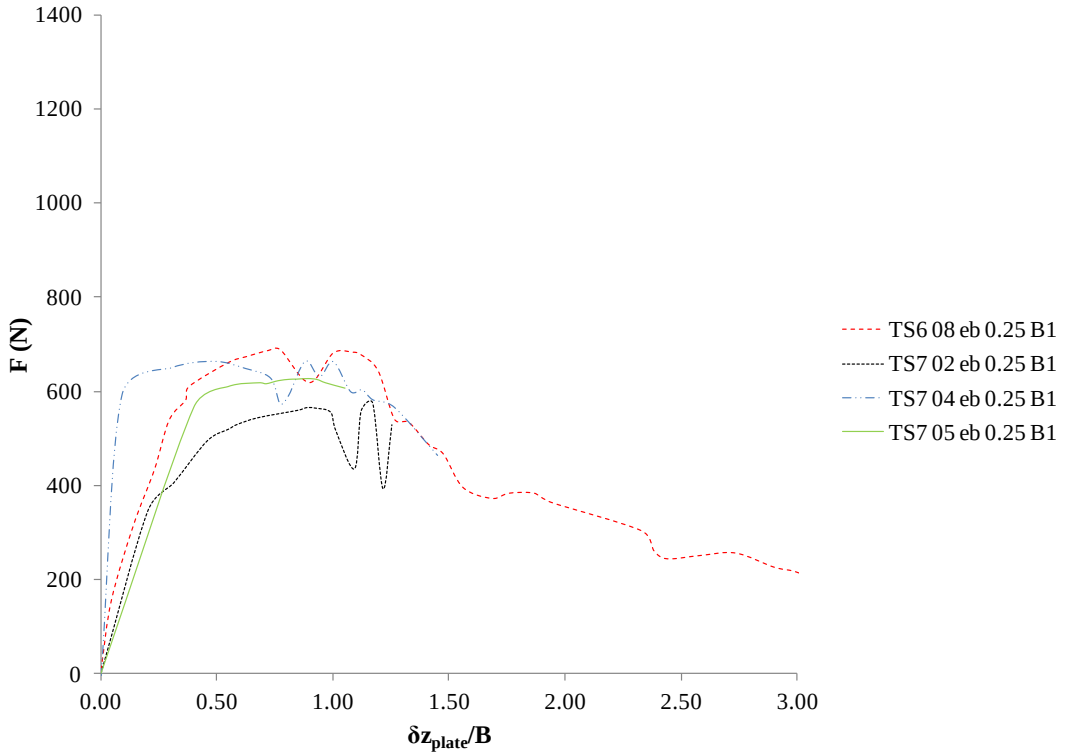


**Figure 4-17 Load - Displacement Response during Keying and Pullout (vertical plate displacement quantified from digital images) (e/B = 0.25)**

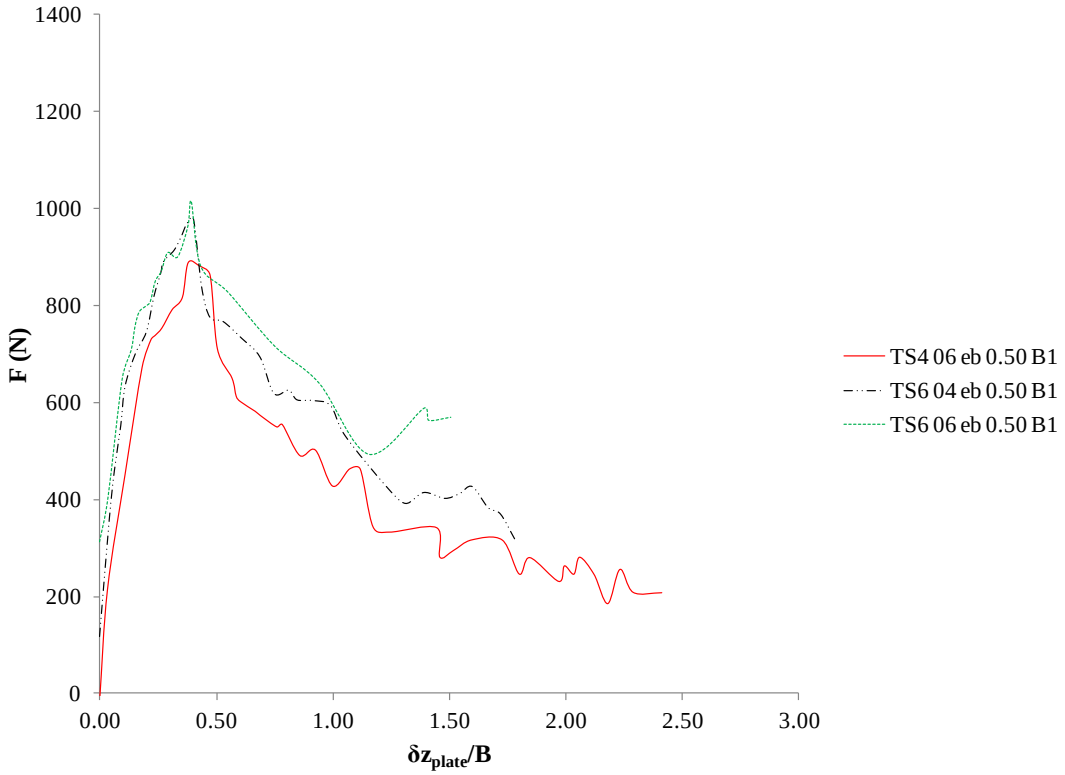


**Figure 4-18 Load - Displacement Response during Keying and Pullout (vertical plate displacement quantified from digital images) (e/B = 0.50)**

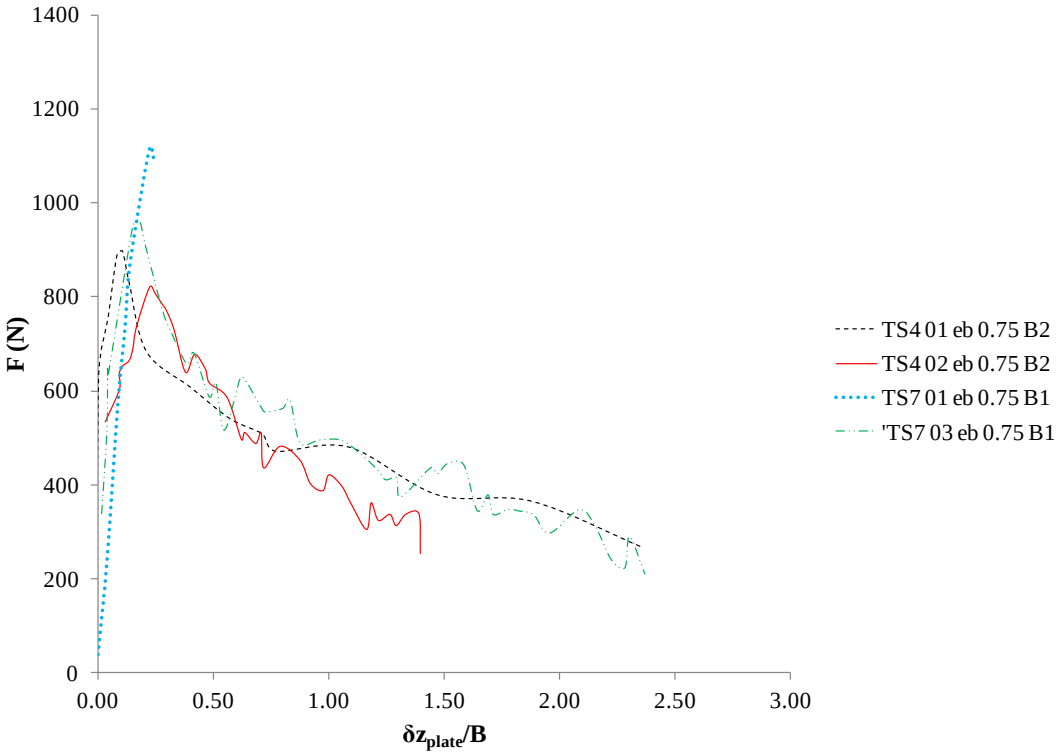


**Figure 4-19 Load - Displacement Response during Keying and Pullout (vertical plate displacement quantified from digital images) (e/B = 0.75)**

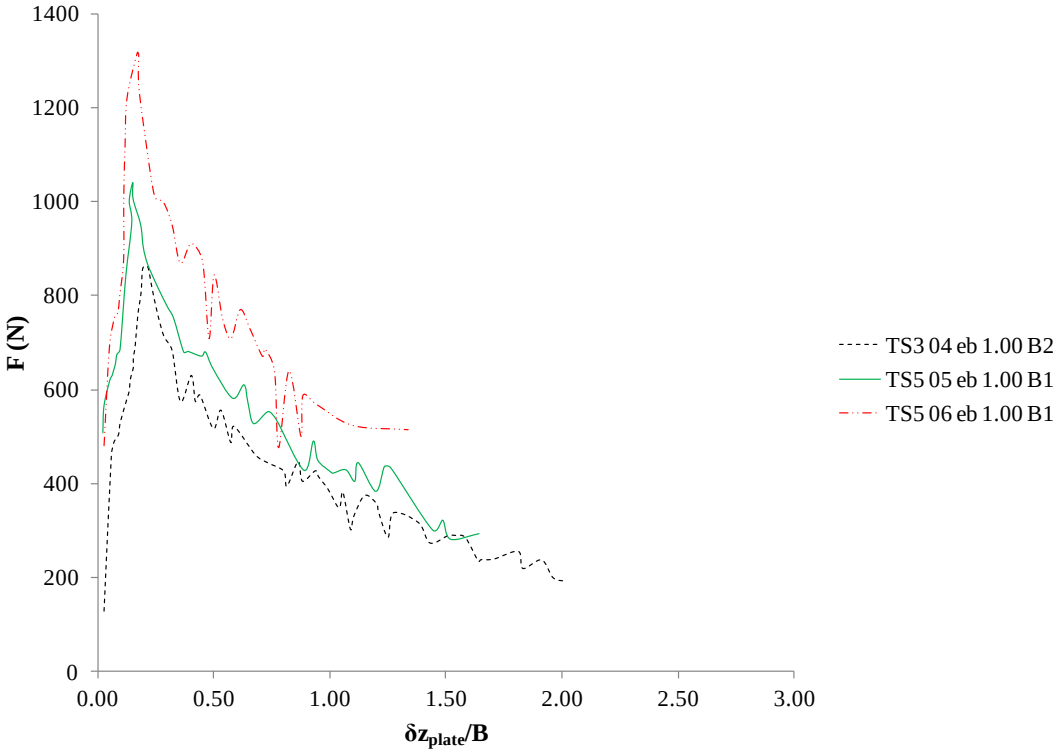


**Figure 4-20 Load - Displacement Response during Keying and Pullout (vertical plate displacement quantified from digital images) (e/B = 1)**

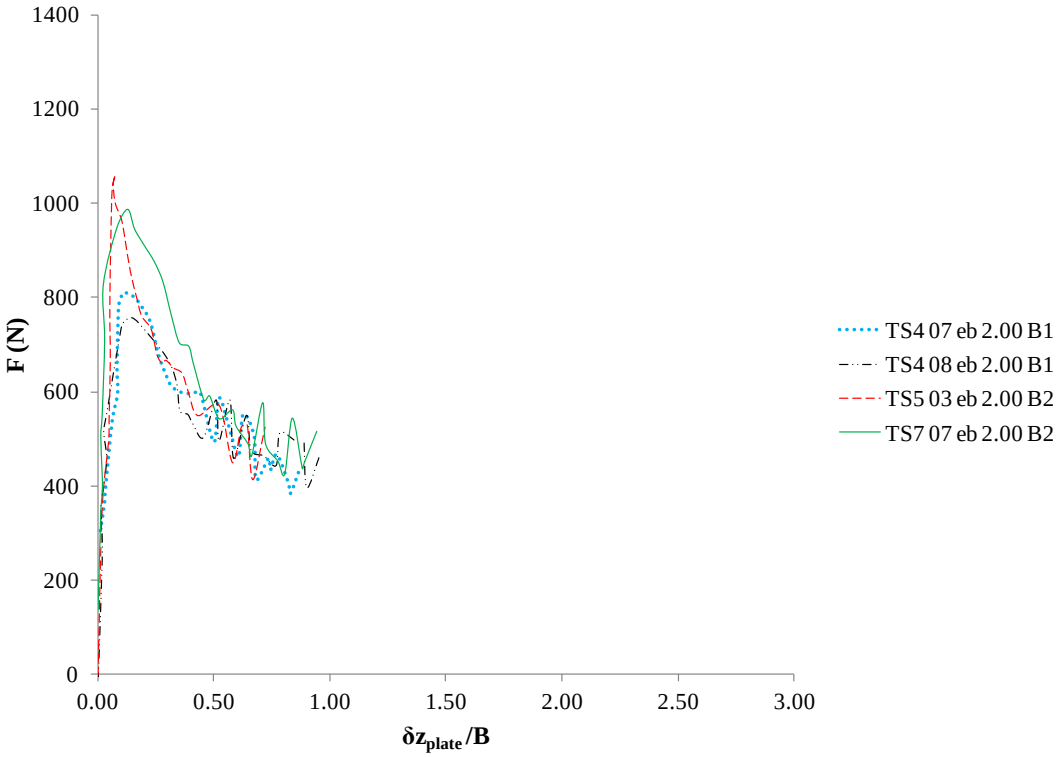


**Figure 4-21 Load - Displacement Response during Keying and Pullout (vertical plate displacement quantified from digital images) (e/B = 2)**

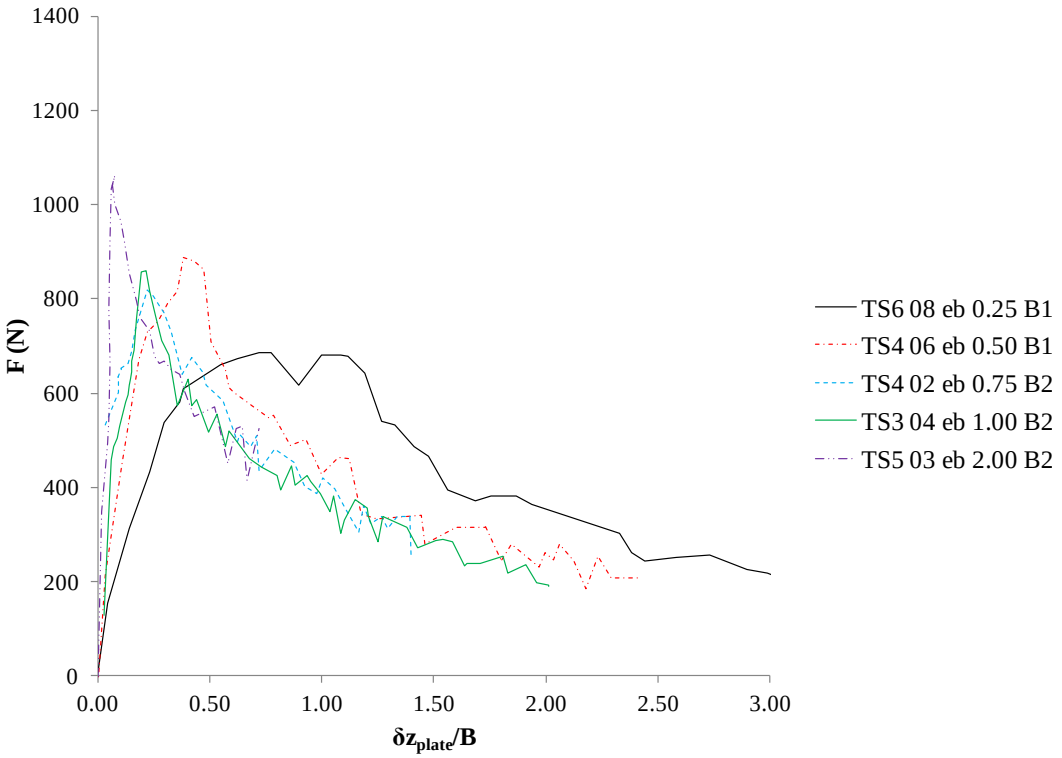


**Figure 4-22 Load - Displacement Response during Keying and Pullout (vertical plate displacement quantified from digital images) (Representative Tests)**

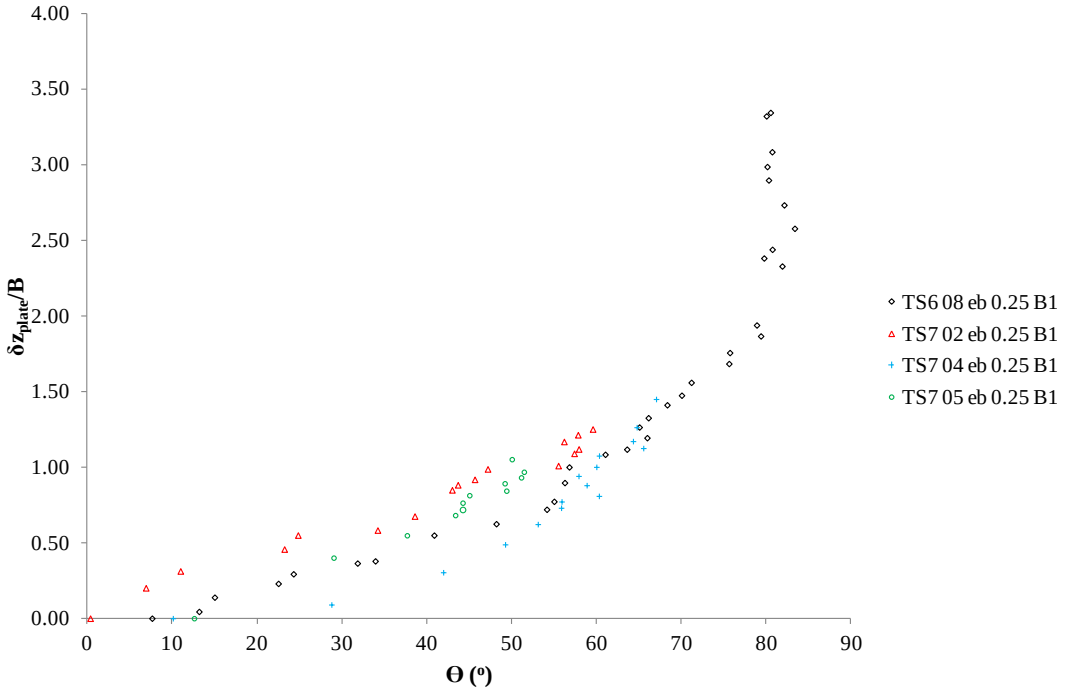


**Figure 4-23 Anchor Rotation (quantified from digital images) (e/B = 0.25)**

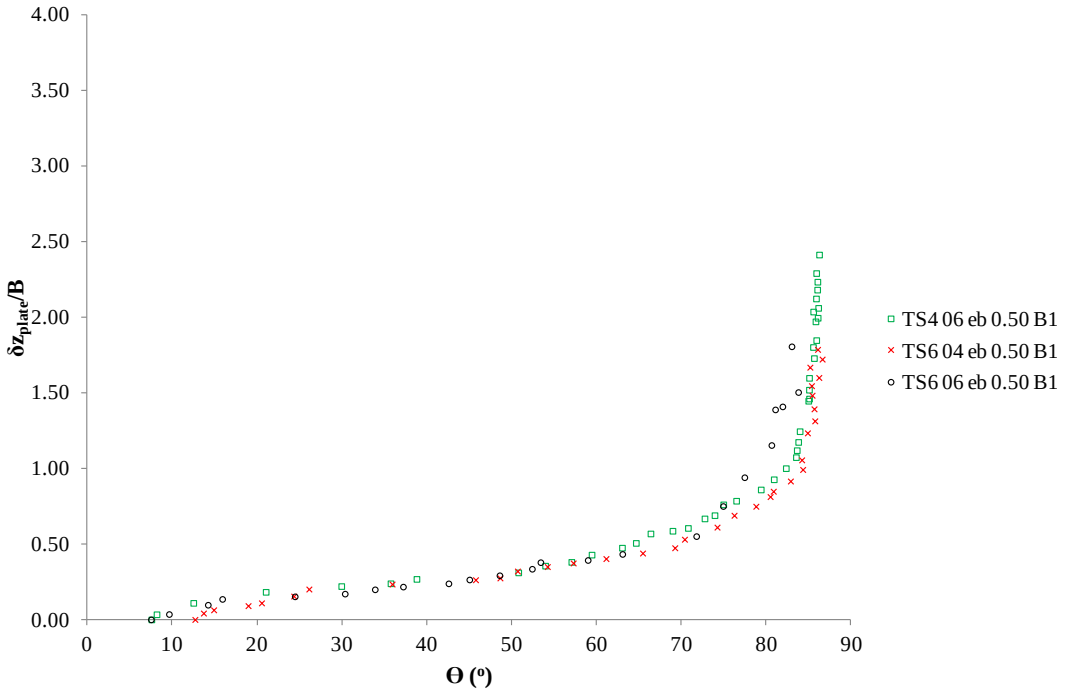


**Figure 4-24 Anchor Rotation (quantified from digital images) (e/B = 0.50)**

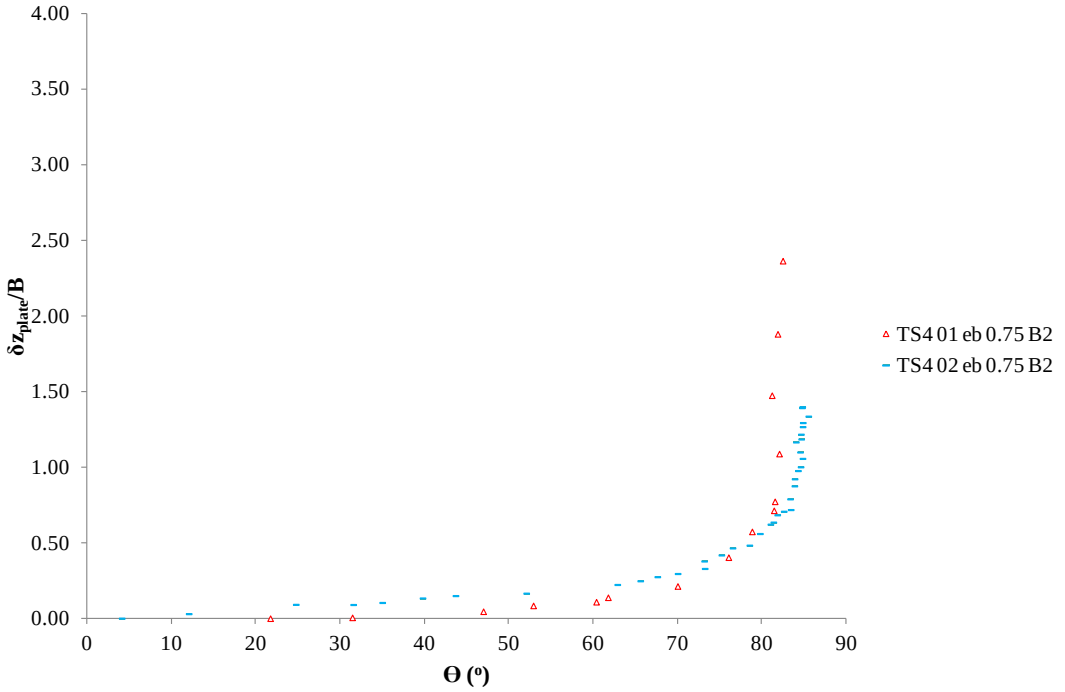


**Figure 4-25 Anchor Rotation (quantified from digital images) (e/B = 0.75)**

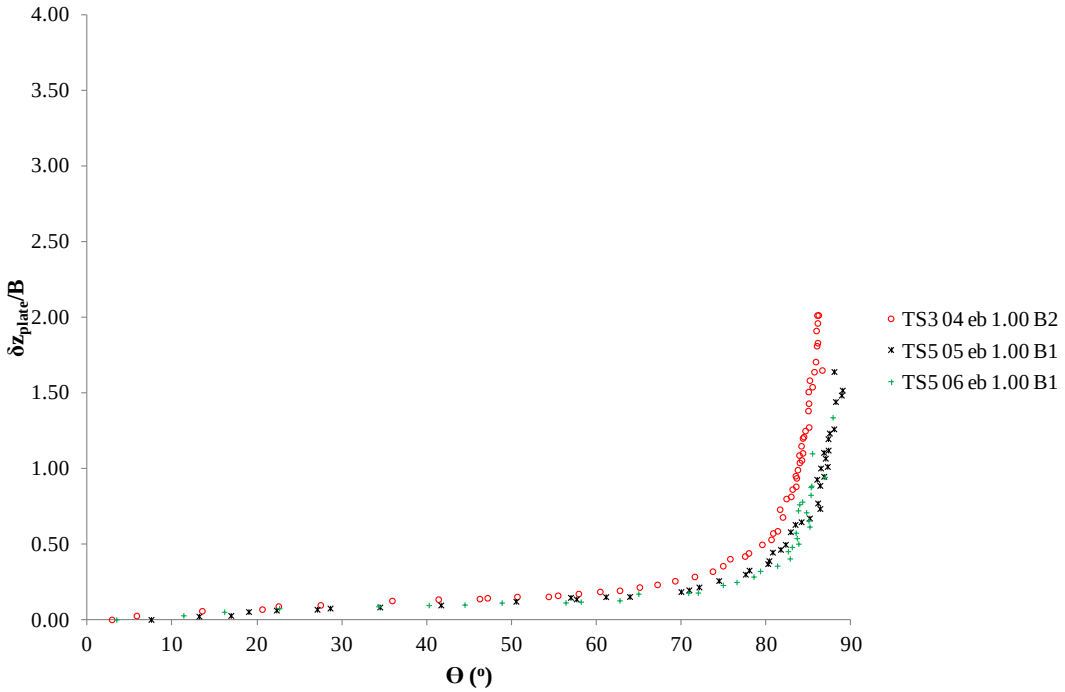


**Figure 4-26 Anchor Rotation (quantified from digital images) (e/B = 1)**

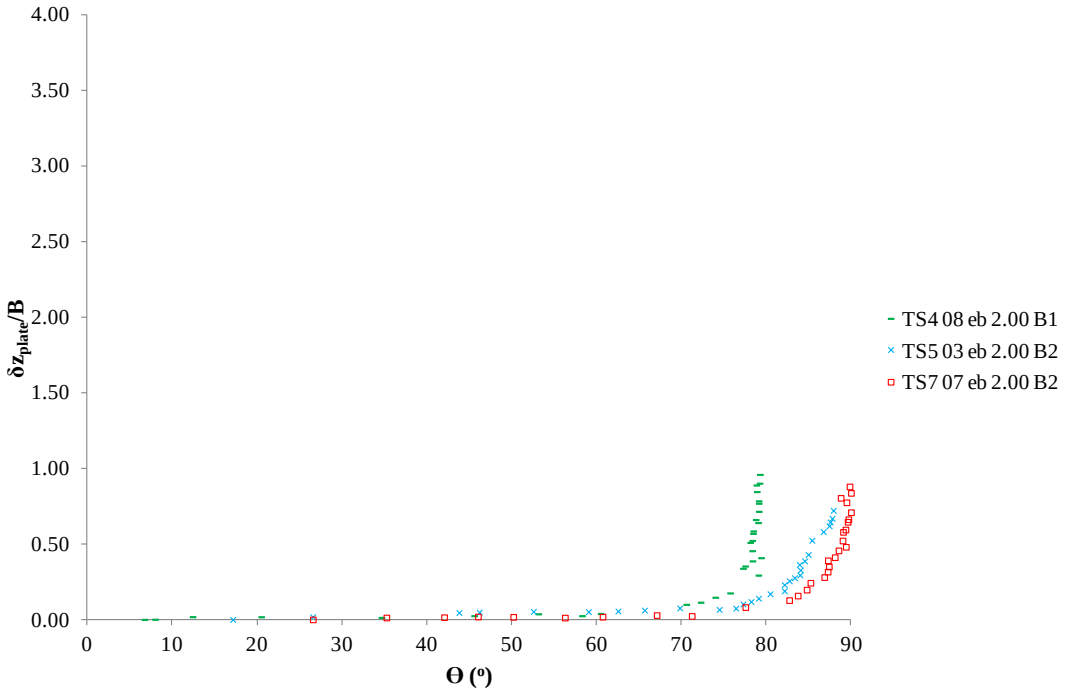


**Figure 4-27 Anchor Rotation (quantified from digital images) (e/B = 2)**

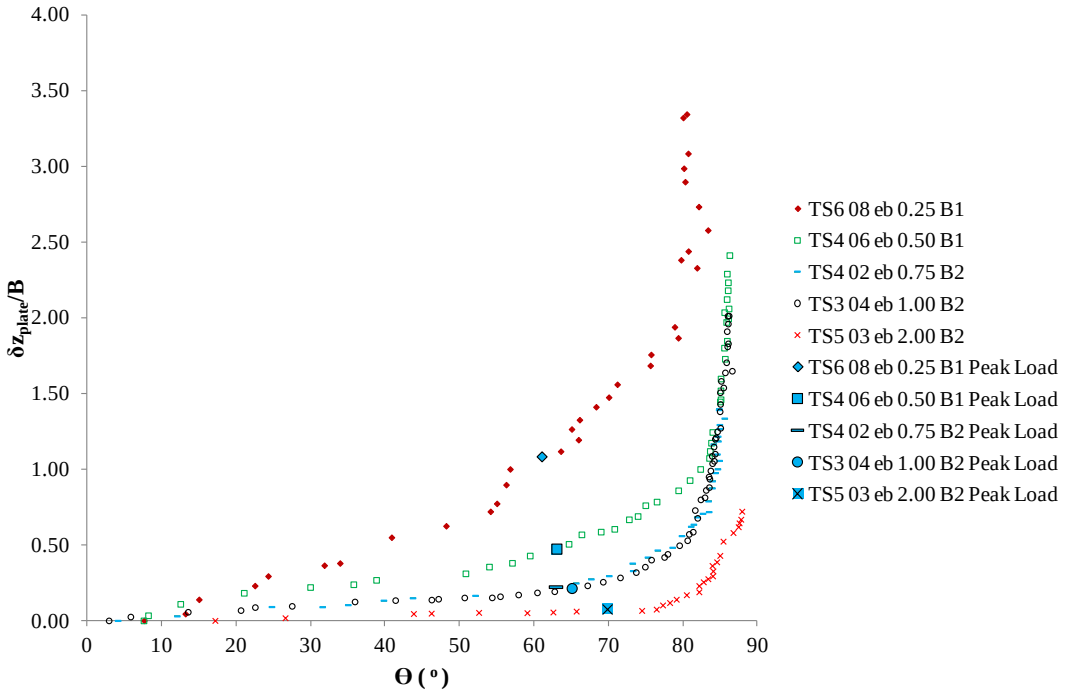


**Figure 4-28 Anchor Rotation (quantified from digital images) (Representative Tests)**

## 4.5 Chapter Summary

This chapter presents the measured data from the soil characterisation and anchor tests. The main findings in this chapter are:

- The CPT results show that the sample preparation method resulted in repeatable samples.
- In this programme of anchor tests frictional resistance developed along the anchor-Perspex interface does not appear to affect the load displacement response.
- The loss of embedment during anchor keying reduces with increasing eccentricity ratio.

# CHAPTER 5.0
# DISCUSSION

## 5.1 Introduction

A series of model strip anchor tests were designed and executed and the results have been analysed. The analysis has been categorised into two sections within this chapter. The first focuses on anchor behaviour during keying, considering the response in terms of the padeye eccentricity, whereas the second focuses on anchor capacity. This chapter concludes by applying the findings to a prototype scenario, sizing a plate anchor for typical floating renewable offshore energy applications.

## 5.2 Keying

In this section a representative anchor test for each eccentricity ratio was chosen to examine the influence of padeye eccentricity during keying. These anchor tests were as follows:

- e/B = 0.25: TS6 08 eb 0.25 B1
- e/B = 0.5: TS4 06 eb 0.50 B1
- e/B = 0.75: TS4 02 eb 0.75 B2
- e/B = 1: TS3 04 eb 1.00 B2
- e/B = 2: TS5 03 eb 2.00 B2

### 5.2.1 Load - Displacement Response

The load development with respect to the normalised line displacement, $\delta z_{line}/B$, and the loss of embedment of the plate, $\delta z/B$, was considered according to the following stages:

A. from zero load to the start of the load plateau
B. from the start of the load plateau to the start of the stiff load increase
C. from the start of the stiff load increase to the peak load
D. from the peak load to when the test ceased

Discussion

The load development response is plotted in Figure 5-1. A labelled insert is given to illustrate where each stage starts.

Stage A: The initial load – displacement response for each eccentricity ratio was found to consist of the load increasing rapidly from zero to the start of the load plateau with very little line displacement. The load at which the load plateau started, was found to decrease as the eccentricity ratio increases. This is summarised for each representative test in Table 5-1.

**Table 5-1 Start of Keying**

| | **Start of Load Plateau** | | | **At Peak Load** | |
|---|---|---|---|---|---|
| | **$F/F_{peak}$** | **F** | **$\delta z_{line}/B$** | **$F_{peak}$** | **$\delta z_{line}/B$** |
| | **(%)** | **(N)** | **(-)** | **(N)** | **(-)** |
| TS6 08 eb **0.25** B1 | 90 | 619 | 0.58 | 690 | 1.45 |
| TS4 06 eb **0.50** B1 | 75 | 667 | 0.55 | 894 | 1.18 |
| TS4 02 eb **0.75** B2 | 68 | 556 | 0.39 | 822 | 1.18 |
| TS3 04 eb **1.00** B2 | 53 | 458 | 0.42 | 862 | 1.36 |
| TS5 03 eb **2.00** B2 | 30 | 317 | 0.52 | 1066 | 2.03 |

Stage B: The line displacement between the start of the load plateau to the start of the stiff load increase, was found to increase with increasing eccentricity ratio. This was found to be true for eccentricity ratios e/B ranging from 0.5 to 2.

Stage C: The strip anchor with an eccentricity ratio, e/B = 0.25 was the only strip anchor not to exhibit the stiff load increase to the peak load (Figure 5-1) in this study. As the eccentricity ratio was increased the load response becomes stiffer.

Stage D: Once the peak load was exceeded, the load reduced with increasing line displacement, before exhibiting random load oscillations (Figure 5-1). This was found to be true for all eccentricity ratio groups and is discussed in more detail in Section 5.2.3.

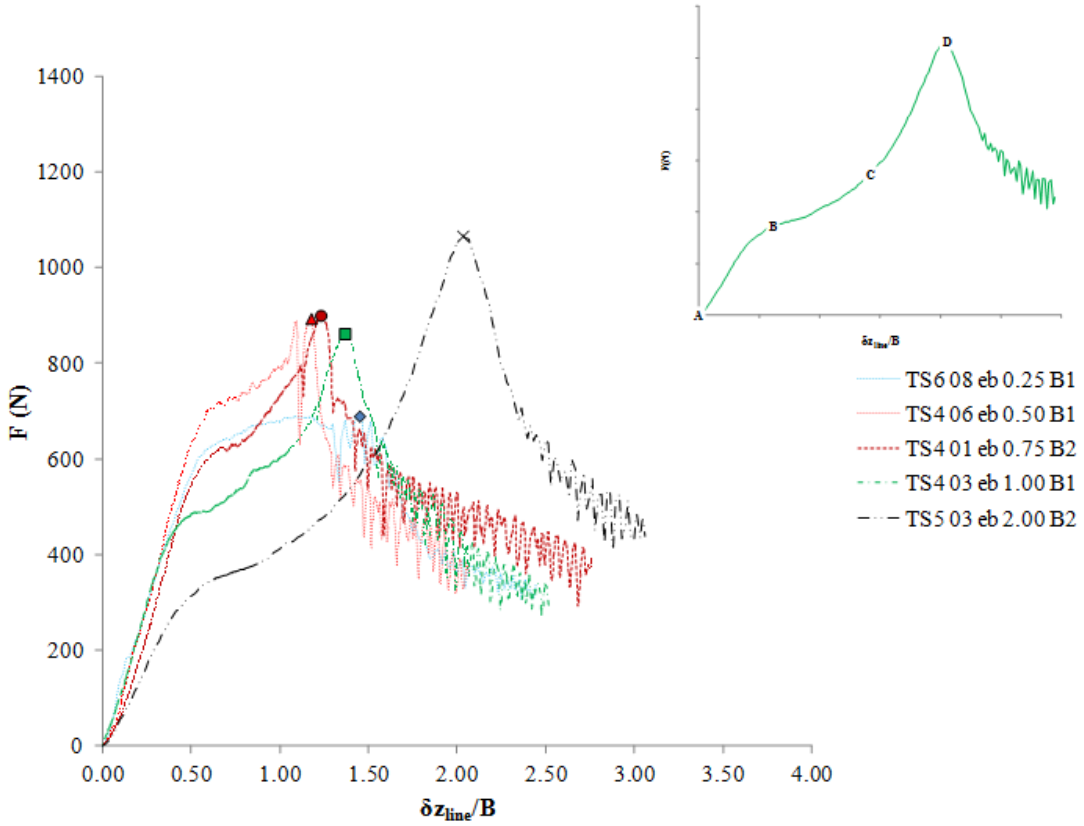


**Figure 5-1 Load – displacement Response during Keying and Pullout (vertical anchor line displacement) - Peak Load (Representative Tests)**

The loss of embedment the anchor underwent to reach the peak load decreased as the eccentricity ratio was increased (Figure 5-2). A summary of the normalised loss of embedment, $\delta z_{plate}/B$, required by each eccentricity ratio to reach the peak load, $F_{peak}$, is presented in Figure 5-3. The largest loss of embedment, $\delta z_{plate,}$ was for the strip anchor with an eccentricity ratio, e/B = 0.25 and the smallest loss of embedment, $\delta z_{plate,}$ was encountered by the strip anchor with an eccentricity ratio, e/B = 2. The loss of embedment, $\delta z_{plate,}$ required to reach the peak load ranged from 0.08B to 1.17B for a strip anchor with an eccentricity ratio, e/B, ranging from 0.25 to 2 respectively. This is shown by Figure 5-3, where it is evident that the loss of embedment reduced suddenly with an increased e/B, but that for e/B > l the loss in embedment was found to be tolerably constant. Hence the lowest eccentricity ratio that resulted in minimal loss of embedment was e/B = 1.

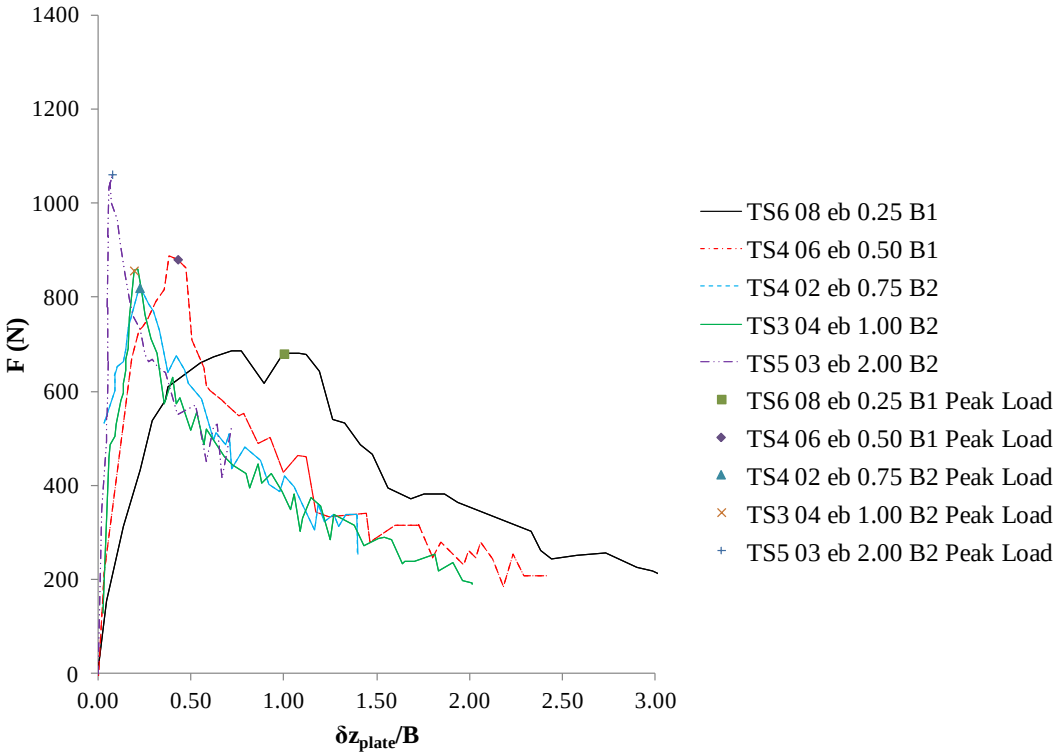


**Figure 5-2 Load – displacement Response during Keying and Pullout (anchor displacement) - Peak Load (Representative Tests)**

O'Loughlin *et al.* (2006), Song *et al.* (2006), Gaudin *et al.* (2009a) and Wang *et al.* (2011) have all reported on the loss of embedment of a plate anchor subjected to vertical loading in clay. O'Loughlin *et al.* (2006), Song *et al.* (2006) and Gaudin *et al.* (2009a) have all investigated the loss of embedment at the peak load for anchor tests conducted in the centrifuge. Wang *et al.* (2011) used finite element analyses to predict the loss of embedment for a plate anchor. These results are presented with the results of this study in Figure 5-3.

O'Loughlin *et al.* (2006) reported the loss of embedment, $\delta z_{plate,}$ at the end of keying for a plate anchor with an aspect ratio, L/B = 2 and a strip anchor with an aspect ratio, L/B of 5.30. The loss of embedment for a strip anchor with an aspect ratio, L/B of 5.3 was found to be almost equal to the loss of embedment reported in this study. This response concurs with the Murray & Geddes (1987) observation, that once the aspect ratio of a plate anchor exceeds five ($L/B \geq 5.00$) the plate anchor starts to behave as a strip anchor. Song *et al.* (2006) reported the loss of embedment

for a plate anchor with an aspect ratio, L/B = 1 where it was found that the loss of embedment is higher than that in this study.

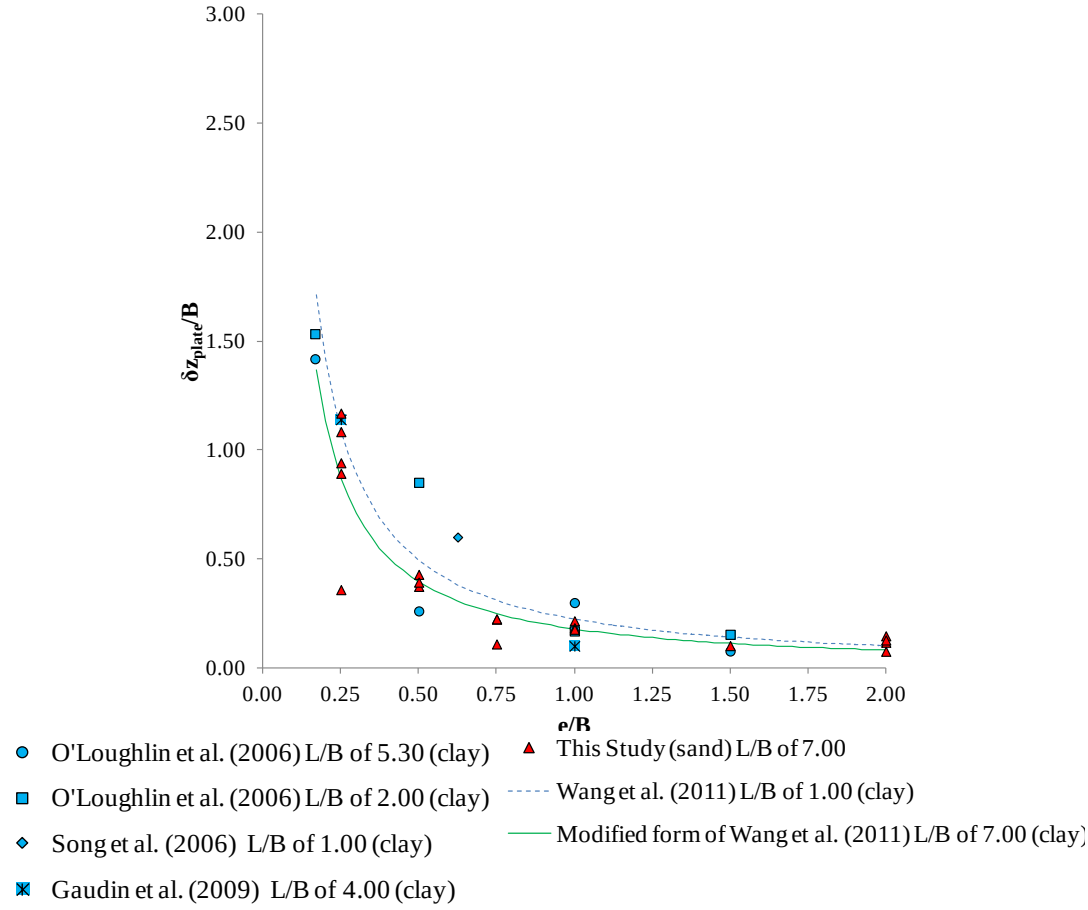


**Figure 5-3 Loss of Embedment at Peak Load**

Wang *et al.* (2011) expressed the loss of embedment of a square plate anchor as:

$$\frac{dz_{max}}{B} \approx a\left\{\left(\frac{e}{B}\right)\left(\frac{t}{B}\right)^{p}\right\}^{q} \qquad \textbf{Equation 5-1}$$

where the three coefficients a = 0.144, p = 0.20, and q = -1.15.

The expression developed by Wang *et al.* (2011) to predict the loss of embedment has been adapted to match the results of this study. The expression was adapted by reducing the coefficient a = 0.144 to a = 0.115, this achieved by using algebra.

Discussion

Example:

TS5 03 eb 2.00 B2:

$$\frac{dz_{max}}{B} \approx a\left\{\left(\frac{e}{B}\right)\left(\frac{t}{B}\right)^{p}\right\}^{q}$$

$$0.08 \approx a\{(2.00)(0.15)^{0.20}\}^{-1.15}$$

$$a = 0.1147$$

Changing the coefficient 'a' in this expression represents a strip anchor with an aspect ratio, L/B = 7 and the embedment depth H ≈ 5.00.

### 5.2.2 Repeatability

In this section the repeatability of the tests was examined by comparing the load-displacement response and the anchor trajectories for an anchor with an eccentricity ratio e/B = 1. The F vs. $\delta z_{line}/B$ for each anchor test is presented in Figure 5-5. The anchor orientation response for the three considered anchor tests are plotted in Figure 5-6 and the padeye trajectories have been overlain on Figure 5-7 to facilitate comparison. As the load develops the inclination of the plate to the vertical was found to be approximately the same for each stage of the anchor test regardless of the load on the anchor. The load – displacement response was found to be qualitatively similar, although the magnitudes of the peak load differ. The repeatability and agreement in the load displacement response is more evident from Figure 5-5, in which the load, F, has been normalised by the peak load, $F_{peak}$, for each anchor test considered. Figure 5-7 shows that the behaviour of the plate anchor from its initial orientation to the orientation at the peak load was almost identical for each anchor test.

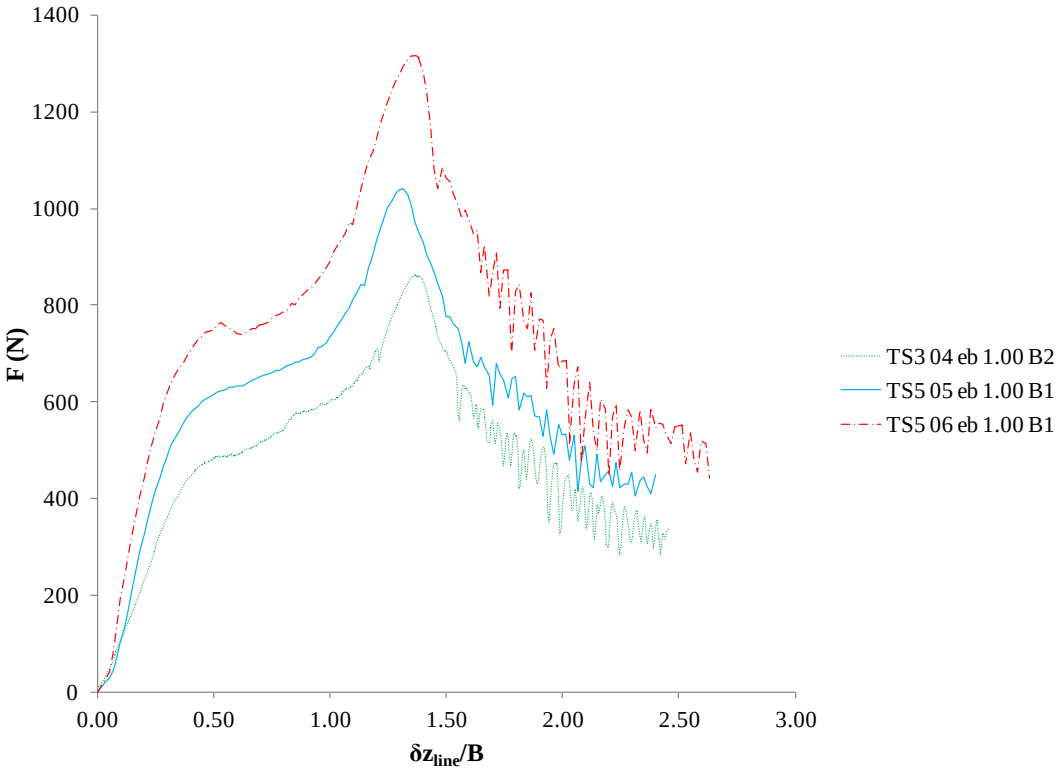


**Figure 5-4 Load – displacement Response during Keying and Pullout (vertical anchor line displacement) – Comparison of Anchor Behaviour (e/B = 1)**

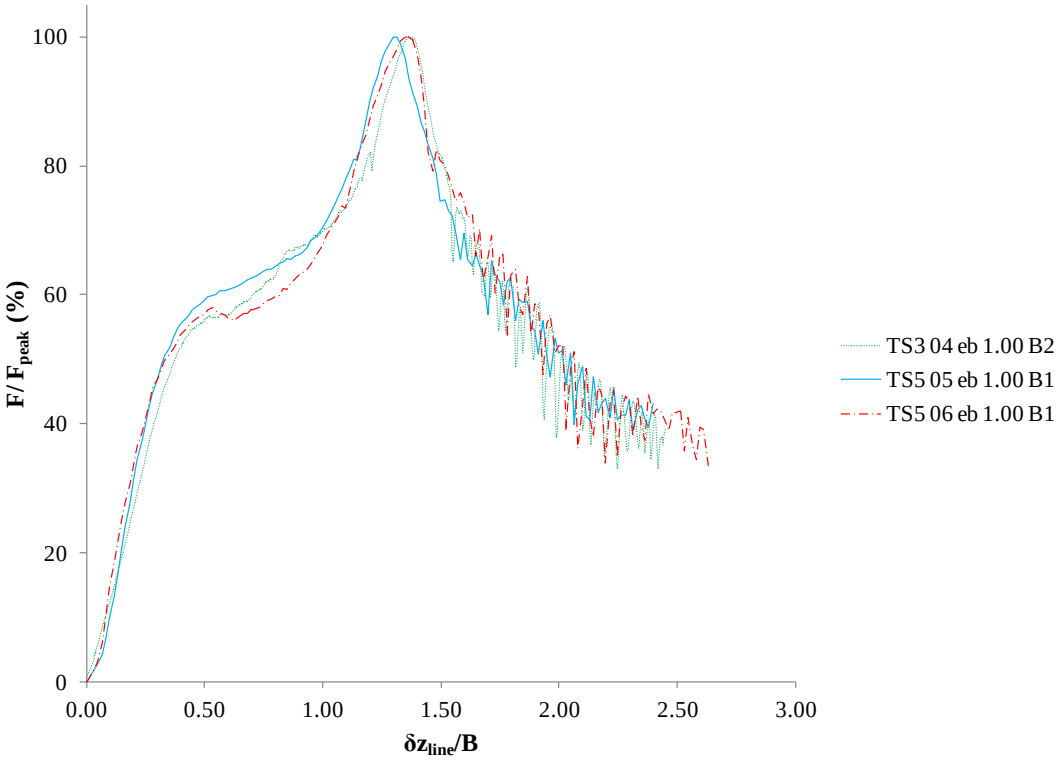


**Figure 5-5 Load – displacement Response during Keying and Pullout (vertical anchor line displacement) – Comparison of Anchor Behaviour (e/B = 1)**

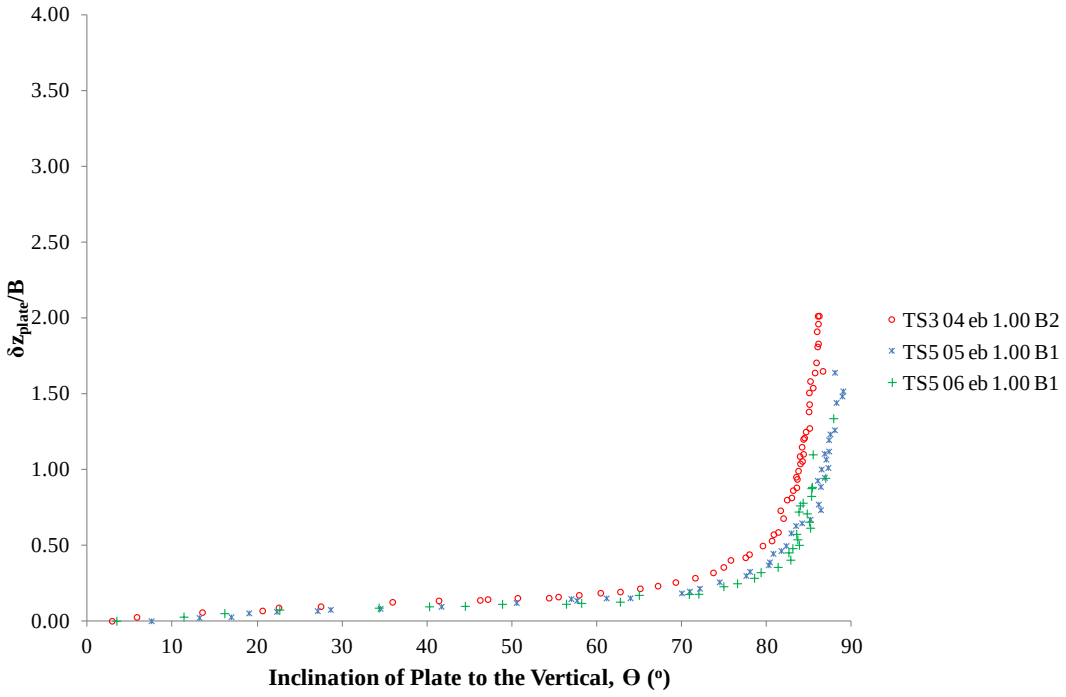


**Figure 5-6 Anchor Rotation – Comparison of Anchor Behaviour (e/B = 1)**

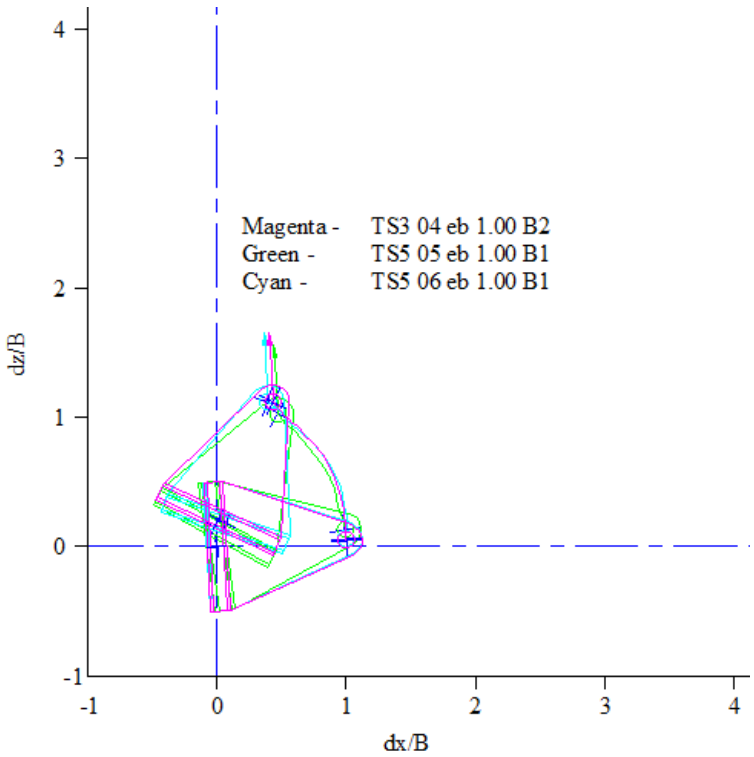


**Figure 5-7 Trajectory of Anchor Padeye – Comparison of Anchor Behaviour (e/B = 1)**

### 5.2.3 Correlation of the Anchor Position to Load

Correlating the anchor orientation to the load $\delta z_{line}/B$ plot has helped in the understanding of the keying response of each eccentricity ratio, e/B, for plate anchors in sand. The result of varying e/B on anchor tests is shown by eight images chosen from the representative anchor tests for each eccentricity ratio with reference to selected stages along the F vs. $\delta z_{line}/B$ plot (Figure 5-8, Figure 5-11, Figure 5-14, Figure 5-17 and Figure 5-20 for e/B = 0.25, 0.5, 0.75, 1 and 2, respectively). Labels A-H on the F vs. $\delta z_{line}/B$ plots (Figure 5-9, Figure 5-12, Figure 5-15, Figure 5-18 and Figure 5-21 for e/B = 0.25, 0.5, 0.75, 1 and 2, respectively) and $\delta z_{plate}$ vs. $\Theta$ plots (Figure 5-10, Figure 5-13, Figure 5-16, Figure 5-19 and Figure 5-22 for e/B = 0.25, 0.5, 0.75, 1 and 2, respectively) represent the following:

- A: the initial orientation of the anchor
- B: the point at which the load plateaus
- C, D and E: selected points between the load plateau and the peak load
- F: the peak load
- G: the start of 'load oscillation'
- H: the final angle

An outline of the anchor has been overlain on each image to clearly show the initial position and orientation of the anchor compared with that for each of the considered stages B-H. The padeye trajectory, load direction at the anchor padeye and original sample surface profile are also shown. Under each set of images a synopsis of the load, loss of embedment, plate inclination, $\Theta$ (measured to the vertical), current embedment depth, $H_{current}/B$, are provided both in absolute and relative terms.

The anchor with an eccentricity ratio, e/B = 0.25 experienced excessive loss of embedment, $\delta z_{plate}$ (Figure 5-8) before the peak load was reached. This suggests that these strip anchors do not experience deep localised failure during any stage of the anchor test.

Examination of Figure 5-8, Figure 5-11, Figure 5-14, Figure 5-17 and Figure 5-20 has revealed that for all eccentricity ratios, the peak load (point F) corresponds with movement of the soil surface. This suggests that at least less than the peak load the

failure mechanism is deep and that at the peak load the failure mechanism transitions to a shallow failure mechanism. This is investigated in more detail in Section 5.2.5.

Before this analysis was carried out it was believed that the peak load, point F, would have coincided with the final angle of rotation where the final angle of rotation would be normal to the loading inclination as reported by, Gaudin *et al.* (2006), O'Loughlin *et al.* (2006) and Gaudin *et al.* (2009a). In the tests considered, the peak load corresponded with a plate inclination, $\Theta$ = 50° to 83°, increasing as the eccentricity ratio increased.

Comparing Figure 5-8, Figure 5-11, Figure 5-14, Figure 5-17 and Figure 5-20 has clearly illustrated that as the eccentricity ratio increased the loss of embedment decreased and the rate of rotation increased. This finding is summarised for each eccentricity ratio in Figure 5-9, Figure 5-12, Figure 5-15, Figure 5-18 and Figure 5-21.

Point G denotes the start of load oscillation in each test. This is evident in the F vs. $\delta z_{line}$ as random load spikes beyond the peak load. Load oscillation started at 82% (±1%) of the final angle for a plate anchor with an eccentricity ratio, e/B = 0.25 and 0.50. This increased to 89% for a plate anchor with an eccentricity e/B = 0.75 and 1 and increased to 95% for a plate anchor with an eccentricity ratio, e/B = 2. Similar load oscillations were reported by Ilamparuthi *et al.* (2002), Dickin (1988), Murray & Geddes (1987) and Rowe & Davis (1982) for strip anchors and Chin *et al.* (2006), Trautmann *et al.* (1985) and Cheuk *et al.* (2008) for pipelines in sand. Cheuk *et al.* (2008) explained the phenomenon as 'miniature slope failures' as sand falls around the periphery of the pipe (or the plate in this case) into the cavity below.

The final inclination of the plate to the vertical, point H, for each eccentricity ratio, e/B = 0.25, 0.5, 0.75, 1 and 2 were found to be $\Theta$ = 80°, 84°, 83°, 81° and 87° respectively. This may have been due to the stress gradient across the plate, resulting in higher normal stresses at the lower half of the plate compared with the upper half, making it difficult for the plate to become truly normal to the loading direction. Similar findings were reported for plate anchors in clay by O'Loughlin *et al.* (2006) and Gaudin *et al.* (2006).

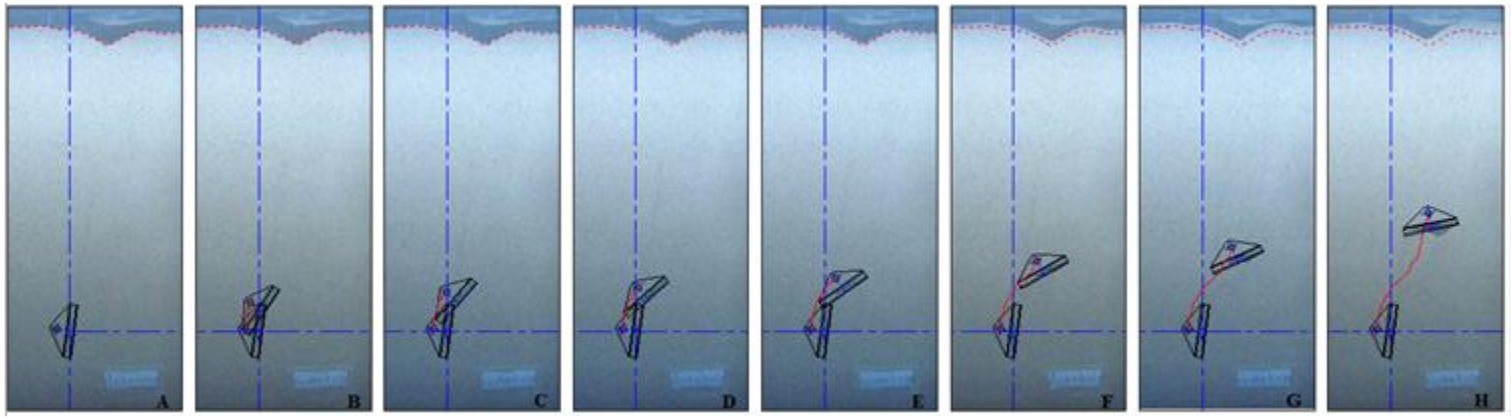


| | A | B | C | D | E | F | G | H |
|---|---|---|---|---|---|---|---|---|
| **F (N)** | 0 | 609 | 660 | 673 | 687 | 682 | 533 | 363 |
| **$\delta z_{line}/B$** | 0.00 | 0.57 | 0.82 | 0.92 | 1.17 | 1.47 | 1.67 | 2.16 |
| **$\Theta$ (°)** | 8 | 34 | 41 | 48 | 55 | 61 | 66 | 79 |
| **$\delta z_{plate}/B$** | 0.00 | 0.38 | 0.55 | 0.63 | 0.77 | 1.08 | 1.33 | 1.94 |
| **$H_{current}/B$** | 5.04 | 4.66 | 4.49 | 4.41 | 4.27 | 3.96 | 3.71 | 3.10 |
| **$F/F_{peak}$ (%)** | 0 | 88 | 96 | 98 | 100 | 99 | 77 | 53 |
| **$\delta z_{line}/ \delta z_{line\ -\ peak\ load}$ (%)** | 0 | 39 | 56 | 63 | 80 | 100 | 115 | 149 |
| **$\delta z_{anchor}/\delta z_{anchor\ -\ peak\ load}$ (%)** | 0 | 35 | 51 | 58 | 71 | 100 | 123 | 180 |
| **$\Theta/\Theta_{final}$ (%)** | 10 | 42 | 51 | 60 | 69 | 76 | 83 | 100 |

**Figure 5-8 Summary of Captured Anchor Orientation (e/B = 0.25)**

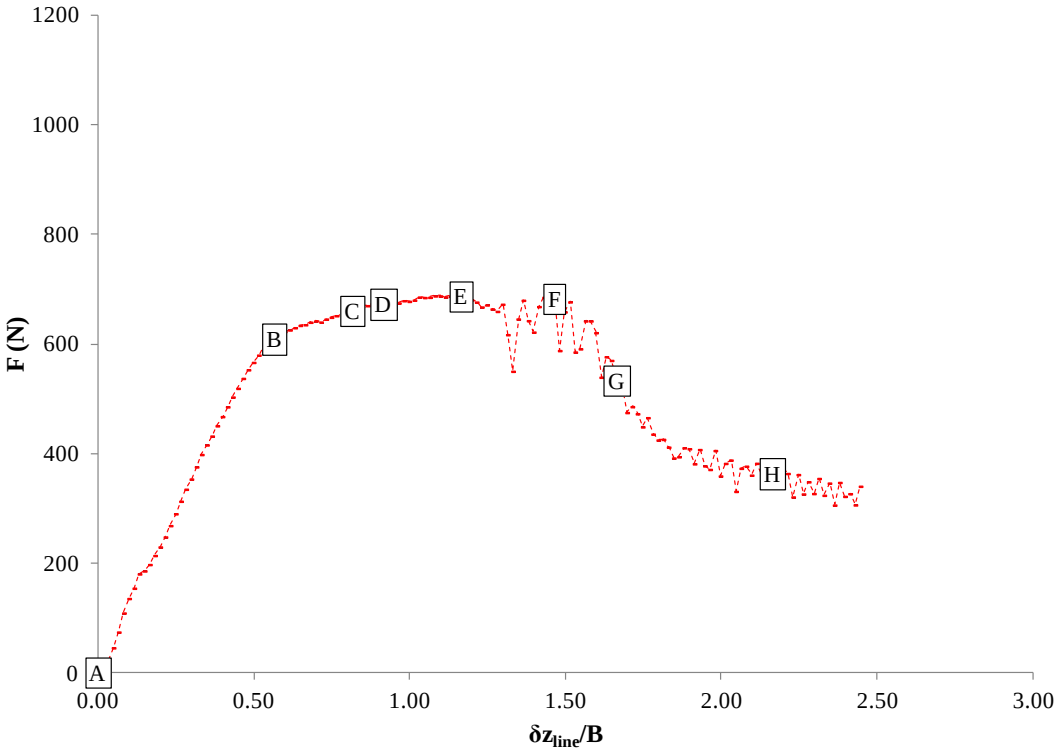


**Figure 5-9 Load – displacement Response during Keying and Pullout (vertical anchor line displacement) (e/B = 0.25)**

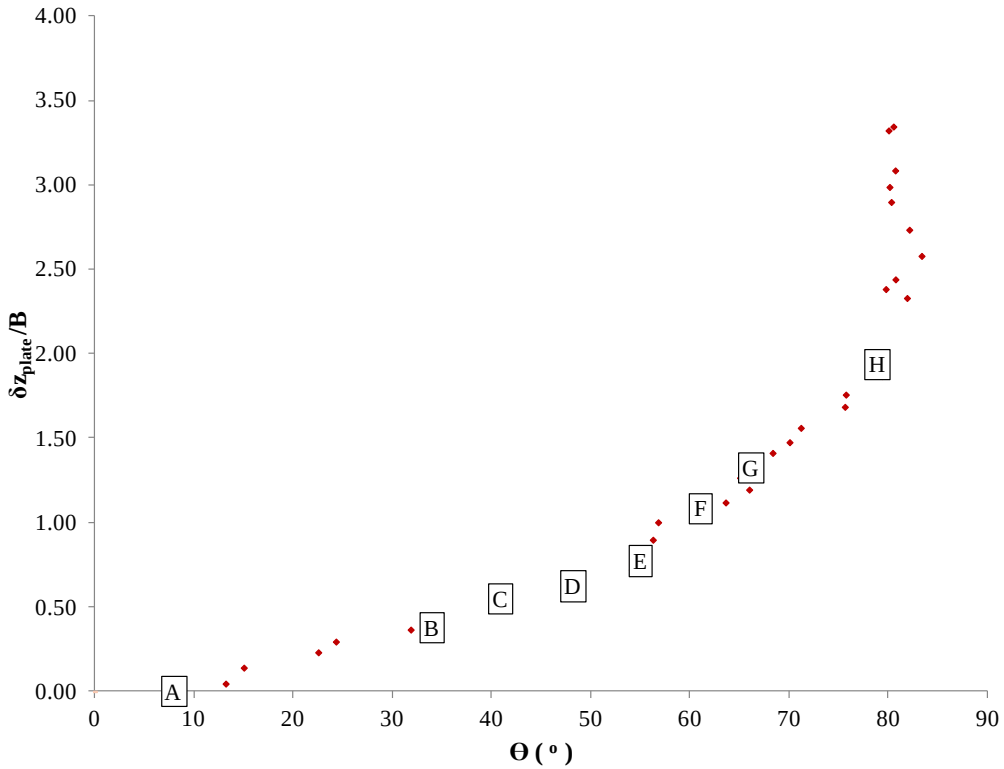


**Figure 5-10 Anchor Rotation (e/B = 0.25)**

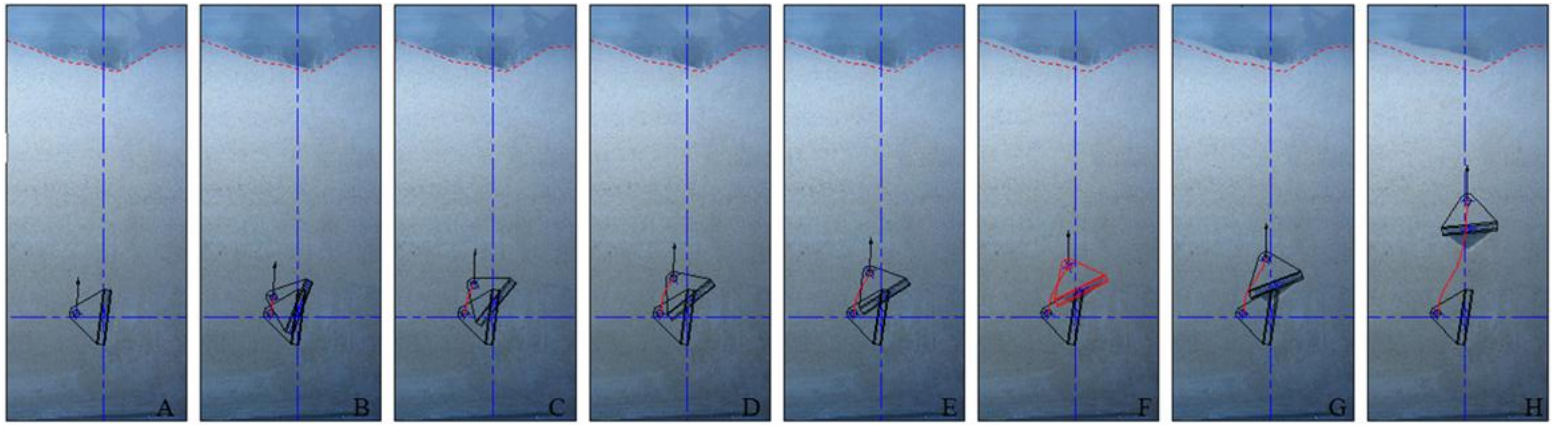


| | A | B | C | D | E | F | G | H |
|---|---|---|---|---|---|---|---|---|
| **F (N)** | 0 | 671 | 753 | 791 | 888 | 862 | 612 | 316 |
| **$\delta z_{line}/B$** | 0.00 | 0.56 | 0.86 | 0.99 | 1.09 | 1.19 | 1.29 | 2.23 |
| **$\Theta$ (°)** | 8 | 21 | 39 | 51 | 57 | 63 | 69 | 85 |
| **$\delta z_{plate}/B$** | 0.00 | 0.18 | 0.27 | 0.31 | 0.38 | 0.48 | 0.59 | 1.60 |
| **$H_{current}/B$** | 4.91 | 4.73 | 4.64 | 4.60 | 4.53 | 4.43 | 4.32 | 3.31 |
| **$F/F_{peak}$ (%)** | 0 | 78 | 87 | 92 | 103 | 100 | 71 | 37 |
| **$\delta z_{line}/ \delta z_{line\ -\ peak\ load}$ (%)** | 0 | 47 | 72 | 83 | 92 | 100 | 108 | 187 |
| **$\delta z_{anchor}/\delta z_{anchor\ -\ peak\ load}$ (%)** | 0 | 38 | 56 | 66 | 80 | 100 | 124 | 337 |
| **$\Theta/\Theta_{final}$ (%)** | 9 | 25 | 46 | 60 | 67 | 74 | 81 | 100 |

**Figure 5-11 Summary of Captured Anchor Orientation (e/B = 0.50)**

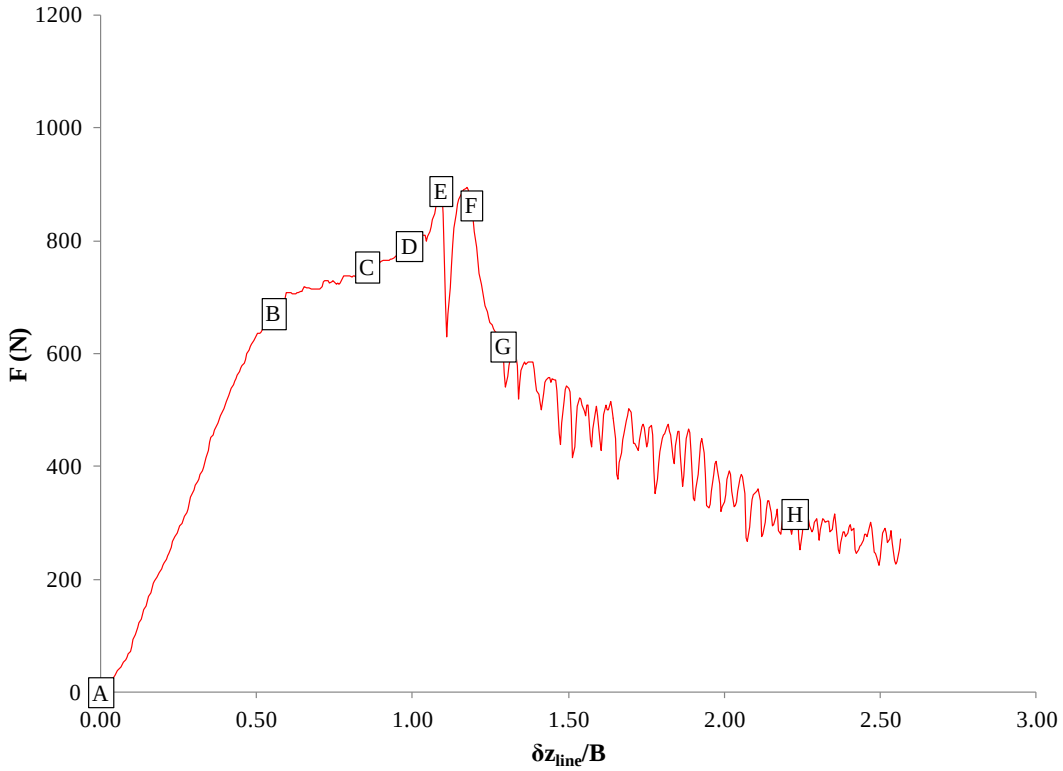


**Figure 5-12 Load – displacement Response during Keying and Pullout (vertical anchor line displacement) (e/B = 0.50)**

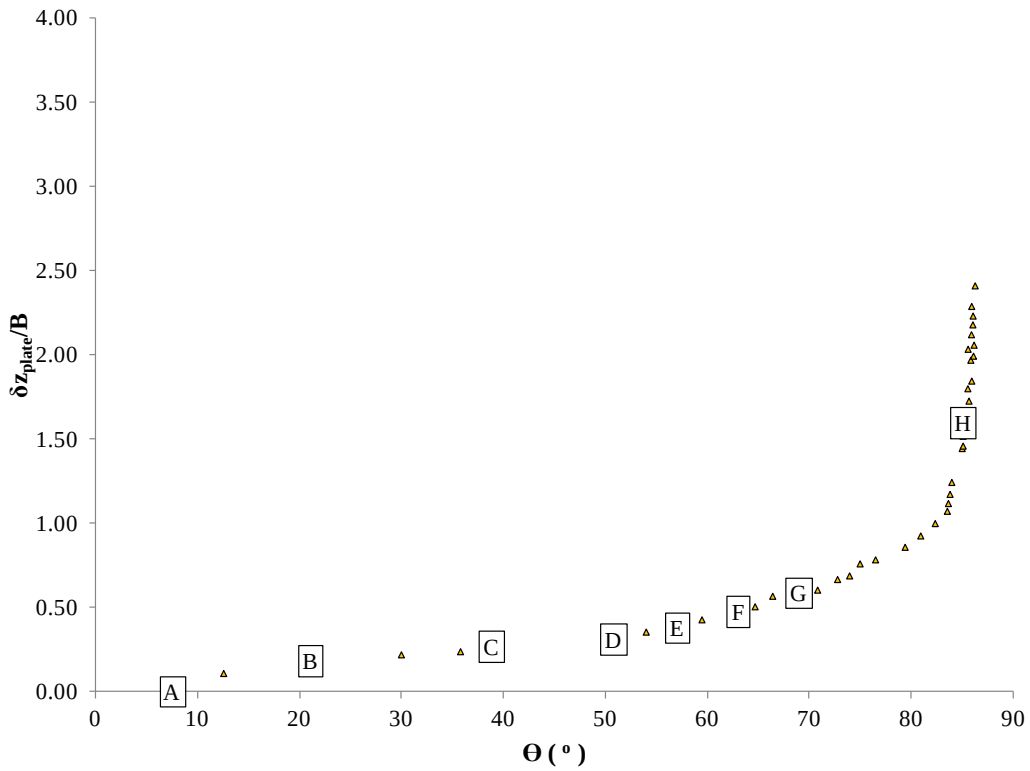


**Figure 5-13 Anchor Rotation (e/B = 0.50)**

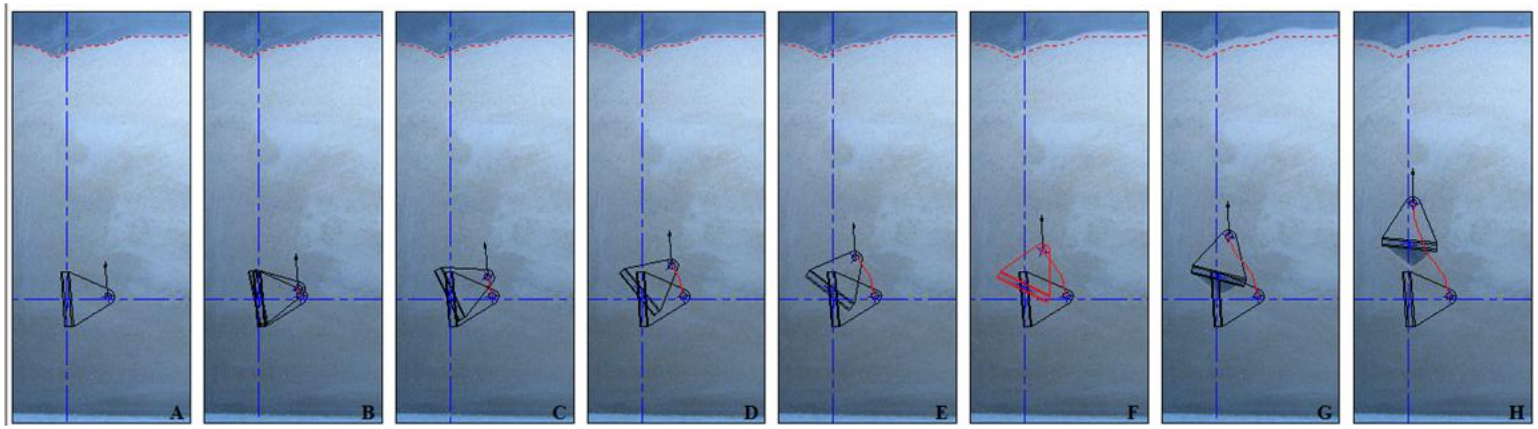


| | A | B | C | D | E | F | G | H |
|---|---|---|---|---|---|---|---|---|
| **F (N)** | 0 | 534 | 603 | 664 | 735 | 820 | 677 | 421 |
| **$\delta z_{line}/B$** | 0.00 | 0.36 | 0.58 | 0.86 | 1.05 | 1.18 | 1.38 | 1.92 |
| **$\Theta$ (°)** | 4 | 12 | 25 | 40 | 52 | 63 | 75 | 85 |
| **$\delta z_{plate}/B$** | 0.00 | 0.03 | 0.09 | 0.13 | 0.17 | 0.22 | 0.42 | 1.00 |
| **$H_{current}/B$** | 4.51 | 4.48 | 4.42 | 4.38 | 4.34 | 4.29 | 4.09 | 3.51 |
| **$F/F_{peak}$ (%)** | 0 | 65 | 73 | 81 | 90 | 100 | 83 | 51 |
| **$\delta z_{line}/ \delta z_{line\ -\ peak\ load}$ (%)** | 0 | 31 | 49 | 73 | 89 | 100 | 117 | 163 |
| **$\delta z_{anchor}/\delta z_{anchor\ -\ peak\ load}$ (%)** | 0 | 14 | 51 | 59 | 77 | 100 | 191 | 455 |
| **$\Theta/\Theta_{final}$ (%)** | 5 | 14 | 29 | 47 | 62 | 74 | 89 | 100 |

**Figure 5-14 Summary of Captured Anchor Orientation (e/B = 0.75)**

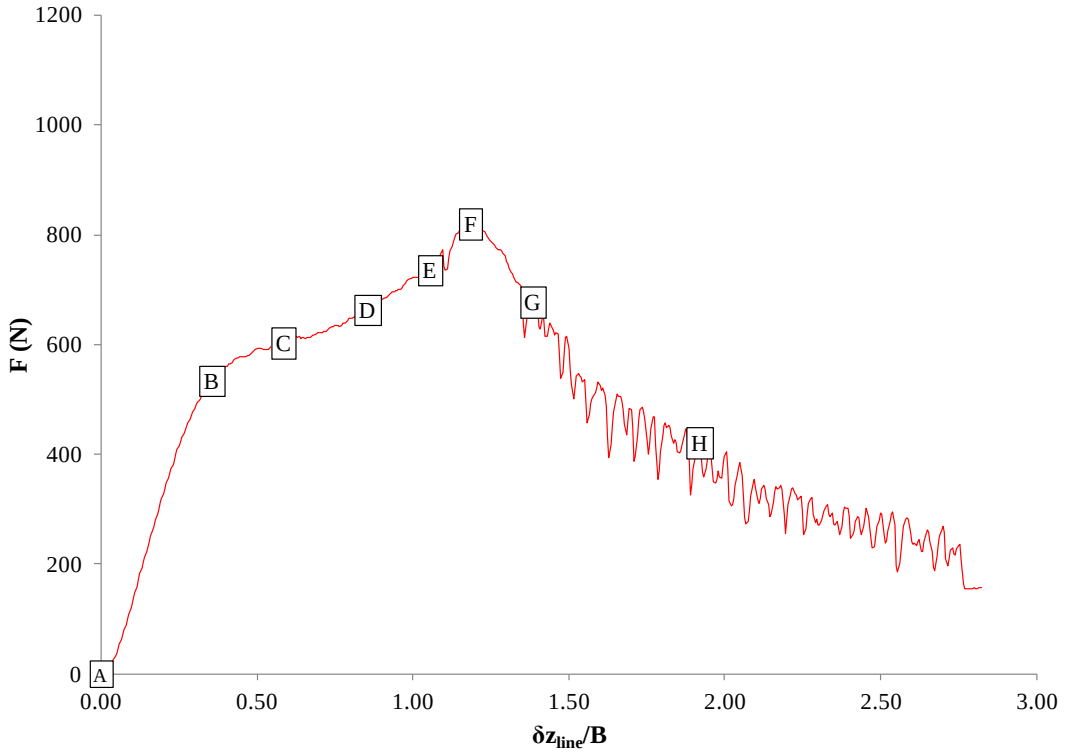


**Figure 5-15 Load – displacement Response during Keying and Pullout (vertical anchor line displacement) (e/B = 0.75)**

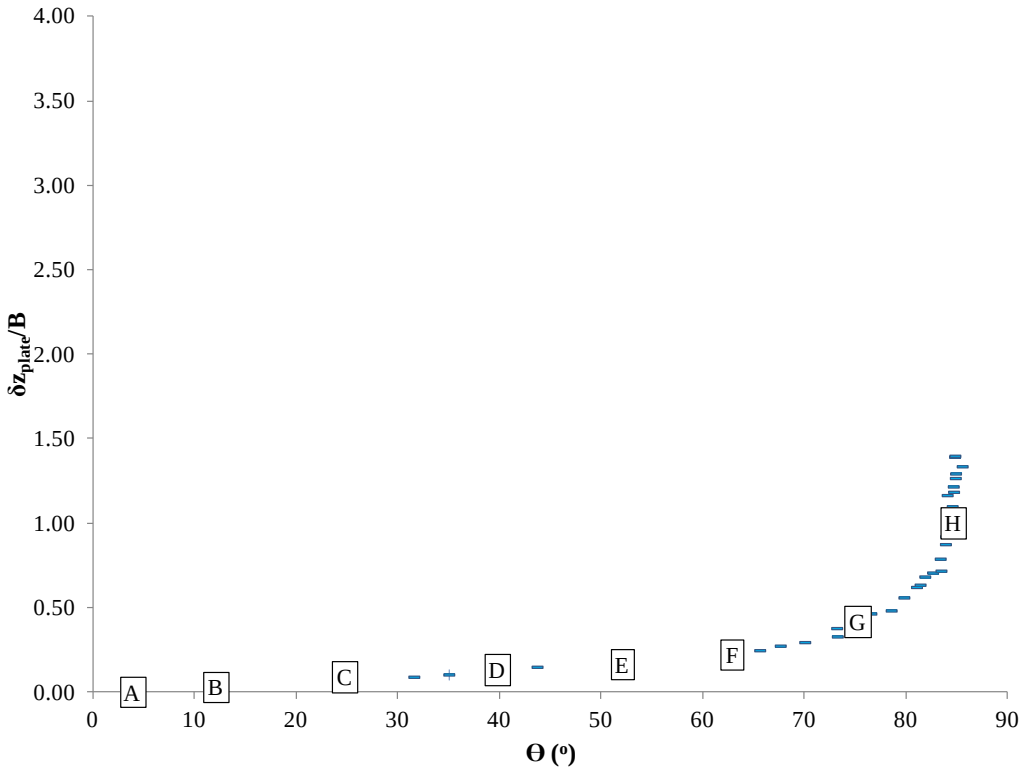


**Figure 5-16 Anchor Rotation (e/B = 0.75)**

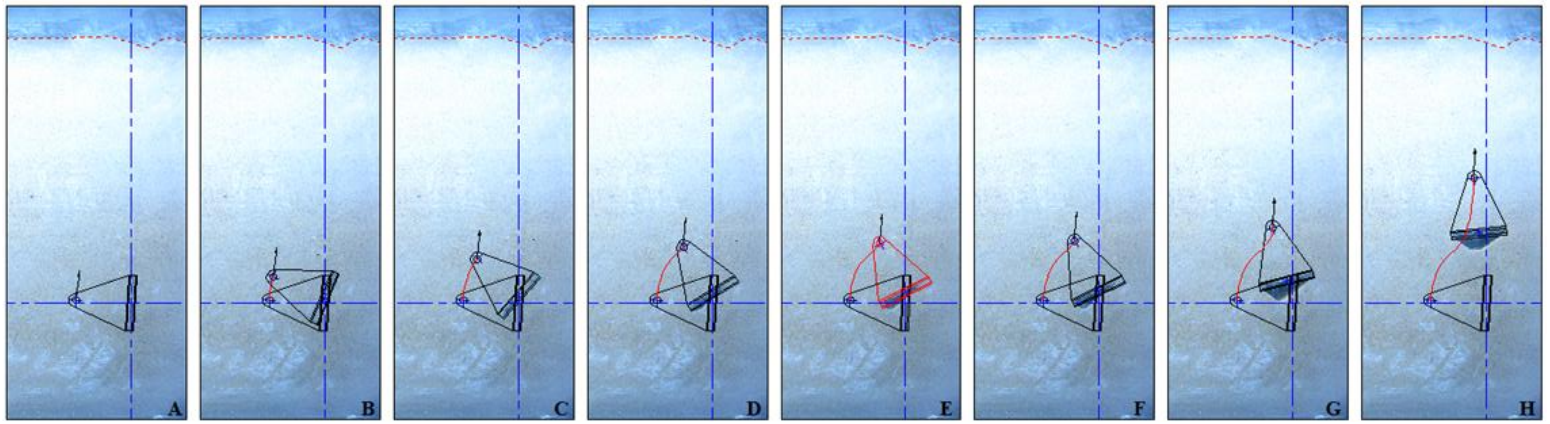


| | A | B | C | D | E | F | G | H |
|---|---|---|---|---|---|---|---|---|
| **F (N)** | 0 | 504 | 596 | 757 | 857 | 860 | 629 | 337 |
| **$\delta z_{line}/B$** | 0.00 | 0.65 | 0.98 | 1.25 | 1.35 | 1.38 | 1.58 | 2.45 |
| **$\Theta$ (°)** | 3 | 23 | 41 | 58 | 63 | 65 | 76 | 85 |
| **$\delta z_{plate}/B$** | 0.00 | 0.09 | 0.13 | 0.17 | 0.19 | 0.21 | 0.40 | 1.27 |
| **$H_{current}/B$** | 4.60 | 4.51 | 4.47 | 4.43 | 4.41 | 4.39 | 4.20 | 3.33 |
| **$F/F_{peak}$ (%)** | 0 | 59 | 69 | 88 | 100 | 100 | 73 | 39 |
| **$\delta z_{line}/ \delta z_{line\ -\ peak\ load}$ (%)** | 0 | 35 | 64 | 89 | 96 | 100 | 116 | 131 |
| **$\delta z_{anchor}/\delta z_{anchor\ -\ peak\ load}$ (%)** | 0 | 47 | 71 | 91 | 98 | 100 | 114 | 178 |
| **$\Theta/\Theta_{final}$ (%)** | 3 | 26 | 49 | 68 | 74 | 77 | 89 | 100 |

**Figure 5-17 Summary of Captured Anchor Orientation (e/B = 1)**

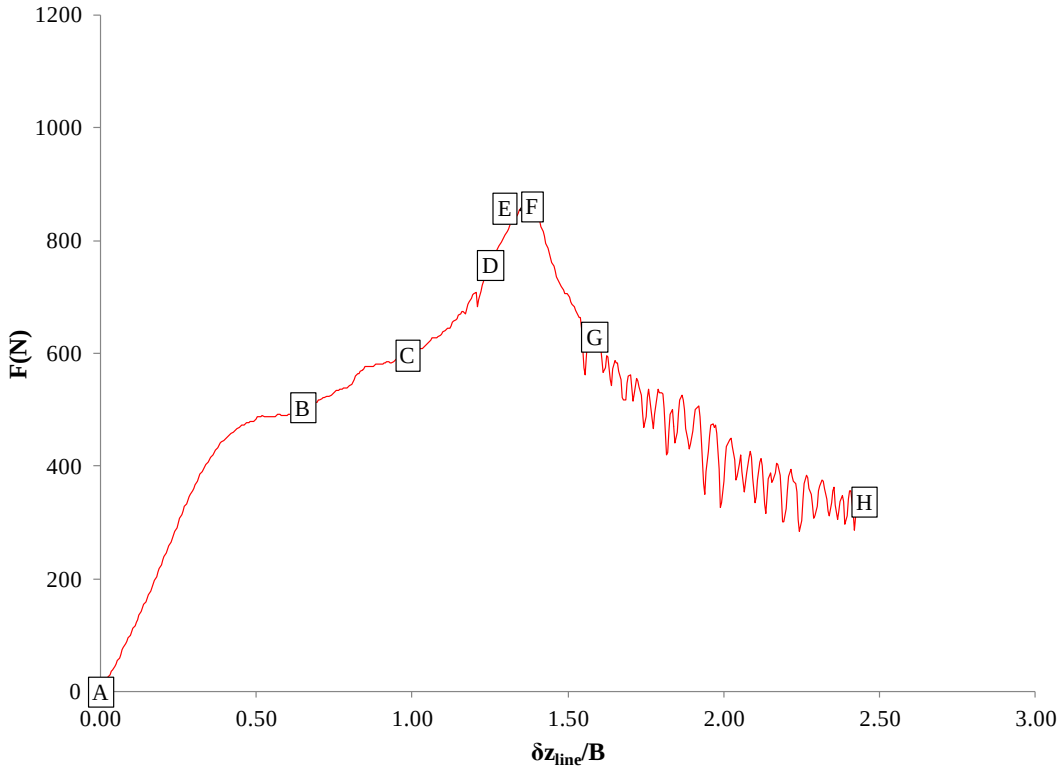


**Figure 5-18 Load – displacement Response during Keying and Pullout (vertical anchor line displacement) (e/B = 1)**

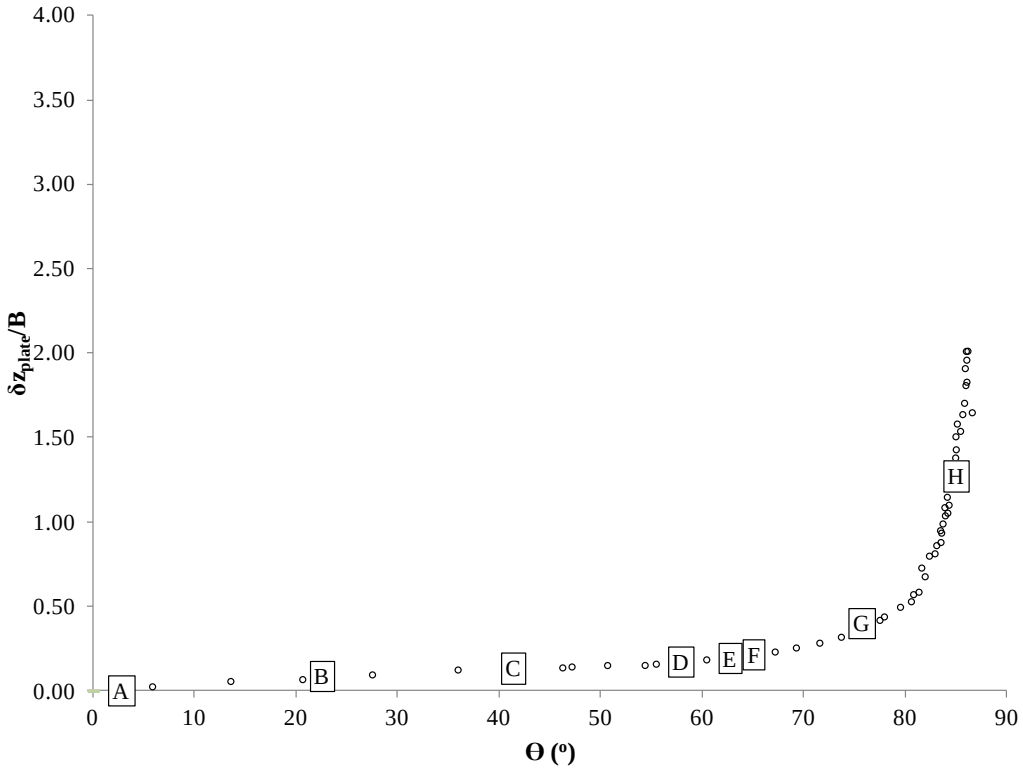


**Figure 5-19 Anchor Rotation (e/B = 1)**

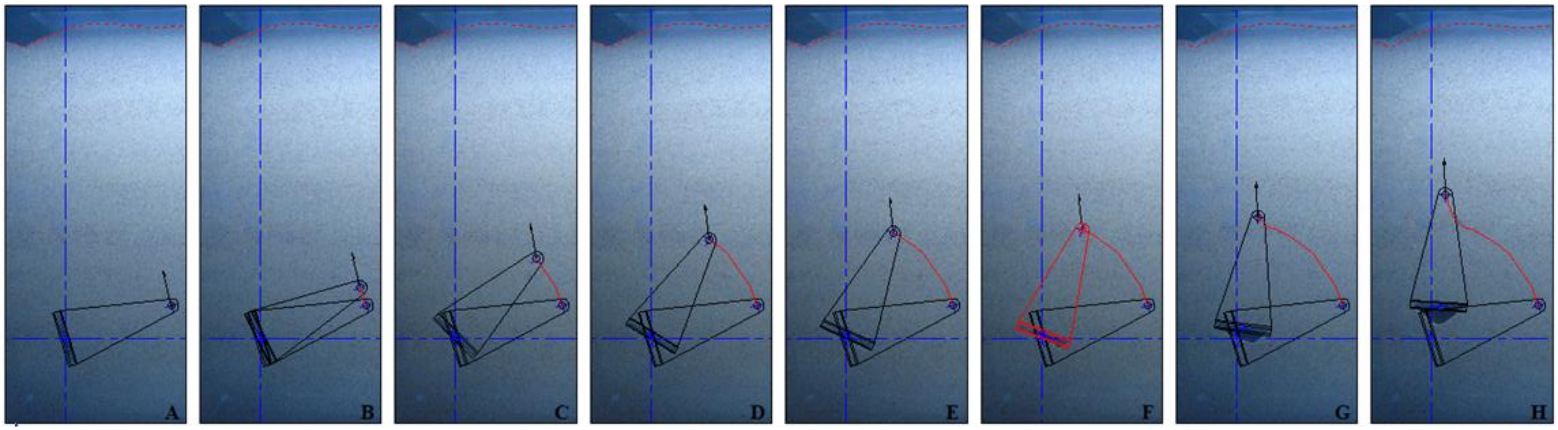


| | A | B | C | D | E | F | G | H |
|---|---|---|---|---|---|---|---|---|
| **F (N)** | 0 | 348 | 494 | 779 | 1033 | 1062 | 761 | 450 |
| **$\delta z_{line}/B$** | 0.00 | 0.62 | 1.30 | 1.75 | 1.98 | 2.05 | 2.28 | 2.78 |
| **$\Theta$ (°)** | 17 | 27 | 44 | 59 | 66 | 70 | 82 | 87 |
| **$\delta z_{plate}/B$** | 0.000 | 0.018 | 0.046 | 0.051 | 0.062 | 0.076 | 0.189 | 0.581 |
| **$H_{current}/B$** | 5.54 | 5.52 | 5.49 | 5.49 | 5.48 | 5.46 | 5.35 | 4.96 |
| **$F/F_{peak}$ (%)** | 0 | 33 | 47 | 73 | 98 | 100 | 72 | 42 |
| **$\delta z_{line}/ \delta z_{line\ -\ peak\ load}$ (%)** | 0 | 30 | 63 | 85 | 97 | 100 | 111 | 136 |
| **$\delta z_{anchor}/\delta z_{anchor\ -\ peak\ load}$ (%)** | 0 | 38 | 63 | 85 | 94 | 100 | 118 | 124 |
| **$\Theta/\Theta_{final}$ (%)** | 20 | 31 | 51 | 68 | 76 | 81 | 95 | 100 |

**Figure 5-20 Summary of Captured Anchor Orientation (e/B = 2)**

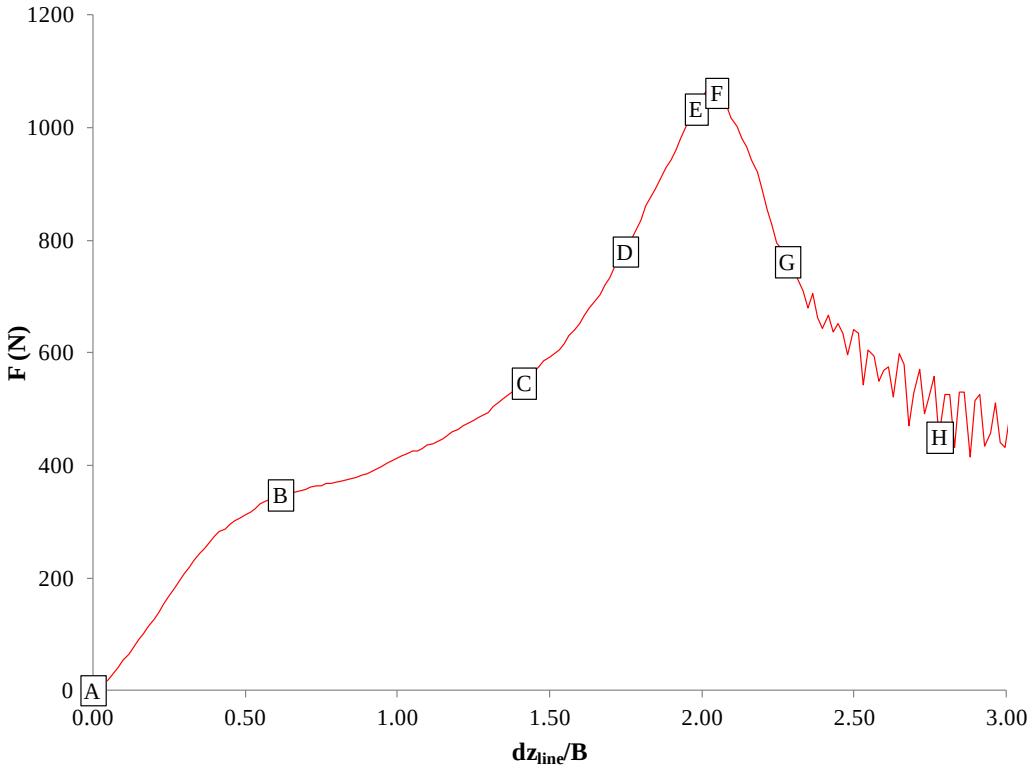


**Figure 5-21 Load – displacement Response during Keying and Pullout (vertical anchor line displacement) (e/B = 2)**

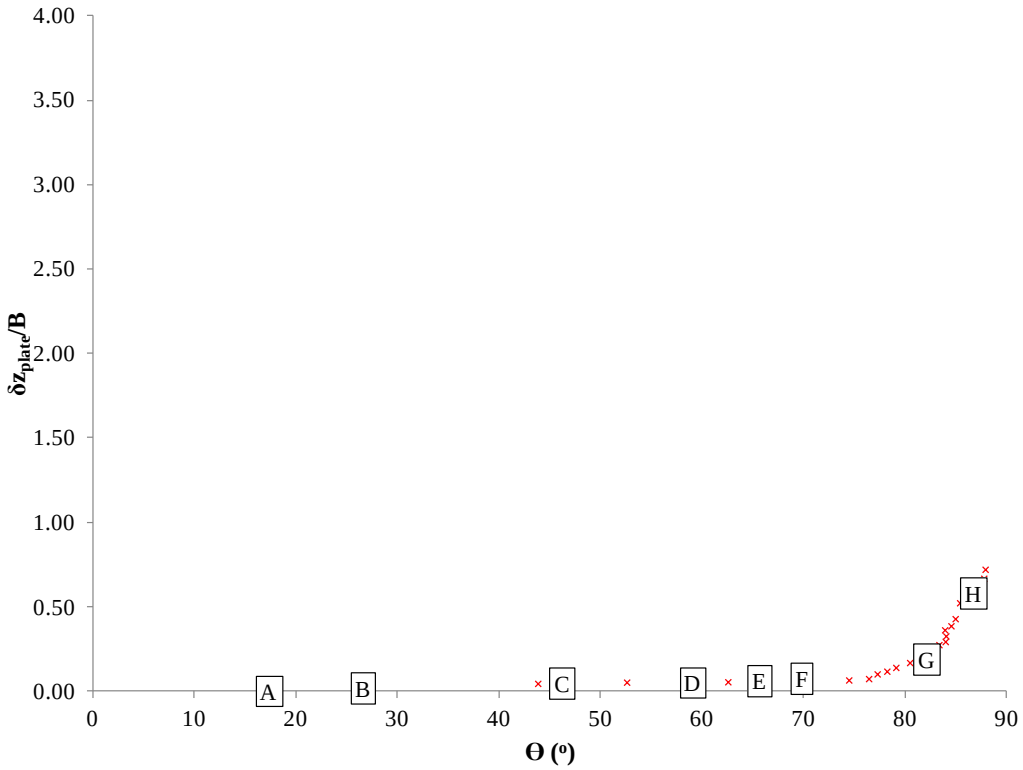


**Figure 5-22 Anchor Rotation (e/B = 2)**

### 5.2.4 Trajectory of Padeye

The influence of the eccentricity ratio, e/B, on the trajectory of the padeye is shown in Figure 5-23, Figure 5-24, Figure 5-25, Figure 5-26 and Figure 5-27 for each eccentricity ratio. The origin of the horizontal and vertical axes coincided with the initial centre of the plate. The trajectory of the padeye is highlighted in green and the anchor at peak load is outlined in red.

Figure 5-23 shows that the strip anchor with an eccentricity ratio, e/B = 0.25 started moving vertically with very little rotation. The applied load at the padeye caused upward vertical loading on the plate minimal moment (and hence rotation) developed at the plate due to the low padeye eccentricity. The padeye trajectory of the strip anchors with an eccentricity ratio, e/B = 0.5 and 0.75 were similar (Figure 5-24 and Figure 5-25), although the anchor with e/B = 0.5 underwent a higher loss in embedment and a lower rate of rotation than the anchor with e/B = 0.75. This is compatible with the higher moment developed at the plate for the anchor with e/B = 0.75. The trend of a reduced vertical loss in embedment and increased rate of rotation due to the higher moment developed at the plate became even more evident when Figure 5-26 and Figure 5-27 were examined for e/B = 1 and e/B = 2 respectively.

Quantification of the loss of embedment of the plate with respect to the inclination of the plate is shown in Figure 5-28. The peak load for each eccentricity ratio is highlighted. Figure 5-28 shows that as the eccentricity ratio increased, the loss of embedment at the peak load decreased and became negligible at e/B = 2. Figure 5-28 shows that the inclination of the plate at the peak load increased as the eccentricity ratio increased. This was made clearer by Figure 5-29, which is a summary of the plate inclination at the peak load as a function of e/B for all tests involving camera measurements and shows that an apparent linear increase in plate inclination occurred (at the peak load) with increasing e/B.

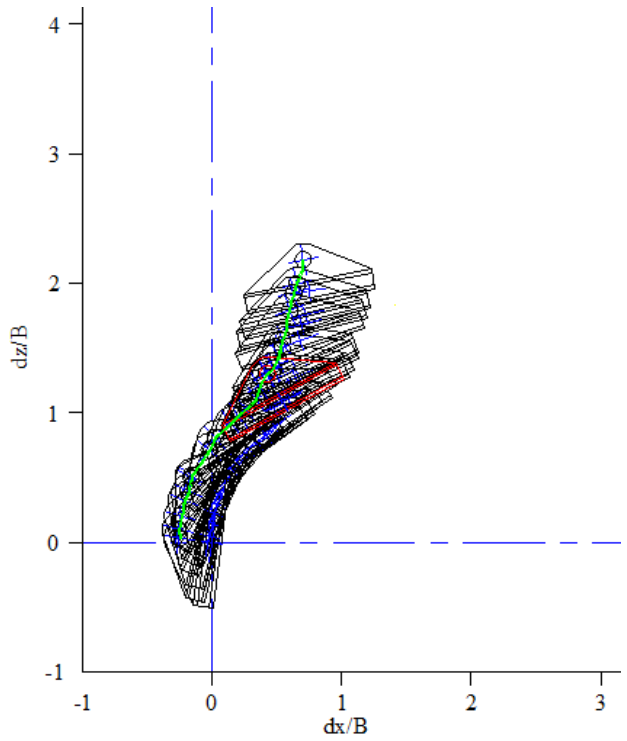


**Figure 5-23 Trajectory of Anchor Padeye (e/B = 0.25) (where dz = $\delta z_{plate}$)**

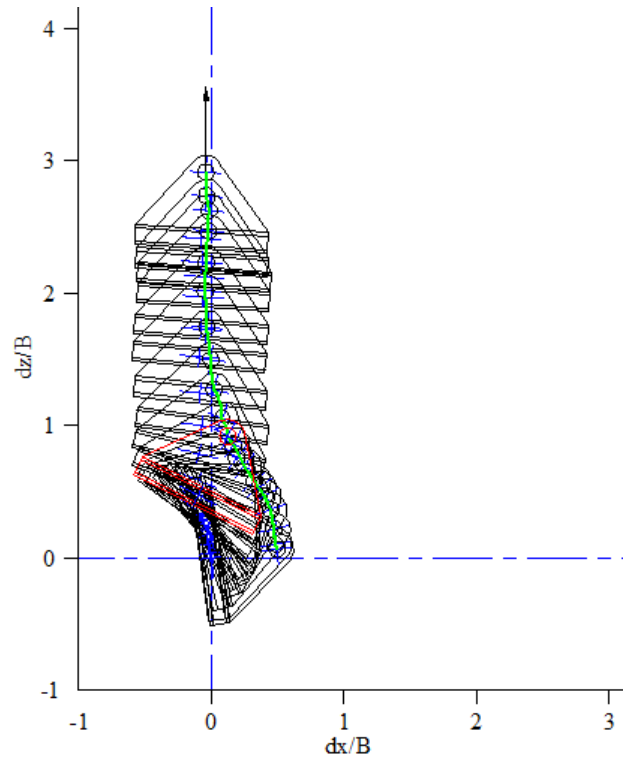


**Figure 5-24 Trajectory of Anchor Padeye (e/B = 0.50) (where dz = $\delta z_{plate}$)**

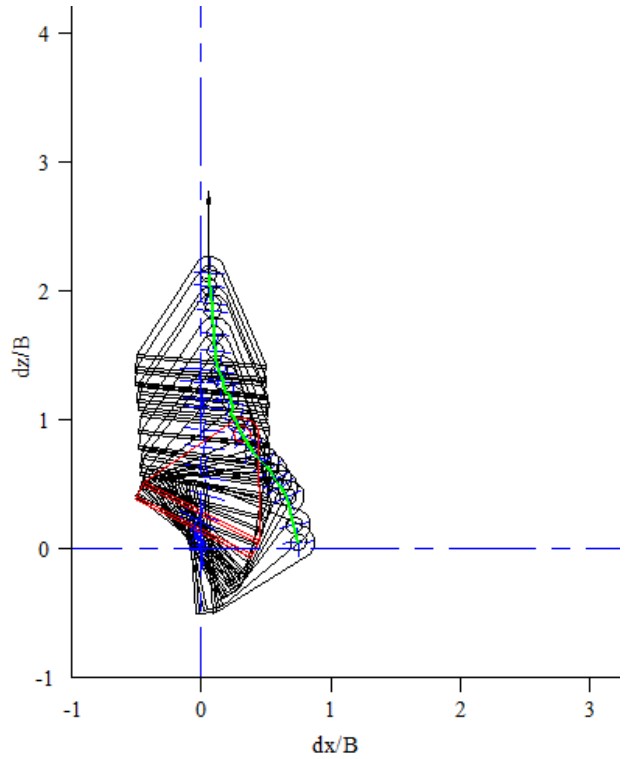


**Figure 5-25 Trajectory of Anchor Padeye (e/B = 0.75) (where dz = $\delta z_{plate}$)**

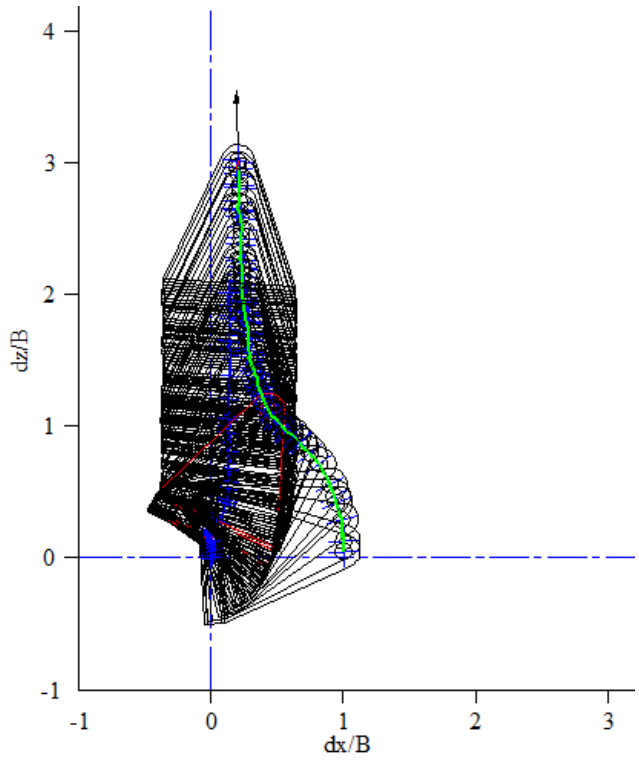


**Figure 5-26 Trajectory of Anchor Padeye (e/B = 1) (where dz = $\delta z_{plate}$)**

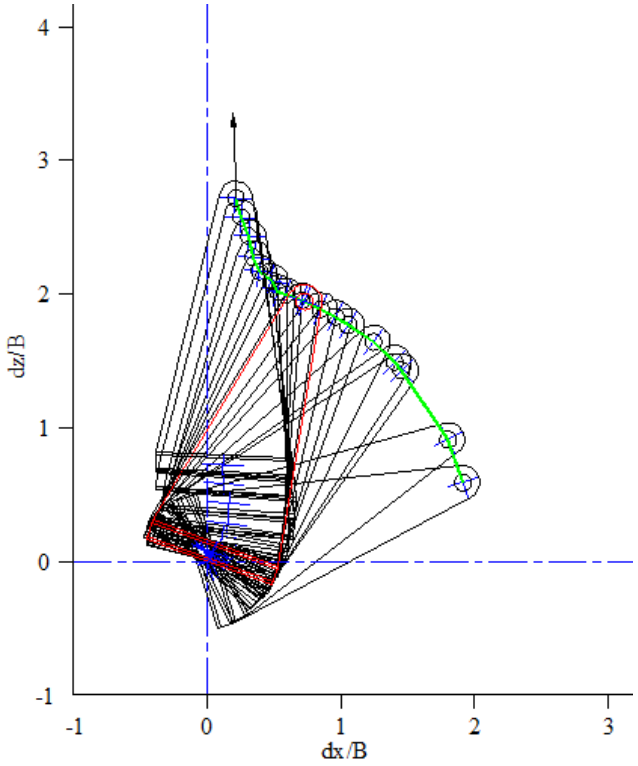


**Figure 5-27 Trajectory of Anchor Padeye (e/B = 2) (where dz = $\delta z_{plate}$)**

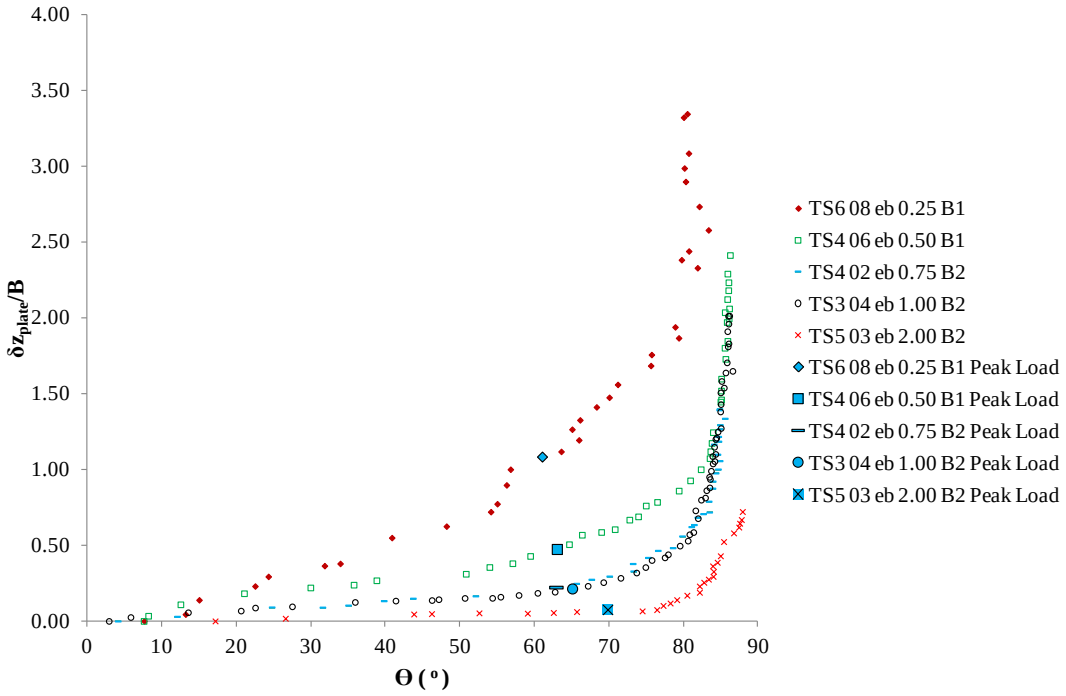


**Figure 5-28 Anchor Rotation (Representative Tests)**

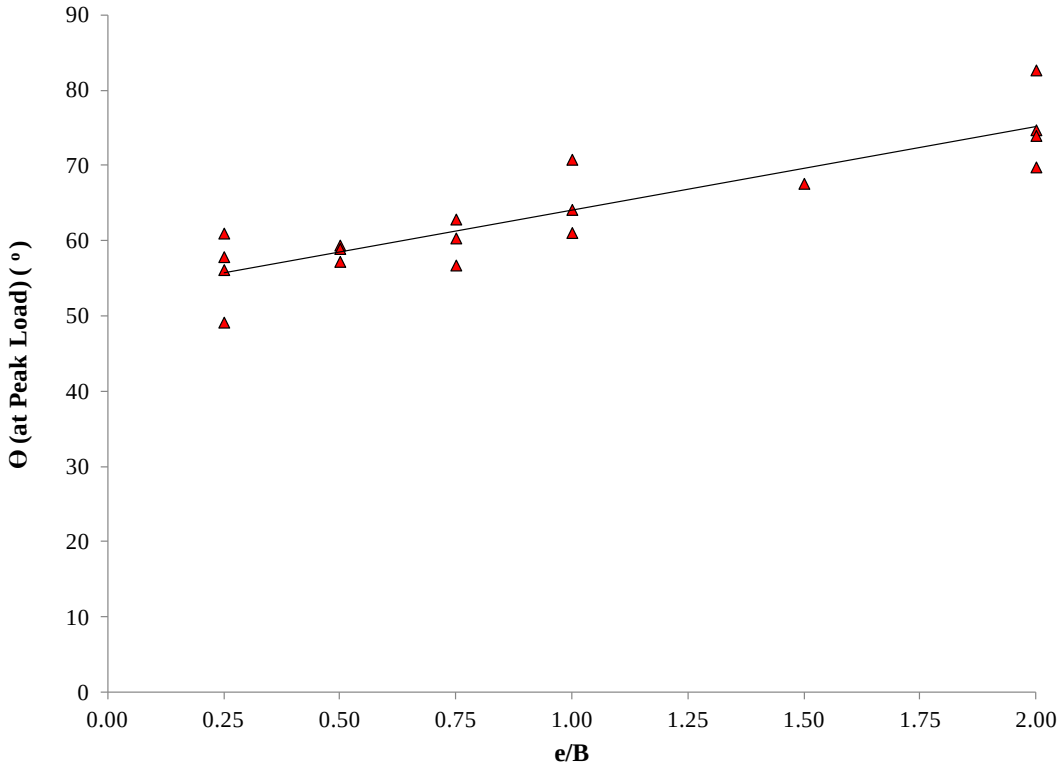


**Figure 5-29 Anchor Rotation at Peak Load**

### 5.2.5 Failure Mechanisms

The PIV analyses were conducted using GeoPIV (White and Take, 2002), which is a software implementation of PIV particularly suited to geotechnical applications. Failure mechanism at various stages during the anchor keying and pullout process were produced using GeoPIV for anchors with e/B = 0.5, 0.75, 1 and 2 and are shown here as instantaneous velocity fields. These analyses were conducted to highlight the two failure mechanisms that occurred during each anchor test.

An outline of the sample surface profile, initial anchor location, current anchor location, the trajectory of the padeye and the direction of the mooring line have been overlain on the vector field for each eccentricity ratio considered. The vertical and horizontal axes represent normalised (by the anchor breadth, B) vertical and horizontal displacements respectively, with the axes origin representing the current anchor position.

Instantaneous velocity fields were produced for stages where: (i) the load was less than the peak load, (ii) at the peak load, and (iii) the load was greater than the peak

load. The corresponding mechanisms identifiable from the velocity fields (displacement vectors) are denoted Deep Localised Failure (FMA), Failure Mechanism at Peak Load (FMB) and Shallow Failure Mechanism (FMC) respectively, and are provided in Figure 5-30, Figure 5-33, Figure 5-36 and Figure 5-39 for e/B = 0.5, 0.75, 1 and 2 respectively. The corresponding position on the F vs. $\delta z_{line}/B$ plot for each eccentricity ratio is highlighted in Figure 5-31, Figure 5-34, Figure 5-37 and Figure 5-40. These positions are also shown on the $\Theta$ vs. $\delta z_{plate}/B$ plot in Figure 5-32, Figure 5-35, Figure 5-38 and Figure 5-41. Further details are summarised in Table 5-2.

The PIV analyses were conducted at approximately the same location on the load – displacement response for each test. FMA was chosen at the mid-point of between the initial stiff response and the peak load, FMB at the peak load and FMC just before the load started to oscillate.

The instantaneous velocity fields have shown that there are two distinctive failure mechanisms, a localised deep failure mechanism (FMA) and a shallow failure mechanism (FMB and FMC). FMA was characterised by soil movements localised to the plate that were typically elliptical in shape and indicate a rotational failure mechanism associated with the large plate rotations that occurred at this stage of the test. No discernible movement of the soil surface was evident at this stage, indicating that the mechanism was deep and localised (Merifield, 2002).

At the peak load (FMB) the failure mechanism transitioned from a deep localised mechanism to a shallow mechanism extending to the soil surface. This change in mechanism triggered the reduction in load (just beyond the peak load) as a more efficient means was found for overcoming the shear resistance of the sand. At the reduced load at FMC the shallow failure mechanism becomes more pronounced, as evident from the greater movement or heave of the soil surface.

**Table 5-2 Stages considered in the PIV Analyses**

| | | F | $F/F_{peak}$ | $\delta z_{line}/B$ | Θ | $\delta z_{plate}/B$ | $H_{curent}/B$ |
|---|---|---|---|---|---|---|---|
| | | (N) | (%) | (-) | (°) | (-) | (-) |
| e/B = 0.5 | Initial Orientation | 0 | - | 0 | 8 | 0.00 | 4.91 |
| | FM A | 719 | 80 | 0.66 | 27 | 0.21 | 4.70 |
| | FM B | 862 | 96 | 1.19 | 63 | 0.47 | 4.44 |
| | FM C | 650 | - | 1.26 | 66 | 0.57 | 4.34 |
| e/B = 0.75 | Initial Orientation | 0 | - | 0 | 4 | 0.00 | 4.51 |
| | FM A | 652 | 79 | 0.82 | 35 | 0.10 | 4.41 |
| | FM B | 820 | 100 | 1.18 | 63 | 0.22 | 4.18 |
| | FM C | 730 | - | 1.32 | 73 | 0.33 | 3.85 |
| e/B = 1 | Initial Orientation | 0 | - | 0 | 3 | 0.00 | 4.60 |
| | FM A | 596 | 70 | 0.98 | 41 | 0.13 | 4.47 |
| | FM B | 857 | 100 | 1.35 | 63 | 0.19 | 4.41 |
| | FM C | 629 | - | 1.58 | 76 | 0.40 | 4.20 |
| e/B = 2 | Initial Orientation | 0 | - | 0 | 17 | 0.00 | 5.54 |
| | FM A | 389 | 37 | 0.92 | 33 | 0.03 | 5.51 |
| | FM B | 1062 | 100 | 2.05 | 70 | 0.08 | 5.46 |
| | FM C | 662 | - | 2.38 | 83 | 0.28 | 5.26 |

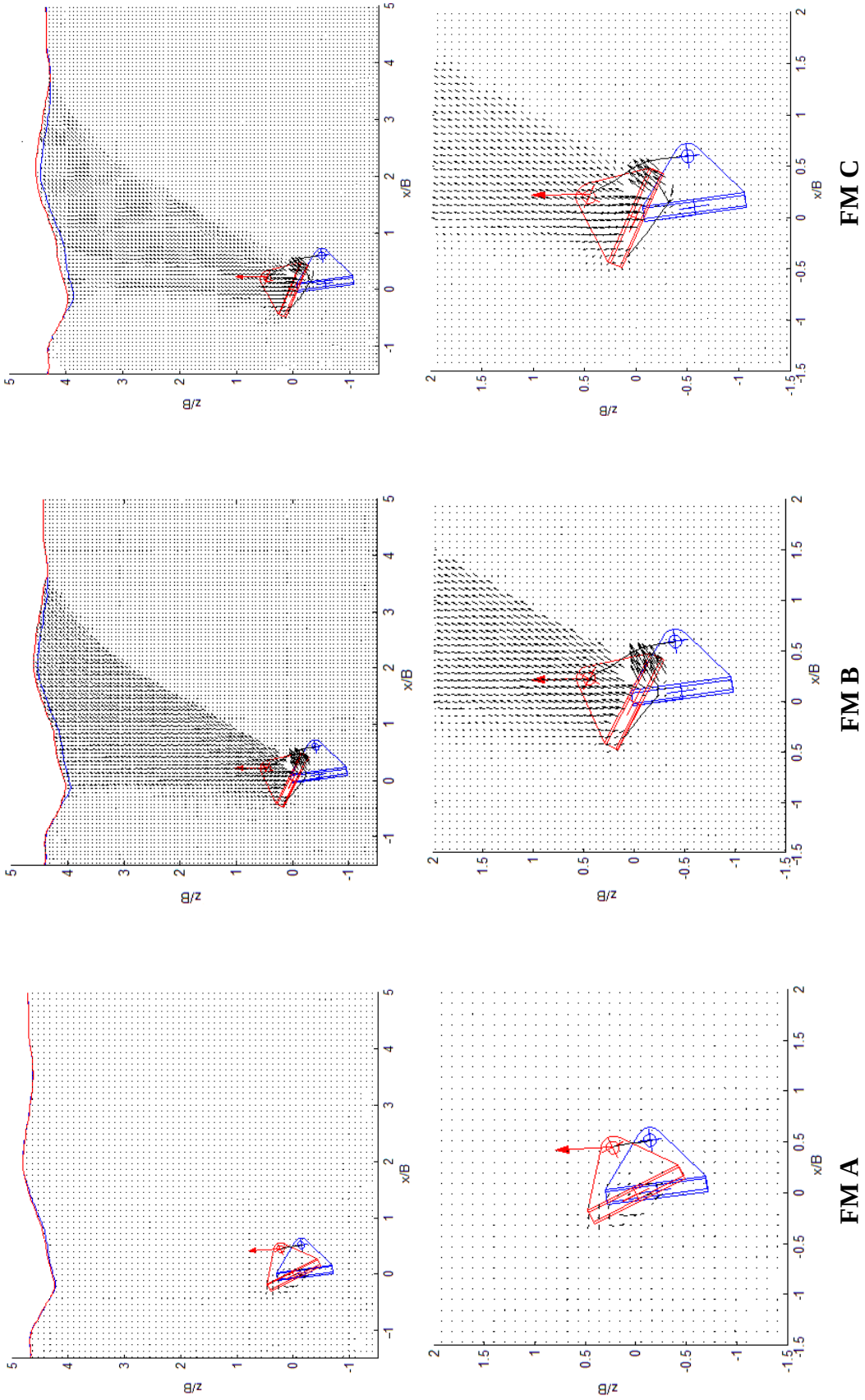


**Figure 5-30 Instantaneous Velocity Field (e/B = 0.50)**

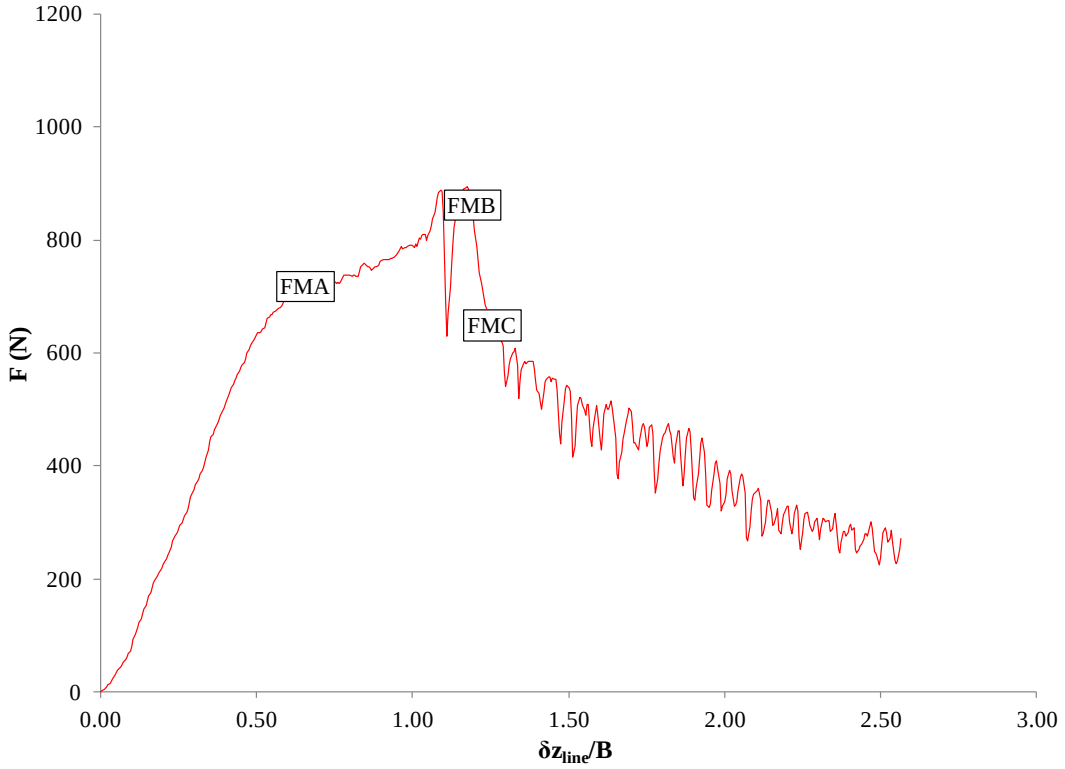


**Figure 5-31 Load – displacement Response during Keying and Pullout (vertical anchor line displacement) - PIV Analysis (e/B = 0.50)**

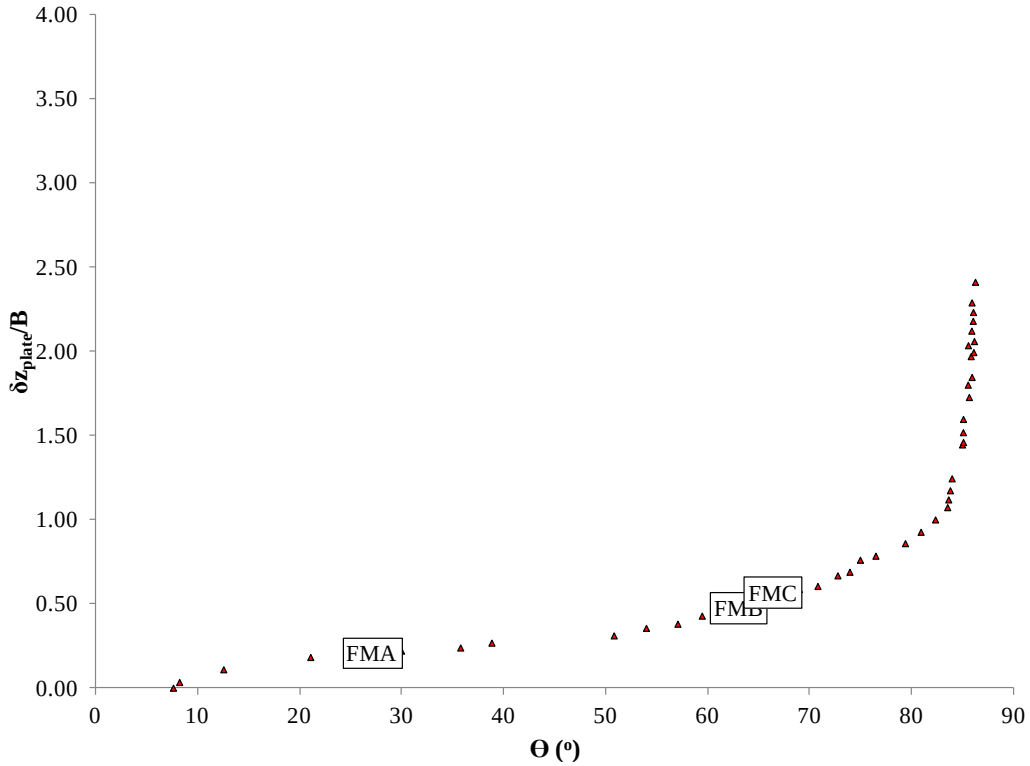


**Figure 5-32 Anchor Rotation – PIV Analysis (e/B = 0.50)**

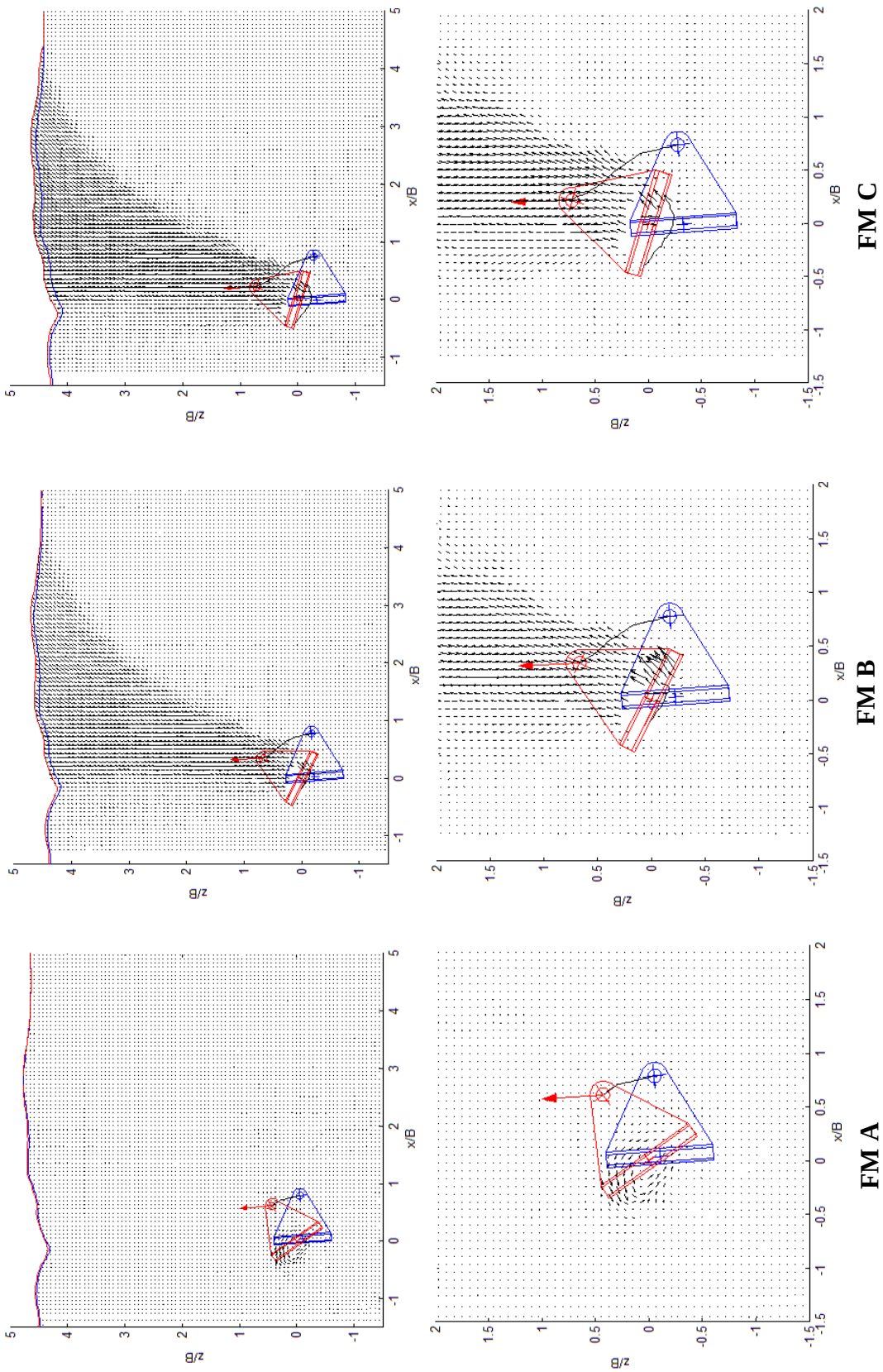


**Figure 5-33 Instantaneous Velocity Field (e/B = 0.75)**

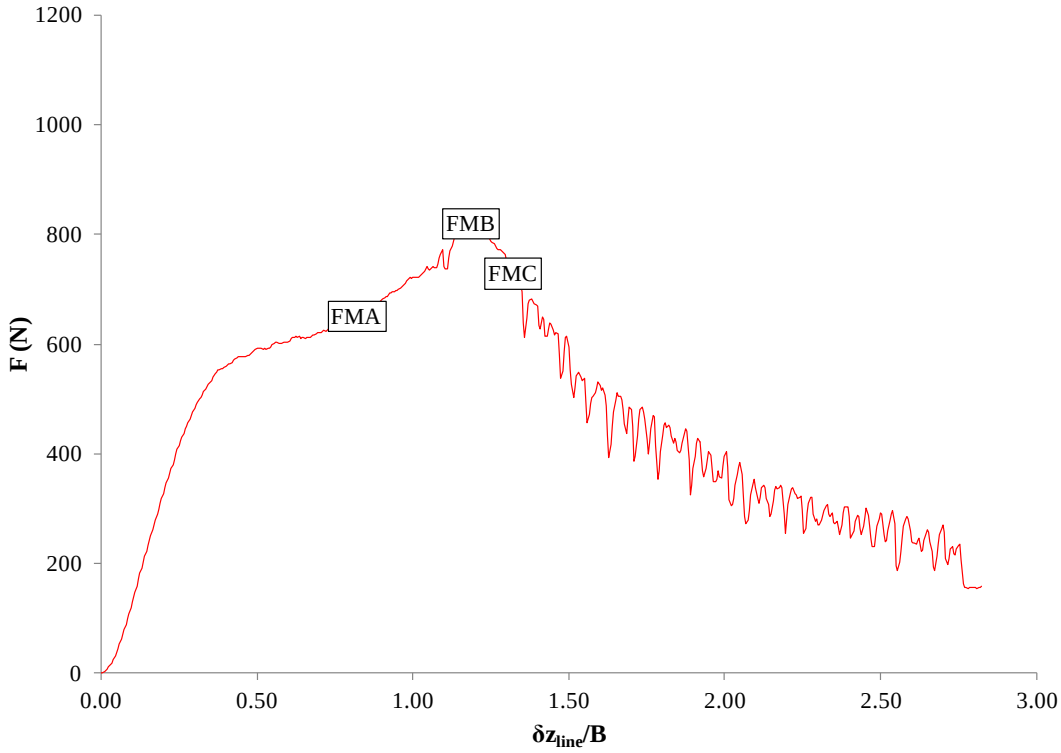


**Figure 5-34 Load – displacement Response during Keying and Pullout (vertical anchor line displacement) - PIV Analysis (e/B = 0.75)**

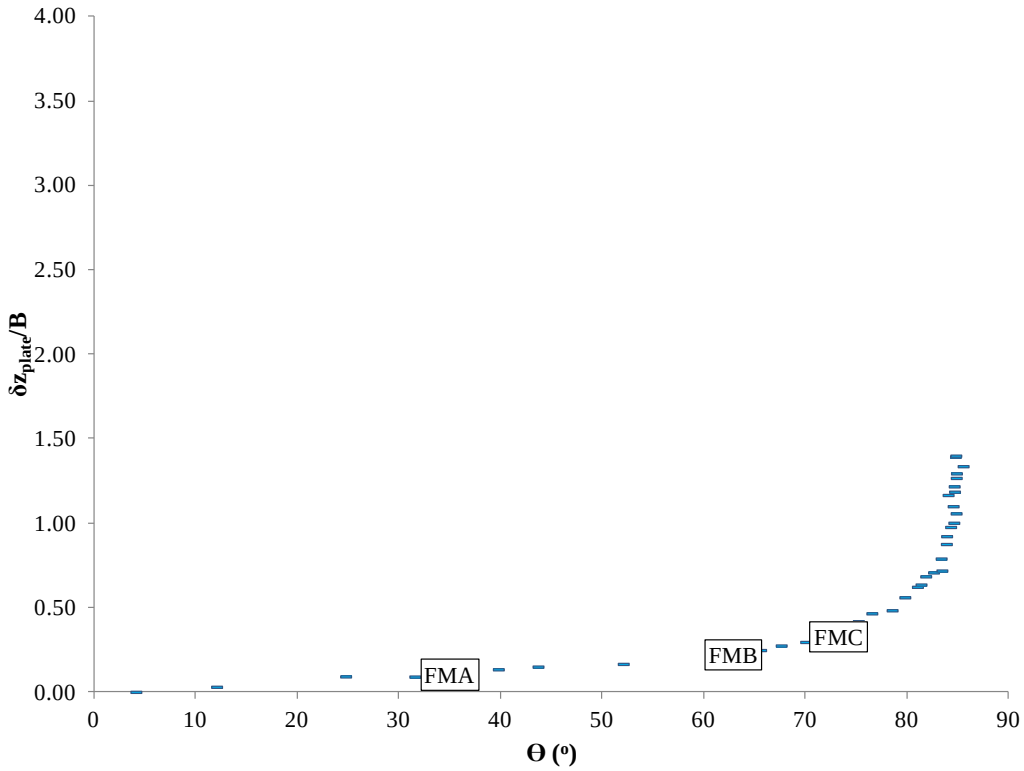


**Figure 5-35 Anchor Rotation – PIV Analysis (e/B = 0.75)**

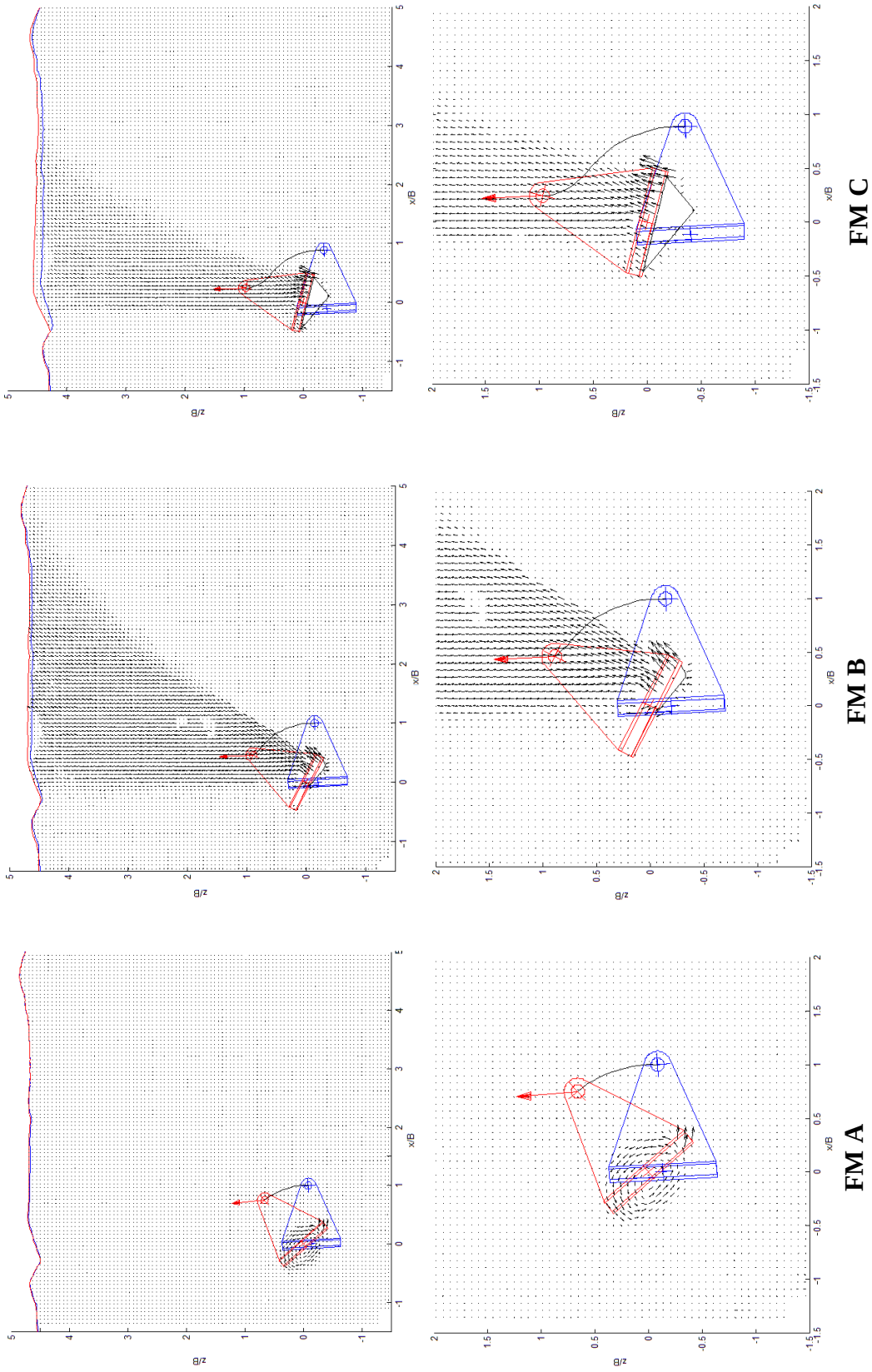


**Figure 5-36 Instantaneous Velocity Field (e/B = 1)**

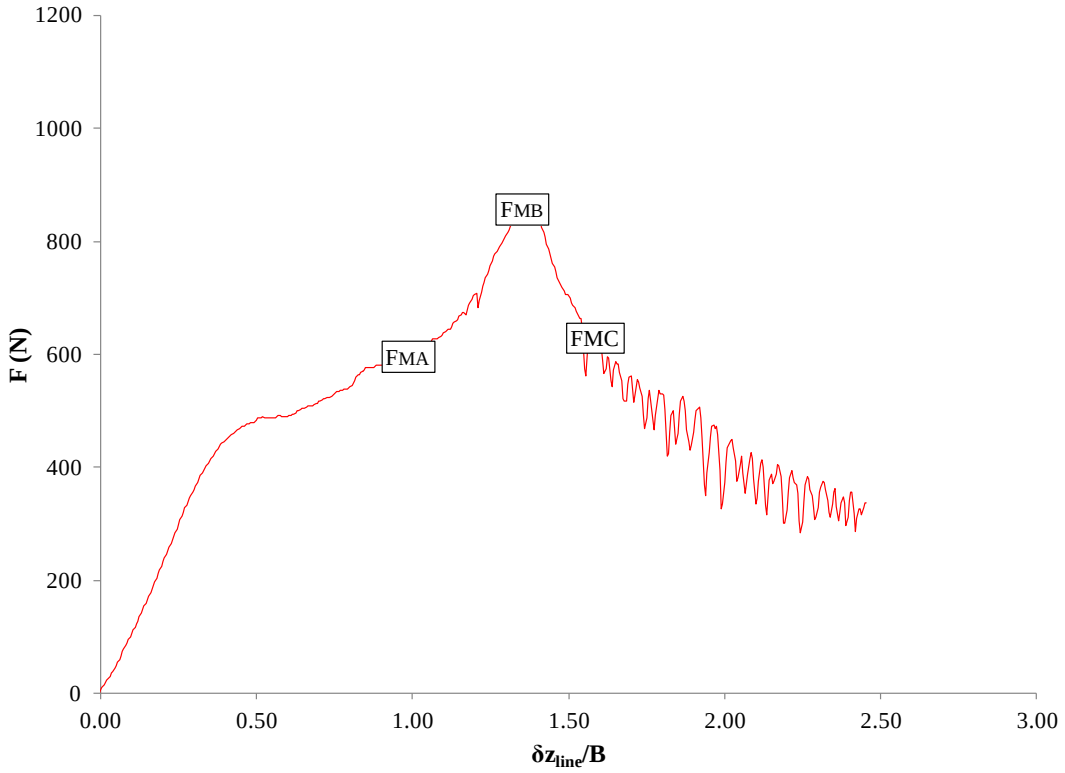


**Figure 5-37 Load – displacement Response during Keying and Pullout (vertical anchor line displacement) - PIV Analysis (e/B = 1)**

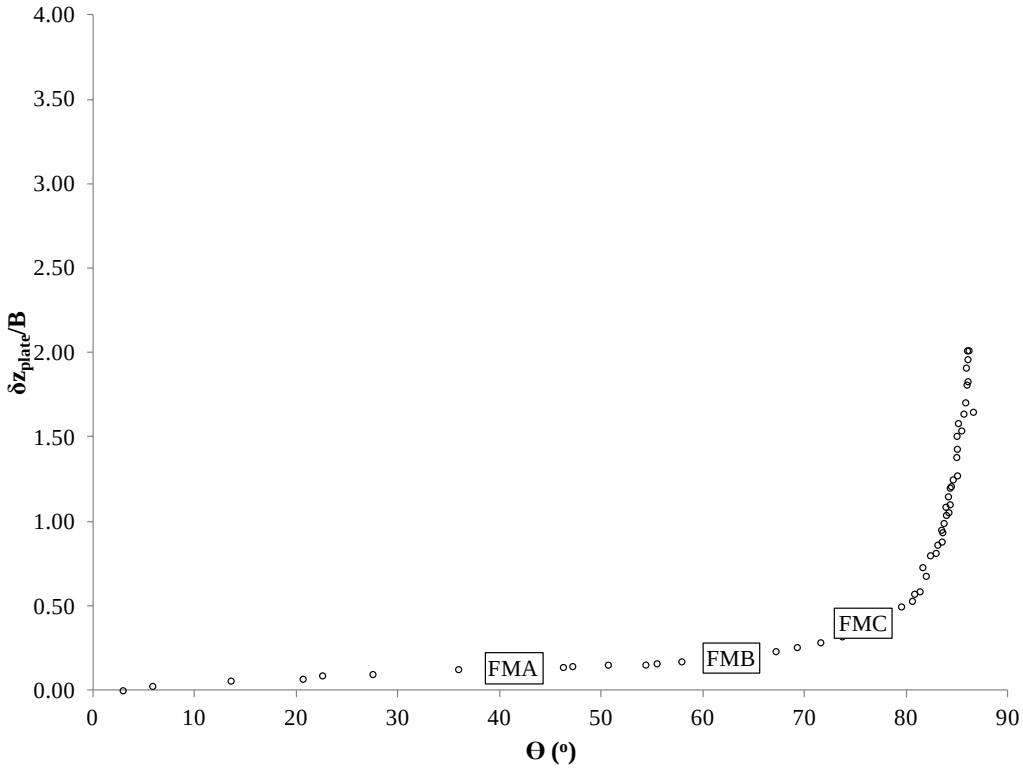


**Figure 5-38 Anchor Rotation – PIV Analysis (e/B = 1)**

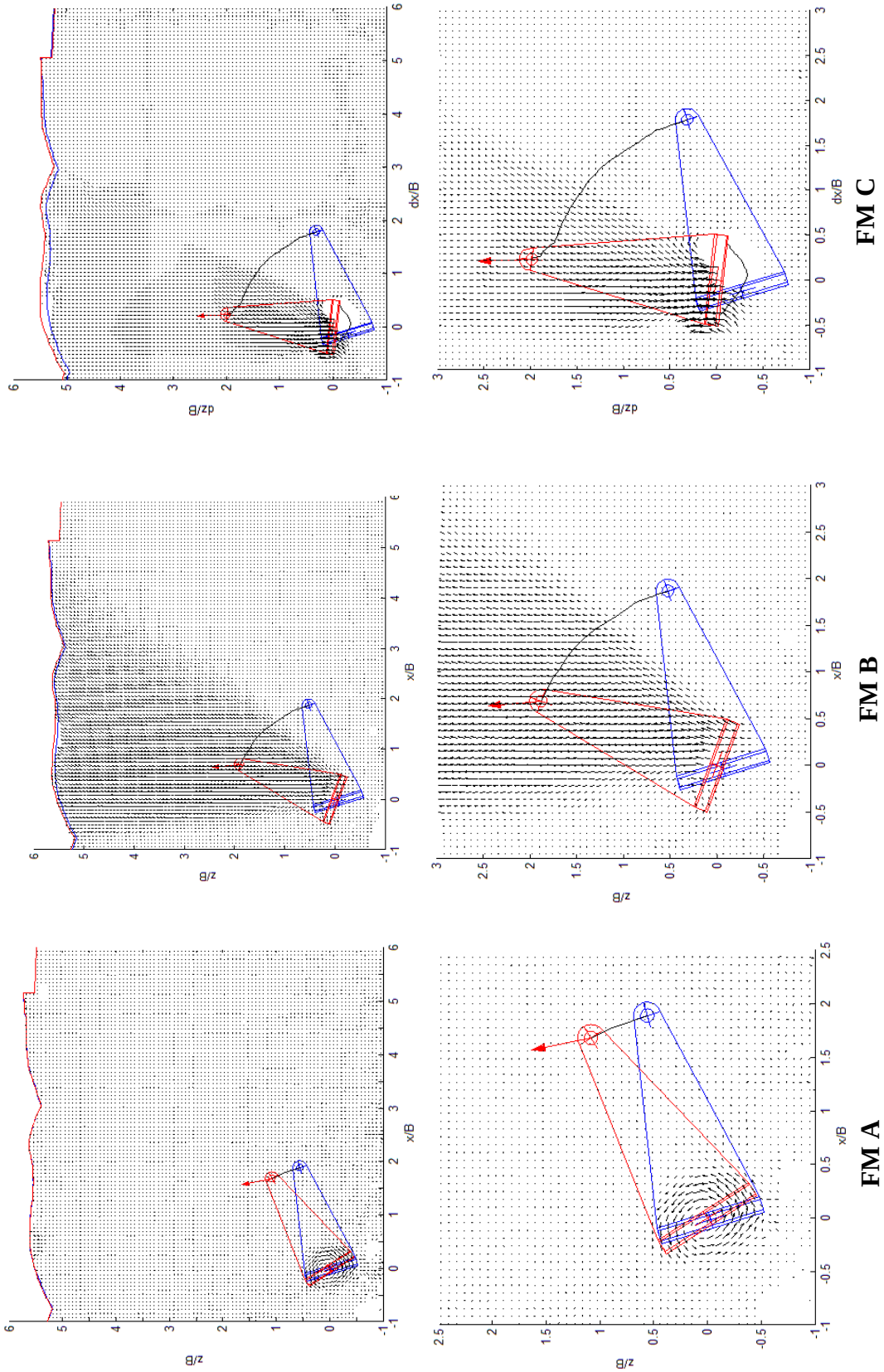


**Figure 5-39 Instantaneous Velocity Field (e/B = 2)**

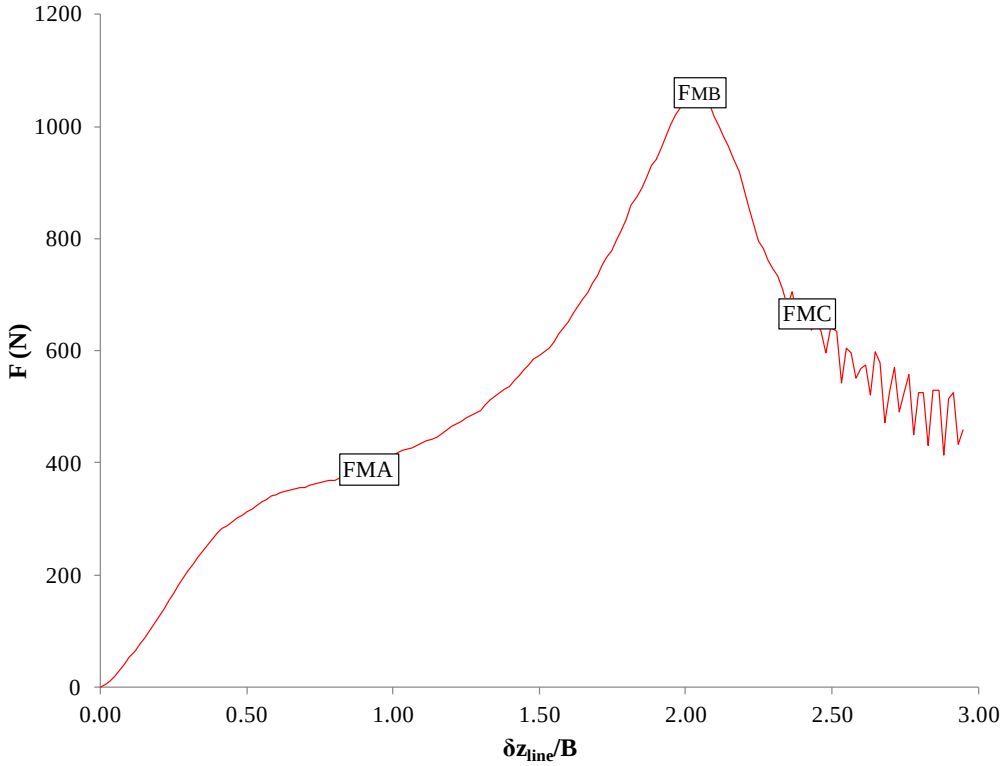


**Figure 5-40 Load – displacement Response during Keying and Pullout (vertical anchor line displacement) - PIV Analysis (e/B = 2)**

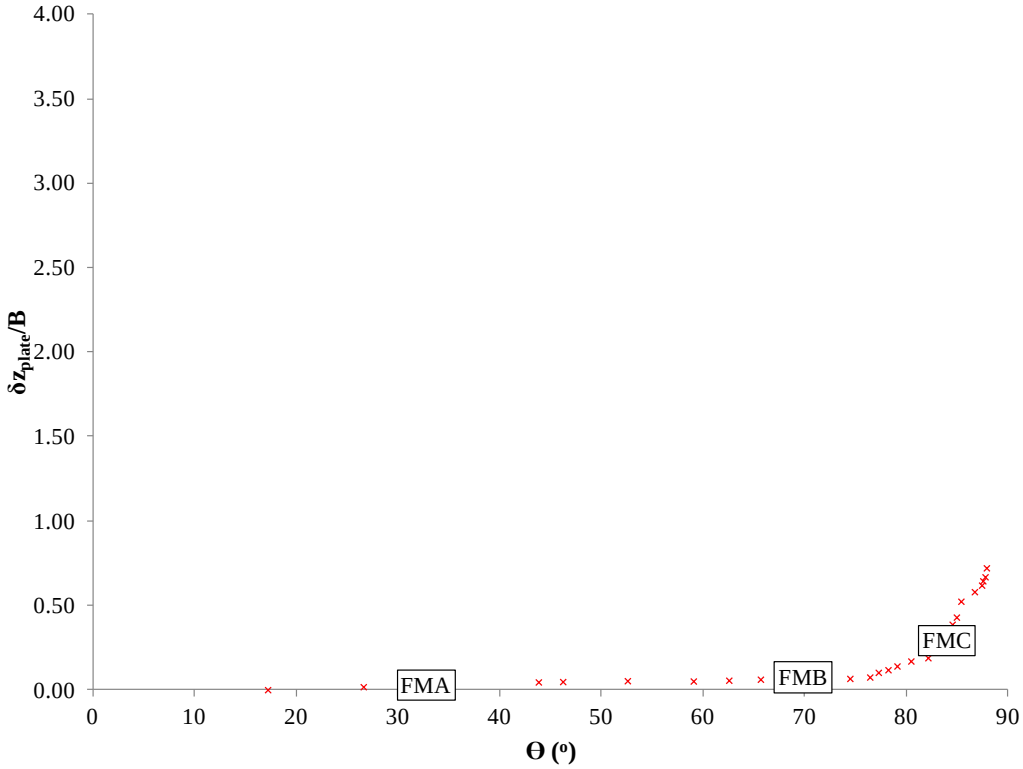


**Figure 5-41 Anchor Rotation – PIV Analysis (e/B = 2)**

### 5.2.6 Summary of Keying Response

In this study, the behaviour of a plate anchor with five different eccentricity ratios during the anchor test was captured and analysed. The loss in embedment from the initial anchor position to that coincident with the peak load was found to be strongly dependent on the eccentricity of the padeye, with a low padeye eccentricity resulting in the highest loss in embedment and vice versa. These results are consistent with that reported for clay and can be described through Equation 5-1, which is a slightly modified form of the loss in embedment equation proposed by Wang *et al.* (2011).

A summary of the behaviour of a strip anchor with a low eccentricity ratio (e/B = 0.50) and a high eccentricity ratio (e/B = 2) during the anchor test is given in Figure 5-42 and Figure 5-43, respectively.

The load – displacement responses for each considered eccentricity ratio was sectioned according to the observed failure mechanisms, *deep*, *transitional* and *shallow*. Five points (**A, B, C, D** and **E**) along the load – displacement response were chosen to illustrate the anchor behaviour during these stages.

*Deep Failure Mechanism*

- Once the mooring line became taut the load was transferred to the strip anchor, which caused the load to increase rapidly. The loss of embedment is almost negligible (see point **A**). As the plate anchor rotates, the sand around the plate anchor is mobilised (see Figure 5-42 and Figure 5-43). The rate of rotation relative to the loss in embedment was found to be higher for an anchor with a low eccentricity ratio than for an anchor with a high eccentricity ratio (see point **B**).

*Transitional Failure Mechanism (Anchor Keying to Peak Load)*

- The failure mechanism changed from a localised deep mechanism into a transitional failure mechanism. During this phase, the failure mechanism extended beyond the vicinity of the anchor in the direction of the soil surface (see point **C**). The load increased rapidly with almost negligible loss of embedment for the higher eccentricity ratio (e/B = 2). The rapid increase of the load was due

to an increase in the projected area of the plate to the direction of loading. A similar response was evident for a lower eccentricity ratio, with the exception that the loss in embedment was not negligible and as a result the load – displacement response was not as stiff.

*Shallow Failure Mechanism*

- At the peak load the failure mechanism infringed on the soil surface (see point **D**). When the peak load was reached the loss of embedment increased rapidly as the plate was almost normal to the direction of loading. As the eccentricity ratio increases, the embedment loss required for the anchor to become normal to the loading direction decreases (see point **E**).

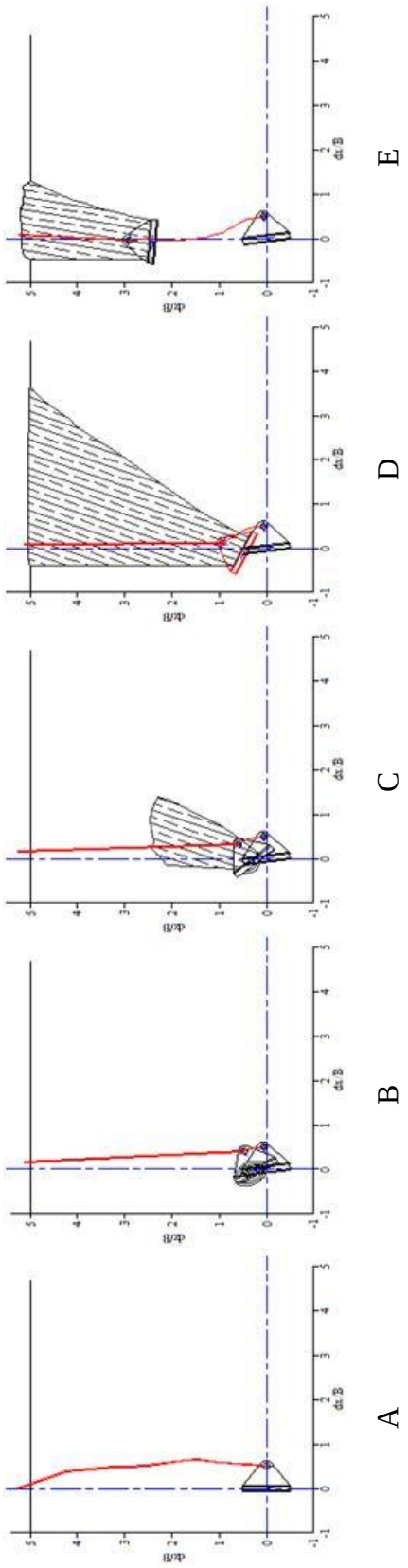


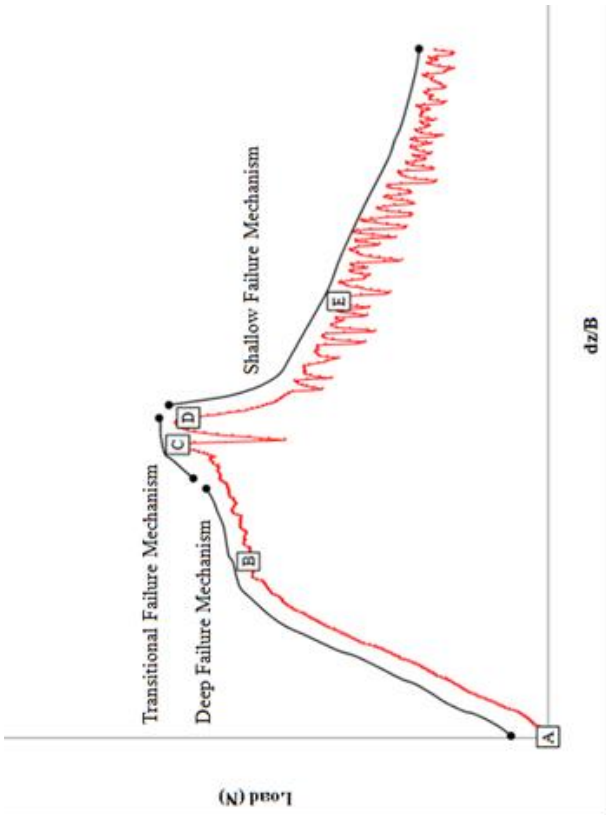


**Figure 5-42 Load – displacement Plot of a Plate Anchor (Low Eccentricity Ratio)**

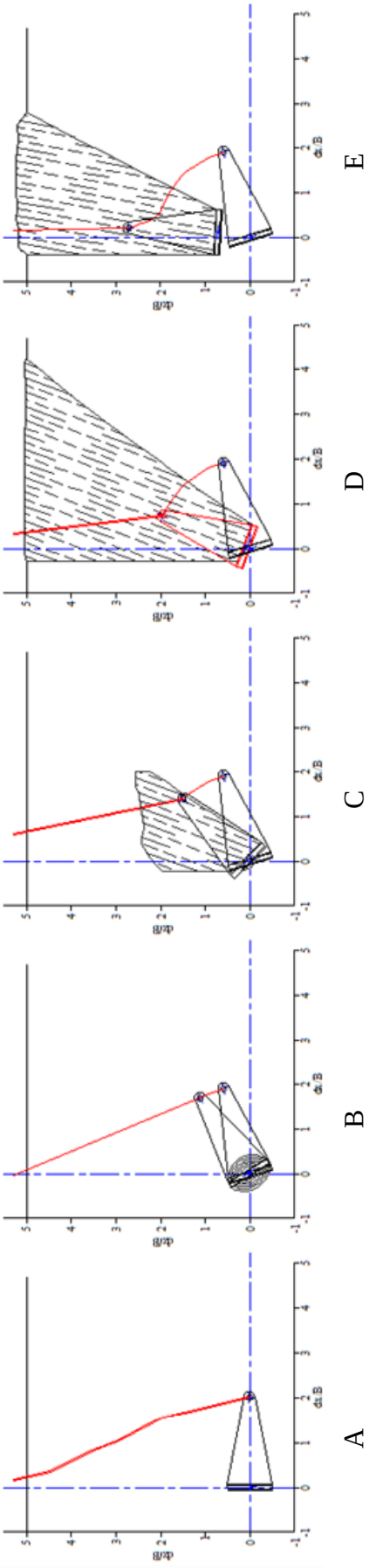


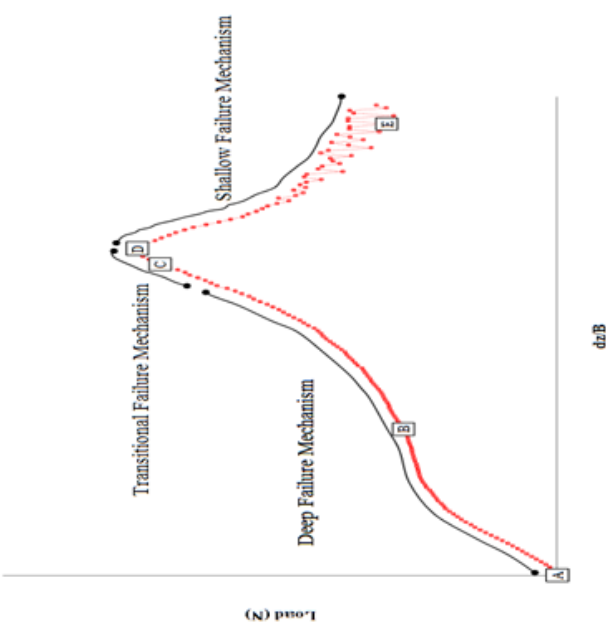


**Figure 5-43 Load – displacement Plot of a Plate Anchor (High Eccentricity Ratio)**

## 5.3 Capacity

In this section the anchor capacity measured in the centrifuge tests was back analysed as the dimensionless capacity factor, $N_\gamma$. The load data and the orientation of the plate anchor were used together to compute the capacity factor for each anchor test. The capacity factor $N_\gamma$ was computed using Equation 5-2.

$$N_\gamma = \frac{F}{\gamma' AH \sin\theta} \qquad \textbf{Equation 5-2}$$

which is identical to Equation 2-4 with the exception that Equation 2-4 expressed the load per unit length and Equation 5-2 accounted for the varying inclination of the plate during keying, which effectively reduced the area presented in the direction of the quasi-vertical loading. In both equations $H = H_{current.}$

The back analysed capacity factor, $N_{\gamma,}$ is shown for selected tests from each eccentricity ratio group on Figure 5-44 to Figure 5-48. Also shown on these figures are predictions obtained using the plasticity solution proposed by Ng and Springman (1994) (Equation 2-7) and the limit equilibrium solution proposed by White *et al.* (2008) (Equation 2-10).

The Ng and Springman (1994) prediction was produced using the peak friction angle, $\phi_{peak}$ = 44° (Lauder, 2010), whereas $F_{up}$ required for the White *et al.* (2008) prediction was calculated using Equation 2-9, which is a function of the peak friction angle, $\phi_{peak}$ = 44°, the dilation angle, $\psi$, the effective unit weight of the soil $\gamma'$ = 17.5kN/m$^3$ and the at rest earth pressure coefficient, $K_0 = 1 - \sin\phi_{crit} = 0.47$ ($\phi_{crit}$ = 32°). The dilation angle, $\psi$, required for Equation 2-9 was selected using Bolton's (1986) correlations that link dilation angle to relative density and grain-crushing strength, relative to the mean effective stress. This approach resulted in the dilation angle ranging from $\psi$ = 24.83 - 25°. In both cases the friction angle was taken as a constant.

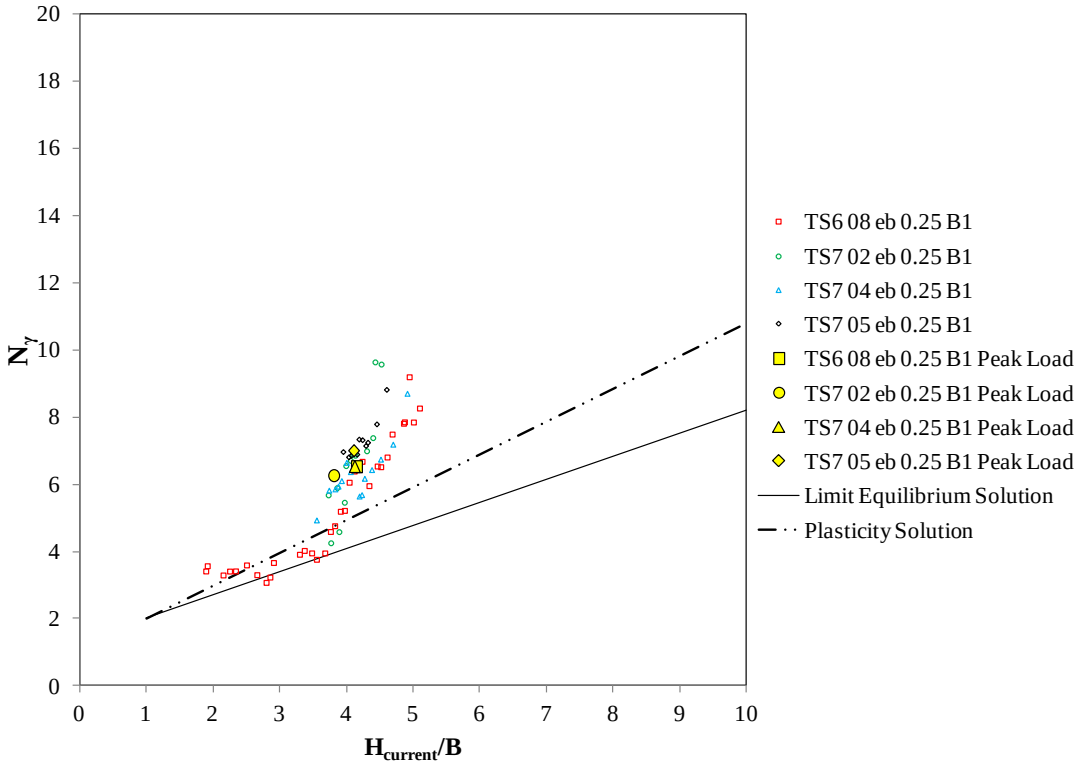


**Figure 5-44 Back Figured Capacity Factor (e/B = 0.25)**

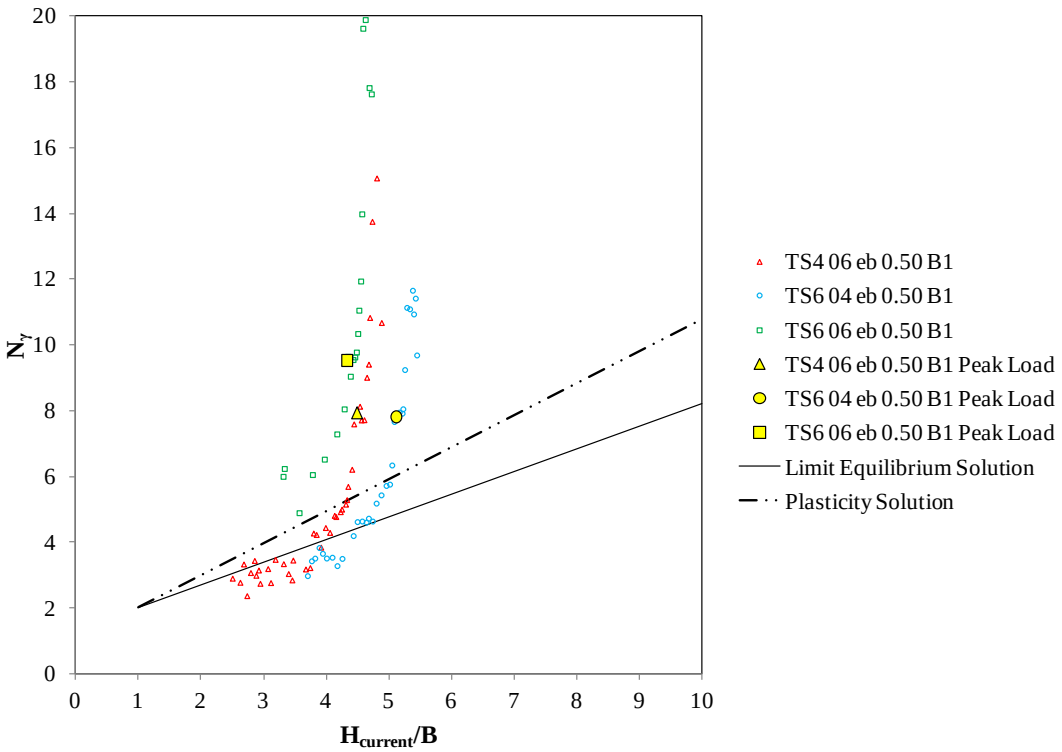


**Figure 5-45 Back Figured Capacity Factor (e/B = 0.5)**

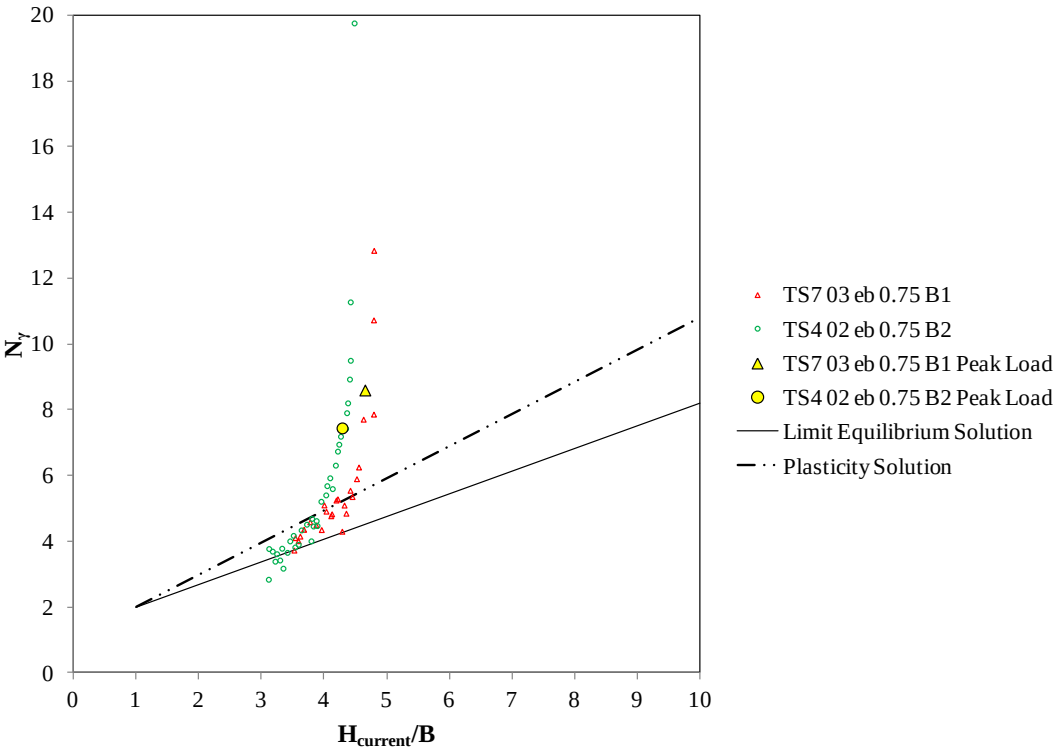


**Figure 5-46 Back Figured Capacity Factor (e/B = 0.75)**

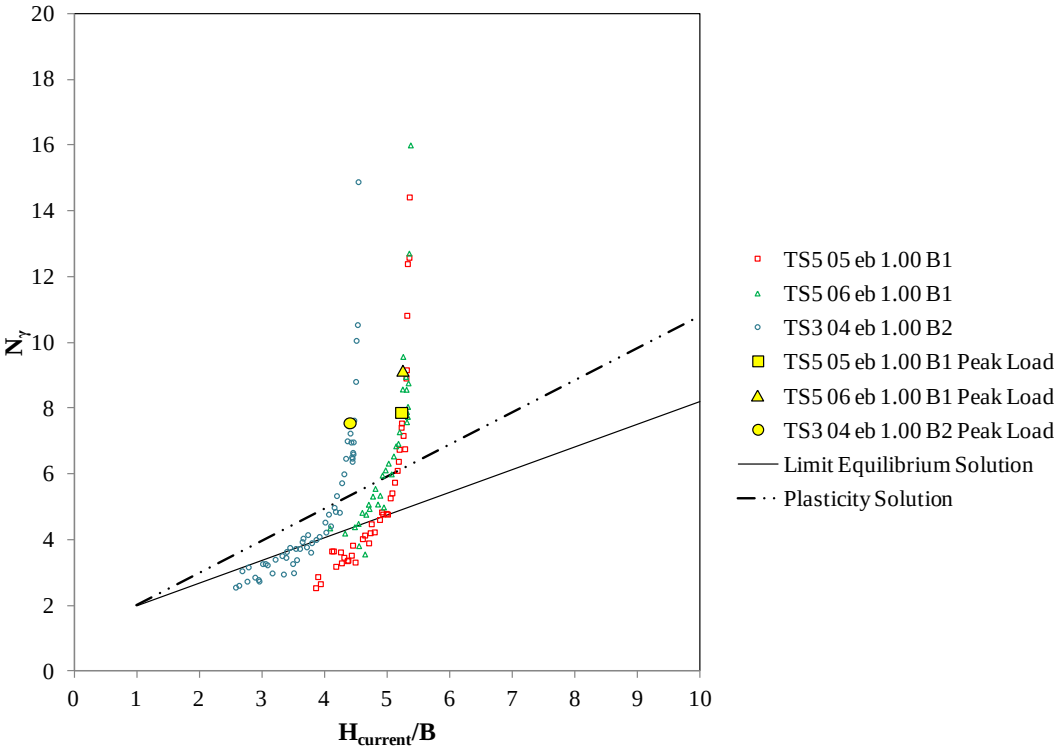


**Figure 5-47 Back Figured Capacity Factor (e/B = 1)**

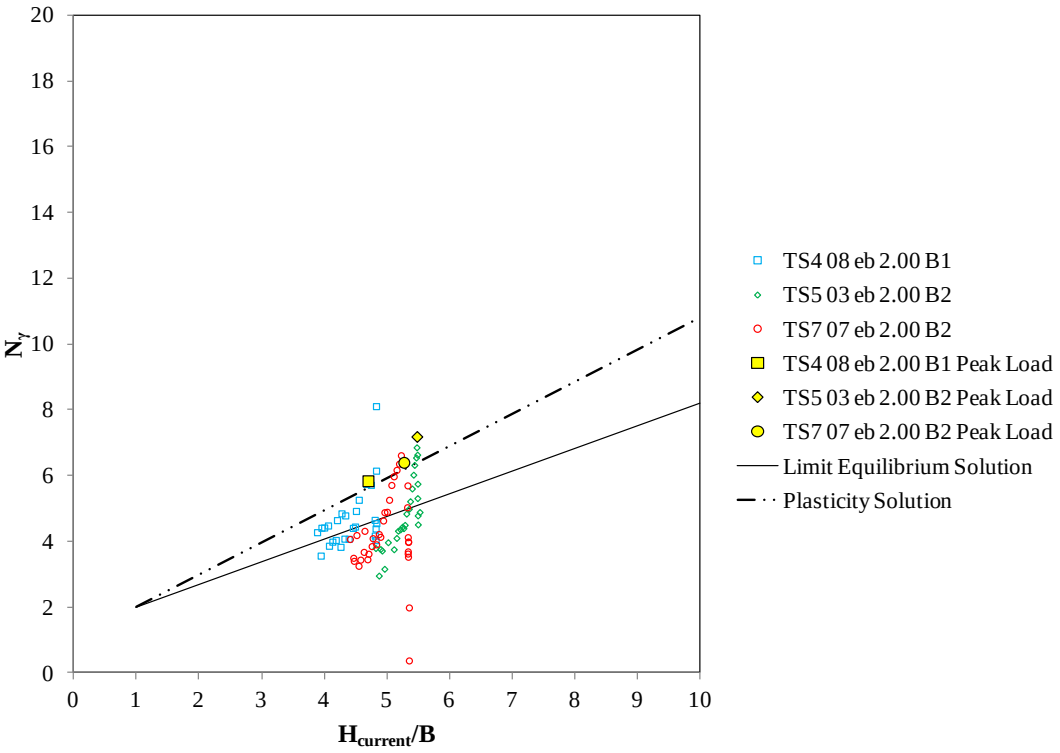


**Figure 5-48 Back Figured Capacity Factor (e/B = 2)**

Back figured $N_\gamma$ values for each eccentricity group are seen to approach the theoretical predictions after the peak load was exceeded. This is to be expected as the theoretical solutions assumed a horizontal plate loaded vertically with a shallow failure mechanism, whereas the failure mechanism was deep and localised to the plate for data before the peak load was reached. After the plate reached its final inclination (typically $\theta$ = 79-90°, i.e. the plate was approximately horizontal) the best agreement was with the limit equilibrium solution proposed by White *et al.* (2008). This is presented in Figure 5-49 and Figure 5-50, which compares the eccentricity groups collectively with the theoretical predictions and other experimental data reported by Trautmann *et al.* (1985), Dickin (1994), White *et al.* (2001) and Chin *et al.* (2006).

The failure mechanism for each eccentricity group at the peak load is shown in Figure 5-51. The mechanisms were found to be remarkably similar to those derived from model tests on buried pipelines reported by Cheuk *et al.* (2008), which form the basis for the White *et al.* (2008) limit equilibrium solution. At the peak load the failure mechanism can be described as a rectangular block inclined so that it is

normal to the plate orientation. The block is bounded by a pair of distributed shear zones, increasing in width as they approach the soil surface. The inclination of the shear zone relative to the rectangular block (Figure 5-51) was in the range 10 - 26°, similar to the 6 - 20° range reported by White *et al.* (2008). If the shear zone was a distinct shear plane, the angle of dilation could be directly determined from the observed mechanisms. However as the shear surface is distributed it is only clear that the soil was not dilating at an angle equal to the peak mobilised friction angle, which must be equal to or greater than the critical friction angle, $\phi_{crit}$ = 32°. Hence the normality condition ($\phi = \psi$), upon which the plasticity solution is based, is violated and the test data were not expected to agree with the Ng and Springman (1994) solution.

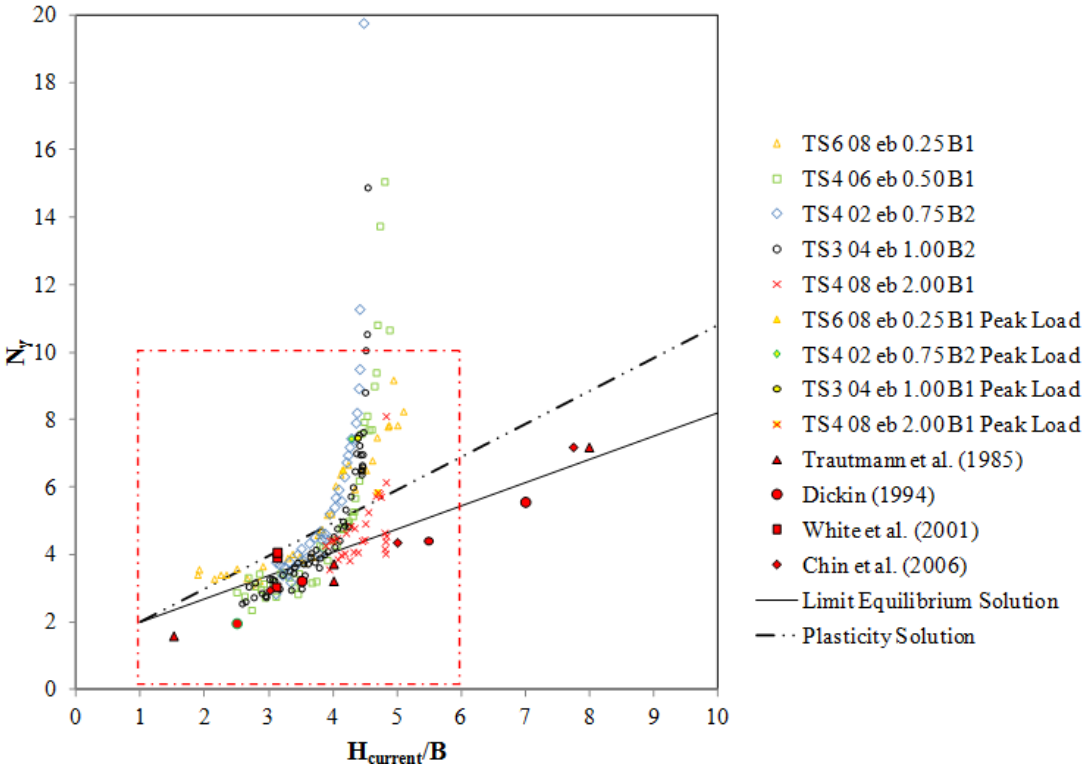


**Figure 5-49 Back Figured Capacity Factor with other experimental data and theoretical solutions (Representative Tests)**

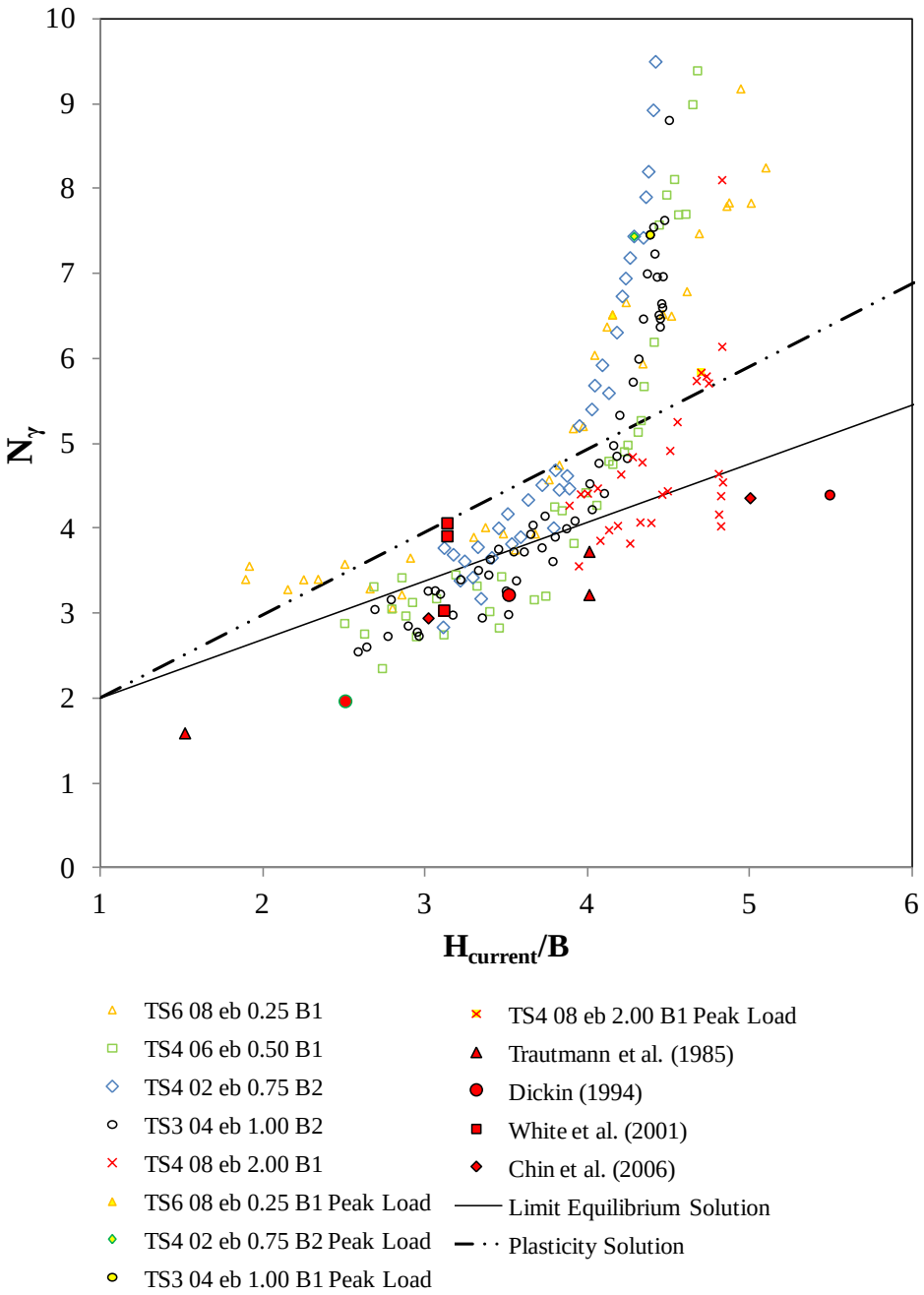


**Figure 5-50 Back Figured Capacity Factor with other experimental data and theoretical solutions (Representative Tests, Enlarged View of Figure 5-49)**

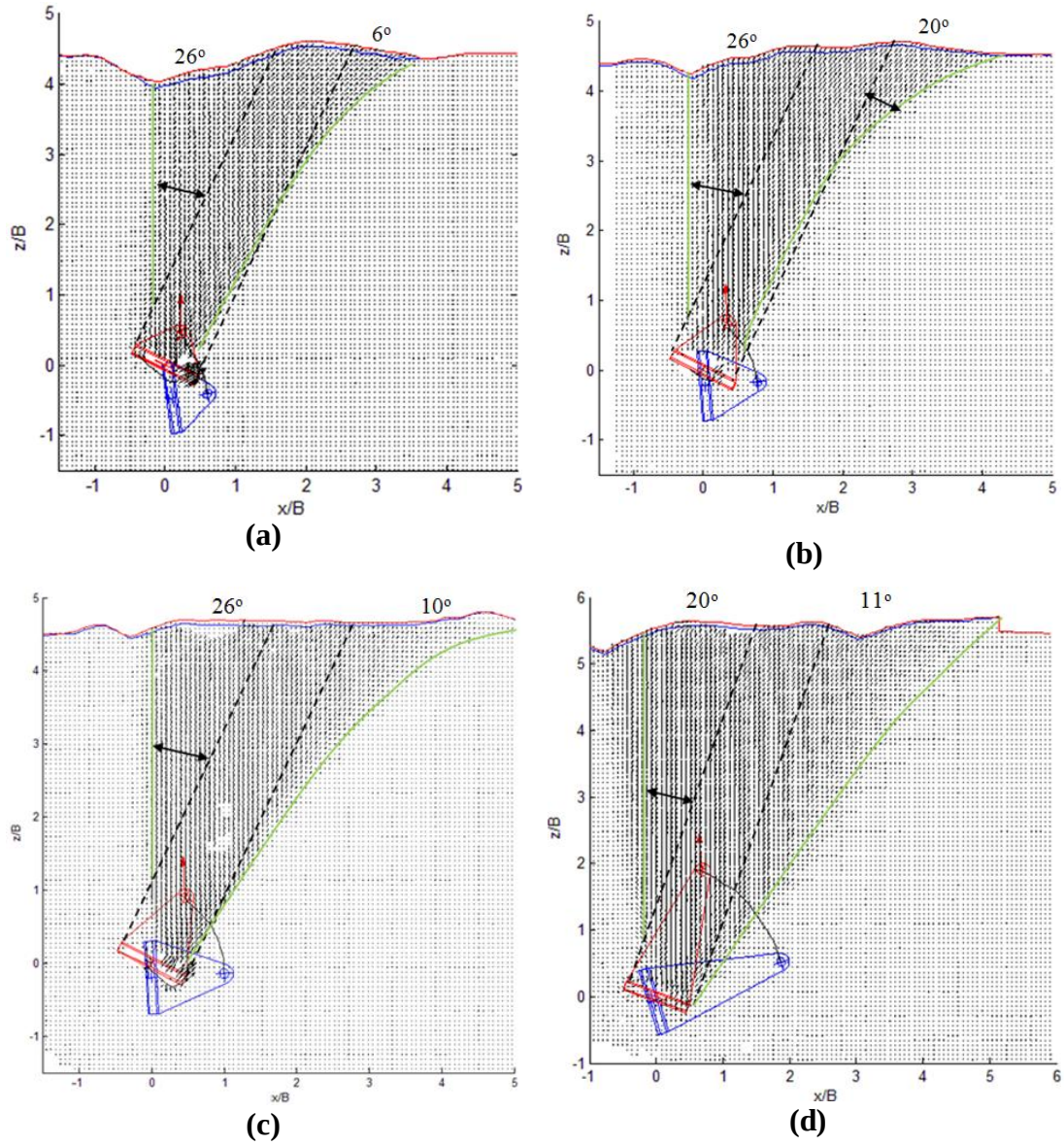


**Figure 5-51 Angle of Dilatancy at Peak Load (FMB) - PIV Analysis (a) e/B = 0.5 (b) e/B = 0.75 (c) e/B = 1 (d) e/B = 2**

## 5.4 Computation of Anchor Size

It is instructive to use the results from this study to compute the scale of plate anchor required to moor a floating renewable energy device. Although an aspect ratio of 7 was adopted for the centrifuge tests to ensure that plane strain conditions were maintained, this would be impractical for a prototype anchor and for this exercise an aspect ratio of 4 was assumed. It is assumed that the results acquired from this study are the same as a plate anchor with an L/B = 4.

Figure 5-52 has been computed using the results of this study at the peak load. This example is based on an anchor with an e/B = 1 installed at $H_{initial}/B = 5$ in dry sand with $\gamma' = 17.19kN/m^3$, $\delta z_{plate} = 0.22B$, $\Theta = 61°$ and $N_\gamma = 4.55$. Although the model test data indicated that at the peak load $N_\gamma$ is higher than calculated using the White *et al.* (2008) limit equilibrium method, for design purposes it is appropriate to use the lower bound $N_\gamma$, from the limit equilibrium method. The capacity of the anchor is presented in relation to the initial embedment depth and the anchor breadth in Figure 5-52. Load is presented in both kN and tonne.

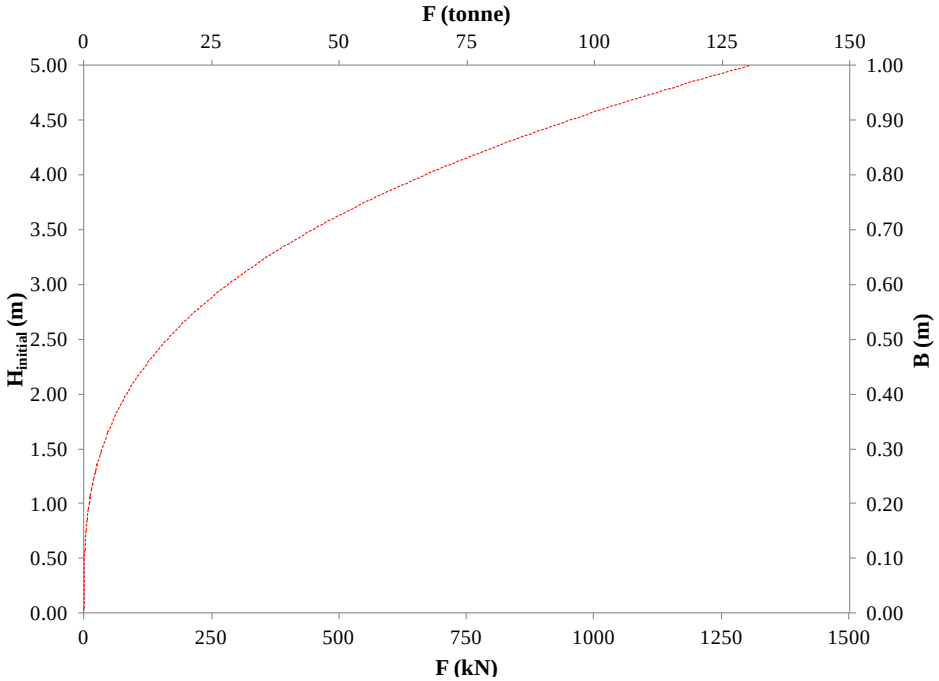


**Figure 5-52 Derived from Model Test Results at the Peak Load (L/B = 4, H/B = 4.78)**

## 5.4.1 Wave Energy Converter (WEC) Devices

### *5.4.1.1 SeaBreath*

The SeaBreath is a floating device that converts energy from oscillating water columns (waves) into electricity (Figure 5-53). The SeaBreath sits perpendicular to the wave direction. As the waves move beneath the SeaBreath, the SeaBreath moves and a pressure differential is created between the compressed and decompressed air in the chamber which causes the turbine to rotate. Marine Renewables Infrastructure

Network for emerging Energy Technologies (2014) give a detailed review of the functions and the principles behind the SeaBreath.

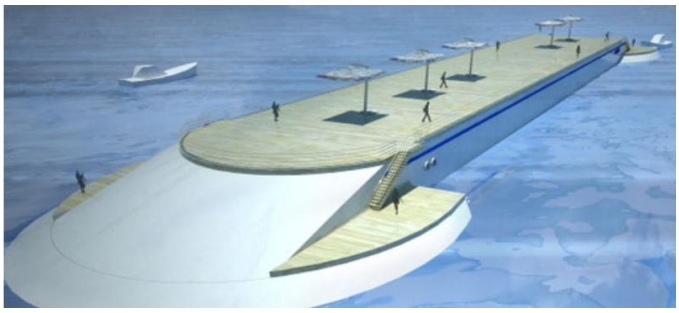

**Figure 5-53 Schematic of SeaBreath (after Martinelli *et al.* 2012)**

Martinelli *et al.* (2012) reported that a 37m long SeaBreath is to be deployed in water depths of approximately 16m. Using a significant wave height, $H_s$ = 5m, they have reported that the expected loading on the mooring system using two anchors is 500kN per anchor.

Using the geometry of the anchor described in Section 5.4, two anchors with B = 0.73m installed at $H_{initial}$ = 3.63m would meet the mooring needs of the SeaBreath (Figure 5-54).

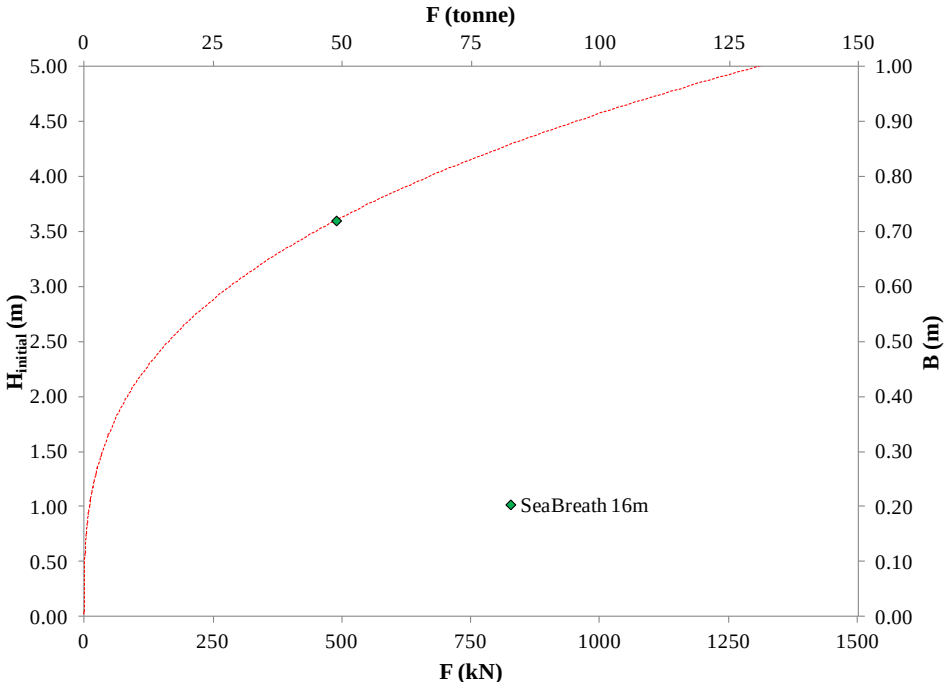


**Figure 5-54 SeaBreath (data from Martinelli *et al.* 2012)**

### *5.4.1.2 Wave Dragon*

The Wave Dragon (Sorensen *et al.,* 2005) is a WEC that utilises low head hydro turbines to generate electricity from the ocean. Water that is splashed into the reservoir creates a head of water in the reservoir that rotates the turbines to generate electricity. A schematic of the Wave Dragon and the mooring arrangement is shown in Figure 5-55. A full scale commercial unit can span an area of 150 m × 260 m. The Wave Dragon is described in more detail by Sorensen *et al.* (2005)

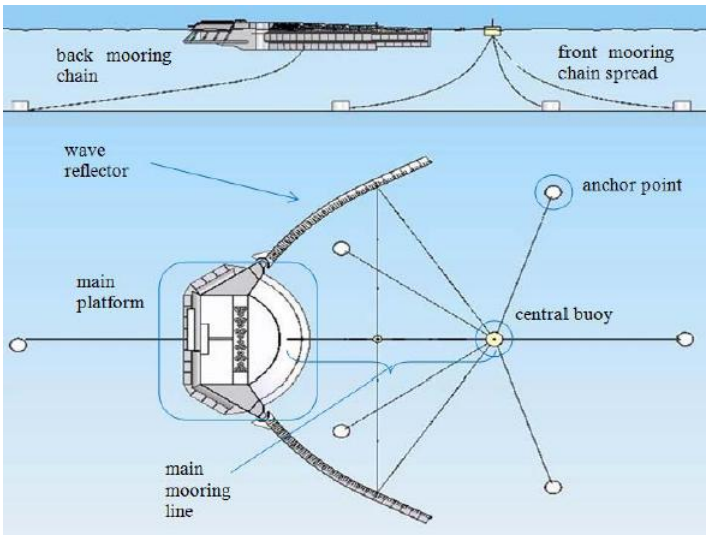


**Figure 5-55 Conceptual Mooring System of Wave Dragon (after Parmeggiani *et al.* 2013)**

Parmeggiani *et al.* (2013) have used 1: 50 reduced scale model tests to investigate the performance of the Wave Dragon. The maximum wave height used during this investigation was 0.15m; at full scale this is the equivalent to a wave height of 7.45m. They have scaled up the results of these tests to determine the required mooring capacity of a full scale commercial unit.

The influence of a range of environmental scenarios has been examined on the mooring line of the Wave Dragon at 30m (Parmeggiani *et al.,* 2013). Parmeggiani *et al.* (2013) reported that the most extreme conditions for a full scale model ranged from 66 – 210kN.

Using the geometry of the anchor described in Section 5.4, the lower bound range of mooring loads (66 kN) could be handled by an anchor with B = 0.37m installed at $H_{initial}$ = 1.85m, whereas the upper bound mooring load would require an anchor with B = 0.55m installed at $H_{initial}$ = 2.73m (Figure 5-56).

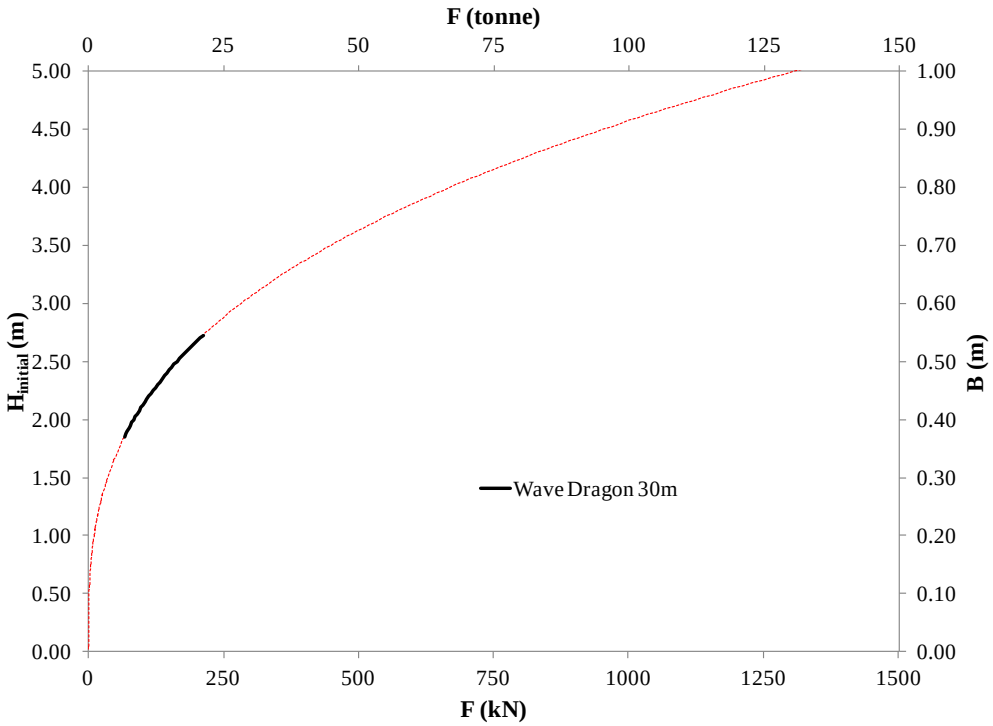


**Figure 5-56 Wave Dragon 30m (after Parmeggiani *et al.* 2013)**

## 5.4.2 Floating Offshore Wind Turbines (FOWTs)

Sclavounos *et al.* (2010) have conducted an investigation on the best mooring system for 3MW and 5MW wind turbines (Figure 5-57). They have adopted methods used by the oil and gas industry, with wind load experimental data from wind turbine reduced scale models and numerical simulations used to mimic wave heights. In this analysis they have investigated the influence of wave heights up to 14m in water depths ranging from 50 to 150m for Tension Leg Platform (TLP) and taut leg buoy mooring systems. The TLP is moored by vertical tethers and the taut leg buoy is moored using taught mooring lines. Both systems use gravity anchors as their anchorage. Sclavounos *et al.* (2010) have used a combination of the worst case scenarios for static and dynamic responses.

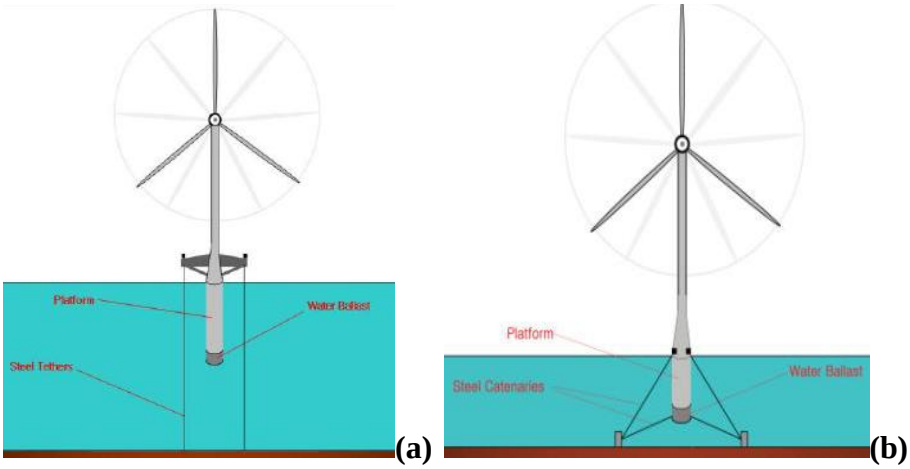


(a) (b)

**Figure 5-57 (a) Tension Leg Platform (b) Taut Leg Buoy (after Sclavounos *et al.* 2010)**

In this study Sclavounos *et al.* (2010) have reported that the best mooring system for water depths exceeding 50m is the TLP. The results from the analyses conducted by Sclavounos *et al.* (2010) for a TLP are presented in Figure 5-58. Figure 5-58 (b) shows that an increase in water depth does not influence the anchor tension for a 5MW wind turbine whilst, for a 3MW turbine the loading is dependent on the water depth, i.e. as the water depth increases the loading on the anchor decreases.

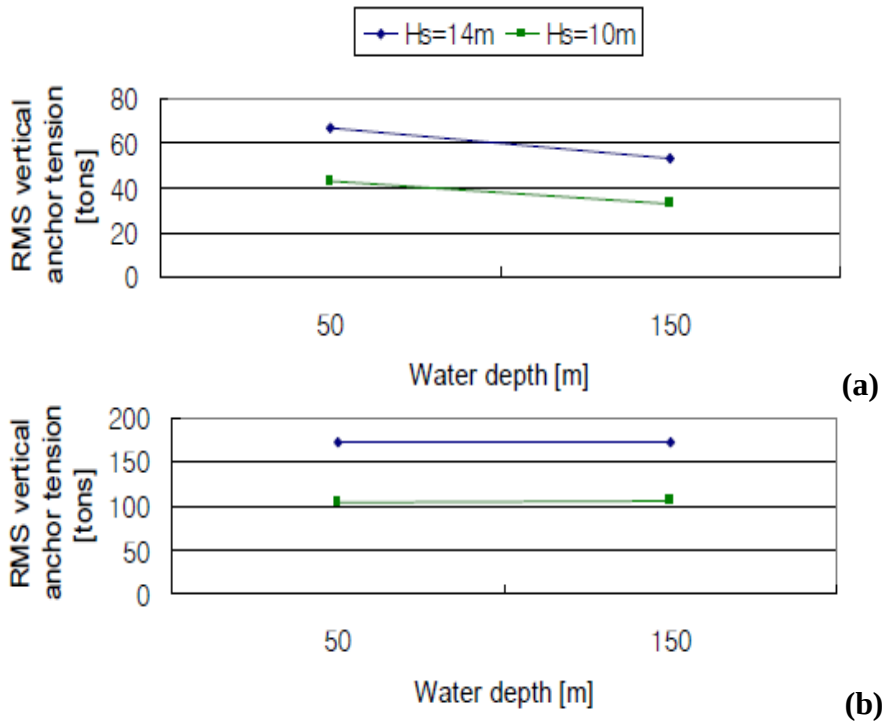


**Figure 5-58 Vertical Anchor Tension of Windward Tether of (a) 3MW (b) 5MW Tension Leg Platform (after Sclavounos *et al.* 2010)**

Discussion

The anchor sizes and embedment depths required to handle these mooring loads are shown in Figure 5-59 and tabulated in Table 5-3. For the most onerous design scenario for a 3MW turbine, the mooring loads would require an anchor with B = 0.8m, installed at $H_{initial}$ = 4m. For a 5 MW turbine, the most onerous design scenario would require an anchor with B = 1.07m, installed at $H_{initial}$ = 5.35. These dimensions are illustrated in Figure 5-59.

**Table 5-3 Wind Turbine Capacity and Anchor Dimensions**

| **3MW Wind Turbine** | | | | |
|---|---|---|---|---|
| **Water Depth** | **$H_s$** | **Capacity** | **$H_{initial}$** | **B** |
| **(m)** | **(m)** | **(kN)** | **(m)** | **(m)** |
| 150 | 10 | 350 | 3.23 | 0.65 |
| 50 | 10 | 420 | 3.43 | 0.69 |
| 150 | 14 | 552 | 3.75 | 0.75 |
| 50 | 14 | 655 | 3.98 | 0.80 |
| **5MW Wind Turbine** | | | | |
| **Water Depth** | **$H_s$** | **Capacity** | **$H_{initial}$** | **B** |
| **(m)** | **(m)** | **(kN)** | **(m)** | **(m)** |
| 50-150 | 10 | 1002 | 4.58 | 0.92 |
| 50-150 | 14 | 1602 | 5.35 | 1.07 |

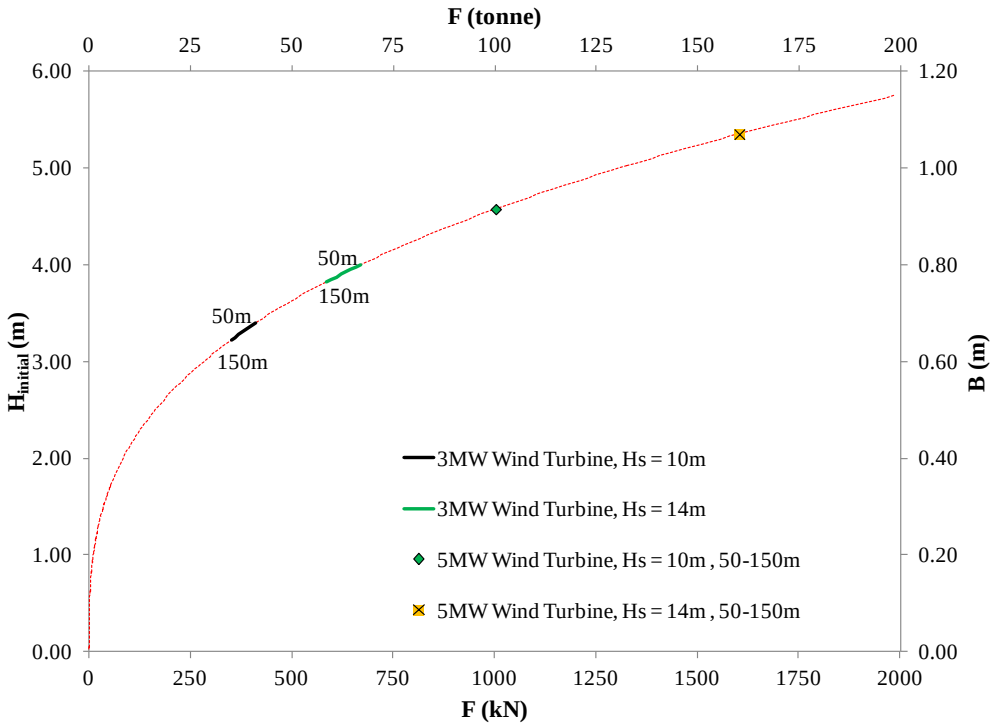


**Figure 5-59 3MW and 5MW Wind Turbine (data from Sclavounos *et al.* 2010)**

## 5.5 Chapter Summary

This chapter has considered the centrifuge data presented in Chapter 4 in terms of the loss in embedment undergone through the keying process and the capacity of the anchor post-keying. The analyses presented in this chapter results in the following findings:

- Loss in anchor embedment during keying (as quantified from the initial anchor position to the position at peak anchor capacity) was found to reduce with increasing anchor padeye eccentricity. The dependence of loss in embedment on the padeye eccentricity is very similar to that reported for clay and can be quantified using a modified form of the loss in embedment expression proposed by Wang *et al.* (2011).
- Minimal loss in embedment during keying (and hence highest potential anchor capacity) can be achieved with an anchor with a padeye eccentricity equal to at least the anchor breadth.
- The peak anchor capacity was found not to correspond with the final angle of rotation. The peak capacity occurred at a plate inclination, $\Theta$ = 50° to 80°, increasing as the eccentricity ratio increased. The final angle of rotation was

found to occur post peak when the plate had underwent excessive displacement. The final angle of rotation increased as the eccentricity ratio increased.

- PIV analyses convincingly demonstrated that the peak load corresponds with a transition in failure mechanism, from a deep localised mechanism to a shallow mechanism that extends to the soil surface. This observation has explained why the peak load does not correspond with the final orientation of the plate.
- The anchor capacity measured in the centrifuge tests was back analysed as the dimensionless capacity factor, $N_\gamma$. The variation in $N_\gamma$ with anchor embedment depth has compared well with other published experimental data for plate anchors and pipelines (subjected to vertical uplift), but only after the peak anchor capacity is exceeded and the anchor behaves like a horizontally oriented anchor subjected to vertical loading.
- The PIV analyses has shown that for each anchor eccentricity group, the inclination of the slip planes in the failure mechanism are at an angle which is much lower than would be reasonable for a mobilised friction angle. This clearly shows that the normality condition, in which the dilation angle and the friction angle are equal, was not met in these tests. This observation, as first shown by Cheuk *et al.* (2008), forms the basis for the White *et al.* (2008) limit equilibrium solution for predicting the capacity of pipelines and plate anchors in sand (subjected to vertical loading). As expected, predictions obtained using the White *et al.* (2008) limit equilibrium method agreed well with the centrifuge data reported here for loads greater than the peak load (i.e. when the anchor is approximately horizontal and vertically loaded).

# CHAPTER 6.0
# CONCLUSIONS AND RECOMMENDATIONS FOR FURTHER RESEARCH

## 6.1 Introduction

The primary focus of this study was to assess the viability of the SEPLA as an anchoring solution for offshore renewable energy devices. This study focused on the most uncertain aspect of the SEPLA design, the loss of embedment of the plate anchor during the keying process. To gain an understanding of this, 37 model anchor tests were conducted in dense silica sand in a geotechnical centrifuge at 30g. Most of the tests were conducted adjacent to a Perspex window to facilitate observation and quantification of the keying response, with other tests conducted away from boundary walls to quantify the friction developed at the anchor ends. Particle Image Velocimetry (PIV) was employed to identify the failure mechanism at various stages during the tests.

This chapter gives a brief overview of the main findings of this study and outlines areas for additional research identified during this study.

## 6.2 Project Summary

This study focused on the keying behaviour and the capacity of plate anchors in sand. To date there is no directly comparable literature. In the literature review, the keying of plate anchors in clay and anchor capacity factor for anchors in sand were examined. The primary finding in the first section was the link between eccentricity ratio and loss of embedment. When the anchor breadth is greater than or equals one, the loss of embedment is almost negligible. The strong relationship between anchor capacity with sample density, anchor geometry and embedment ratio was identified.

Model scale anchor tests were conducted using the geotechnical centrifuge in dense silica sands ($I_D$ = 89%). Six anchor tests with the same geometry with varying eccentricity ratios ($0.25 < e/B > 2$) were used. To facilitate observation of the anchor orientation and quantification of the loss in embedment during the test, anchor tests

were conducted adjacent to a Perspex panel on the centrifuge strongbox. Vertical loading was achieved by pulling a mooring line attached to the anchor padeye at a constant velocity (1mm/s) above the plate centre. The location and orientation of the anchor during each anchor test was captured using a high resolution digital camera mounted directly in front of the Perspex panel. Particle image velocimetry was employed to reveal the failure mechanisms during the keying process.

## 6.3 Main Findings

### 6.3.1 Keying

The analysis conducted on anchor keying included correlating the load to the orientation of the plate anchor, analysis of the padeye trajectory and analysis of the failure mechanism using PIV. The main findings in this section are summarised below.

- Loss in anchor embedment during keying (as quantified from the initial anchor position to the position at peak anchor capacity) reduces with increasing anchor padeye eccentricity. The dependence of loss in embedment on the padeye eccentricity is very similar to that reported for clay and can be quantified using a modified form of the loss in embedment expression proposed by Wang *et al.* (2011).
- Minimal loss in embedment during keying (and hence highest potential anchor capacity) can be achieved with an anchor with a padeye eccentricity equal to at least the anchor breadth.
- Contrary to prior thinking, the peak anchor capacity did not correspond with the final angle of rotation, with the load direction normal to the orientation of the plate. Rather, the peak capacity occurred at a plate inclination, $\Theta = 50°$ to 80°, increasing as the eccentricity ratio increased.
- PIV analyses convincingly demonstrate that the peak load corresponds with a transition in failure mechanism, from a deep localised mechanism to a shallow mechanism that extends to the soil surface. This observation explains why the peak load does not correspond with the final orientation of the plate.

### 6.3.2 Capacity

The anchor capacity measured in the centrifuge tests was back analysed as the dimensionless capacity factor, $N_\gamma$. The variation in $N_\gamma$ with anchor embedment depth compares well with other published experimental data for plate anchors and pipelines (subjected to vertical uplift), but only when after the peak anchor capacity is exceeded and the anchor behaves like a horizontally oriented anchor subjected to vertical loading.

The PIV analyses shows that for each anchor eccentricity group, the failure mechanism at the peak load is remarkably similar to that derived from model tests on buried pipelines reported by Cheuk *et al.* (2008). In particular the inclination of the slip planes in both the tests reported here and in those reported by Cheuk *et al.* (2008) are at an angle which is much lower than would be reasonable for a mobilised friction angle. This clearly shows that the normality condition, in which the dilation angle and the friction angle are equal, was not met in these tests. This observation, as first shown by Cheuk *et al.* (2008), forms the basis for the White *et al.* (2008) limit equilibrium solution for predicting the capacity of pipelines and plate anchors in sand (subjected to vertical loading). As expected, predictions obtained using the White *et al.* (2008) limit equilibrium method agree well with the centrifuge data reported here for loads greater than the peak load (i.e. when the anchor is approximately horizontal and vertically loaded).

## 6.4 Recommendations for Further Work

The work reported in this thesis is limited to a single aspect ratio and soil density. It would clearly be useful to extend the research to consider lower aspect ratios (closer to those that could practically be managed in practice) and the effect of soil density.

The initial embedment depth was limited to five times the anchor breadth. At the peak load the failure mechanism was shallow. It would be useful to conduct further tests where the initial embedment depth was greater to ascertain what embedment depth ratio would be required to generate a deep failure mechanism. This would evidently result in much higher anchor capacity.

If the plate anchor is to be installed using a suction caisson (as with the original SEPLA concept), then work is required to assess the viability of this installation method in sand. Issues that would need to be considered include the effect of the installation process on the sand density and the limiting caisson aspect ratio (height/diameter) that can be installed in sand.

Anchors for floating renewable energy devices will be subjected to continuous cyclic loading. Further work is recommended to assess the influence of cyclic loading on the plate anchor.

## References


ASTM D 4253-00 (2000). *Standard Test Methods for Maximum Index Density and Unit Weight of Soils Using a Vibratory Table*. Annual Book of ASTM Standards. West Conshohocken, PA. 04 (08).

Aubeny CP, Murff DJ and Roesset JM. (2001). Geotechnical issues in deep and ultra deep waters. *International Journal of Geo-mechanics* **1** (2): 225– 247.

Bolton MD. (1986). The strength and dilatancy of sands. *Géotechnique*, 36(1), 65–78.

Bolton MD, Gui MW, Garnier J, Corte JF, Bagge G, Laue J and Renzi R. (1999). Centrifuge cone penetration tests in sand. *Géotechnique* **49**: 543–552.

Bransby MF, Brown M, Hatherly A and Lauder K. (2010). Pipeline plough performance in sand waves. Part 1: model testing. *Canadian Geotechnical Journal* **47**: 49–64.

Broadbent T and Sons Limited. (2010). *Operating Manual for GT6/0.75 Geotechnical Beam Centrifuge H83111-OM*, Issue 01, November, Huddersfield, England.

BS 1377-2 1990. *Methods of test for Soils for civil engineering purposes - Part 2: Classification tests*. British Standards Institute.

Cassidy MJ, Gaudin C, Randolph MF, Wong PC, Wang D and Tian Y. (2012). A plasticity model to assess the keying of plate anchors. *Geotechnique*, **62** (9): 825-836.

Chin EL, Craig WH and Cruickshank M. (2006). Uplift resistance of pipelines buried in cohesionless soil. *Proceedings of the 6th International Conference on Physical Modelling in Geotechnics*. Vol. 1, Taylor & Francis Group, London, 723–728.

Das BM, Seeley GR and Das SC. (1977). Ultimate resistance of deep vertical anchor in sand. *Soils and Foundations*, **17** (2): 52-56.

Dickin EA. (1988). Uplift behaviour of horizontal anchor plates in sand. *Journal of Geotechnical Engineering* **114** (11): 1300-1317.

Dickin EA. (1994). Uplift resistance of buried pipelines in sand. *Soils and Foundations* **34**: 41–48.

Ernst & Young Global Ltd. 2013 'Rising Tide: Global trends in the emerging ocean energy market', accessed 6th September 2014, from http://www.ey.com/Publication/vwLUAssets/EY-Ocean-energy-Rising-tide-2013/$FILE/EY-Ocean-energy-Rising-tide-2013.pdf

EWEA 2009, 'The Economics of Wind Energy', By the European Wind Energy Association, accessed 2nd August 2013, from http://www.ewea.org/fileadmin/ewea_documents/documents/publications/reports/Economics_of_Wind_Main_Report_FINAL-lr.pdf

Fitzgerald J. (2009). "Position mooring of wave energy converters". PhD Thesis, Chalmers University of Technology.

Gaudin C, Randolph MF and O'Loughlin CD. (2006). New insights from model tests of foundation and anchoring systems in offshore geo-mechanics. *Proceeding of the 6th International Conference of Physical Modelling in Geotechnics*, Hong Kong **1**:47–61.

Gaudin C, Tham KH and Ouahsine S. (2009a). Keying of plate anchors in NC clay under inclined loading. *International Journal of Offshore and Polar Engineering.* 19(2): 1-8

Gaudin C, White DJ, Boylan N, Breen J, Brown T, De Catania S and Hortin P. (2009b). A wireless high-speed data acquisition system for geotechnical centrifuge model testing. *Measurement Science and Technology*, 20(9): 1 – 11.

Gourvenec S and O' Loughlin C. (2006). Drum centrifuge tests of shallow skirted foundations on soft clay, *6th International Conference on Physical Modelling in Geotechnics*, London, 1, pp. 645-650.

Gui MW, Bolton MD, Garnier J, Corte JF, Bagge G, Laue J and Renzi R. (1998). Guidelines for cone penetration tests in sand. *Proceeding of the International Centrifuge 98,* Rotterdam, 155 -160.

Ilamparuthi K, Dickin EA and Muthukrisnaiah K. (2002). Experimental investigation of the uplift behaviour of circular plate anchors embedded in sand. *Canadian Geotechnical Journal*, **39** (3), 648- 64.

Irish Marine Institute (2013). 'Galway Bay Wave Energy Test Site', accessed 1st August 2013, from http://www.marine.ie/home/aboutus/organisationstaff/researchfacilities/Ocean+Energy+Test+Site.htm?mode=printerfriendly

JoJo Tanks (2013). Blog Image: Offshore Wind Farm – Wind Energy', accessed 31 July 2013, from http://jojotanks.co.za/blog/wp-content/uploads/2013/07/Offshore-Wind-Farm-wind-energy.png

Lauder K. (2010). The performance of pipeline ploughs. *PhD Thesis*, University of Dundee

Marine Renewables Infrastructure Network for emerging Energy Technologies (2014). 'Infrastructure Access Report– Multi - chamber oscillating water column device for harvesting Ocean Renewable Energy', accessed 9th September 2014, from http://www.fp7-marinet.eu/public/docs/Infrastructure%20Access%20Report_MORE.pdf

Martinelli L, Ruol P and Cortellazzo G. (2012). On mooring design of wave energy converters: the SeaBreath application. *Proceedings of the 33 rd International Conference on Coastal Engineering*, Santander, Spain

Merifield RS & Sloan SW. (2006). The ultimate pullout capacity of anchors in frictional soils. *Canadian Geotechnical Journal* **43**: 852–868.

Merifield RS. (2002). Numerical Modelling of Soil Anchors. *PhD Thesis*, University of Newcastle, United Kingdom

Murray EJ & Geddes JD. (1987). Uplift of anchor plates in sand. *Journal of Geotechnical Engineering* **113**: 202–215.

Musial W, Butterfield S and Ram B. (2006). Energy from offshore wind: preprint. *In Offshore Technology Conference, Houston*, NREL/CP-500-39450.

Neubecker, S. R., and Randolph, M. F. (1995). Profile and frictional capacity of embedded anchor chains. Journal of Geotechnical Engineering, **121**(11), 797–803.

Ng CWW & Springman SM. (1994). Uplift resistance of buried pipelines in granular materials. *Proceeding of the International Conference. Centrifuge 1994*, Singapore 753– 758.

O'Loughlin CD & Barron B. (2012). Capacity and keying response of plate anchors in sand. *Proceedings from the 7th International Conference on Offshore Site Investigation and Geotechnics,* London, UK 1: 649-656

O'Loughlin CD, Lowmass A, Gaudin C and Randolph MF. (2006). Physical modelling to assess keying characteristics of plate anchors. *Proceedings of the 6th International Conference of Physical Modelling in Geotechnics*, Hong Kong. **1**: 659–665.

O'Loughlin CD, Naughton P, Baker N and Ainsworth A. (2010). Establishing a beam centrifuge facility at the Institute of Technology, Sligo, Ireland. *Proceedings of the 7th International Conference of Physical Modelling in Geotechnics*, Zurich, Switzerland.

Ocean Energy (2013). 'Ocean Energy – A World of Power: A New Power Generation Platform', accessed 1st August 2013, from http://www.oceanenergy.ie/oe-technology/platform.html

Ovesen NK. (1981). Centrifuge tests of the uplift capacity of anchors. *Proceedings of the 10th International Conference of Soil Mechanics and Foundation Engineering*, Stockholm **1:**717–722.

Parmeggiani S, Kofoed JP and Friis-Madsen E. (2013). Experimental study related to the mooring design for the 1.5 MW Wave Dragon WEC demonstrator at DanWEC. E*nergies*, **6**: 1863–1886.

Pelamis (2013). Pelamis Wave Power: Image Library, accessed 1st August 2013, from http://www.pelamiswave.com/image-library

Rowe RK and Davis H. (1982). The behaviour of anchor plates in sand. *Géotechnique* **32**: 25–41.

Schaminee PEL, Zorn NF and Schotman GJM. (1990). Soil response for pipeline upheaval buckling analyses: full-scale laboratory tests and modelling, *Proceedings of the 22nd Offshore Technology Conference*, OTC 6486:563-572.

Sclavounos P, Lee S, DiPietro J, Potenza G, Caramuscio P and Michele GD. (2010). Floating offshore wind turbines: Tension leg platform taught leg buoy concepts supporting 3-5 MW wind turbines. *In Proceedings of European wind energy conference, European Wind Energy Conference,* Warsaw (Poland)

Song Z, Hu Y, O'Loughlin CD and Randolph MF. (2009). Loss in anchor embedment during plate anchor keying in clay. *Journal of Geotechnical and Geoenvironmental Engineering* **135**: 1475– 1485.

Song Z, Hu Y, Wang D, O'Loughlin CD. (2006). Pullout capacity and rotational behaviour of square anchors. *Proceedings of 6th International Conference on Physical Modelling in Geotechnics*, Hong Kong (2):1325–31.

Sorensen H, Friis-Madsen E, Christensen L, Kofoed JP, Frigaard P and Knapp W. (2005). The results of two years testing in real sea of Wave Dragon. *6th European Wave and Tidal Energy Conference*, Glasgow: 481–487.

Taylor, RN. (1995). Geotechnical Centrifuge Technology. *Blackie Academic and Professional*.

Trautmann CH, O'Rourke TD and Kulhawy FH. (1985). Uplift force-displacement response of buried pipe. *Journal of Geotechnical Engineering* **111**:1061–1076.

Wang D, Hu Y and Randolph M. (2011). Keying of Rectangular Plate Anchors in Normally Consolidated Clays. *Journal of Geotechnical and Geoenvironmental Engineering* **137**(12): 1244–1253.

White DJ, Barefoot AJ and Bolton MD. (2001). Centrifuge modelling of upheaval buckling in sand. *International Journal of Physical Modelling in Geotechnics*, **2**(1): 19–28.

White DJ, Cheuk CY and Bolton MD. (2008). The uplift resistance of pipes and plate anchors buried in sand. *Géotechnique* **58**: 771–779.

White DJ, Take WA and Bolton MD. (2003). Soil deformation measurement using particle image velocimetry (PIV) and photogrammetry. *Géotechnique* **53**: 619–631.

Wilde B, Treu H and Fulton T. (2001). Field testing of suction embedded plate anchors. *Proceeding of the 11th International offshore and Polar Engineering Conference, International Society of Offshore and Polar Engineers*, Mountain View, CA, 544–551.

Zhao J, Zhang L and Wu H. (2012). Motion performance and mooring system of a floating offshore wind turbine. *Journal of Marine Science and Application* 11: 328-334.

# Appendix A

# Appendix A

**Eccentricity Ratio of 0.25**

Table 8-1 TS6 08 eb 0.25 B1

| **Load** | **$\delta z_{line}/B$** | **Θ** | **$\delta z_{plate}/B$** | **$\delta x/B$** |
|---|---|---|---|---|
| **(kN)** | **(-)** | **(°)** | **(-)** | **(-)** |
| 8 | 0.02 | 8 | 0 | 0 |
| 155 | 0.12 | 13 | 0.04 | 0.02 |
| 314 | 0.27 | 15 | 0.14 | 0 |
| 433 | 0.37 | 23 | 0.23 | 0.02 |
| 538 | 0.47 | 24 | 0.29 | 0.04 |
| 580 | 0.52 | 32 | 0.36 | 0.05 |
| 609 | 0.57 | 34 | 0.38 | 0.05 |
| 660 | 0.82 | 41 | 0.55 | 0.17 |
| 673 | 0.92 | 48 | 0.63 | 0.19 |
| 686 | 1.07 | 54 | 0.72 | 0.29 |
| 687 | 1.17 | 55 | 0.77 | 0.35 |
| 618 | 1.32 | 56 | 0.90 | 0.48 |
| 680 | 1.37 | 57 | 1.00 | 0.50 |
| 682 | 1.47 | 61 | 1.08 | 0.54 |
| 677 | 1.52 | 64 | 1.12 | 0.58 |
| 643 | 1.57 | 66 | 1.19 | 0.61 |
| 540 | 1.62 | 65 | 1.26 | 0.63 |
| 533 | 1.67 | 66 | 1.33 | 0.63 |
| 486 | 1.71 | 68 | 1.41 | 0.67 |
| 466 | 1.76 | 70 | 1.48 | 0.65 |
| 395 | 1.86 | 71 | 1.56 | 0.67 |

| Load | $\delta z_{line}/B$ | Θ | $\delta z_{plate}/B$ | $\delta x/B$ |
|---|---|---|---|---|
| (kN) | (-) | (°) | (-) | (-) |
| 372 | 1.96 | 76 | 1.68 | 0.68 |
| 383 | 2.01 | 76 | 1.76 | 0.71 |
| 383 | 2.11 | 79 | 1.87 | 0.74 |
| 363 | 2.16 | 79 | 1.94 | 0.74 |
| 303 | 2.56 | 82 | 2.33 | 0.81 |
| 261 | 2.71 | 80 | 2.38 | 0.82 |
| 244 | 2.79 | 81 | 2.44 | 0.84 |
| 250 | 2.89 | 83 | 2.58 | 0.88 |
| 256 | 2.99 | 82 | 2.73 | 0.90 |
| 226 | 3.14 | 80 | 2.90 | 0.94 |
| 217 | 3.19 | 80 | 2.99 | 0.95 |
| 201 | 3.24 | 81 | 3.09 | 0.97 |
| 193 | 3.34 | 80 | 3.32 | 0.98 |
| 183 | 3.39 | 81 | 3.35 | 0.97 |

**Eccentricity Ratio of 0.25**

Table 8-2 TS7 02 eb 0.25 B1

| **F** | **$\delta z_{line}/B$** | **Θ** | **$\delta z_{plate}/B$** | **$\delta x/B$** |
|---|---|---|---|---|
| **(kN)** | **(-)** | **(°)** | **(-)** | **(-)** |
| 0 | 0 | 0 | 0 | 0 |
| 346 | 0.33 | 7 | 0.20 | 0.01 |
| 406 | 0.43 | 11 | 0.31 | 0.03 |
| 496 | 0.63 | 23 | 0.46 | 0.07 |
| 521 | 0.73 | 25 | 0.55 | 0.10 |
| 530 | 0.80 | 34 | 0.58 | 0.13 |
| 545 | 0.93 | 39 | 0.68 | 0.18 |
| 561 | 1.10 | 43 | 0.85 | 0.27 |
| 566 | 1.13 | 44 | 0.88 | 0.30 |
| 566 | 1.17 | 46 | 0.92 | 0.32 |
| 557 | 1.23 | 47 | 0.99 | 0.37 |
| 518 | 1.30 | 56 | 1.01 | 0.41 |
| 436 | 1.33 | 57 | 1.09 | 0.46 |
| 560 | 1.37 | 58 | 1.12 | 0.48 |
| 576 | 1.40 | 56 | 1.17 | 0.48 |
| 393 | 1.43 | 58 | 1.21 | 0.51 |
| 530 | 1.47 | 60 | 1.25 | 0.53 |

**Eccentricity Ratio of 0.25**

Table 8-3 TS7 04 eb 0.25 B1

| **F** | **$\delta z_{line}/B$** | **Θ** | **$\delta z_{plate}/B$** | **$\delta x/B$** |
|---|---|---|---|---|
| **(kN)** | **(-)** | **(°)** | **(-)** | **(-)** |
| 0 | 0 | 10 | 0 | 0 |
| 592 | 0.50 | 29 | 0.09 | 0.04 |
| 649 | 0.80 | 42 | 0.30 | 0.16 |
| 663 | 1.00 | 49 | 0.49 | 0.27 |
| 648 | 1.10 | 53 | 0.62 | 0.38 |
| 627 | 1.20 | 56 | 0.73 | 0.46 |
| 572 | 1.23 | 56 | 0.77 | 0.48 |
| 591 | 1.26 | 60 | 0.81 | 0.53 |
| 663 | 1.30 | 59 | 0.88 | 0.55 |
| 630 | 1.33 | 58 | 0.94 | 0.56 |
| 662 | 1.36 | 60 | 1.00 | 0.61 |
| 598 | 1.40 | 60 | 1.08 | 0.64 |
| 602 | 1.43 | 66 | 1.13 | 0.67 |
| 581 | 1.46 | 64 | 1.17 | 0.70 |
| 565 | 1.5 | 65 | 1.26 | 0.71 |
| 463 | 1.60 | 67 | 1.45 | 0.78 |

**Eccentricity Ratio of 0.25**

Table 8-4 TS7 05 eb 0.25 B1

| **F** | **$\delta z_{line}/B$** | **Θ** | **$\delta z_{plate}/B$** | **$\delta x/B$** |
|---|---|---|---|---|
| **(kN)** | **(-)** | **(°)** | **(-)** | **(-)** |
| 0 | 0 | 13 | 0 | 0 |
| 566 | 0.53 | 29 | 0.40 | 0.12 |
| 610 | 0.73 | 38 | 0.55 | 0.17 |
| 618 | 0.83 | 43 | 0.68 | 0.25 |
| 616 | 0.87 | 44 | 0.71 | 0.27 |
| 622 | 0.90 | 44 | 0.76 | 0.29 |
| 625 | 0.93 | 45 | 0.81 | 0.35 |
| 626 | 0.97 | 49 | 0.84 | 0.37 |
| 627 | 1.00 | 49 | 0.89 | 0.40 |
| 625 | 1.03 | 51 | 0.93 | 0.43 |
| 618 | 1.07 | 51 | 0.97 | 0.45 |
| 606 | 1.10 | 50 | 1.05 | 0.50 |

**Eccentricity Ratio of 0.5**

Table 8-5 TS4 06 eb 0.50 B1

| **F** | **$\delta z_{line}/B$** | **Θ** | **$\delta z_{plate}/B$** | **$\delta x/B$** |
|---|---|---|---|---|
| **(kN)** | **(-)** | **(°)** | **(-)** | **(-)** |
| 0 | 0 | 8 | 0 | 0 |
| 213 | 0.19 | 8 | 0.03 | 0.01 |
| 451 | 0.36 | 13 | 0.11 | 0.01 |
| 671 | 0.56 | 21 | 0.18 | 0.02 |
| 719 | 0.66 | 27 | 0.21 | 0.03 |
| 729 | 0.73 | 30 | 0.22 | 0.03 |
| 738 | 0.79 | 36 | 0.24 | 0.04 |
| 753 | 0.86 | 39 | 0.27 | 0.07 |
| 791 | 0.99 | 51 | 0.31 | 0.07 |
| 816 | 1.06 | 54 | 0.36 | 0.10 |
| 888 | 1.09 | 57 | 0.38 | 0.07 |
| 881 | 1.16 | 59 | 0.43 | 0.09 |
| 862 | 1.19 | 63 | 0.47 | 0.10 |
| 710 | 1.23 | 65 | 0.51 | 0.09 |
| 650 | 1.26 | 66 | 0.57 | 0.10 |
| 613 | 1.29 | 69 | 0.59 | 0.10 |
| 601 | 1.33 | 71 | 0.61 | 0.07 |
| 581 | 1.36 | 73 | 0.67 | 0.08 |
| 573 | 1.39 | 74 | 0.69 | 0.07 |
| 549 | 1.43 | 75 | 0.76 | 0.08 |
| 554 | 1.46 | 76 | 0.79 | 0.09 |

| F | $\delta z_{line}/B$ | Θ | $\delta z_{plate}/B$ | $\delta x/B$ |
|---|---|---|---|---|
| (kN) | (-) | (°) | (-) | (-) |
| 490 | 1.56 | 79 | 0.86 | 0.08 |
| 501 | 1.63 | 81 | 0.93 | 0.08 |
| 427 | 1.73 | 82 | 1.00 | 0.07 |
| 462 | 1.83 | 84 | 1.07 | 0.07 |
| 462 | 1.86 | 84 | 1.12 | 0.06 |
| 343 | 1.90 | 84 | 1.17 | 0.08 |
| 332 | 1.96 | 84 | 1.25 | 0.08 |
| 341 | 2.09 | 85 | 1.45 | 0.08 |
| 280 | 2.13 | 85 | 1.46 | 0.09 |
| 294 | 2.16 | 85 | 1.52 | 0.09 |
| 316 | 2.23 | 85 | 1.60 | 0.09 |
| 316 | 2.36 | 86 | 1.73 | 0.08 |
| 245 | 2.43 | 86 | 1.80 | 0.07 |
| 279 | 2.46 | 86 | 1.85 | 0.07 |
| 230 | 2.56 | 86 | 1.97 | 0.06 |
| 262 | 2.59 | 86 | 2 | 0.07 |
| 245 | 2.63 | 86 | 2.04 | 0.06 |
| 280 | 2.66 | 86 | 2.06 | 0.06 |
| 245 | 2.69 | 86 | 2.12 | 0.05 |
| 185 | 2.72 | 86 | 2.18 | 0.06 |
| 255 | 2.75 | 86 | 2.23 | 0.07 |
| 208 | 2.79 | 86 | 2.29 | 0.07 |
| 207 | 2.85 | 86 | 2.41 | 0.07 |

**Eccentricity Ratio of 0.5**

Table 8-6 TS6 04 eb 0.50 B1

| **F** | **$\delta z_{line}/B$** | **Θ** | **$\delta z_{plate}/B$** | **$\delta x/B$** |
|---|---|---|---|---|
| **(kN)** | **(-)** | **(°)** | **(-)** | **(-)** |
| 117 | 0.04 | 13 | 0 | 0 |
| 359 | 0.14 | 14 | 0.04 | 0.01 |
| 458 | 0.19 | 15 | 0.06 | 0.02 |
| 552 | 0.24 | 19 | 0.09 | 0.03 |
| 633 | 0.29 | 21 | 0.11 | 0.03 |
| 702 | 0.34 | 24 | 0.15 | 0.05 |
| 746 | 0.39 | 26 | 0.20 | 0.08 |
| 820 | 0.54 | 36 | 0.23 | 0.08 |
| 867 | 0.64 | 46 | 0.26 | 0.10 |
| 891 | 0.69 | 49 | 0.27 | 0.12 |
| 914 | 0.74 | 51 | 0.32 | 0.11 |
| 941 | 0.79 | 54 | 0.35 | 0.13 |
| 968 | 0.84 | 57 | 0.37 | 0.15 |
| 981 | 0.94 | 61 | 0.40 | 0.16 |
| 837 | 0.99 | 65 | 0.44 | 0.13 |
| 776 | 1.04 | 69 | 0.47 | 0.11 |
| 767 | 1.09 | 70 | 0.53 | 0.10 |
| 732 | 1.14 | 74 | 0.61 | 0.09 |
| 694 | 1.19 | 76 | 0.69 | 0.09 |
| 619 | 1.24 | 79 | 0.75 | 0.08 |
| 625 | 1.34 | 80 | 0.81 | 0.07 |

| F | $\delta z_{line}/B$ | Θ | $\delta z_{plate}/B$ | $\delta x/B$ |
|---|---|---|---|---|
| (kN) | (-) | (°) | (-) | (-) |
| 606 | 1.39 | 81 | 0.85 | 0.08 |
| 604 | 1.44 | 83 | 0.92 | 0.07 |
| 593 | 1.54 | 84 | 0.99 | 0.07 |
| 531 | 1.59 | 84 | 1.06 | 0.08 |
| 425 | 1.79 | 85 | 1.23 | 0.08 |
| 392 | 1.84 | 86 | 1.31 | 0.07 |
| 414 | 1.89 | 86 | 1.39 | 0.07 |
| 402 | 1.94 | 85 | 1.48 | 0.07 |
| 412 | 1.99 | 85 | 1.55 | 0.07 |
| 426 | 2.04 | 86 | 1.60 | 0.08 |
| 383 | 2.14 | 85 | 1.67 | 0.09 |
| 370 | 2.19 | 87 | 1.72 | 0.09 |
| 315 | 2.24 | 86 | 1.79 | 0.09 |

**Eccentricity Ratio of 0.5**

Table 8-7 TS6 06 eb 0.50 B1

| F | $\delta z_{line}/B$ | Θ | $\delta z_{plate}/B$ | δx/B |
|---|---|---|---|---|
| (kN) | (-) | (°) | (-) | (-) |
| 312 | 0.13 | 8 | 0 | 0 |
| 401 | 0.18 | 10 | 0.04 | 0 |
| 648 | 0.33 | 14 | 0.10 | 0.02 |
| 708 | 0.38 | 16 | 0.14 | 0.01 |
| 759 | 0.43 | 24 | 0.15 | 0.04 |
| 788 | 0.48 | 30 | 0.17 | 0.06 |
| 799 | 0.53 | 34 | 0.20 | 0.06 |
| 808 | 0.58 | 37 | 0.22 | 0.07 |
| 850 | 0.68 | 43 | 0.24 | 0.09 |
| 871 | 0.73 | 45 | 0.26 | 0.11 |
| 910 | 0.83 | 49 | 0.29 | 0.11 |
| 901 | 0.88 | 52 | 0.34 | 0.09 |
| 965 | 0.92 | 53 | 0.38 | 0.09 |
| 1015 | 0.97 | 59 | 0.39 | 0.10 |
| 882 | 1.08 | 63 | 0.43 | 0.10 |
| 827 | 1.18 | 72 | 0.55 | 0.06 |
| 716 | 1.28 | 75 | 0.75 | 0.06 |
| 640 | 1.38 | 77 | 0.94 | 0.07 |
| 493 | 1.58 | 81 | 1.15 | 0.07 |
| 588 | 1.68 | 81 | 1.39 | 0.06 |
| 563 | 1.73 | 82 | 1.41 | 0.07 |

| **F** | **$\delta z_{line}/B$** | **Θ** | **$\delta z_{plate}/B$** | **$\delta x/B$** |
|---|---|---|---|---|
| **(kN)** | **(-)** | **(°)** | **(-)** | **(-)** |
| 570 | 1.78 | 84 | 1.5 | 0.07 |
| 421 | 1.98 | 83 | 1.81 | 0.04 |

**Eccentricity Ratio of 0.75**

Table 8-8 TS4 01 eb 0.75 B2

| **F** | **$\delta z_{line}/B$** | **Θ** | **$\delta z_{plate}/B$** | **$\delta x/B$** |
|---|---|---|---|---|
| **(kN)** | **(-)** | **(°)** | **(-)** | **(-)** |
| 0 | 0 | 22 | 0 | 0 |
| 628 | 0.74 | 31 | 0.01 | 0 |
| 754 | 1.05 | 47 | 0.05 | 0.03 |
| 887 | 1.21 | 53 | 0.08 | 0.03 |
| 897 | 1.25 | 60 | 0.11 | 0.02 |
| 828 | 1.28 | 62 | 0.14 | 0.02 |
| 683 | 1.38 | 70 | 0.21 | 0.04 |
| 607 | 1.54 | 76 | 0.40 | 0.05 |
| 541 | 1.74 | 79 | 0.57 | 0.06 |
| 508 | 1.91 | 81 | 0.71 | 0.05 |
| 471 | 1.94 | 82 | 0.77 | 0.05 |
| 480 | 2.24 | 82 | 1.09 | 0.04 |
| 378 | 2.57 | 81 | 1.48 | 0.04 |
| 365 | 2.90 | 82 | 1.88 | 0.03 |
| 266 | 3.27 | 83 | 2.37 | 0.01 |

**Eccentricity Ratio of 0.75**

Table 8-9 TS4 02 eb 0.75 B2

| F | $\delta z_{line}/B$ | Θ | $\delta z_{plate}/B$ | δx/B |
|---|---|---|---|---|
| (kN) | (-) | (°) | (-) | (-) |
| 0 | 0 | 4 | 0 | 0 |
| 534 | 0.36 | 12 | 0.03 | 0.02 |
| 603 | 0.58 | 25 | 0.09 | 0.02 |
| 635 | 0.76 | 32 | 0.09 | 0.03 |
| 652 | 0.82 | 35 | 0.10 | 0.04 |
| 664 | 0.86 | 40 | 0.13 | 0.05 |
| 688 | 0.92 | 44 | 0.15 | 0.07 |
| 735 | 1.05 | 52 | 0.17 | 0.07 |
| 820 | 1.18 | 63 | 0.22 | 0.03 |
| 806 | 1.22 | 66 | 0.25 | 0.02 |
| 786 | 1.25 | 68 | 0.27 | 0.01 |
| 771 | 1.28 | 70 | 0.30 | 0.01 |
| 730 | 1.32 | 73 | 0.33 | 0.01 |
| 639 | 1.35 | 73 | 0.38 | 0.03 |
| 677 | 1.38 | 75 | 0.42 | 0.03 |
| 646 | 1.42 | 77 | 0.47 | 0.04 |
| 616 | 1.45 | 79 | 0.48 | 0.04 |
| 585 | 1.48 | 80 | 0.56 | 0.03 |
| 496 | 1.55 | 81 | 0.62 | 0.03 |
| 511 | 1.58 | 81 | 0.64 | 0.01 |
| 488 | 1.62 | 82 | 0.68 | 0.02 |

| F | $\delta z_{line}/B$ | Θ | $\delta z_{plate}/B$ | $\delta x/B$ |
|---|---|---|---|---|
| (kN) | (-) | (°) | (-) | (-) |
| 511 | 1.65 | 83 | 0.71 | 0.02 |
| 436 | 1.68 | 83 | 0.72 | 0.02 |
| 482 | 1.73 | 83 | 0.79 | 0.02 |
| 453 | 1.82 | 84 | 0.88 | 0.02 |
| 402 | 1.85 | 84 | 0.92 | 0.02 |
| 388 | 1.88 | 84 | 0.98 | 0.02 |
| 421 | 1.92 | 85 | 1.00 | 0.02 |
| 398 | 1.95 | 85 | 1.06 | 0.02 |
| 359 | 1.98 | 85 | 1.10 | 0.01 |
| 305 | 2.02 | 84 | 1.17 | 0.01 |
| 362 | 2.05 | 85 | 1.19 | 0.01 |
| 324 | 2.08 | 85 | 1.22 | 0 |
| 337 | 2.12 | 85 | 1.27 | 0 |
| 313 | 2.15 | 85 | 1.29 | 0.01 |
| 337 | 2.18 | 86 | 1.34 | 0 |
| 338 | 2.22 | 85 | 1.39 | 0.01 |
| 254 | 2.25 | 85 | 1.40 | 0.01 |

**Eccentricity Ratio of 0.75**

Table 8-10 TS7 01 eb 0.75 B1

| **F** | **$\delta z_{line}/B$** | **Θ** | **$\delta z_{plate}/B$** | **$\delta x/B$** |
|---|---|---|---|---|
| **(kN)** | **(-)** | **(°)** | **(-)** | **(-)** |
| 38.7 | 0.05 | 7.60 | 0 | 0 |
| 241.8 | 0.18 | 9.65 | 0.04 | 0.01 |
| 578.3 | 0.35 | 13.64 | 0.09 | 0.01 |
| 732.8 | 0.45 | 24.31 | 0.12 | 0 |
| 840.0 | 0.65 | 30.76 | 0.13 | 0 |
| 957.0 | 0.95 | 45.03 | 0.17 | 0.04 |
| 1116.1 | 1.12 | 56.79 | 0.22 | 0.09 |
| 1082.7 | 1.22 | 62.63 | 0.25 | 0.10 |

**Eccentricity Ratio of 0.75**

Table 8-11 TS7 03 eb 0.75 B1

| F | $\delta z_{line}/B$ | Θ | $\delta z_{plate}/B$ | δx/B |
|---|---|---|---|---|
| (kN) | (-) | (°) | (-) | (-) |
| 339 | 0.20 | 2 | 0.02 | 0 |
| 514 | 0.30 | 17 | 0.04 | 0.06 |
| 649 | 0.60 | 26 | 0.04 | 0.05 |
| 627 | 0.70 | 35 | 0.04 | 0.05 |
| 951 | 1.07 | 56 | 0.15 | 0.05 |
| 964 | 1.10 | 57 | 0.18 | 0.03 |
| 908 | 1.17 | 62 | 0.21 | 0.02 |
| 770 | 1.27 | 70 | 0.28 | 0 |
| 730 | 1.30 | 72 | 0.32 | 0 |
| 658 | 1.33 | 74 | 0.39 | 0 |
| 681 | 1.37 | 75 | 0.42 | 0 |
| 588 | 1.40 | 76 | 0.48 | 0.01 |
| 617 | 1.43 | 77 | 0.51 | 0.01 |
| 517 | 1.47 | 77 | 0.55 | 0.02 |
| 629 | 1.5 | 79 | 0.62 | 0.01 |
| 622 | 1.53 | 79 | 0.64 | 0.03 |
| 563 | 1.57 | 79 | 0.71 | 0.03 |
| 556 | 1.60 | 80 | 0.73 | 0.02 |
| 563 | 1.63 | 81 | 0.80 | 0.03 |
| 581 | 1.67 | 82 | 0.83 | 0.03 |
| 490 | 1.70 | 81 | 0.88 | 0.03 |

| F | $\delta z_{line}/B$ | Θ | $\delta z_{plate}/B$ | $\delta x/B$ |
|---|---|---|---|---|
| (kN) | (-) | (°) | (-) | (-) |
| 496 | 1.77 | 82 | 0.96 | 0.03 |
| 495 | 1.83 | 83 | 1.06 | 0.03 |
| 458 | 1.93 | 83 | 1.16 | 0.03 |
| 429 | 1.97 | 83 | 1.22 | 0.03 |
| 411 | 2 | 83 | 1.25 | 0.03 |
| 415 | 2.03 | 83 | 1.30 | 0.03 |
| 375 | 2.07 | 83 | 1.31 | 0.03 |
| 436 | 2.10 | 83 | 1.44 | 0.03 |
| 424 | 2.17 | 84 | 1.47 | 0.02 |
| 446 | 2.20 | 84 | 1.52 | 0.02 |
| 443 | 2.27 | 85 | 1.59 | 0.02 |
| 346 | 2.30 | 84 | 1.65 | 0.03 |
| 379 | 2.33 | 84 | 1.69 | 0.03 |
| 338 | 2.37 | 85 | 1.71 | 0.03 |
| 348 | 2.40 | 85 | 1.78 | 0.03 |
| 345 | 2.43 | 85 | 1.83 | 0.03 |
| 337 | 2.47 | 85 | 1.89 | 0.03 |
| 298 | 2.50 | 85 | 1.96 | 0.04 |
| 348 | 2.60 | 84 | 2.09 | 0.04 |
| 313 | 2.63 | 85 | 2.16 | 0.04 |
| 242 | 2.67 | 86 | 2.23 | 0.04 |
| 224 | 2.70 | 86 | 2.29 | 0.04 |
| 290 | 2.73 | 86 | 2.31 | 0.04 |

| **F** | **$\delta z_{line}/B$** | **Θ** | **$\delta z_{plate}/B$** | **$\delta x/B$** |
|---|---|---|---|---|
| **(kN)** | **(-)** | **(°)** | **(-)** | **(-)** |
| 211 | 2.80 | 86 | 2.37 | 0.04 |

**Eccentricity Ratio of 1**

Table 8-12 TS3 04 eb 1.00 B2

| **F** | **$\delta z_{line}/B$** | **Θ** | **$\delta z_{plate}/B$** | **$\delta x/B$** |
|---|---|---|---|---|
| **(kN)** | **(-)** | **(°)** | **(-)** | **(-)** |
| 0 | 0 | 3 | 0 | 0 |
| 128 | 0.12 | 6 | 0.03 | 0.12 |
| 458 | 0.42 | 14 | 0.06 | 0.27 |
| 487 | 0.55 | 21 | 0.07 | 0.17 |
| 504 | 0.65 | 23 | 0.09 | 0.15 |
| 531 | 0.75 | 27 | 0.10 | 0.25 |
| 581 | 0.88 | 36 | 0.13 | 0.16 |
| 596 | 0.98 | 41 | 0.13 | 0.04 |
| 617 | 1.05 | 46 | 0.14 | 0.25 |
| 630 | 1.08 | 47 | 0.14 | 0.19 |
| 645 | 1.12 | 51 | 0.15 | 0.21 |
| 668 | 1.15 | 54 | 0.15 | 0.32 |
| 691 | 1.18 | 55 | 0.16 | 0.31 |
| 757 | 1.25 | 58 | 0.17 | 0.25 |
| 805 | 1.29 | 60 | 0.19 | 0.12 |
| 857 | 1.35 | 63 | 0.19 | 0.04 |
| 860 | 1.38 | 65 | 0.21 | 0.20 |
| 817 | 1.42 | 67 | 0.23 | 0.55 |
| 762 | 1.45 | 69 | 0.26 | 0.99 |
| 712 | 1.48 | 72 | 0.28 | 1.34 |
| 682 | 1.52 | 74 | 0.32 | 1.71 |

| F | $\delta z_{line}/B$ | Θ | $\delta z_{plate}/B$ | $\delta x/B$ |
|---|---|---|---|---|
| (kN) | (-) | (°) | (-) | (-) |
| 574 | 1.55 | 75 | 0.36 | 1.92 |
| 629 | 1.58 | 76 | 0.40 | 2.20 |
| 574 | 1.62 | 77 | 0.42 | 2.30 |
| 587 | 1.65 | 78 | 0.44 | 2.41 |
| 516 | 1.68 | 80 | 0.50 | 2.56 |
| 555 | 1.72 | 81 | 0.53 | 2.48 |
| 487 | 1.75 | 81 | 0.57 | 2.62 |
| 521 | 1.78 | 81 | 0.59 | 2.65 |
| 461 | 1.85 | 82 | 0.68 | 2.75 |
| 444 | 1.88 | 82 | 0.73 | 2.63 |
| 426 | 1.95 | 82 | 0.80 | 2.76 |
| 394 | 1.98 | 83 | 0.81 | 2.69 |
| 446 | 2.02 | 83 | 0.86 | 2.74 |
| 404 | 2.05 | 84 | 0.88 | 2.65 |
| 426 | 2.08 | 84 | 0.94 | 2.93 |
| 413 | 2.12 | 83 | 0.95 | 2.68 |
| 388 | 2.15 | 84 | 0.99 | 2.56 |
| 348 | 2.18 | 84 | 1.04 | 2.64 |
| 381 | 2.22 | 84 | 1.05 | 2.52 |
| 303 | 2.25 | 84 | 1.09 | 2.58 |
| 330 | 2.28 | 84 | 1.10 | 2.63 |
| 374 | 2.32 | 84 | 1.15 | 2.67 |
| 357 | 2.35 | 84 | 1.20 | 2.76 |

| F | $\delta z_{line}/B$ | Θ | $\delta z_{plate}/B$ | $\delta x/B$ |
|---|---|---|---|---|
| (kN) | (-) | (°) | (-) | (-) |
| 338 | 2.38 | 84 | 1.21 | 2.72 |
| 285 | 2.42 | 85 | 1.25 | 2.63 |
| 337 | 2.45 | 85 | 1.27 | 2.65 |
| 316 | 2.58 | 85 | 1.38 | 2.78 |
| 273 | 2.62 | 85 | 1.43 | 2.81 |
| 288 | 2.68 | 85 | 1.51 | 2.93 |
| 289 | 2.72 | 85 | 1.54 | 2.66 |
| 285 | 2.75 | 85 | 1.58 | 2.99 |
| 234 | 2.79 | 86 | 1.64 | 2.72 |
| 237 | 2.82 | 87 | 1.65 | 2.74 |
| 239 | 2.85 | 86 | 1.71 | 2.80 |
| 255 | 2.95 | 86 | 1.81 | 2.93 |
| 219 | 2.98 | 86 | 1.83 | 2.93 |
| 237 | 3.05 | 86 | 1.91 | 2.85 |
| 199 | 3.08 | 86 | 1.96 | 2.64 |
| 192 | 3.18 | 86 | 2.01 | 2.41 |
| 191 | 3.22 | 86 | 2.01 | 2.74 |

**Eccentricity Ratio of 1**

Table 8-13 TS5 05 eb 1.00 B1

| F | $\delta z_{line}/B$ | Θ | $\delta z_{plate}/B$ | δx/B |
|---|---|---|---|---|
| (kN) | (-) | (°) | (-) | (-) |
| 0 | 0 | 8 | 0 | 0 |
| 509 | 0.32 | 13 | 0.02 | 0.01 |
| 567 | 0.38 | 17 | 0.03 | 0.02 |
| 622 | 0.52 | 19 | 0.05 | 0.02 |
| 631 | 0.58 | 22 | 0.06 | 0.02 |
| 641 | 0.65 | 27 | 0.07 | 0.01 |
| 654 | 0.72 | 29 | 0.08 | 0.01 |
| 676 | 0.82 | 34 | 0.08 | 0.02 |
| 686 | 0.88 | 42 | 0.10 | 0.03 |
| 841 | 1.15 | 51 | 0.12 | 0.03 |
| 956 | 1.22 | 57 | 0.15 | 0.07 |
| 1001 | 1.25 | 58 | 0.14 | 0.02 |
| 1041 | 1.32 | 61 | 0.15 | 0.01 |
| 1006 | 1.35 | 64 | 0.15 | 0.01 |
| 951 | 1.38 | 70 | 0.18 | 0.04 |
| 903 | 1.42 | 71 | 0.20 | 0.06 |
| 867 | 1.45 | 72 | 0.21 | 0.07 |
| 819 | 1.48 | 74 | 0.26 | 0.09 |
| 777 | 1.52 | 78 | 0.30 | 0.09 |
| 752 | 1.55 | 78 | 0.33 | 0.11 |
| 681 | 1.58 | 80 | 0.37 | 0.11 |

| F | $\delta z_{line}/B$ | Θ | $\delta z_{plate}/B$ | $\delta x/B$ |
|---|---|---|---|---|
| (kN) | (-) | (°) | (-) | (-) |
| 682 | 1.62 | 80 | 0.39 | 0.12 |
| 672 | 1.67 | 81 | 0.45 | 0.12 |
| 680 | 1.71 | 82 | 0.46 | 0.12 |
| 644 | 1.75 | 82 | 0.50 | 0.12 |
| 582 | 1.81 | 83 | 0.58 | 0.11 |
| 611 | 1.85 | 83 | 0.63 | 0.11 |
| 572 | 1.88 | 84 | 0.65 | 0.11 |
| 528 | 1.91 | 85 | 0.67 | 0.12 |
| 554 | 1.98 | 86 | 0.73 | 0.12 |
| 535 | 2.01 | 86 | 0.77 | 0.12 |
| 429 | 2.11 | 86 | 0.89 | 0.13 |
| 491 | 2.15 | 86 | 0.93 | 0.12 |
| 451 | 2.18 | 87 | 0.95 | 0.13 |
| 426 | 2.21 | 86 | 1 | 0.13 |
| 423 | 2.25 | 87 | 1.01 | 0.12 |
| 430 | 2.28 | 87 | 1.07 | 0.11 |
| 406 | 2.31 | 87 | 1.11 | 0.11 |
| 445 | 2.35 | 87 | 1.12 | 0.11 |
| 385 | 2.41 | 87 | 1.20 | 0.11 |
| 437 | 2.45 | 87 | 1.23 | 0.11 |
| 434 | 2.48 | 88 | 1.26 | 0.11 |
| 302 | 2.65 | 88 | 1.44 | 0.12 |
| 323 | 2.68 | 89 | 1.48 | 0.11 |

| **F** | **$\delta z_{line}/B$** | **Θ** | **$\delta z_{plate}/B$** | **$\delta x/B$** |
|---|---|---|---|---|
| **(kN)** | **(-)** | **(°)** | **(-)** | **(-)** |
| 283 | 2.75 | 89 | 1.52 | 0.10 |
| 295 | 2.85 | 88 | 1.64 | 0.10 |

**Eccentricity Ratio of 1**

Table 8-14 TS5 06 eb 1.00 B1

| F | $\delta z_{line}/B$ | Θ | $\delta z_{plate}/B$ | δx/B |
|---|---|---|---|---|
| (kN) | (-) | (°) | (-) | (-) |
| 0 | 0 | 3 | 0 | 0 |
| 480 | 0.22 | 11 | 0.03 | 0.03 |
| 691 | 0.38 | 16 | 0.05 | 0.03 |
| 756 | 0.55 | 23 | 0.07 | 0.03 |
| 762 | 0.72 | 34 | 0.09 | 0.04 |
| 801 | 0.85 | 40 | 0.10 | 0.03 |
| 835 | 0.92 | 44 | 0.10 | 0.03 |
| 877 | 0.98 | 49 | 0.11 | 0.02 |
| 1009 | 1.12 | 56 | 0.11 | 0.03 |
| 1117 | 1.18 | 58 | 0.12 | 0.03 |
| 1220 | 1.25 | 63 | 0.13 | 0.03 |
| 1316 | 1.35 | 65 | 0.17 | 0.05 |
| 1311 | 1.38 | 71 | 0.18 | 0.07 |
| 1237 | 1.42 | 72 | 0.18 | 0.07 |
| 1055 | 1.52 | 75 | 0.23 | 0.09 |
| 1008 | 1.55 | 77 | 0.25 | 0.10 |
| 998 | 1.58 | 79 | 0.28 | 0.12 |
| 948 | 1.62 | 79 | 0.32 | 0.12 |
| 868 | 1.65 | 81 | 0.36 | 0.13 |
| 910 | 1.71 | 83 | 0.40 | 0.14 |
| 872 | 1.75 | 83 | 0.45 | 0.14 |

| F | $\delta z_{line}/B$ | Θ | $\delta z_{plate}/B$ | $\delta x/B$ |
|---|---|---|---|---|
| (kN) | (-) | (°) | (-) | (-) |
| 708 | 1.78 | 83 | 0.48 | 0.14 |
| 843 | 1.81 | 84 | 0.50 | 0.12 |
| 751 | 1.85 | 84 | 0.54 | 0.14 |
| 708 | 1.88 | 83 | 0.57 | 0.15 |
| 769 | 1.91 | 85 | 0.61 | 0.15 |
| 731 | 1.95 | 85 | 0.65 | 0.14 |
| 671 | 1.98 | 85 | 0.71 | 0.13 |
| 686 | 2.01 | 84 | 0.72 | 0.12 |
| 639 | 2.05 | 84 | 0.76 | 0.12 |
| 476 | 2.08 | 84 | 0.78 | 0.13 |
| 639 | 2.11 | 85 | 0.82 | 0.14 |
| 500 | 2.15 | 85 | 0.88 | 0.13 |
| 587 | 2.18 | 85 | 0.88 | 0.13 |
| 568 | 2.21 | 87 | 0.94 | 0.13 |
| 523 | 2.35 | 85 | 1.10 | 0.11 |
| 514 | 2.61 | 88 | 1.34 | 0.18 |

**Eccentricity Ratio of 2**

Table 8-15 TS4 07 eb 2.00 B1

| **F** | **$\delta z_{line}/B$** | **Θ** | **$\delta z_{plate}/B$** | **$\delta x/B$** |
|---|---|---|---|---|
| **(kN)** | **(-)** | **(°)** | **(-)** | **(-)** |
| 0 | 0 | 4 | 0 | 0 |
| 307 | 0.43 | 6 | 0.01 | 0.01 |
| 306 | 0.63 | 10 | 0.01 | 0.01 |
| 328 | 0.76 | 14 | 0.02 | 0.01 |
| 338 | 0.93 | 17 | 0.02 | 0.01 |
| 340 | 1.20 | 24 | 0.02 | 0 |
| 361 | 1.47 | 31 | 0.03 | 0.01 |
| 384 | 1.74 | 40 | 0.03 | 0 |
| 538 | 2.40 | 55 | 0.06 | 0.02 |
| 596 | 2.50 | 62 | 0.09 | 0.03 |
| 652 | 2.56 | 65 | 0.08 | 0.03 |
| 751 | 2.66 | 68 | 0.09 | 0.03 |
| 786 | 2.70 | 70 | 0.09 | 0.03 |
| 808 | 2.73 | 74 | 0.11 | 0.04 |
| 812 | 2.76 | 75 | 0.12 | 0.05 |
| 807 | 2.80 | 77 | 0.13 | 0.07 |
| 801 | 2.83 | 78 | 0.16 | 0.09 |
| 787 | 2.86 | 79 | 0.18 | 0.10 |
| 751 | 2.90 | 81 | 0.23 | 0.12 |
| 680 | 2.93 | 82 | 0.26 | 0.15 |
| 633 | 2.96 | 83 | 0.30 | 0.15 |

| F | $\delta z_{line}/B$ | Θ | $\delta z_{plate}/B$ | $\delta x/B$ |
|---|---|---|---|---|
| (kN) | (-) | (°) | (-) | (-) |
| 611 | 3.00 | 84 | 0.32 | 0.15 |
| 599 | 3.03 | 84 | 0.36 | 0.15 |
| 597 | 3.06 | 84 | 0.41 | 0.17 |
| 598 | 3.10 | 85 | 0.44 | 0.17 |
| 494 | 3.16 | 86 | 0.50 | -0.18 |
| 588 | 3.20 | 86 | 0.52 | 0.17 |
| 523 | 3.23 | 87 | 0.57 | 0.19 |
| 463 | 3.26 | 87 | 0.61 | 0.19 |
| 553 | 3.30 | 87 | 0.63 | 0.18 |
| 506 | 3.33 | 87 | 0.67 | 0.18 |
| 414 | 3.36 | 88 | 0.68 | 0.19 |
| 459 | 3.40 | 88 | 0.74 | 0.18 |
| 435 | 3.43 | 88 | 0.74 | 0.18 |
| 467 | 3.46 | 88 | 0.77 | 0.20 |
| 406 | 3.50 | 88 | 0.82 | 0.19 |
| 385 | 3.53 | 89 | 0.83 | 0.19 |
| 438 | 3.56 | 88 | 0.87 | 0.19 |

**Eccentricity Ratio of 2**

Table 8-16 TS4 08 eb 2.00 B1

| **F** | **$\delta z_{line}/B$** | **Θ** | **$\delta z_{plate}/B$** | **$\delta x/B$** |
|---|---|---|---|---|
| **(kN)** | **(-)** | **(°)** | **(-)** | **(-)** |
| 0 | 0 | 7 | 0 | 0 |
| 0 | 0 | 8 | 0 | 0 |
| 242 | 0.41 | 12 | 0.02 | 0 |
| 299 | 0.61 | 21 | 0.02 | 0.01 |
| 359 | 1.11 | 35 | 0.01 | 0.01 |
| 399 | 1.51 | 46 | 0.02 | 0.01 |
| 461 | 1.71 | 53 | 0.04 | 0.01 |
| 517 | 1.81 | 58 | 0.02 | 0.04 |
| 559 | 1.88 | 61 | 0.04 | 0.03 |
| 735 | 2.08 | 71 | 0.10 | 0.02 |
| 751 | 2.11 | 72 | 0.11 | 0.02 |
| 758 | 2.15 | 74 | 0.15 | 0.03 |
| 747 | 2.18 | 76 | 0.18 | 0.03 |
| 676 | 2.28 | 79 | 0.29 | 0.07 |
| 622 | 2.31 | 77 | 0.34 | 0.07 |
| 560 | 2.35 | 78 | 0.35 | 0.08 |
| 553 | 2.38 | 78 | 0.39 | 0.09 |
| 534 | 2.41 | 79 | 0.41 | 0.08 |
| 503 | 2.45 | 78 | 0.45 | 0.10 |
| 583 | 2.48 | 78 | 0.51 | 0.11 |
| 496 | 2.51 | 78 | 0.52 | 0.12 |

| F | $\delta z_{line}/B$ | Θ | $\delta z_{plate}/B$ | $\delta x/B$ |
|---|---|---|---|---|
| (kN) | (-) | (°) | (-) | (-) |
| 584 | 2.55 | 78 | 0.57 | 0.11 |
| 459 | 2.58 | 78 | 0.59 | 0.12 |
| 551 | 2.61 | 79 | 0.64 | 0.12 |
| 476 | 2.65 | 79 | 0.66 | 0.12 |
| 465 | 2.71 | 79 | 0.72 | 0.12 |
| 444 | 2.76 | 79 | 0.77 | 0.13 |
| 513 | 2.81 | 79 | 0.78 | 0.13 |
| 498 | 2.88 | 79 | 0.85 | 0.14 |
| 492 | 2.91 | 79 | 0.89 | 0.13 |
| 397 | 2.95 | 79 | 0.90 | 0.13 |
| 469 | 2.98 | 79 | 0.96 | 0.13 |

**Eccentricity Ratio of 2**

Table 8-17 TS5 03 eb 2.00 B2

| **F** | **$\delta z_{line}/B$** | **Θ** | **$\delta z_{plate}/B$** | **$\delta x/B$** |
|---|---|---|---|---|
| **(kN)** | **(-)** | **(°)** | **(-)** | **(-)** |
| 0 | 0 | 17 | 0 | 0 |
| 348 | 0.62 | 27 | 0.02 | 0.01 |
| 389 | 0.92 | 33 | 0.03 | 0.02 |
| 494 | 1.30 | 44 | 0.05 | 0.01 |
| 546 | 1.42 | 46 | 0.05 | 0.02 |
| 667 | 1.62 | 53 | 0.05 | 0.03 |
| 779 | 1.75 | 59 | 0.05 | 0.02 |
| 930 | 1.88 | 63 | 0.06 | 0.04 |
| 1033 | 1.98 | 66 | 0.06 | 0.02 |
| 1062 | 2.05 | 70 | 0.08 | 0.02 |
| 1042 | 2.08 | 74 | 0.07 | 0.05 |
| 1002 | 2.11 | 76 | 0.07 | 0.06 |
| 966 | 2.15 | 77 | 0.10 | 0.08 |
| 921 | 2.18 | 78 | 0.12 | 0.09 |
| 856 | 2.21 | 79 | 0.14 | 0.10 |
| 796 | 2.25 | 80 | 0.17 | 0.11 |
| 761 | 2.28 | 82 | 0.19 | 0.12 |
| 733 | 2.31 | 82 | 0.23 | 0.11 |
| 679 | 2.35 | 83 | 0.26 | 0.12 |
| 662 | 2.38 | 83 | 0.28 | 0.13 |
| 667 | 2.41 | 84 | 0.29 | 0.13 |

| F | $\delta z_{line}/B$ | Θ | $\delta z_{plate}/B$ | $\delta x/B$ |
|---|---|---|---|---|
| (kN) | (-) | (°) | (-) | (-) |
| 651 | 2.45 | 84 | 0.33 | 0.14 |
| 640 | 2.50 | 84 | 0.36 | 0.13 |
| 605 | 2.55 | 85 | 0.39 | 0.13 |
| 550 | 2.58 | 85 | 0.43 | 0.12 |
| 571 | 2.71 | 85 | 0.52 | 0.13 |
| 450 | 2.78 | 87 | 0.58 | 0.13 |
| 526 | 2.81 | 87 | 0.62 | 0.13 |
| 530 | 2.85 | 88 | 0.64 | 0.12 |
| 414 | 2.88 | 88 | 0.67 | 0.12 |
| 526 | 2.91 | 88 | 0.72 | 0.11 |

**Eccentricity Ratio of 2**

Table 8-18 TS7 07 eb 2.00 B2

| **F** | **$\delta z_{line}/B$** | **Θ** | **$\delta z_{plate}/B$** | **$\delta x/B$** |
|---|---|---|---|---|
| **(kN)** | **(-)** | **(°)** | **(-)** | **(-)** |
| 17 | 0.02 | 18 | 0 | 0 |
| 137 | 0.12 | 27 | 0 | 0.01 |
| 354 | 0.88 | 35 | 0.01 | 0.02 |
| 363 | 1.08 | 42 | 0.01 | 0.02 |
| 401 | 1.28 | 46 | 0.02 | 0.01 |
| 435 | 1.38 | 50 | 0.02 | 0.01 |
| 509 | 1.58 | 56 | 0.01 | 0.02 |
| 552 | 1.68 | 61 | 0.02 | 0.03 |
| 711 | 1.88 | 67 | 0.03 | 0.04 |
| 828 | 1.98 | 71 | 0.02 | 0.03 |
| 948 | 2.08 | 78 | 0.08 | 0.04 |
| 987 | 2.15 | 83 | 0.13 | 0.04 |
| 945 | 2.18 | 84 | 0.16 | 0.05 |
| 912 | 2.22 | 85 | 0.20 | 0.06 |
| 876 | 2.25 | 85 | 0.24 | 0.06 |
| 833 | 2.28 | 87 | 0.28 | 0.07 |
| 762 | 2.32 | 87 | 0.32 | 0.07 |
| 704 | 2.35 | 87 | 0.35 | 0.07 |
| 697 | 2.38 | 87 | 0.39 | 0.07 |
| 658 | 2.42 | 88 | 0.41 | 0.07 |
| 582 | 2.45 | 89 | 0.46 | 0.07 |

| F | $\delta z_{line}/B$ | Θ | $\delta z_{plate}/B$ | $\delta x/B$ |
|---|---|---|---|---|
| (kN) | (-) | (°) | (-) | (-) |
| 592 | 2.48 | 89 | 0.48 | 0.07 |
| 543 | 2.53 | 89 | 0.52 | 0.07 |
| 562 | 2.58 | 89 | 0.58 | 0.07 |
| 527 | 2.62 | 89 | 0.59 | 0.07 |
| 490 | 2.65 | 90 | 0.65 | 0.07 |
| 466 | 2.68 | 90 | 0.66 | 0.06 |
| 577 | 2.72 | 90 | 0.71 | 0.06 |
| 490 | 2.75 | 90 | 0.72 | 0.06 |
| 453 | 2.78 | 89 | 0.77 | 0.05 |
| 426 | 2.82 | 89 | 0.80 | 0.04 |
| 544 | 2.85 | 90 | 0.84 | 0.04 |
| 438 | 2.88 | 90 | 0.88 | 0.03 |
| 449 | 2.92 | 91 | 0.89 | 0.02 |
| 516 | 2.95 | 90 | 0.94 | 0 |

# Appendix B

# Capacity and keying response of plate anchors in sand

C.D. O'Loughlin

*Centre for Offshore Foundation Systems, Perth, Australia*

B. Barron

*Institute of Technology Sligo, Sligo, Ireland*

**Abstract**

The capacity and keying behaviour of strip anchors in dense silica sand is examined in this paper through a series of centrifuge tests conducted at 30 g. Tests were conducted adjacent to the Perspex side panel of the centrifuge strongbox to facilitate optical observation and measurements of the keying response. Image analysis shows the failure mechanism to transition from a deep localised rotational mechanism to a shallow block mechanism extending to the soil surface. The onset of this transition coincides with the peak uplift resistance of the plate which occurs at approximately 65°. The uplift resistance of the plate as it becomes horizontal is in good agreement with a limit equilibrium solution that neglects the normality condition and assumes a failure mechanism that is broadly similar to the eventual failure mechanism of the plate after keying.

## 1. Introduction

Much work has been conducted in recent years on the capacity and keying behaviour of plate anchors in clay, with notable contributions from Gaudin et al. (2006), Song et al. (2009) and Yang et al. (2012). There have been very few corresponding studies in sand as clay is the dominant soil type in the deep water environment that plate anchors are currently used. However the foreseeable installation of floating wave energy converters and wind turbines in water depths typically less than 100 m will require anchoring systems that are suitable for sand deposits.

Prior studies on the performance of plate anchors in sand have either considered vertically loaded horizontal anchors (Figure 1a, e.g. Ovesen, 1981; Murray and Geddes, 1987; Dickin, 1994) or horizontally loaded vertical anchors (Figure 1b, e.g. Das et al., 1977, Rowe and Davis, 1982; Merifield and Sloan, 2006). To the authors' knowledge no studies have addressed vertically loaded vertical anchors (Figure 1c). In this problem the plate rotates or keys from a vertical to horizontal orientation before loading to failure as a vertically loaded horizontal anchor. This problem is addressed here through centrifuge model tests on a strip anchor in dense silica sand. This paper firstly describes in detail the experimental approaches adopted for these tests before presenting and discussing the results.

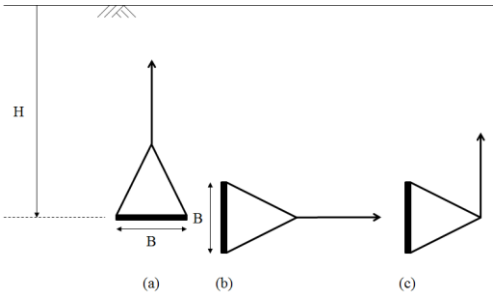


Figure 1. Problem notation: (a) vertically loaded horizontal anchors, (b) horizontally loaded vertical anchors, (c) vertically loaded vertical anchors.

## 2. Experimental Program

### *2.1 Institute of Technology Sligo Centrifuge*

The centrifuge tests were carried out using the recently commissioned Institute of Technology Sligo beam centrifuge, which is a 9 g-tonne beam centrifuge, that can spin two strongboxes at either end of a 0.75 m beam rotor at a maximum (effective radius) acceleration level of 300 g. The strongboxes adopted for this study are plane strain boxes with Perspex side panels and internal (sample) dimensions of 300 mm (length), 180 mm (depth) and 140 mm (width). Each strongbox acts as a counterweight to the other and doubles the available testing plan area (84,000 $mm^2$).

The centrifuge features a rotary stack that allows for the passage of fluid, air (2 channels) and electrical signals or power (16 slip rings). Although the number of rings is low, they are not required for data transfer as this is achieved using an extremely compact and robust wireless data acquisition system, described by Gaudin et al. (2009), allowing combined low and high speed (up to 1 MHz) sampling on 16 channels (expandable to 64 channels) at 16 bit resolution. A full technical description of the centrifuge is provided by O'Loughlin et al. (2010).

*2.2 Model anchors*

The model plate anchor and mandrel used for installation is shown on Figure 2 together with the geometrical notation adopted throughout this paper. The 3 mm stainless steel plate had a length, L = 140 mm and breadth, B = 20 mm. 3 mm thick plate was chosen to accommodate an 'O' ring at the plate-Perspex interface. The surface of the anchor was not treated and may be considered relatively smooth. As the model anchor spans the width of the centrifuge strongbox, the soil-Perspex interface constrains out-of-plane soil displacements at the anchor ends, such that the anchor exhibits plane strain behaviour. The anchor padeye was located on the triangular shank at an eccentricity, e = 20 mm from the centreline of the plate, such that the eccentricity ratio, e/B = 1.

*2.3 Sample preparation and characterisation*

Congleton sand was used in the centrifuge tests. It is a uniform silica sand ($C_u$ = 1.4) with rounded particles and a mean particle size ($D_{50}$) of 0.14 mm. The sand has a critical state friction angle, $\varphi'_{crit}$ = 32°, and density limits of $\rho_{max}$ = 1763 kg/m$^3$ and $\rho_{min}$ = 1461 kg/m$^3$ (Lauder, 2010; Bransby et al. 2010). Samples were prepared by compacting dry sand in 13 to 14 mm layers in the centrifuge strongbox at 1g. This preparation technique produced samples with relative densities that remain tolerably constant with depth and equal to $I_D$ = 91±2% between samples.

Prior to the anchor tests, two cone penetration tests (CPTs) were conducted in each strongbox to characterise the sample using a 10 mm diameter model CPT inserted at a rate of 1 mm/s. The CPTs were located along the centreline of the box (70 mm from the closest rigid boundary). As such the CPT location is less than the recommended minimum spacing of 10 times the cone diameter (Bolton et al., 1999). However as the CPT locations are the same in each sample the profiles serve as a useful indication of the repeatability of each sample. The CPT profiles for the three strongboxes considered in this paper are provided on Figure 3. As expected for a sample with constant $I_D$ with depth, the tip resistance increases linearly with increasing stress level after 3 to 4 cone diameters ($\sigma_v$ = 15 to 20 kPa). The good agreement between profiles both within and between strongboxes indicates that the preparation technique produced repeatable samples.

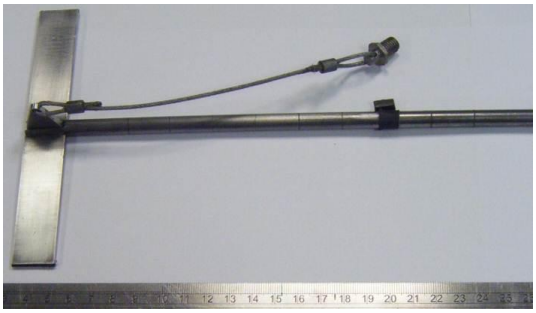

(a)

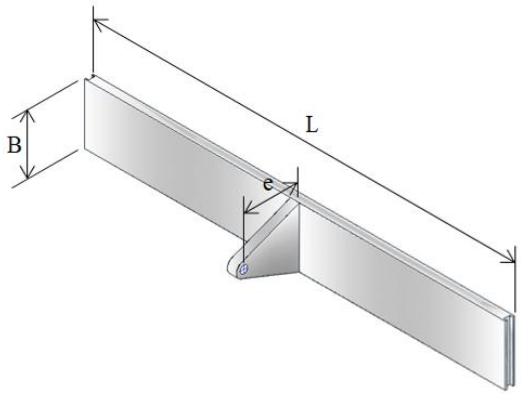


(b)

Figure 2. Model plate anchor: (a) photograph showing anchor and installation mandrel and (b) schematic and geometrical notation

*2.4 Testing arrangement and procedure*

To facilitate viewing and image capture during anchor keying, tests were conducted adjacent to Perspex panels. A digital camera was placed within a custom made cradle which supports the camera lens at high acceleration levels. The cradle was mounted securely on a bracket extending from the viewing face of the strongbox and oriented so the camera lens axis was perpendicular to the Perspex panel (see Figure 4).

A Canon S80 camera with 8 Mega Pixel resolution (3264 × 2448 pixels) was used for digital image capture. Synchronisation of the logged data and the captured images was achieved by logging the signal sent via the centrifuge sliprings to trigger the camera shutter and initiate continuous shooting.

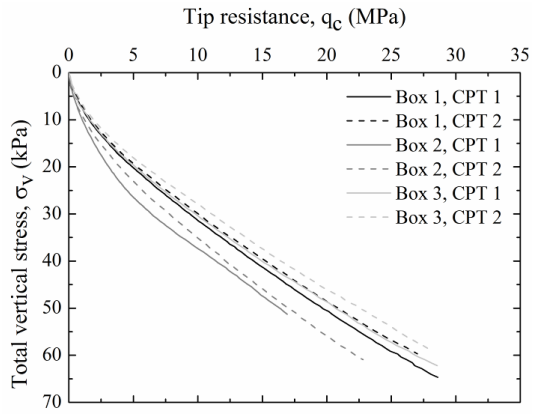


Figure 3. CPT profiles

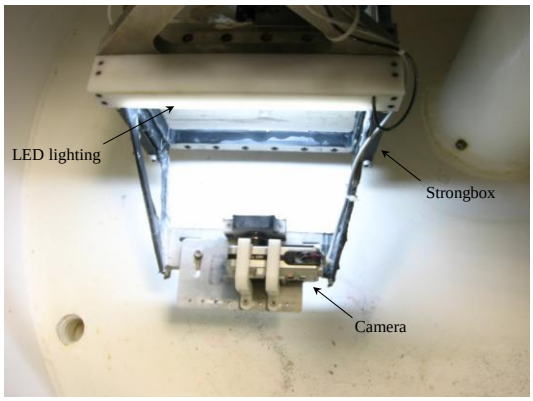


Figure 4. Testing arrangement in the centrifuge

Soil movements at the sand Perspex interface were determined from particle image velocimetry (PIV) analysis of the images captured during testing (White et al., 2003). The zone of interest from each digital image was divided into ~7,500 interrogation patches, each covering a zone of soil approximately 5 mm square. Each of these patches was tracked using a correlation algorithm to identify the movement of that patch of soil between a pair of images, with a measurement precision of 0.5 µm for the field of view used during these experiments.

The model anchor was installed in a vertical orientation at 1 g using a custom made installation mandrel (see Figure 2a) to a mid anchor depth, H = 100 mm (5B). This installation process caused a wedge of sand to translate vertically downwards with adjacent surface heave either side of the installation site (see Figure 5). This surface disturbance was not "repaired" after anchor installation as similar surface disturbance is also likely to occur in situ.

After removing the installation mandrel from the sample, the anchor line was attached to the linear actuator. As shown by Figure 5, the actuator was positioned directly over the vertically oriented plate, rather than the anchor padeye. The model was then transferred to the centrifuge and spun up to 30 g. The digital camera was then triggered remotely and the actuator moved vertically upwards at a rate of 1 mm/s.

Figure 5. Anchor installation at 1 g showing disturbance of the sample surface

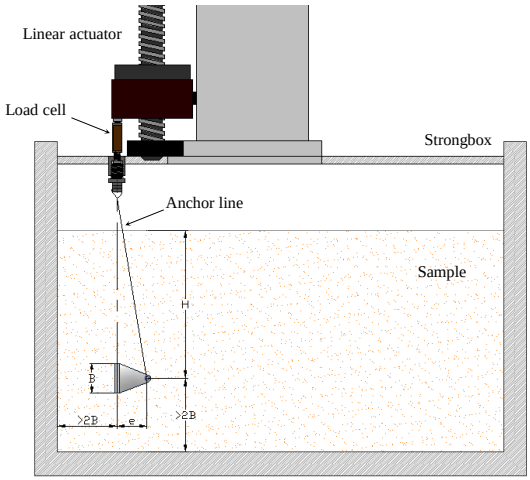


Figure 6. Position of anchor and actuator prior to anchor keying and pullout

In addition to the anchor tests conducted adjacent to the Perspex panel, a number of tests were conducted where the anchor was installed in the middle of the strongbox such that the anchor ends were not adjacent to the Perspex panels. These tests were included to provide load-displacement data that was not compromised by friction developing between the anchor ends and the Perspex. A total of six tests are considered in this paper; four where the anchor is tested adjacent to the Perspex panel and two where the anchor is tested in the interior of the strongbox.

## 3. Experimental Results and Discussion

### *3.1 Pullout response*

The load displacement response during anchor keying and pullout is shown on Figure 7. The response is typical of that for clay (e.g. Gaudin et al. 2006) with an initial stiff response as the anchor begins to rotate, followed by a softer

response as the rotation angle increases, and a final stiff response as the effective eccentricity of the padeye reduces and anchor capacity is fully mobilised. A softening response is evident after the peak load, with significant oscillation in the load (up to 200 N). These oscillations are typical of those observed in pullout tests of anchors and pipes in loose and dense sand (e.g. Trautmann et al., 1985; Dickin,1994; Cheuk et al., 2008) and is due to the progressive infilling of the void behind the anchor plate as it moves through the sand.

Interestingly the peak loads measured during tests conducted in the interior of the strongbox are similar to those measured during tests conducted adjacent to the Perspex panel, indicating that the friction between the anchor ends and the Perspex is small relative to the bearing resistance of the plate. Similar findings were reported by Gourvenec and O'Loughlin (2006), who showed similar bearing resistance profiles for half model footing tests conducted adjacent to a Perspex panel and full footing model footing tests conducted in the interior of the strongbox. Hence it is reasonable to use the load data from the tests conducted adjacent to the Perspex panel.

The actuator displacement to the peak load in Figure 7 is 27.2 ±1.2 mm. However this displacement represents the travel of the anchor padeye rather than the vertical loss in embedment of the plate during keying. The loss in embedment of the plate anchor during keying is more conveniently determined from the images captured during the tests and is in the range $\Delta z_e$ = 3.7 to 4.3 mm or $\Delta z_e/B$ = 0.19 to 0.22. Interestingly this is within the range, $\Delta z_e/B$ = 0.09 to 0.22 reported by O'Loughlin et al. (2006) for plate anchors in clay with the same e/B = 1 ratio. However in the latter case the loss in embedment to the peak load also corresponded with completion of keying, whereas for the tests reported here the plate orientation to the vertical was in the range 60 to 65°. This is discussed further in the following section.

*3.2 Deformation mechanisms*

Figure 8 shows the load – displacement response for Test 4 together with plate rotation angles (θ, measured to the vertical) at various stages of the keying and pullout response. The plate rotation angles were determined from the digital images of the sand-Perspex interface shown on Figure 9 for points A to F (corresponding with Figure 8). A schematic overlay of the anchor and the loading direction is also shown for clarity. In comparing Figure 8 and Figure 9 it is evident that the plate anchor does not fully key when it reaches peak capacity. The plate rotates from the initial quasi-vertical orientation to θ = 61° (to the vertical) at the peak load. Beyond this load the anchor continues to rotate during post peak softening, reaching an orientation of θ = 84° (at point F) and gradually increasing to θ ≈ 90° over the remainder of the pull-out.

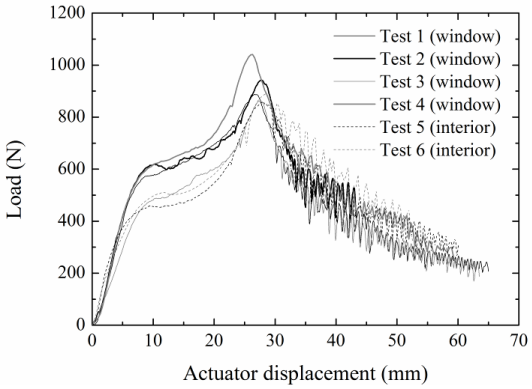


Figure 7. Load displacement response during keying and pullout

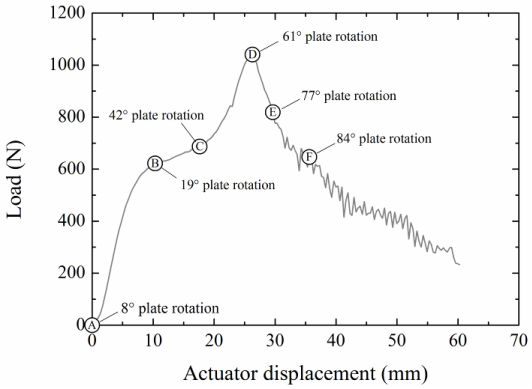


Figure 8: Load – displacement response for Test 4 showing plate rotation at various stages during keying

The reason why the peak load does not correspond with the maximum projected area becomes evident after examining the soil surface on Figure 9 for each stage of the pullout. As the load increases towards the peak load, soil movements are deep and localised to the plate. However when the peak load is reached (point D on Figure 8) heave at the soil surface is evident, becoming more prominent as the

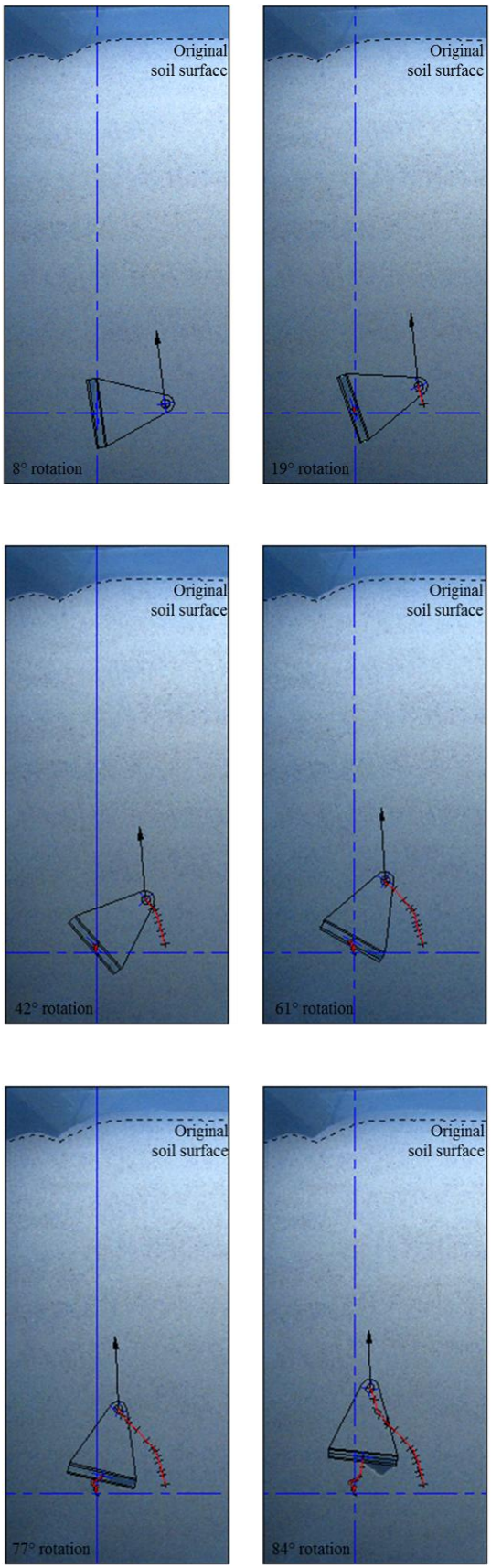


Figure 9: Images from Test 4 at various rotation angles during keying the plate continues to key (points E and F). This indicates that the failure mechanism transitions from a deep localised mechanism to a shallow mechanism extending to the soil surface at approximately 60° plate rotation.

PIV analyses of images pairs selected before and at the peak load demonstrate the mechanism transition quite clearly. Figure 10 shows the instantaneous velocity fields for Test 3. The "pre-peak" deformation mechanism ($\theta$ = 46°, $F/F_{peak}$ = 71%) is shown on Figure 10a and is characterised by localised flow-around soil movements at the plate, similar to flow-around mechanisms observed by Gaudin et al (2006) during keying of plate anchors in clay. Figure 10b shows the deformation mechanism at the peak load ($\theta$ = 64°). The mechanism is now dominated by soil movements extending from the plate to the soil surface and explains the onset of heave at the ground surface for Test 4 (Figure 9d). Although asymmetrical due to the inclination of the plate, the inclined slip plane is curved rather than straight, reflecting an increase in the dilation angle at the lower stress levels close to the ground surface. The inclination of the left slip plane, relative to a line orthogonal to the plate, is in the range 6 to 11°, whereas the right slip plane is vertical, making an angle of 26° to a line orthogonal to the plate. Normality requires that the soil dilates at an angle equal to the friction angle. Normality is evidently violated here as the soil is dilating at an angle less than or equal to 26°, which is much lower than the peak friction angle of 44° (Lauder, 2010) and lower than the critical friction angle of 32°.

*3.3 Comparisons of experimental break-out factors with theoretical solutions*

The uplift resistance of a vertically loaded horizontal anchor may be expressed in terms of an anchor breakout factor, $N_\gamma$:

$$N_\gamma = \frac{P}{H\gamma' B} \qquad (1)$$

where P is the uplift resistance per unit length, H is the depth to the plate anchor (as defined in Figure 6), $\gamma'$ is the effective unit weight of the soil and B is the breadth of the anchor plate (as defined in Figure 2).

Values of $N_\gamma$ are generally obtained from finite element analyses (e.g. Merrifield and Sloan, 2006), plasticity solutions (e.g. Equation 2; Ng and Springman, 1994) and limit equilibrium solutions (e.g. Equation 3; White et al., 2008).

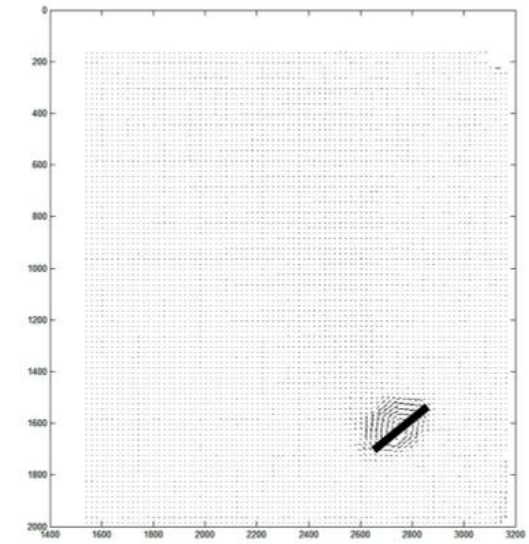

(a)

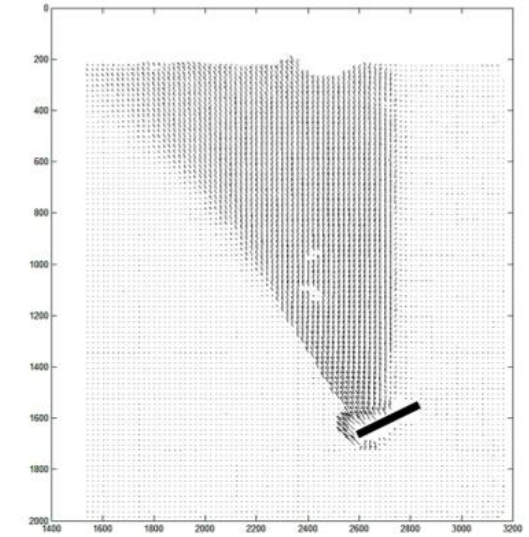

(b)

Figure 10: Instantaneous velocity field for Test 3: (a) at 71% of the peak load (θ = 46°), and (b) at the peak load (θ = 64°); note axes are in pixels

$$N_\gamma = 1 + \frac{H}{B}\tan\varphi \qquad (2)$$

$$N_\gamma = 1 + F_{up}\frac{H}{B} \qquad (3)$$

where $F_{up}$ is a function of the peak friction angle, $\varphi_{peak}$, the dilation angle, $\psi$ and the at rest earth pressure coefficient, $K_0 = 1 - \sin\varphi_{crit}$.

$$F_{up} = \tan\psi + \left(\tan\varphi_{peak} - \tan\psi\right)\left[\frac{1+K_0}{2} - \frac{1-K_0\left(\cos 2\psi\right)}{2}\right] \qquad (4)$$

Equations 2 and 3 are plotted on Figure 11 together with back figured values of $N_\gamma$ from Tests 3 and 4 and other available data in the literature for pipes and plate anchors in dense sand. The dilation angle required for Equation 4 was selected using Bolton's (1986) correlations that link dilation angle to relative density and grain-crushing strength, relative to the mean effective stress. $N_\gamma$ derived from finite element analyses and reported by Merrifield and Sloan (2006) are essentially identical to those produced by Equation 2 are for clarity are not show on Figure 11. The back figured $N_\gamma$ from the tests reported here were calculated using the following slightly modified form of Equation 1:

$$N_\gamma = \frac{P}{H\gamma' B\sin\theta} \qquad (5)$$

where the sin θ term accounts for the varying inclination of the plate during keying, which effectively reduces the area presented in the direction of the quasi-vertical loading.

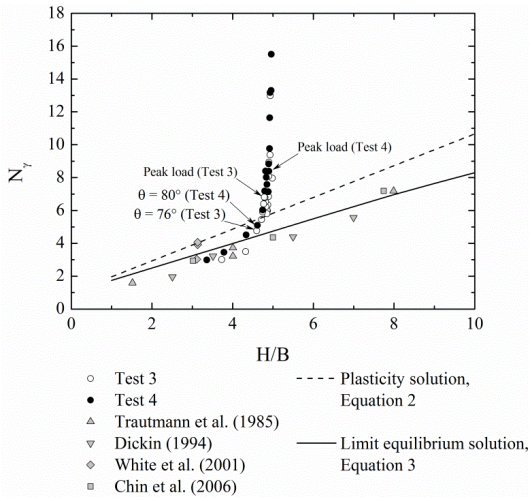


Figure 11: Comparison of back figured $N_\gamma$ from Tests 3 and 4 with other experimental data and theoretical solutions

Back figured $N_\gamma$ from Tests 3 and 4 are seen to approach the theoretical and experimental range on Figure 11 after the peak load is exceeded and the plate approaches a horizontal orientation (i.e. consistent with the other experimental and theoretical data on Figure 11). After θ = 76° (Test 3) and θ = 80° (Test 4) the best agreement is with the limit equilibrium solution proposed by White et al. (2008). This is to be expected as this solution assumes $\varphi \neq \psi$ and a failure mechanism that is broadly similar to the eventual mechanism reached in the plate anchor tests reported here. Conversely the Ng and Springman (1994) plasticity solution predicts higher uplift resistance as a result of the higher dilation angle required by the normality condition and hence a larger soil mass mobilised in uplift.

## 4. Conclusions

The keying behaviour of plate anchors in dense silica sand has been examined through centrifuge tests. Image analysis allowed the

rotation and position of the plate to be tracked during loading. The most striking observation from the tests was the failure mechanism transition during keying, from a deep localised rotational mechanism to a shallow block mechanism extending to the soil surface. This transition coincided with the peak resistance of the plate and occurred when the plate was approximately 65° to the vertical. A limit equilibrium solution proposed by White et al. (2008) in which normality is neglected, predicts the plate uplift resistance satisfactorily when the plate approaches a horizontal inclination.

**References**


Bolton, M.D. (1986). The strength and dilatancy of sands. *Géotechnique*, 36(1), 65–78.

Bolton, M.D., Gui, M.W., Garnier, J., Corte, J.F., Bagge, G., Laue, J. and Renzi, R. (1999). Centrifuge cone penetration tests in sand. *Géotechnique*, 49(4), 543–552.

Bransby, M.F., Brown, M., Hatherly, A. and Lauder, K. (2010). Pipeline plough performance in sand waves. Part 1: model testing. *Canadian Geotechnical Journal*, 47, 49–64.

Cheuk, C.Y., White, D.J. and Bolton, M.D. (2007). Uplift mechanisms of pipes buried in sand. *ASCE Journal of Geotechnical and Geoenvironmental Engineering*, 134(2), 154–163.

Chin, E.L., Craig, W.H. and Cruickshank, W. (2006). Uplift resistance of pipelines buried in cohesionless soil. *Proceedings of the 6th International Conference on Physical Modelling in Geotechnics*, 723–728.

Das, B.M., Seeleye, G.R. and Das, S.C. (1977). Ultimate resistance of deep vertical anchor in sand. *Soils and Foundations*, 17(2), 52–56.

Dickin, E.A. (1994). Uplift resistance of buried pipelines in sand. *Soils and Foundations*, 34(2), 41–48.

Gaudin C, O'Loughlin C.D., Randolph M.F. and Lowmass A.C. (2006). Influence of the installation process on the performance of suction embedded plate anchors. *Géotechnique*, 56(6), 38–391.

Gaudin, C., Randolph, M.F. and O'Loughlin, C.D. (2006). New insights from model tests of foundation and anchoring systems in offshore geomechanics. *Proceedings of the 6th International Conference on Physical Modelling in Geotechnics*, Hong Kong, 1, 47 – 61.

Gaudin, C., White, D.J., Boylan, N., Breen, J., Brown, T., De Catania, S. and Hortin, P. (2009). A wireless high-speed data acquisition system for geotechnical centrifuge model testing. *Measurement Science and Technology*, 20(9), 1–11.

Gaudin, C., Simkin, M. White, D.J. and O'Loughlin, C.D. (2010). Experimental investigation into the influence of keying flap on keying of plate anchors. *Proceedings of the 20th International Offshore and Polar Engineering Conference*, Beijing, China.

Gourvenec, S. and O'Loughlin, C.D. (2006). Drum centrifuge tests of shallow skirted foundations on soft clay. *Proceedings of the 6th International Conference on Physical Modelling in Geotechnics*, Hong Kong, 1, 645–650.

Lauder, K. (2010). The performance of pipeline ploughs. PhD Thesis, University of Dundee.

Merifield, R.S. and Sloan, S.W. (2006). The ultimate pullout capacity of anchors in frictional soils. *Canadian Geotechnical Journal*, 43(8), 852–868.

Murray, E. J. & Geddes, J. D. (1987). Uplift of anchor plates in sand. *ASCE Journal of Geotechnical Engineering* 113(3), 202–215.

Ng, C.W.W. and Springman, S.M. (1994). Uplift resistance of buried pipelines in granular materials. *Proceedings of the International Conference Centrifuge 94*, 753–758.

O'Loughlin, C.D., Lowmass, A., Gaudin, C., and Randolph, M.F. (2006). Physical modelling to assess keying characteristics of plate anchors. *Proceedings of the 6th International Conference on Physical Modelling in Geotechnics*, Hong Kong, 1, 659–665.

O'Loughlin, C.D., Naughton, P., Baker, N. and Ainsworth, A. (2010). Establishing a beam centrifuge facility at the Institute of Technology, Sligo, Ireland. *Proceedings of the 7th International Conference on Physical Modelling in Geotechnics*, Zurich, Switzerland.

Ovesen, N.K. (1981). Centrifuge tests of the uplift capacity of anchors. *Proceedings of the 10th International Conference on Soil Mechanics and Foundation Engineering*, Stockholm, 1, 717–722.

Rowe, R.K. and Davis, H. (1982). The behaviour of anchor plates in sand. *Géotechnique* 32(1), 25–41.

Song, Z., Hu, Y., O'Loughlin, C.D. and Randolph, M.F. (2009). Loss in anchor embedment during plate anchor keying in clay. *ASCE Journal of Geotechnical and Geoenvironmental Engineering*, 135 (10), 1475–1485.

Trautmann, C.H., O'Rourke, T.D. and Kulhawy, F.H. (1985). Uplift force–displacement response of buried pipe. *ASCE Journal of Geotechnical Engineering*, 111(9), 1061–1076.

White, D.J., Barefoot, A.J. and Bolton, M.D. (2001). Centrifuge modelling of upheaval buckling in sand. *International Journal of Physical Modelling in Geotechnics*, 2, 19–28.

White, D.J., Take, W.A. and Bolton, M.D. (2003). Soil deformation measurement using particle image velocimetry (PIV) and photogrammetry. *Géotechnique* 53(7), 619–631.

White, D.J., Cheuk, C.Y. and Bolton, M.D. (2008). The uplift resistance of pipes and plate anchors buried in sand. *Géotechnique* 58(10), 771–779

Yang, M., Aubeny, C.P. and Murff, J.D. (2012). Behavior of suction embedded plate anchors during keying process. *ASCE Journal of Geotechnical and Geoenvironmental Engineering*, 138(2), 174–183.